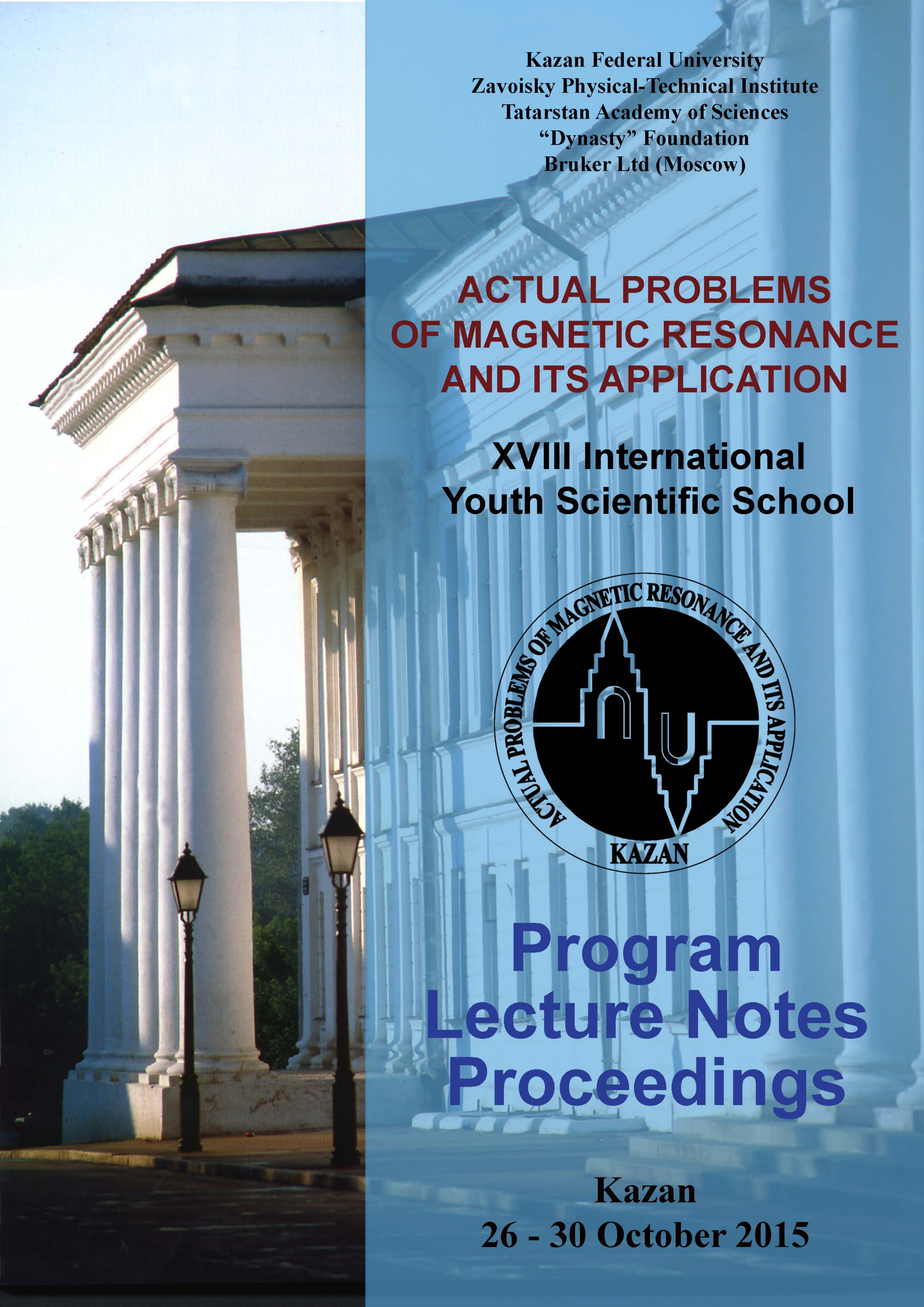

Kazan Federal University
Zavoisky Physical-Technical Institute
Tatarstan Academy of Sciences
"Dynasty" Foundation
Bruker Ltd (Moscow)

ACTUAL PROBLEMS OF MAGNETIC RESONANCE AND ITS APPLICATION

XVIII International Youth Scientific School

Program
Lecture Notes
Proceedings

Kazan
26 - 30 October 2015

Kazan Federal University
Zavoisky Physical-Technical Institute
Tatarstan Academy of Sciences
“Dynasty” Foundation
Bruker Ltd (Moscow)

ACTUAL PROBLEMS OF MAGNETIC RESONANCE AND ITS APPLICATION

XVIII International Youth Scientific School

Program
Lecture Notes
Proceedings

Kazan
26 – 30 October 2015

KAZAN
2015

UDC 537
LBC 22.334
A 19

The administration of School

Professor M.S. Tagirov (KFU, Kazan) — rector
Professor V.A. Zhikharev (KSTU, Kazan) — vice-rector
V.K. Voronkova (KFTI RAS, Kazan) — scientific secretary
I.P. Volodina (KFU, Kazan) — secretary

The program committee

The chairman
Professor V.A. Atsarkin (IREE, Moscow)

Committee members

Professor A.V. Aganov (KFU, Kazan)
Professor I.A. Garifullin (KFTI RAS, Kazan)
Academician of RAS K.M. Salikhov (KFTI RAS, Kazan)
Professor V.D. Skirda (KFU, Kazan)
Professor L.R. Tagirov (KFU, Kazan)

The organizing committee

M.S. Tagirov, V.A. Zhikharev, I.P. Volodina, I.G. Motygullin, A.V. Klochkov,
V.V. Semashko, A.S. Nizamutdinov, A.K. Naumov, E.M. Alakshin, I.V. Romanova,
O.N. Chibisova, M.P. Rodionova, R.R. Gazizulin, E.I. Kondratyeva, T.R. Safin,

A19 **Actual problems of magnetic resonance and its application:** program lecture notes proceedings of the XVIII International Youth Scientific School (Kazan, 26 – 30 October 2015) / edited by M.S. Tagirov, V.A. Zhikharev. – Kazan: Kazan University Press, 2015. – 148 p.

ISBN 978-5-00019-490-4

The reports of young scientists submitted on XVIII International Youth Scientific School “Actual problems of magnetic resonance and its application” carry out by Kazan Federal University and Zavoisky Physical-Technical Institute are included in the present collection.

UDC 537
LBC 22.334

ISBN 978-5-00019-490-4

Program

Monday, October 26

Conference Hall of Lobachevsky Scientific Library

8:30 **Registration**
10:00 – 10:30 **Opening Ceremony of School-2015**

Lectures

Conference Hall of Lobachevsky Scientific Library

10:30 – 11:15 **Yu.M. Bunkov** (Grenoble, France), “The difference between BEC of quasiparticles (magnons) and elementary particles”

11:15 – 12:00 **E.B. Fel’dman** (Chernogolovka, Moscow region, Russia), “Multiple quantum NMR in one-dimensional and nanoscale systems: theory, computer simulations and experimental investigations”

12:00 – 13:00 **Lunch**

Oral Session

Conference Hall of Lobachevsky Scientific Library

13:00 – 13:15 **T. Salikhov,** “Nuclear magnetic resonance in low-dimensional compound $A_3Ni_2SbO_6$ (A = Na, Li)”

13:15 – 13:30 **M.R. Mohebbifar,** “The energy shift of one level quantum dot that interact with two leads”

13:30 – 13:45 **D. Shurtakova,** “Spin-lattice relaxation of NO_3^{2-} complexes and Mn^{2+} ions in hydroxyapatite”

13:45 – 14:00 **A.A. Sukhanov,** “Influence of minor changes of ligand environment of Dy^{3+} on the magnetic properties of single molecule magnets based on Me_2Dy_2 heteronuclear complexes”

14:00 – 14:15 **E.I. Kondratyeva,** “Magnetic resonance studies of heat treated wood”

14:15 – 14:30 **E.A. Arkhipova,** “High resolution NMR spectroscopy of water-soluble p-tert-butylthiacalix[4]arenes”

14:30 – 14:45 **L.B. Magomedova,** “Studies of self-diffusion of p-tert-butylthiacalix[4]arene based water soluble compounds”

14:45 – 15:00 **K.M. Yunusova,** “Spin relaxation of NV^- center in diamond”

15:00 – 15:30 **Coffee break**

15:30 – 15:45 **I.V. Yatsyk,** “Magnetic properties in nanocomposite materials $(SrFe_{12}O_{19})_x(CaCu_3Ti_4O_{12})_{1-x}$”

15:45 – 16:00 **I.I. Gimazov,** “Electron spin resonance study of the demagnetization fields of the ferromagnetic and paramagnetic films”

16:00 – 16:15 **M.A. Fayzullin,** “Temperature dependence of ESR linewidth and spin-spin correlation functions in one dimensional magnets”

16:15 – 16:30 **A.V. Alekseev,** “FMR investigation of magnetic anisotropy in ion-beam synthesized thin iron silicide films”

16:30 – 16:45 **A.A. Stanislavovas,** “Separation of ^3He from $^3He – ^4He$ mixture using adsorption for NMR investigation”

16:45 – 17:00 **I.A. Goenko,** “ESR study of electron-beam-irradiated calcium gluconate”

17:00 – 17:15 **A.M. Kusova,** “Studying nutation effects with pulsed EPR techniques”

17:15 – 17:30 **T.R. Safin,** “CW magnetic resonance investigations of $MnCO_3$”

18:00 **Welcome Party**

Tuesday, October 27

Lectures

Conference Hall of Lobachevsky Scientific Library

9:00 – 9:45 **V.A. Atsarkin** (Moscow, Russia), “Spin currents in the ferromagnet-metal structures”

9:45 – 10:30 **V.V. Fedorov (**St. Petersburg, Russia), “A neutron spin precession in noncentrosymmetric crystals in vicinity of the Bragg resonance. New feasibility of a search for neutron EDM”

10:30 – 11:00 **Coffee break**

Oral Session

Conference Hall of Lobachevsky Scientific Library

11:00 – 11:15 **A.I. Dmitriev,** “Anomalous spin dynamics near the spin-reorientation transition in ε-$In_{0.24}Fe_{1.76}O_3$ nanowires”

11:15 – 11:30 **Yu.Yu. Titova,** “Study of the formation of hydrogenation catalysts based on bis-(acetylacetonate)cobalt by ESR spectroscopy”

11:30 – 11:45 **T.A. Soldatov,** “Electron spin resonance in a model $S = 1/2$ chain antiferromagnet with a uniform Dzyaloshinskii–Moriya interaction $K_2CuSO_4Br_2$”

11:45 – 12:00 **R.V. Skoryunov,** “Nuclear magnetic resonance study of atomic motion in the complex hydride $Li_3(NH_2)_2I$”

12:00 – 12:15 **A.S. Poryvaev,** “Mobility and reactivity of 4-substituted TEMPO derivatives in metal-organic framework MIL-53(Al)”

12:15 – 12:30 **M.I. Gilmanov,** “New experimental method of measurement of ESR oscillating magnetization value in strongly-correlated metals”

12:30 – 12:45 **A. Germov,** “^{55}Mn NMR study of magnetic inhomogeneities in cubic perovskite-type manganite $Sr_{0.98}La_{0.02}MnO_3$”

12:45 – 13:00 **Yu.V. Krasnikova,** “Low temperature ESR in spin ladder with uniform Dzyaloshinskii-Moriya interaction”

13:00 – 14:00 **Lunch**

14:00 – 14:15 **A.A. Soldatov,** “The interaction between transverse and longitudinal resonant modes in polar phase of superfluid ^{3}He”

14:15 – 14:30 **D.A. Nevostruev,** “Charge recombination kinetics in P3HT/PC$_{60}$BM/5CB blend studied by light-induced EPR”

14:30 – 14:45 **A.N. Samarin,** “High frequency electron spin resonance in $Eu_{1-x}Gd_xB_6$ and $Eu_{1-x}Ca_xB_6$”

14:45 – 15:00 **D. Nazipov,** “Ab initio study of exchange interaction in $Lu_2V_2O_7$, $Y_2V_2O_7$”

15:00 – 15:15 **D.A. Mainichev,** “Analyzing ^{103}Rh NMR shielding in $[Cp^*{}_2Rh_2X_2]_2$ X = Cl, Br, I using spin-free localized molecular orbitals”

15:15 – 15:30 **D.R. Rudovskaya,** “Static and dynamic magnetic properties of quasi-2D Honeycomb lattice tellurates $A_2Ni_2TeO_6$ (A = Li, Na, K)”

15:30 – 15:45 **R.S. Denisov,** “EPR study of frustrated antiferromagnets A_2MnXO_4 (A = Li, Na, Ag; X = Si, Ge)”

16:00 – 18:00 Master-classes
Formation of groups for masters-classes will be made at registration.

Wednesday, October 28

Lectures

Conference Hall of Lobachevsky Scientific Library

9:00 – 9:45 **A.V. Klochkov** (Kazan, Russia), “NMR of ^{3}He in nanostructures”

9:45 – 10:30 **R.V. Yusupov** (Kazan, Russia), “Intrinsic vs impurity-indused features of $SrTiO_3$:Mn as probed by EPR”

10:30 – 11:00 **Coffee break**

Oral Session

Conference Hall of Lobachevsky Scientific Library

11:00 – 11:15 **A.S. Polovkova,** “Spin dynamics in layered triangular lattice antiferromagnet $MnSb_2O_6$”

11:15 – 11:30 **M.I. Stratan,** “Spin dynamics in quasi 2D-honeycomb-lattice tellurate $Na_2Co_2TeO_6$”

11:30 – 11:45 **A.V. Koshelev,** “ESR and magnetization measurements in honeycomb layered mineral urusovite $CuAl(AsO_4)O$”

11:45 – 12:00 **A.I. Chushnikov,** “EPR spectra peculiarities of sportsmen’s blood plasma”

12:00 – 12:15 **M.Yu. Zakharov,** “Synthesis of lanthanide trifluorides for magnetic resonance research”

12:15 – 12:30 **B.F. Gabbasov,** “Electric field effect in electron paramagnetic resonance of the $SrTiO_3$:Mn crystals”

12:30 – 12:45 **N.A. Tukmakova,** “Coherent precession of magnetization in yttrium iron garnet”

12:45 – 13:00 **M.G. Morozov,** “Selective multidimensional multinuclear NMR spectroscopy: radiofrequency pulse shapes in the MUSLE experiment”

13:00 – 14:00 **Lunch**

Assembly Hall of Kazan Federal University

15:00 Awarding Ceremony of Zavoisky Youth Scientific Prize Winners

Thursday, October 29

Lectures

Conference Hall of Lobachevsky Scientific Library

9:00 – 9:45 **M.V. Eremin** (Kazan, Russia), “$FeCr_2S_4$ as a new multiferroic material”

9:45 – 10:30 **N.A. Balakirev** (Kazan, Russia), “Computer simulation of 2D magnetic cluster growth”

10:30 – 11:15 **Coffee break**

11:15 – 12:00 **V.V. Kuzmin** (Paris, France), “Nonlinear NMR in highly polarised liquids”

12:00 – 12:45 **I.V. Romanova** (Kazan, Russia), “Simulations of equilibrium magnetic and magnetoelastic properties of non-conducting rare-earth compounds”

13:00 – 14:00 **Lunch**

14:00 **Closing Ceremony of School-2015**

Friday, October 30

Excursions

10:00 E.A. Eversmann Zoological Museum of KFU

13:00 A.A. Shtukenberg Geological Museum of KFU

Multiple quantum NMR in one-dimensional and nanoscale systems: theory, computer simulations and experimental investigations

E.B. Fel'dman

Institute of Problems of Chemical Physics of RAS,
Chernogolovka, 142432, Moscow region, Russia

e-mail: efeldman@icp.ac.ru

Multiple quantum (MQ) NMR spectroscopy is a powerful tool to study nuclear spin distributions in a great range of materials: liquid crystals, simple organic substances, amorphous hydrogenated silicon and many others [1]. It brings information about the dynamics of spin clusters and sheds light on quantum decoherence mechanisms in highly correlated spin states.

The free induction decay (FID), the most common observable in NMR, is determined by a small fraction of the density matrix elements due to a limited number of non-zero matrix elements of the spin projection operators. At the same time, the state of a spin system in the MQ NMR experiment is determined by all elements of the density matrix. Thus, MQ NMR experiments provide more information than the usual NMR [2]. In particular, this information resource can be used for the transfer of quantum information.

The dependence of the intensities of MQ NMR coherences on their orders (the profile of MQ NMR coherences) is an important characteristic of the above classes of systems because it contains a wealth of physical-chemical information. A simple combinatorial model [1] predicts a Gaussian profile of MQ NMR coherences. This conclusion was confirmed qualitatively in some experiments [1]. Since the model is based on very rough assumptions, one can expect discrepancies with experimental data in many cases. Numerous experimental data were reviewed in [3] and the authors found that the profiles of the MQ NMR intensities are rather exponential than Gaussian.

Our main goal is to create a full quantum-mechanical theory which would explain the observed profiles of the intensities of MQ NMR coherences. At this time, the problem cannot be solved for arbitrary three-dimensional spin systems. Thus, as a first step, we consider one-dimensional systems. We introduce a model of an isolated spin chain and show that the MQ NMR Hamiltonian of such a system is an XY Hamiltonian which can be diagonalized exactly in the approximation of the nearest neighbor interactions [4]. Eventually, we have found [4] that only the intensities of MQ NMR coherences of the zeroth and +/− second orders do not vanish. Such result means that the model does not yield a full solution to the problem. The situation does not change when we consider MQ NMR dynamics of one-dimensional systems at low temperatures and even in alternating spin chains in the approximation of the nearest neighbor interactions.

Next, we consider nanopore materials whose nanopores are filled with spin-carrying atoms (molecules). Since molecular spin diffusion is faster than spin flip-flop processes, one can average the dipole-dipole interactions (DDI) over molecular diffusion. The DDI coupling constants are the same for all spin pairs and we can investigate the MQ NMR dynamics in systems with several hundred spins [5]. Our numerical analysis showed that the profile of the intensities of the MQ NMR coherences is exponential in agreement with the experimental data [3].

In conclusion we note that modern NMR spectrometers have allowed us to perform experimental investigations of dynamics and relaxation in low-dimensional systems [6] which are in a good agreement with the developed theory [2, 4].

References

[1] 1.J. Baum, M. Munowitz, A.N. Garroway, and A. Pines, J. Chem. Phys**.,** **83**, 2015 (1985).

[2] E.B. Fel’dman, Applied magnetic resonance, **45**, 797 (2014).

[3] S. Lacelle, S.J. Hwang, B.G. Gerstein, J. Chem. Phys., **99**, 8407 (1993).

[4] S.I. Doronin, I.I. Maximov, E.B. Fel’dman, JETP, **91**, 597(2000)

[5] S.I. Doronin, A.V. Fedorova, E.B. Fel’dman, A.I. Zenchuk, J. Chem. Phys., **131**, 104109 (2009).

[6] S.I. Doronin, S.G. Vasil’ev, A.A. Samoilenko, E.B. Fel’dman, B.A. Shumm, JETP Letters, **101**,613 (2015).

Spin currents in the ferromagnet-metal structures

V.A. Atsarkin

Kotel’nikov Institute of Radio Engineering and Electronics RAS, 125009, 11 Mokhovaya Str., Moscow, Russia

e-mail: atsarkin@cplire.ru

Discovery and studying spin currents in multilayer structures opened a new area in spin physics, with great prospective for applications in nano-electronics and spintronics [1, 2]. In this lecture, a brief review is given on basic physical principles and the most important experimental techniques allowing producing and detection of spin currents in structures consisting of ferromagnetic and non-magnetic (“normal”) metals. Various methods of the spin-torque transfer are considered, including the polarized electric currents and spin Hall effect. The most attention is given to the “pure” spin currents produced by excitation of ferromagnetic resonance [3] and detected with the inverse spin Hall effect [4]. Experimental examples are demonstrated, both taken from literature [5] and obtained recently by the authors.

References

[1] Y. Tserkovnyak, A. Brataas, G. E. W. Bauer, B. I. Halperin, *Rev. Mod. Phys*. **77**, 1375 (2005)

[2] N. Locatelli, V. Cros and J. Grollier, *Nature Mater*. **13**, 11 (2014)

[3] A. Brataas, Y. Tserkovnyak, G. E. W. Bauer, B. I. Halperin, Phys. Rev. B **66**, 060404 (2002)

[4] E. Saitoh, M. Ueda, H. Miyajima, G. Tatara, Appl. Phys. Lett. **88**, 182509 (2006)

[5] H. L. Wang, C. H. Du, Y. Pu, R. Adur, P. C. Hammel, F. Y. Yang, Phys. Rev. Lett. **112**, 197201 (2014)

A neutron spin precession in noncentrosymmetric crystals in vicinity of the Bragg resonance. New feasibility of a search for neutron EDM

V.V. Fedorov[1,2,3], V.V. Voronin[1,2,3]

[1]Petersburg Nuclear Physics Institute NRC KI, 188300, Gatchina, Leningrad district, Russia
[2]St. Petersburg Polytechnical University, 195251, 29 Polytechnicheskaya st, St. Petersburg, Russia
[3]St. Petersburg State University, 199034, 7/9 Universitetskaya nab., St. Petersburg, Russia

e-mail: vfedorov@pnpi.spb.ru

1. Recently strong electric interplanar fields (up to 10^9 V/cm) have been discovered, which affect the neutrons moving in noncentrosymmetric crystals. The values of such fields depend on a momentum direction and energy of neutron in crystal reaching maxima in vicinities of the exact Bragg directions or energies. Such fields give rise for new polarization phenomena in the neutron diffraction and in the optics and provide, for instance, a new method of a search for the neutron electric dipole moment (EDM). Measurement of a spin precession angle for neutron, moving close to the Bragg condition through a thick crystal in such a strong electric field gives hope to improve the limits on the neutron EDM, achieved with the magnetic resonance method using ultra cold neutrons (UCN method).

2. The electric dipole moment of the neutron (nEDM) is one of a very sensitive probe for CP violation beyond the Standard Model of particle physics [1]. The importance of nEDM searches is additionally highlighted by an additional possibility to reach understanding a nature of baryon–antibaryon asymmetry in the Universe that is one of the most exciting puzzle in modern physics. The most precise experiments today use Ramsey’s magnetic resonance method and ultra cold neutrons (UCNs) [2,3]. Further progress is presently limited by systematics [4] and the low density of UCNs available. Here we discuss an alternative approach based on spin rotation in non-centrosymmetric crystals.

The statistical sensitivity of any experiment to measure the EDM is determined by the product $E\tau N^{1/2}$, where τ is the duration of the neutron interaction with the electric field E and N the number of the counted neutrons. New projects to measure the nEDM with UCNs aim to increase the UCN density and thus N by orders of magnitude [5] (see also Ref. [6] for a recent overview). In contrast, experiments with crystals exploit the electric field inside matter, which for some crystals can be by a few orders of magnitude higher than the electric field achievable in vacuum.

EDM experiments with absorbing crystals were pioneered by Shull and Nathans [7]. Their experiment was based on the interference of the electromagnetic amplitude with the imaginary part of the nuclear one. Abov with his colleagues [8] were the first who paid attention to the presence of a spin dependent term due to the interference of nuclear and spin–orbit parts of the structure amplitude in the interaction of neutrons with a noncentrosymmetric non-absorptive crystal. Spin rotation in noncentrosymmetric crystals due to such interference effects as a way to search for a nEDM was first discussed by Forte [9]. In our papers Refs. [10,11] we have shown that the interference of the nuclear and the electromagnetic parts of the structure amplitude leads to a constant strong electric field, acting on a neutron during all time of its movement in the non-centrosymmetric crystal. This field was measured first in a Laue geometry diffraction experiment [11], in agreement with the calculated value. Forte and Zeyen [12] attempt to test experimentally an interference of nuclear and spin–orbit structure amplitudes by measuring a spin rotation angle in a non-centrosymmetric crystal, but their measured result turned out to be a few times less than estimated one. Authors considered that the cause was the crystal imperfection. The neutron spin rotation in crystals can be studied in Bragg [8,11,12] and Laue [13–16] diffraction geometry. The more recent experimental situation was described in [17].

3. How do strong electric fields acting on a neutron in a non-centrosymmetric crystal arise? It should be noted first of all that the wave function of a diffracting neutron in a nonmagnetic crystal (as well as neutron-density distribution in the crystal) is determined exclusively by nuclear interaction. Thus, the periodic nuclear potential forms the diffraction pattern, while an electromagnetic interaction affects only the neutron spin (magnetic moment and EDM, which are both proportional to spin) without changing the spatial distribution of neutrons in the crystal.

Any potential of neutron interaction with a crystal (nuclear, electric, and so on) can be represented in the form of an expansion in the reciprocal-lattice vectors **g** as

$$V(\mathbf{r}) = \sum_a V_a(\mathbf{r}-\mathbf{r}_a) = \sum_g V_g e^{i\mathbf{gr}} = V_0 + \sum_g 2v_g \cos(\mathbf{gr}+\varphi_g), \tag{1}$$

where $V_a(\mathbf{r}-\mathbf{r}_a)$ is the potential of an individual atom; $\mathbf{r}_a$ is the atom position; $V_g = v_g\exp(i\varphi_g)$; and $g = 2\pi/d$, where d is the interplanar spacing. For the sake of simplicity, we disregard here absorption, in which case $V_g = V_{-g}^*$. The amplitudes for g harmonics are related to the total crystal potential by the equation

$$V_g = \int_{V=1} d^3r\, e^{-i\mathbf{gr}} V(\mathbf{r}), \tag{2}$$

In general, the potential of neutron interaction with a crystal is the sum of all possible potentials: the nuclear potential $V^N(\mathbf{r})$ is determined by distribution of the Fermi pseudopotentials (scattering lengths for neutrons interacting with nuclei of crystal atoms), the electric potential $V^E(\mathbf{r})$ is determined by distribution of charge in crystal. We should notice that the electromagnetic interaction of neutron with crystal is determined by potential $V^{EM}(\mathbf{r})$ associated with the Schwinger interaction of the magnetic moment of a moving neutron and its EDM with electric field $\mathbf{E}(\mathbf{r}) = -\nabla V^E(\mathbf{r})$ (not by electric potential $V^E(\mathbf{r})$ itself). We will consider two parts (nuclear and electric) of crystal potential:

$$V(\mathbf{r}) = V^N(\mathbf{r}) + V^E(\mathbf{r}).$$

For centrosymmetric crystal, by choosing a center of symmetry as the origin of coordinates, one can reduce to zero the phases of the amplitudes for all harmonics of the total potential (and of each potential individually): $\phi_g = \phi_g^N = \phi_g^E \equiv 0$, thereby, one renders all harmonics real-valued (with the result that all potentials become purely cosine). But for noncentrosymmetric crystals, there arises a nonzero shift between harmonics of potentials that belong to different types.

The electric field inside the crystal created by the system of crystallographic planes, which is characterized by the reciprocal-lattice vector **g**, is determined by the electric potential of this system of planes; that is,

$$\mathbf{E}(\mathbf{r}) = -grad\, V_g^E(\mathbf{r}) = 2v_g^E \mathbf{g} \sin(\mathbf{gr}+\varphi_g^E), \tag{3}$$

where v_g^E and ϕ_g^E are the amplitude and phase of the g harmonic of the crystal electric potential respectively. Hereafter, we will choose the origin of coordinates at the maximum of the nuclear potential harmonic; that is, $\phi_g^N = 0$. In non-centrosymmetric crystals, for some planes $\phi_g^E \neq 0$, and the positions of the maxima of electric and nuclear potentials are not coincident in space and are different for different **g**. We emphasize once again that namely the nuclear potential determines the propagation of neutrons in a crystal, so that the structure of the neutron wave function replicates the structure of the nuclear potential – in particular, the positions of the maxima and minima of the squared modulus of this function coincide with the positions of the maxima and minima of $V^N(\mathbf{r})$ (see fig.1).

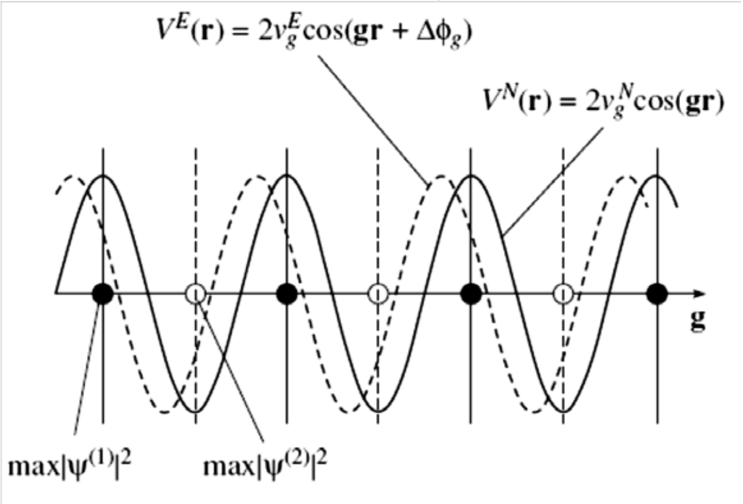

Fig.1. Nuclear and electric potentials of a non-centrosymmetric crystal. Neutrons, concentrating at minima (or maxima) of nuclear potential, will be in a strong electric field

It is easy to understand how such neutron concentration arises. In the first order of perturbation theory, the wave function for a neutron in a crystal under conditions close to Bragg's one can be represented in the form [19]:

$$\psi(\mathbf{r}) = e^{i\mathbf{kr}} + \frac{V_g^N}{E_k - E_{k_g}} e^{i\mathbf{k_g r}} \equiv e^{i\mathbf{kr}}\left[1 - \frac{U_g^N}{2\Delta_g} e^{i\mathbf{gr}}\right]. \tag{4}$$

Here, the phase of V_g^N is zero; $\mathbf{k}_g = \mathbf{k} + \mathbf{g}$; $E_k = \hbar^2k^2/2m$; $E_{k_g} = \hbar^2k_g^2/2m$; $V_g^N = \hbar^2U_g^N/2m$; $\Delta_g = (k_g^2 - k^2)/2$ is a parameter that characterizes the deviation from Bragg's conditions; and

$$|\psi(\mathbf{r})|^2 = 1 - \frac{U_g^N}{\Delta_g}\cos(\mathbf{gr}), \tag{5}$$

For a noncentrosymmetric crystal, a nonzero electric field arises in the region of the maximum neutron concentration — that is, in the region of maxima (or minima) of $|\psi(\mathbf{r})|^2$ (fig.1) because of the shift of the electric potential maxima with respect to the nuclear-potential ones. The strength of the field acting on neutrons can be determined by averaging (3) over the state (4); that gives

$$\mathbf{E} = \langle\psi(\mathbf{r})|\mathbf{E}(\mathbf{r})|\psi(\mathbf{r})\rangle = \frac{U_g^N}{\Delta_g}\cdot v_g^E\mathbf{g}\sin\phi_g^E \equiv \mathbf{E}_g\cdot\frac{U_g^N}{\Delta_g} \equiv \mathbf{E}_g\cdot\Delta_B, \tag{6}$$

where $\Delta_B \equiv U_g^N/\Delta_g$, is a dimensionless parameter that characterizes the deviation from the Bragg condition, $\mathbf{E}_g = v_g^E\mathbf{g}\sin\phi_g^E$. Expression (6) is written for the case of $\Delta_B \ll 1$. An accurate calculation of the electric-field strength in the two-wave approximation yields

$$\mathbf{E} = \mathbf{E}_g\cdot\frac{\Delta_B}{\sqrt{1+\Delta_B^2}}. \tag{6′}$$

The presence of a nonzero neutron EDM leads to spin rotation around the reciprocal lattice vector $\mathbf{g} \parallel \mathbf{E}$ by the angle

$$\varphi_d = \frac{2d_n E}{\hbar}\tau. \qquad (7)$$

Here, τ is the time a neutron spends in the crystal.

It is noteworthy that the main false effects due to the Schwinger interaction of moving neutrons with an electric field, tends to zero in the case of diffraction at the angle of $\pi/2$ since the neutron velocity is nearly parallel to the electric field. The residual effects do not exceed in magnitude similar effects for ultracold neutrons. Moreover, the axis of neutron-spin rotation owing to the Schwinger interaction is strictly orthogonal to the electric field by virtue of its definition: $\boldsymbol{H}^S = [\boldsymbol{E}_g \times \mathbf{v}]/c$. This circumstance makes it possible to separate these effects by using the system for a three-dimensional analysis of polarization [20].

4. The layout of the experiment aimed at searches for the effect of neutron-spin rotation owing to the EDM as neutrons traverse a noncetrosymmetric crystal is depicted in fig.2.

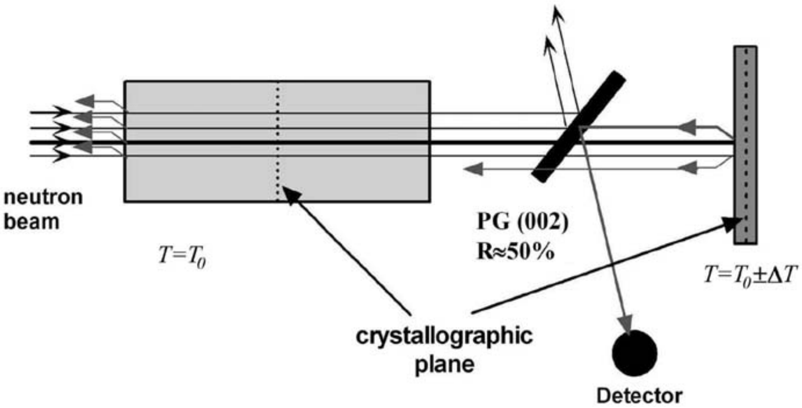

Fig.2. Scheme of experiment to search for the neutron EDM.

The working system of crystallographic planes is parallel to the entrance face of the crystal. Only neutrons of wavelengths not equal to the Bragg one can pass through the thick working crystal. They are moving in the direction normal to the working planes and undergo reflection from the second crystal (analyzer) whose interplanar spacing is controllable. After that, they are directed to detector by semitransparent mirror of pyrolytic graphite.

Neutrons that satisfy Bragg's condition for the first crystal are completely reflected by its entrance face and therefore cannot find their way to the second crystal and, accordingly, to the detector. The neutrons propagating in the working crystal are affected by a strong electric field whose strength and sign depend on the magnitude and sign of the parameter of deviations from the Bragg condition for this crystal. The analyzer crystal is a thin crystal from the same material and has the same orientation of planes. Its interplanar spacing is controlled by changing the analyzer temperature. Upon heating or cooling the analyzer, one can select the neutrons of specific wavelength, which passed through the working crystal in electric field of the corresponding sign and strength; that is, we can control the sign and strength of the electric field acting on the detected neutron in the crystal without touching the crystal itself.

An artificial quartz crystal $140\times140\times35$ mm in size was used in our experiment. The perfectness of the crystal was studied by the method proposed in [21], and the uniformity of the interplanar spacing was $\Delta d/d < 5 \times 10^{-6}$ over the whole crystal volume. The parameters of the (110) plane used in experiment were $g = 2{,}56\cdot10^{10}\,\text{m}^{-1}$ and $E_g = 2\cdot10^{8}$ V/cm [11].

For the case where the deviation from Bragg's conditions is $\Delta_B \cong 0{,}5$, the experimental value obtained for the electric-field strength from the measured angle of neutron-spin rotation because of Schwinger interaction is $E_{\exp} = (0{,}7 \pm 0{,}1)\times 10^{8}$ V/cm [22], which agrees with the calculated field strength and with the field strength measured earlier by different methods [11]. The electric field was determined from the angle of spin rotation,

$$\varphi_S = \frac{2}{\hbar c v}\mu\boldsymbol{\sigma}\cdot\left[\mathbf{E}_g \times \mathbf{v}\right]L,$$

about the Schwinger field $\mathbf{H}^S$, where L is the crystal thickness and μ is the neutron magnetic moment. In order to obtain a nonzero value for the spin-rotation angle φ_S around the Schwinger field $\mathbf{H}^S$, the crystal was rotated by an angle of about 4°. The respective diffraction angle was $\theta_B = 86°$ (see fig.2). In that case $[\mathbf{E}_g \times \mathbf{v}] \neq 0$. An example, of the experimental dependence of the angle of spin rotation caused by Schwinger interaction on the temperature difference between the analyzer crystal and the working crystal (that is, on the parameter of deviation from Bragg's conditions) is given in fig.3. The measurements in question were performed at the PNPI WWR-M reactor.

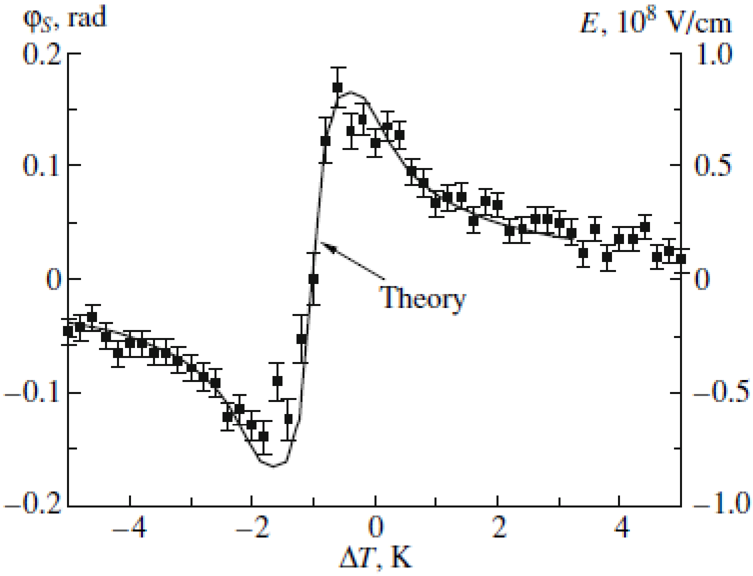

Fig.3. Spin-rotation angle as a function of the temperature differencebetween the analyzer crystal and the working crystal

Neutrons were propagating through an alpha-quartz crystal of thickness $L = 14$ cm at the angle of 86° with respect to the (110) working plane of the crystal, which is parallel to the entrance face. The respective values of the electric-field strength are plotted along the right-hand ordinate. The curve has a pronounced resonance character. It is described by the convolution of expression (6) and a finite spectral width of the beam. This width is equal to the Darwin (Bragg) width. The curve passes through zero at $\Delta T \neq 0$. This means that there is a small (at a level of 10^{-5}) but quite measurable difference in interplanar distances between the analyzer crystal that grew under natural conditions and the artificially grown working crystal.

5. A test experiment devoted to a search for the neutron EDM was recently performed in the PF1b beam from the ILL reactor [23]. The layout of that experiment similar to that shown in fig.1. For a more detailed description of the setup used in that experiment see [23, 24].

The experiment in question yielded zero result in measuring the angle of neutron-spin rotation around the electric field (reciprocal lattice vector) [23]:

$$\varphi_g = (0{,}9 \pm 2{,}3)\times 10^{-4}.$$

The following constraint on the neutron EDM corresponds to this result:

$$d_n < 9 \cdot 10^{-24} e \cdot \text{см}, (90\%)$$

This constraint is already by two orders of magnitude better than that in Shull’s diffractive experiment [7].

The preparation of a full-scale experiment aimed at searches for the neutron EDM by the method outlined above is now under way. A composite quartz crystal 100×100×500 mm in size and with an interplane distance uniformity of $\Delta d/d < 5\times10^{-6}$ over the whole volume has been prepared. A system for a three-dimensional analysis of polarization is being created on the basis of employing a superconductor magnetic screen. An accuracy at the level of $2\times10^{-26} e$ cm for the neutron EDM is planned to be achieved with the aid of this setup.

6. This work was supported by Ministry of Science and Education of the Russian Federation (program 3.329.2014/K).

References

[1] M. Pospelov, A. Ritz, Annals of Physics 318 (2005) 119.

[2] I.S. Altarev, et al., Yad. Fiz. 59 (1996) 1204.

[3] C.A. Baker, et al., Phys. Rev. Lett. 97 (2006) 131801.

[4] J.M. Pendlebury, et al., Phys. Rev. A 70 (2004) 032102.

[5] A.P. Serebrov, et al., Nucl. Instr. and Meth. A 611 (2009) 276.

[6] S.K. Lamoreaux, R. Golub, J. Phys. G 36 (2009) 104002.

[7] C.G. Shull, R. Nathans, Phys. Rev. Lett. 19 (1967) 384.

[8] Yu.G. Abov, A.D. Gulko, P.A. Krupchitsky, Polarized Slow Neutrons, Atomizdat, Moscow, 1966, 256p. (in Russian).

[9] M. Forte, J. Phys. G 9 (1983) 745.

[10] V.L. Alekseev, et al., JETP 67 (1988) 1727.

[11] V.L. Alexeev, et al., Nucl. Instr. Meth. A 284 (1989) 181;
V.L. Alexeev, et al., JETP 69 (1989) 1083.

[12] M. Forte, C.M.E. Zeyen, Nucl. Instr. Meth. A 284 (1989) 147.

[13] V.G. Baryshevskii, S.V. Cherepitsa, Phys. Stat. Sol. b 128 (1985) 379.

[14] V.V. Fedorov, et al., J. Phys. G 18 (1992) 1133.

[15] [a] V.V. Fedorov, et al., Tech. Phys. Lett. 21 (1995) 884;
[b] V.V. Fedorov, Phys. B 234–236 (1997) 8.

[16] V.V. Fedorov, et al., Phys. B 297 (2001) 293.

[17] V.V. Fedorov, V.V. Voronin, Nucl. Instr. and Meth. B 201 (2003) 230.

[18] V.V. Fedorov, V.V. Voronin, Phys. of Atomic Nucl. 77 (2014) 695–703.

[19] V.V. Fedorov, XXVI Winter LNPI School, vol. 1, Leningrad, 1991, 65p.

[20] E. Leli`evre-Berna, et al., Physica B **397** (2007) 120.

[21] V. V. Fedorov, et al., Nucl. Instr. Meth. A 593(2008) 472.

[22] V.V. Voronin, et al., JETP Lett. 74 (2001) 251.

[23] V.V. Fedorov, et al., Phys. Lett. B **694** (2010) 22.

[24] V. V. Fedorov, et al., Nucl. Instr. Meth. A **611** (2009) 124.

NMR of ^{3}He in nanostructures

A.V. Klochkov[1,2], E.M. Alakshin[1,2], R.R. Gazizulin[1], V.V. Kuzmin[1], K.R. Safiullin[1,2],
M.S. Tagirov[1,2]

[1]Kazan Federal University, 420008, Kremlevskaja 18, Kazan, Russia
[2]Institute of Perspective Research, TAS, 420111, L.Bulachnaya 36a, Kazan, Russia

e-mail: alexander.klochkov@kpfu.ru

Nuclear magnetic resonance (NMR) of ^{3}He in contact with nanostructures is a powerful method for obtaining rich information about structure and properties of the substrates. The NMR characteristics of normal liquid ^{3}He strongly depend on size of volume where ^{3}He is located. The main reason for that is highly effective spin diffusion, which allows seeing space restriction starting from several mm and down to atomic size. Usually, the nuclear magnetic relaxation of liquid ^{3}He (both T_1 and T_2) takes place by means of fast spin diffusion from liquid ^{3}He to adsorbed ^{3}He and further effective surface relaxation in adsorbed layer of ^{3}He [1 – 5]. Thus, the ^{3}He spin kinetics and the spectral characteristics are strongly dependable on size of geometry filled by liquid ^{3}He. Additionally, the study of spin kinetics of ^{3}He in porous media at low temperatures is in the matter of interest due to direct magnetic coupling between ^{3}He and solid state substrate [2, 6, 7].

The main subject of the present work is the study of spin kinetics of ^{3}He in contact with different types of nanostructures, i.e.: silica aerogels, charcoals, inverse opals, clay minerals and nanosized crystal powders of Van Vleck paramagnet PrF_3 and its diamagnetic analogue LaF_3. The experimental results, obtained in Kazan Federal University in the last 10 years are published in [4, 8 – 15].

This work is partially supported according to the Russian Government Program of Competitive Growth of Kazan Federal University.

References

[1] V.V. Naletov, M.S. Tagirov, D.A. Tayurskii, M.A. Teplov, JETP. **81**, 311 (1995).
[2] L.J. Friedman, P.J. Millet, R.C. Richardson, Phys. Rev. Lett. **47**, 1078 (1981).
[3] L.J. Friedman, T.J. Gramila, R.C. Richardson, J. Low Temp.Phys. **55**, 83 (1984).
[4] A.V. Klochkov et al., JETP Letters. **88.**, 823 (2008).
[5] Brian P. Cowan, J. Low Temp.Phys. **50**, 135 (1983).
[6] A.V. Egorov et al., JETP Letters. **39**, 584 (1984).
[7] A.V. Egorov et al., JETP Letters. **86**, 416 (2007).
[8] E.M. Alakshin et al., JETP Letters. **93**, 223 (2011).
[9] R.R. Gazizulin et al., Appl. Magn. Resonance. **38**, 271 (2010).
[10] M.S. Tagirov et al., J. Low. Temp. Phys. **162**, 645 (2011).
[11] E.M. Alakshin et al., JETP Letters. **97,** 579 (2013).
[12] E.M. Alakshin et al., Journal of Physics: Conf.Ser. **568,** 012001 (2014).
[13] A.V. Klochkov et al., Low temperature physics. **41**, 50 (2015).
[14] E.M. Alakshin et al., Low temperature physics. **41**, 47 (2015).
[15] E.M. Alakshin et al. Low temperature physics. **41**, 39 (2015).

Intrinsic vs impurity-indused features of $SrTiO_3$:Mn as probed by EPR

R.V. Yusupov

Kazan Federal University, Kremlevskaya 18, 420008 Kazan, Russia

e-mail: Roman.Yusupov@kpfu.ru

Strontium titanate $SrTiO_3$ (STO) is the bright representative strongly-polarizable ABO_3 perovskite-structure oxide family that reveals a variety of unusual phenomena. Recent interest to Mn-doped STO is related to the so-called “magnetoelectric multiglass” state that was reported in STO:Mn ceramics and considered as an intrinsic effect associated with the presence of the 12-fold coordinated Mn^{2+} off-center impurities [1]. Later, e.g., in [2], magnetic counterpart was shown to be an extrinsic one originating from the precipitates of the ferrimagnetic Mn_3O_4 [2]. Dielectric anomalies were found also in Mn-doped STO single crystals [3]. The microscopic origin of Mn-related impurity-induced ferroelectricity in STO remains an open question.

In the lecture the report on extensive EPR study of a series of high-quality Verneuil-grown STO:Mn crystals from Furuuchi Corp. (Tokyo, Japan) will be presented. It was found that the development of the dielectric anomalies correlates well with the concentration of the Mn^{2+} impurity centers. EPR spectra of these cubic-symmetry centers at $T > 100$ K experience drastic broadening on cooling from 500 K to ~ 60 K. This behavior originates from the slowing down of the Mn^{2+}-center dynamics with characteristic activation energy of ~ 34 meV. Interestingly, this dynamic at high temperature Mn^{2+} center gives rise to two types of static centers at $T < 10$ K. The higher symmetry one is oriented along the quasi-cubic [110]-direction revealing C_2 orthorhombic point symmetry. Another one is monoclinic C_s, whose principal axis is slanted by ~12 degrees from [100] towards [110]-type axes. In general, the EPR spectra of all the STO:Mn samples reveal the presence of both centers with the sample-dependent concentrations. We found that most likely the Mn^{2+} center of C_s-symmetry are formed in perturbed metastable regions of the sample while centers possessing the C_2-symmetry — in the relaxed ones. This follows from the observed transformation of the EPR spectrum on a weeks-long timescale at room temperature. This situation reveals the presence of the two energetically near-degenerate microscopic structures of the Mn^{2+} impurity centers in STO.

Regarding the origin of the long-lived perturbation in STO, it follows from the EPR studies of the Mn^{4+} ion centers that one of the possible sources is a residual stress. It looks that the structure of STO has a pronounced tendency towards tetragonal distortion in the (100)-oriented platelets and [100]-needles with the sign and a value of a distortion depending on the samples size and shape. At last, a huge irreversible quadratic electric-field effect on the EPR spectrum of the Mn^{4+} ions in STO in the cubic phase ($T > 105$ K) was observed. So, $SrTiO_3$:Mn single crystals are complex objects providing researchers with a lot of new information and revealing a strong interplay of the intrinsic and extrinsic properties of STO and peculiar features of Mn-impurities.

References

[1] V.V. Shvartsman et al. Phys. Rev. Lett. **101** 165704 (2008).

[2] M. Valant et al., Adv. Funct. Mater. **22** 2114 (2012).

[3] M. Savinov et al., J. Phys.: Condens. Matter. **20** 095221 (2008).

FeCr$_2$S$_4$ as a new multiferroic material

M.V. Eremin[1], R.A. Fatykhova[1], J. Deisenhofer[2]

[1]Institute of Physics, Kazan Federal University, Russian Federation.
[2]Institute for Physics, Augsburg University, D-86135 Augsburg, Germany

e-mail: meremin@kpfu.ru

The compound FeCr$_2$S$_4$ comes to focus as a potentially new multiferroic material [1]. The Cr^{3+} ions occupy the octahedral sites and their ground configuration is t_{2g}^3. The Fe^{2+} ions are at the centre of S^{2-} tetrahedra and as a result the ground configuration is $t_{2g}^3 e_g^3$. The ground state $t_{2g}^3 e_g^3 (^5E)$ possesses orbital degrees of freedom and yields very rich low energy excitation spectrum. Besides, at low temperatures at Fe^{2+} spins sites there is strong enough exchange field from surrounding Cr^{3+} and Fe^{2+} spins. The system is a ferrimagnet with two ferromagnetic sublattices.

In paramagnetic state we use the effective Hamiltonian

$$H_1 = -\left(\rho_s + \frac{\lambda^2}{\Delta}\right)\left\{\left[3S_z^2 - S(S+1)\right]U_\theta + \frac{\sqrt{3}}{2}\ \ S_+^2 + S_-^2\ \ U_\varepsilon\right\} + V\rho(U_\theta \cos\phi + U_\varepsilon \sin\phi)\,. \quad (1)$$

The first term takes into account the spin-spin and spin-orbit interactions. The second one describes possible distortion of the S^{2-} tetrahedron at low temperatures. Here $S = 2$, U_θ and U_ε are Pauli-like matrices within the orbital doublet ($|\theta\rangle$ and $|\varepsilon\rangle$ states).

Considering FeCr$_2$S$_4$ compound we switch the additional term $H_2 = \sum J_{il}\ \ \mathbf{S}_{Fe}\mathbf{S}_l$, which describes the superexchange interactions (B_z — effective internal magnetic field) of Fe^{2+} ($S = 2$) with surrounding magnetic ions.

To take into account electric field effect of incident light we have constructed the following effective operator in second order perturbation theory via excited 3d^{5}4p configuration

$$\begin{aligned} H_{eff} = & -\frac{1}{|\Delta_{dp}|}\frac{2}{7}\sqrt{\frac{2}{7}}\Big[\ \ B_2^{(3)}U_2^{(2)} + B_{-2}^{(3)}U_{-2}^{(2)}\ \ D_0^{(1)} - \sqrt{2}\ \ B_2^{(3)}D_{-1}^{(1)}U_1^{(2)} + B_{-2}^{(3)}D_1^{(1)}U_{-1}^{(2)}\ \ \Big] + \\ & + \frac{18}{7|\Delta_{dp}|}\sqrt{\frac{6}{35}}\left[\begin{array}{l} B_2^{(3)}U_2^{(4)} + B_{-2}^{(3)}U_{-2}^{(4)}\ \ D_0^{(1)} + \frac{1}{2}\ \ B_2^{(3)}D_{-1}^{(1)}U_1^{(4)} + B_{-2}^{(3)}D_1^{(1)}U_{-1}^{(4)} \\ + \frac{\sqrt{7}}{2}\ \ B_2^{(3)}D_1^{(1)}U_3^{(4)} + B_{-2}^{(3)}D_{-1}^{(1)}U_{-3}^{(4)} \end{array}\right]. \end{aligned} \quad (2)$$

Here is $B_{\pm 2}^{(3)} \cong \mp i\frac{4e^2 < r^3 >_{dp}}{3R_{Fe-S}^4}\sqrt{\frac{10}{3}}$, $D_0^{(1)} = \frac{\varepsilon + 2}{3}e < r >_{pd}\ E_z$, ε — dielectric permittivity, $D_{\pm 1}^{(1)} = \mp\frac{\varepsilon + 2}{3}e < r >_{pd}\ \frac{1}{\sqrt{2}}\ \ E_x \mp iE_y$. Finally, combining this operator with spin–orbit coupling and Zeeman energy operator we have established the magnetoelectric coupling expressions

$$\begin{aligned} H_3 = & \frac{B_2^{(3)} - B_{-2}^{(3)} \quad \mu_B e < r >_{pd}}{7\left|\Delta_{dp}\Delta_{cr}\right|} \frac{\varepsilon+2}{3}\sqrt{\frac{2}{5}} \quad 2E_z g_z H_z - \quad E_x g_x H_x + E_y g_y H_y \quad U_\varepsilon + \\ & + \frac{B_2^{(3)} - B_{-2}^{(3)} \quad \lambda_{SO} e < r >_{pd}}{7\left|\Delta_{dp}\Delta_{cr}\right|} \frac{\varepsilon+2}{3}\sqrt{\frac{2}{5}} \quad 2E_z S_z - \quad E_x S_x + E_y S_y \quad U_\varepsilon \end{aligned} . \qquad (3)$$

This expression where used for calculations the relative intensities of absorption spectra induced by incident electric component of light with different polarizations. It is interesting to note that electric polarization induced by spin ordering very sensitive to Jahn-Teller distortions at Fe^{2+} sites (see fig.1).

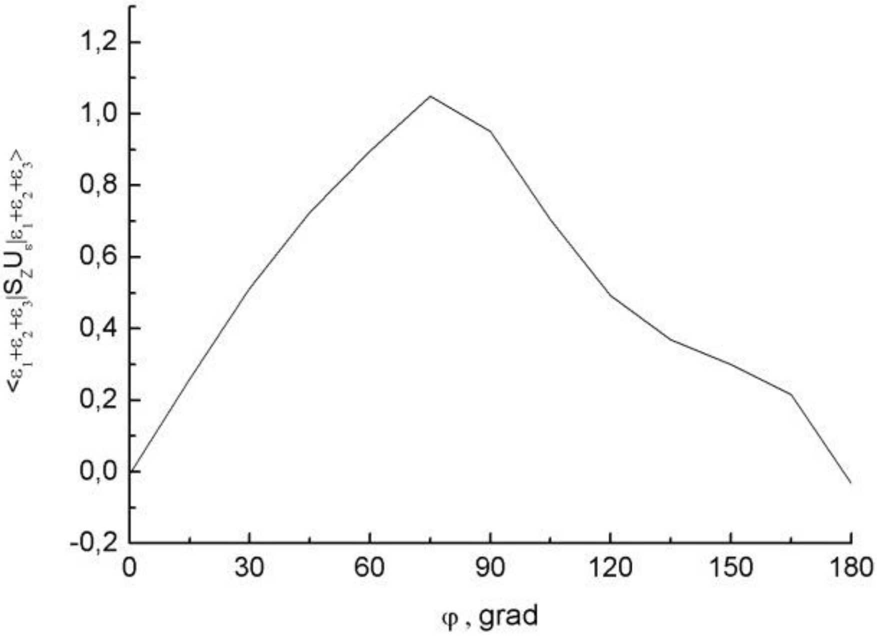

Fig.1. Calculated electric dipole moment per one Fe site induced by spin polarization. Parameters are: $V\rho = 20\,\mathrm{cm}^{-1}$, $\rho_s + \lambda^2/\Delta = 2\,\mathrm{cm}^{-1}$, $B_Z = 20\,\mathrm{cm}^{-1}$, $T = 5$ K.

References

[1] J. Bertinshaw, C. Ulrich, A. Guenther, F. Schrettle, M. Wohlauer, S. Krohns, M. Reehuis, A.J. Studer, M. Avdeev, D.V. Quach, J.R. Groza, V. Tsurkan, A. Loidl, J. Deisenhofer. FeCr2S4 in magnetic fields: possible evidence for a multiferroic ground state. Scientific Reports. 2014, V. 4: 6079.

Computer simulation of 2D magnetic cluster growth

N.A. Balakirev, V.A. Zhikharev

Kazan national research technological university, 420015, K.Marx, 68, Kazan, Russia
e-mail:balakirevnikita2009@gmail.com

The method of ion-beam synthesis is a very effective way to obtain thin films of new chemical phases within the surface layer of any target. In particular, high-dose implantation of iron ions into the silicon results in the formation of thin films of different silicides FeSi, Fe_2Si, Fe_3Si [1] depending on the implantation dose. It is assumed that the synthesized films are not continuous, and consist of clusters of the silicide phase. Of particular interest are thin films of magnetic silicide Fe_3Si as a promising material for microelectronics and spintronics. It is obvious that the magnetic properties of Fe_3Si cluster strongly depend on their shape and structure. The formation of magnetic Fe_3Si silicide clusters begins with a creation of stable "grain" of this new phase. During ion bombardment along with the creation of the grains the process of their destruction due to atomic collisions takes place. Hence, an initial randomly created grain of the Fe_3Si phase should reach a certain critical size to become stable and serve as a nucleus of the Fe_3Si cluster growth. It can be assumed that the process has the noticeable probability only within thin layer, where the concentration of implanted Fe atoms is maximal. In this paper the simple model of 2D clusters (quasi 2D) formation is suggested and computer simulation of the cluster growth is performed.

There is a well-known and efficient method of the cluster formation simulation, makes it possible to study the geometrical properties of generated clusters. This is the classic Witten – Sander model of the particle–cluster diffusion-limited aggregation (DLA) [2]. In the DLA model and in all its modifications the cluster grows by taking the diffusing atoms up one by one, and each of the atoms becomes a new unit of the cluster. However, the atoms embedded into the solid react with the host atoms and form a new chemical compound. Such a situation occurs during the ion-beam synthesis of Fe_3Si silicide when not one but several Fe atoms must come near the cluster boundary at a time to add a new unit (with Fe_3Si structure) to the cluster. In the model, putted forward in this paper, a new unit is added to the cluster in the site of the cluster perimeter near which the local concentration of Fe atoms randomly walking in implanted layer becomes sufficient to provide the Fe_3Si phase composition. The examples of clusters generated in DLA approach and according to the suggested model are presented in fig.1

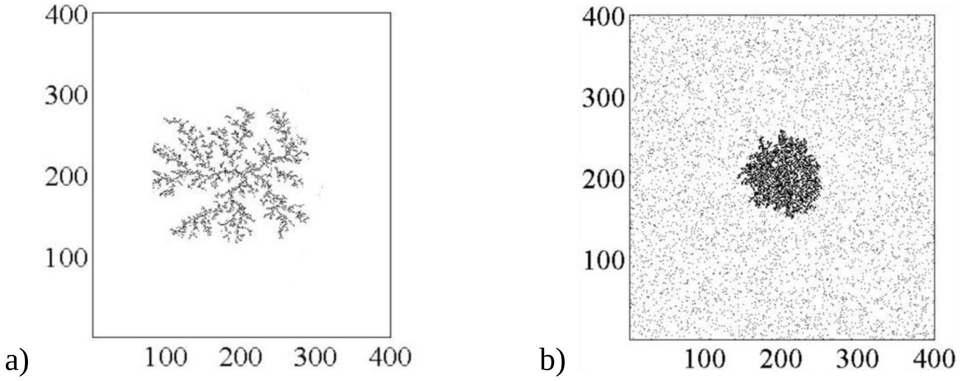

Fig.1. Clusters generated according to DLA model a) and in frame of the model considered in present paper b). The number of Fe atoms included in the cluster in both cases is the same.

The fig.1 shows that in case b) generated cluster has a much denser structure. It is more interesting that a magnetic field created by the cluster of magnetic silicide Fe_3Si significantly affects the motion of iron atoms near the cluster. The modified DLA model, taking into account the effect of the dipole-dipole magnetic interaction between the cluster and randomly walking atoms was developed in [3]. It was shown that the interaction results in cluster elongation in the direction of the cluster magnetization. Consequently, in the presence of an external magnetic field clusters elongate in the direction of this field. Accounting of the magnetic interaction in the frame of the model considered in this paper also results in cluster elongation (see fig.2).

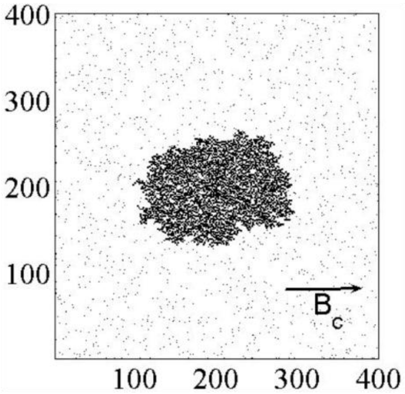

Fig.2. Cluster simulated in the presence of the external magnetic field B_c directed along the OX axis.

The parameters of simulation corresponding to fig.2 were following. The critical size of the stable “grain” is taken to be $3a$ (a is the lattice constant). Each of 10000 free iron atoms placed on the lattice (400×400) makes 10 steps during each stage of the simulation. It is assumed that the magnetization of the growing ferromagnetic cluster is equal to the saturation magnetization of silicide Fe_3Si.

All calculations were performed using the C++ code compiled under Linux OS.

Finally, a simple model of the formation of Fe_3Si clusters during high-dose Fe ion implantation into silicon is developed. The reconfiguration of several Fe atoms into the unit of Fe_3Si cluster is supposed. The magnetic interaction between growing cluster and randomly walking Fe atom results in the cluster elongation in the cluster magnetization direction. This can explain the origin of the uniaxial in-plane magnetic anisotropy in films ion-beam synthesized in the presence of an external magnetic field [1].

References

[1] Gumarov G.G., Petukhov V.Yu., Zhikharev V.A., ValeevV. F., Khaibullin R.I. Nucl. Instr. and Meth. in Phys. Res. **B 267**, 1600, (2009)

[2] T.A. Witten, L.M. Sander, Phys. Rev. Lett. 47 (1981) 1400.

[3] Balakirev N.A., Gumarov G.G., Zhikharev V.A.,Petukhov V.Yu. Comp. Mater. Science **50**, 2925 (2011)

Nonlinear NMR in highly polarised liquids

V.V. Kuzmin[1,2], G. Tastevin[2], P.-J. Nacher[2]

[1]Institute of Physics, Kazan Federal University, 420008 Kazan, Russia
[2]Laboratoire Kastler Brossel, ENS – CNRS – UPMC, 24 rue Lhomond, 75005, Paris, France
e-mail: slava625@yandex.ru

Hyperpolarisation (HP) or high magnetic fields provide high signal-to-noise ratios in liquid-state NMR but also lead to ill-controlled dynamics [1] (bizarre signals and cross-peaks, precession instabilities; multiple spin echoes; and multiple maser emissions) associated with distant dipolar fields (DDFs) and radiation damping (RD). We have performed systematic low field studies (3 mT) with condensed laser polarised ^{3}He–^{4}He mixtures (0.3-5% of ^{3}He, with ~ 10% polarisation at low temperature (1 K) and controlled RD using active feedback in the detection circuit.

I will report investigations of DDF-induced precession instabilities after 90^0 RF flipping pulses that characterize the development of unstable magnetization patterns and probe the effect of the sample size and shape on spin dynamics at high DDF. We have developed MRI-based techniques to probe the evolution of the magnetization patterns. Parametric amplification of initially imprinted patterns and spatial harmonic generation are observed, in experiments and simulations alike (numerical simulations rely on time integration of the nonlinear Bloch equations with DDF, RD, diffusion, and applied gradients for magnetic moments on a cubic lattice).

I will also report on a quantitative investigation of the impact of the rf noise power, static field homogeneity, and DDFs on the onset of transient maser or multiple maser emissions. Focus will be put on experimental work, with emphasis on the control of the sample/coils coupling (RD) which is needed for reliable measurements at high Q-factor and high magnetisation. The effect of broadband electronic RF noise on maser initiation will be discussed.

Our work directly probes sample size and shape effects that have previously only been inferred from MSE features in HP ^{129}Xe and ^{3}He [1], but which are expected to be important whenever strong DDFs are encountered. It also opens the door to better control of DDF- and RD-dominated magnetisation dynamics.

References

[1] H. Desvaux, Non-linear liquid-state NMR, Progress in NMR Spectroscopy, **70**, (2013).

Simulations of equilibrium magnetic and magnetoelastic properties of non-conducting rare-earth compounds

I.V. Romanova

Kazan Federal University, 420008, Kremlevskaya str., 16a, Kazan, Russia

e-mail: romanova.irina.vladimirovna@gmail.com

The Hamiltonian of the magnetic subsystem containing rare-earth ions involves energies of the localized 4f-electrons in free ions, energies of interactions of the 4f-electrons with the static crystal field in the perfect crystal lattice as well as in the homogeneously deformed lattice, interactions with the external magnetic field and lattice vibrations (electron-phonon interaction), magnetic dipolar and exchange interactions between the ions [1]. This Hamiltonian is used in calculations of different measurable physical parameters versus temperature and the magnetic field strength and direction (energy levels of rare earth ions, the magnetization, magnetic dc- and ac-susceptibilities, elastic constants, lattice deformations) [2]. The calculation codes are considered within the MATLAB software.

References

[1] I.V. Romanova, B.Z. Malkin, M.S. Tagirov, 2014, Optika i Spektroskopiya, 2014, Vol. 116, No. 6, pp. 973–981.

[2] Aminov L.K., Malkin B.Z., Teplov M.A. Magnetic properties of nonmetallic lanthanide compounds. In: Handbook on the Physics and Chemistry of the Rare-Earths. V. 22. Amsterdam: North-Holland, 1996. P. 295.

Nuclear magnetic resonance in low-dimensional compound $A_3Ni_2SbO_6$ (A = Na, Li)

T. Salikhov[1], M. Iakovleva[1], K. Safiullin[2], A. Klochkov[2], M. Tagirov[2], M. Stratan[3],
E. Zvereva[3], V. Nalbandyan[4], H.-J. Grafe[5], E. Vavilova[1]

[1]Zavoisky Physical-Technical Institute, 420029, Kazan, Russia
[2]Institute of Physics, Kazan Federal University, 420008, Kazan, Russia
[3]Faculty of Physics, Moscow State University, 119991, Moscow, Russia
[4]Chemistry Faculty, Southern Federal University, 344090, Rostov-on-Don, Russia
[5]IFW Dresden, Dresden, Germany

e-mail: tmsalikhov@gmail.com

In recent decades the layered oxides of alkali and transition metals are intensively investigated due to their potential applications as solid electrolytes and electrode materials in modern ionics. Recently, a new generation of layered complex metal oxides with honeycomb-based crystal structure where ordered mixed-layers of magnetic cations alternate with non-magnetic alkali metal layers has been a subject of intense research worldwide. This work is devoted to the investigation of new quasi two-dimensional (2D) honeycomb-lattice compounds $Li_3Ni_2SbO_6$, $Na_3Ni_2SbO_6$. We are here to present the results of studies a systematic study of their electronic and magnetic behavior by nuclear magnetic resonance. Basic magnetic properties of $Li_3Ni_2SbO_6$ and $Na_3Ni_2SbO_6$ have been reported recently [1, 2].

^{7}Li (I = 3/2) and ^{23}Na (I = 3/2) NMR experiments were performed and we found that the behavior of the NMR spectrum and relaxation at low temperature is caused by the interaction with the magnetic Ni^{2+} ions and reflects the dynamics of magnetic subsystem. In the region of Neel temperatures the temperature dependence of NMR line shape of the sodium and lithium spectra have a sharp peak, that indicate the onset of long-range magnetic order. In addition, the calculations of different models of ordering have been performed. The best fit of the experimental data was obtained assuming a *zigzag* spin structure with spins oriented perpendicular to the plane. At $T > 300$ K the deviation of the $\chi T T_1^{-1}$ from constant shows the additional relaxation mechanism which becomes effective at these temperatures. We propose that the reason of this additional relaxation is the growth of in-plane lithium mobility. At 4.5 T the spin-flop phase is observed.

The work was supported by Foundation for Basic Research (grant 14-02-01194 and 14-02-00245)

References

[1] E.A. Zvereva, *et al.*, *Dalton Trans.* **41**, 572 (2012).
[2] V.V. Politaev, *et al.*, *J. Solid State Chem.* **183**, 684 (2010).

The energy shift of one level quantum dot that interact with two leads

R.Kh. Gainutdinov, M.R. Mohebbifar, M.A. Khamadeev, A.A. Mutygullina

Optics and Nanophotonics Department, Institute of Physics, Kazan Federal University,
Kazan, Russia

e-mail: Renat.Gainutdinov@kpfu.ru

Abstract

The Energy shift level of a quantum dot in single electron transistor model is investigated. The self-energy function which related to Energy shift levels, describing this interaction is added to a bare energy of a dot state. In the standard way of determining the self-interaction corrections to bare energies of quantum dots, the variations of the self-energy functions with energy are ignored, and these corrections are considered to be equal to the values of the self-energy functions for bare energies of states. We show that actually in the case of quantum dots the variations of the self-energy functions in the energy interval between the bare and true energies can be strong, and this can have a significant effect on the values of the tunneling-induced shifts of energy levels of quantum dots.

Introduction

Single Electron Transistor has been made with critical dimensions of just a few nanometer using metal, semiconductor, carbon nanotubes or individual molecules. A SET consists of a small conducting island coupled to source and drain leads by tunnel junctions and capactively coupled to one or more gate. Unlike Field Effect transistor, Single electron device based on an intrinsically quantum phenomenon, the tunnel effect [1]. In the case of quantum dots the role of the virtual photons in the self-interaction of ordinary atoms can be played, for example, by electrons that leave the quantum dot and then come back. Such a self-interaction can be much more significant than the interaction of an atom with its own radiation field. In this paper by using generalized dynamical equation we investigate the effect of such a self-interaction on the tunneling-induced energy shift levels of a quantum dot.

Theory

In our study we use non-perturbative methods of its description based on the GDE, which in [2] has been derived as a direct consequence of the first principles of quantum physics. Being equivalent to the Schrödinger equation in the case when the interaction in a quantum system is instantaneous, GDE allows one to extend dynamics to the case of nonlocal-in-time interactions. This equation provides a new insight into many problems in atomic physics [3], nuclear physics [4] and quantum optics [5]. The contribution to the Green operator G(z), which comes from the processes associated with the self-interaction of particles, has the same structure as the free Green operator $G_0(z)$. So it is natural to replace $G_0(z)$ by the operator $G_0^{(\nu)}(z)$, which describes the evolution of the system when particles propagate freely or interact with vacuum, and, hence, has the structure

$$\langle m'|G_0^{(\nu)}(z)|m\rangle = \frac{\langle m'|m\rangle}{z - E_m - C_m(z)} \tag{1}$$

with $|m\rangle$ being the eigenvectors of the free Hamiltonian $\left(H_0|m\rangle = E_0|m\rangle\right)$. Other contributions are described by the operator $G^{(I)}(z) = G_0^{(\nu)}(z)M(z)G_0^{(\nu)}(z)$: $G(z) = G_0^{(\nu)}(z) + G^{(I)}(z) \equiv G_0^{(\nu)}(z) + G_0^{(\nu)}(z)M(z)G_0^{(\nu)}(z)$, where the operator *M*(z) describes the processes in which some particles interact each with other. The equations for $C(z)$ and $M(z)$ are derived from GDE. The equation for the function $C_m(z)$ referred to as the self-energy function reads

$$\frac{dC_m(z)}{dz} = -\langle m|M(z)\left[G_0^{(\nu)}(z)\right]^2 M(z)|m\rangle, \quad \langle m|m\rangle = 1. \tag{2}$$

The condition

$$z - E_m^{(0)} - C_m(z) = 0 \tag{3}$$

determines the physical masses of particles. In the case when we deal with an atom and $|m\rangle$ describes an atomic state, equation (3) determines the self-energy correction (the Lamb shift) to the energy E$_m$ of the state $|m\rangle$. An approximated solution of this equation is $E_m \equiv E_m^{(0)} + C_m^{(0)}(E_m^{(0)}) \equiv E_m^{(0)} + \Delta E_m^L - i\Gamma_m/2$, with ΔE_m^L and Γ_m being the Lamb shift and the natural width of the energy level of the state |mi respectively. For this approximation to be valid the variation of $C_m(z)$ in the energy interval between $E_m^{(0)}$ and E_m must be negligible. This is the case for atoms in free space. In fact, at leading order in α the equation for $C_m(z)$ is reduced to the equation [6]

$$\frac{dC_m^{(0)}(z)}{dz} = -\langle m|H_I\left[G_0^{(\nu)}(z)\right]^2 H_I|m\rangle, \quad \langle m|m\rangle = 1 \tag{4}$$

with H_I being the interaction Hamiltonian. By solving this equation with an appropriate boundary condition we arrive at the ordinary expressions for the self-energy shifts and widths of energy levels. However, in the case of quantum dots the variation of the self-energy function in the relevant vicinity of the point $z = E_m^{(0)}$ can be very significant and, as a result, the above approximation is invalid. In this case the self-interaction function cannot be parameterized by a shift and a width, and one has to derive the self-energy function from a non-perturbative solution of the equations for $C_m(z)$ and $M(z)$.

Results and Discussion

We study the self-interaction of a single-level quantum dot with arbitrary strong one-site Coulomb interaction tunnel coupled to two non-interacting leads. The Hamiltonian of system consisting of quantum dot and leads is described by [7]

$$H = H_{Q.D} + H_{T.P} + H_L, \tag{5}$$

where $H_{Q.D}$ is the Hamiltonian of quantum dot, $H_{T.P}$ is the Hamiltonian of tunneling process between leads and quantum dot and the Hamiltonian of leads is H_L.

The quantum dot can be described by the single-level Anderson impurity model, and $H_{Q.D}$ equal to

$$H_{Q.D} = \sum_{\sigma=\uparrow,\downarrow} E d_\sigma^\dagger d_\sigma + U n_\uparrow n_\downarrow, \tag{6}$$

where the creation (annihilation) operator for an electron with spin σ on the dot is given by $d_\sigma^\dagger$ and d_σ, also $n_\sigma = d_\sigma^\dagger d_\sigma$ is the number operator. The on-site repulsion U describes the energy cost for double occupation (when we have two electrons in quantum dot) and stems from Coulomb interaction. The Hamiltonian $H_{T.P}$ is given by

$$H_{T.P} = \sum_{\alpha,k,\sigma} V_\alpha C_{\alpha,k,\sigma}^\dagger d_\sigma + H.C., \tag{7}$$

where V_α is the momentum and spin-independent tunnel matrix element, $C^{\dagger}_{\alpha,k,\sigma}(C_{\alpha,k,\sigma})$ is creation (annihilation) operators for electrons with spin σ and momentum k in lead and $\alpha = l, r$. The Hamiltonian H_L is given by

$$H_L = \sum_{\alpha,k,\sigma} E_{\alpha,k} C^{\dagger}_{\alpha,k,\sigma} C_{\alpha,k,\sigma} . \tag{8}$$

The chemical potentials of the two leads differ by the applied bias $\mu_l - \mu_r = -eV$. We assume that the density of states ρ_α in the leads is constant for transport and defines the tunnel coupling strength R_α as $R_\alpha = 2\pi\rho_\alpha|V_\alpha|^2$, where V_α is the tunnel matrix element and $R = R_l + R_r$. We will denote the states of quantum dots as $|\Psi_\sigma\rangle$ for a singly occupied dot with spin $\sigma = \uparrow, \downarrow$ and an empty dot $|\Psi_0\rangle$. The corresponding energies are E_σ and E_0.

In this model we assume that reservoirs are in equilibrium and we average over the reservoir part of the initial states according to the Fermi distribution [7]

$$f_\alpha(\omega) = \left(1 + \exp(\frac{\omega - \mu_\alpha}{K_B T})\right)^{-1} \tag{9}$$

by solving this equation with an appropriate boundary condition we arrive at the ordinary expressions for the self-energy shifts and widths of energy levels. Solving the leading-order equation (4) yields the following expressions for the self-energy function $C_\sigma(z)$ of the quantum-dot state $|\Psi_\sigma\rangle$

$$C_\sigma(z) = \sum_\alpha \frac{R_\alpha}{2\pi} \int d\omega (\frac{1 - f_\alpha(\omega)}{z - \omega} + \frac{f_\alpha(\omega)}{z + \omega - 2\varepsilon - U}) \tag{10}$$

and the self-energy function $C_0(z)$ of the quantum-dot state $|\Psi_0\rangle$

$$C_0(z) = 2\sum_\alpha \frac{R_\alpha}{2\pi} \int d\omega (\frac{f_\alpha(\omega)}{z + \omega - \varepsilon}) . \tag{11}$$

In our calculations we have used the fact that the part that is independent of the Fermi distribution function of $C_\sigma(z)$ can be included into the correction to the energy of empty level. Taking into account this fact and using equation (1), self-energy function $C_\sigma(z)$ will be

$$C_\sigma(z) = \sum_\alpha \frac{R_\alpha}{2\pi} \int_0^\infty d\omega \left[\frac{1}{\left(1 + \exp(\beta(\omega - \mu))\right)(\omega - z)} + \frac{1}{\left(1 + \exp(\beta(\omega - \mu))\right)(\omega - (2\varepsilon + U - z))} \right] \tag{12}$$

let us assume that the variations of these self-energy functions with z are weak. In this case the trivial Energy shift level of Q.D $\delta E^{(ap)}$ can be considered as the approximated energy shifts of the corresponding energy levels of the quantum dot

$$\delta E^{(ap)} = C_\sigma(z = E_\sigma = \varepsilon) - C_0(z = E_0 = 0) \tag{13}$$

and the non-trivial Energy shift level of Q.D which describe fully Energy shift level of Q.D is

$$\delta E^{(ap)} = C_\sigma(z = E_\sigma = \varepsilon) - C_0(z = E_0 = 0) = \sum_\alpha \frac{R_\alpha}{2\pi} \left(\ln\left|\frac{\varepsilon}{\varepsilon + U}\right| + \ln\left|\frac{\varepsilon + U - \mu}{\varepsilon - \mu}\right| \right). \tag{14}$$

However, as it follows from the results of our calculations the variations with z of the self-energy functions of the quantum-dot states are strong, and one has to solve equation (3) exactly. Fig.1 where the results of calculations of the self-energy correction

$\delta\varepsilon = C_\sigma(z) - C_0(z)$ are depicted shows that the energy shifts obtained in this way can differ dramatically from their approximated values.

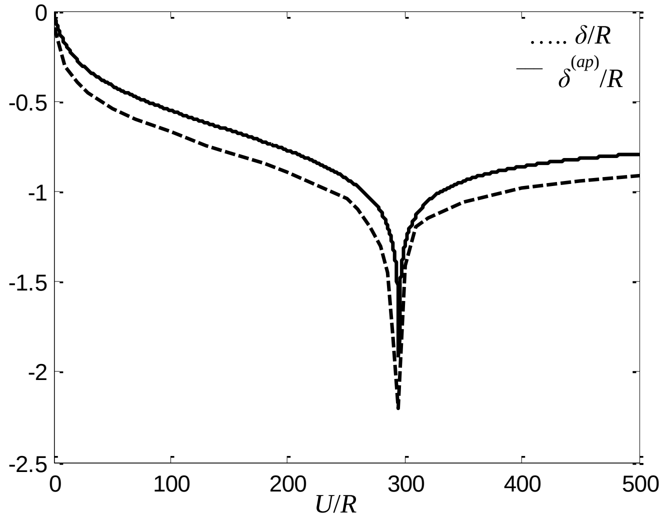

Fig.1. Calculation results of the trivial (solid line) and non-trivial (dashed line) energy shifts of level of Q.D for the parameters $\varepsilon = 5R$, $\mu = 300R$ and for different values of the U at the zero temperature and in the assumption that the left lead is the same as the right lead.

Conclusion

In this paper by using equation (4) we have derived equations (10) and (11) for the self-energy functions of the quantum-dot states in SET. By putting $z=E_\sigma$ and $z=E_0$ in equation (10) and equation (11) respectively we arrive at the expressions for the energy shifts in quantum dots derived in [7]. If the variations of the self-energy functions $C_0(z)$ and $C_\sigma(z)$ were weak enough, then in solving equation (2) one could restrict oneself to this approximated solution. However, as it follows from the results of calculation, this is not the case, and equation (3) must be solved exactly. Fig.1 shows that the self-interaction energy shifts obtained by solving equation (3) exactly differ dramatically from the approximated shifts.

References

[1] K. Gloos, R. S. Poikolainen, and J. P. Pekola, Appl. Phys. Lett. 77, 2915 (2000).

[2] Gainutdinov R Kh 1999 J. Phys. A 32 5657

[3] Gainutdinov R. Kh., Khamadeev M. A., Mohebbifar M. R., Petrova A. S., Ziyatdinova K. A., Salakhov M. Kh. // J. Phys.: Conf. Ser. 2015. V. 613. P. 012001.

[4] Gainutdinov R Kh and Mutygullina A A 2002 Physics of Atomic Nuclei 65 1421

[5] Gainutdinov R. Kh., Khamadeev M. A. Mohebbifar M. R. Mutygullina A. A. // J. Phys.: Conf. Ser. 2015. V. 613. P. 012002.

[6] Gainutdinov R Kh 1989 J. Phys. A 22 269

[7] Splettstoesser J, Governale M and König J 2012 Phys. Rev. B 86 035432

Spin-lattice relaxation of NO_3^{2-} complexes and Mn^{2+} ions in hydroxyapatite

D. Shurtakova, M. Gafurov, T. Biktagirov, G. Mamin, S. Orlinskii

Kazan Federal University, Institute of Physics, 420008 Kazan, Russian Federation.

e-mail: darja-shurtakva@mail.ru

Hydroxyapatite (HAp) is a major inorganic substance of bones and teeth. Since hydroxyapatite is widely used in medicine as bioceramic dental and orthopedic implants, because it has chemical and crystallographic similarities to the mineral part of the bone.

To study the spin-lattice relaxation were used "undoped" and "doped" by Mn 0.05 mol% hydroxyapatite powder. Its size were 30 nm and 1 micron. These samples were synthesized at the Faculty of Sciences of new materials of the Moscow State University by deposition from colloidal solutions.

The chemical reaction used to synthesize [1]:

$$(10–x)Ca(NO_3)_2 + (6–x)(NH_4)2HPO_4 + xNaHCO_3 + 8NH_4OH \rightarrow$$

$$\rightarrow Ca_{10–x}Na_x(PO_4)_{6–x}(CO_3)_x(OH)_2\downarrow + (20–2x)NH_4NO_3 + 6H_2O \text{ [1]}$$

The sequence consist inverted π-pulse and two $\pi/2–\pi$ pulses for electron spin echo observation. The process of spin-lattice relaxation was measured from the recovery of the longitudinal magnetization after the pulse inverting. The longitudinal magnetization is proportional to the integral amplitude of the spin echo. The measurements were performed by an EPR spectrometer Elexsys-580/680 (center of physicochemical measurements of KFU) in a pulsed mode, in the X-band. The temperature varied 10 ÷ 250 K.

The aim of the work was to determine the temperature dependence of spin-lattice relaxation time of paramagnetic centers in the samples of hydroxyapatite "undoped" size of 30 nm and 1 micron, and in samples of hydroxyapatite doped by impurity Mn 0.05 mol.%.

The EPR spectra of NO_3^{2-} complexes were observed in all the samples studied after x-ray exposure [2]. The structure of an EPR spectrum is shown in fig.1. The nuclear spin of nitrogen equals one so that the spectrum contains 3 lines. The distance between them corresponds to the hyperfine coupling constant. Form of lines controls due to averaging over all orientations of the grains of powder.

EPR spectrum of ions Mn^{2+} was observed in samples of HAp:Mn (for doped sample). There were six lines in the W-band spectrum, due to the nuclear spin of manganese ion was I = 5/2. In X-band the broaden inhomogeneous line is observed, due to $-1/2 \leftrightarrow 1/2$ electron transition angle dependence in powder.

Two-exponential curve was observed in the process of recovery of the "undoped" HAp longitudinal magnetization. We believe that an exhibitor with a short relaxation time refers to the spin diffusion and hardware effects and we won't discuss it further. Usually, the process with the longest characteristic time has a true spin-lattice relaxation.

The temperature dependence of the spin-lattice relaxation in samples doped hydroxyapatite with the size of 30 nm and 1000 nm is shown in the fig.2. There are three main ranges. Dependence T_1^{-1} NO_3^{2-} centers temperature particles having an average diameter is described by $\sim T^4$ in the temperature range 20 – 100 K. The dependence is different from normal T^9 and T^5. T_1^{-1} measured values are described by $T^{3.5}$ particles having an average diameter of 30 nm.

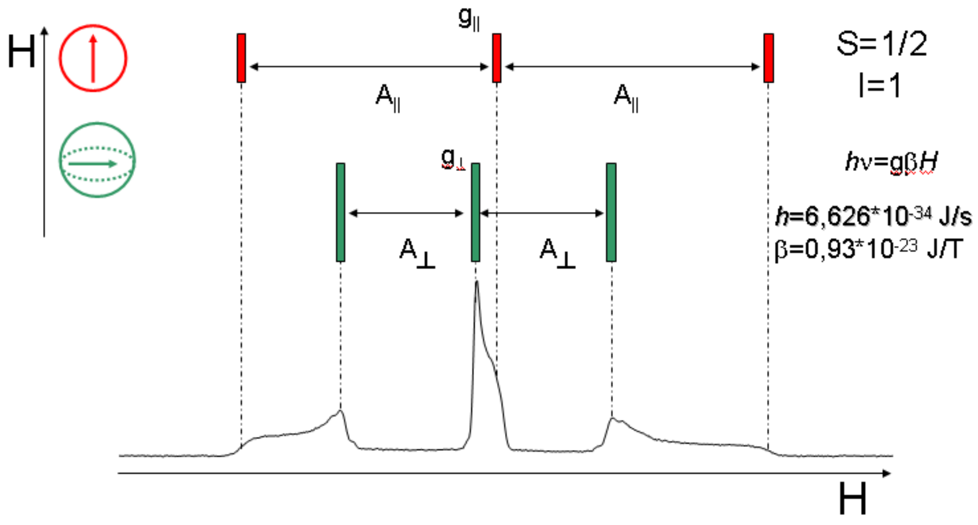

Fig.1. The structure of the EPR spectrum of NO_3^{2-} complexes in hydroxyapatite powder.

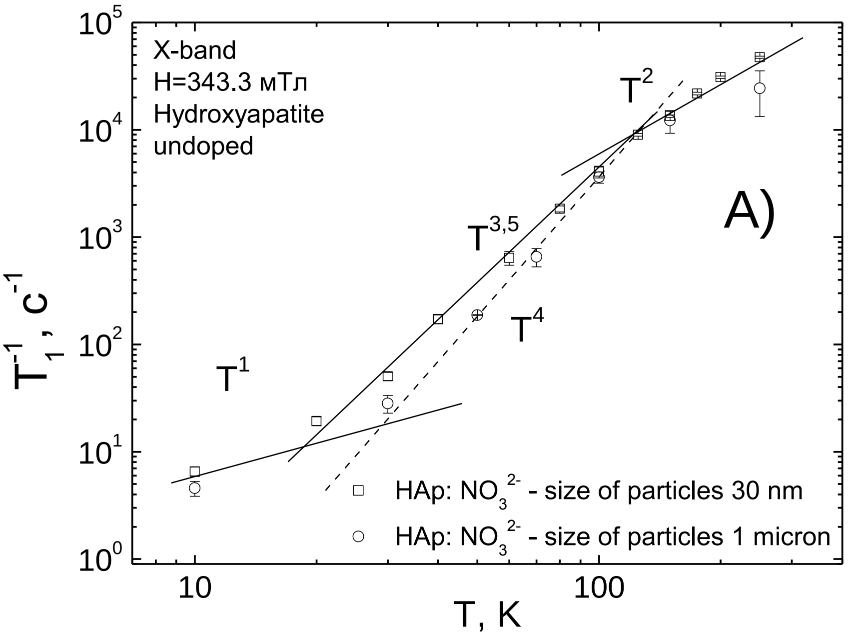

Fig.2. The temperature dependence of T_1^{-1} of NO_3^{2-} complexes in undoped hydroxyapatite with 30 nm and 1000 nm particles size.

This allows you to make preliminary conclusions on the effect of nanoparticle size on the spin-lattice relaxation rate. We are seeing deviation of depending on the above values with decreasing temperature. We assume that it should be a direct process, which is proportional to *T*.

The spectrum of complex NO_3^{2-} ($H = 343.3$ mT) superimposed on the spectrum of Mn^{2+} ions for measurement of relaxation times in the HAp doped by manganese. Therefore, to receive the longitudinal magnetization recovery curve we used a two-step process. Firstly we measured the relaxation time of the manganese ions in the $H = 326$ mT field, then we had used that time during the measures in the field of *H* = 343.3 mT as a third exponent. Thus, time for relaxation centers of NO_3^{2-} in a sample doped by Mn had been determined more correctly.

Temperature dependences of the spin-lattice relaxation time for the "undoped" hydroxyapatite of 30 nm at the centers NO_3^{2-} and "doped" impurity Mn^{2+} ions at the centers NO_3^{2-} and in the centers Mn^{2+} are shown in fig.3. Relaxation at impurity centers manganese corresponds Raman process and is proportional to T^2 in the field of high and medium temperatures. The increase in the relaxation rate can be seen for the centers NO_3^{2-} in the HAp doped by ion Mn^{2+}. Since HAp crystal structure with manganese and without manganese are identical then this means that the effect of manganese on the spin-lattice relaxation. However, manganese can affect only when both centers are in the same particle.

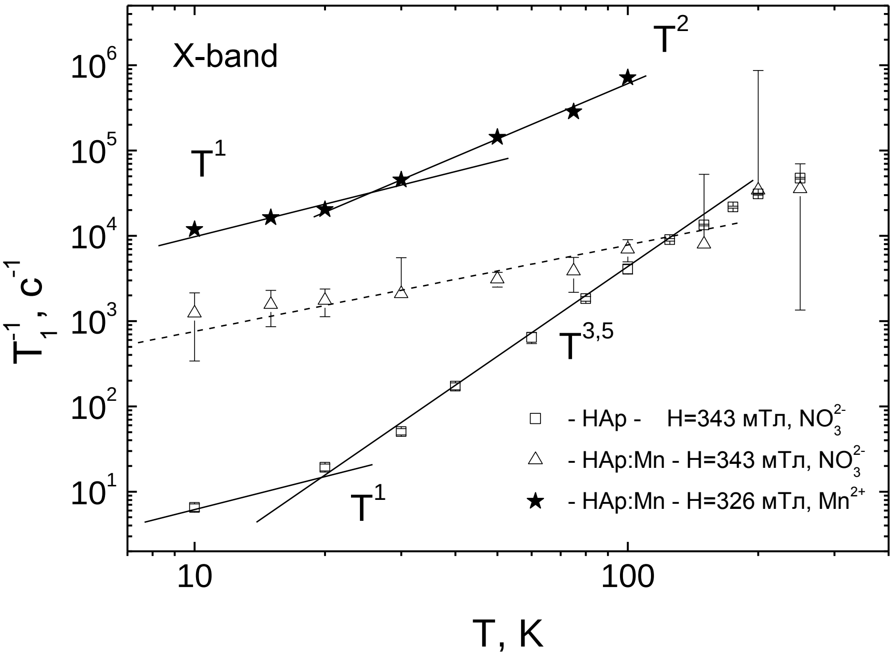

Fig.3. The temperature dependence of T_1^{-1} of NO_3^{2-} complexes in hydroxyapatite (30 nm) doped by Mn^{2+} and without it.

Thus, the temperature dependence of the spin-lattice relaxation can reveal new data on the distribution of impurities in the nanoparticles and their size.

References

[1] Kovaleva, E.S. Bioresorbable carbonated hydroxyapatite Ca10-xNax(PO4)6-x(CO3)x(OH)2 powders for bioactive materials preparation / E.S. Kovaleva, M.P. Shabanov, V.I. Putlyaev, Y.D. Tretyakov, V.K. Ivanov, N.I. Silkin // Cent. Eur. J. Chem. -2009. –V.7(2). –P. 168.

[2] Gafurov, M. Nitrogen-containing species in the structure of the synthesized nano-hydroxyapatite / M.Gafurov et. all // Pis'ma v ZhETF. -2014. –V. 99. -N.4. -P. 223 – 230.

Influence of minor changes of ligand environment of Dy^{3+} on the magnetic properties of single molecule magnets based on Me_2Dy_2 heteronuclear complexes

A.A. Sukhanov[1], V.K. Voronkova[1], A. Baniodeh[2], A.K. Powell[2]

[1]Zavoisky Physical-Technical Institute, Russian Academy of Sciences,
420029, Sibirsky tract 10/7, Kazan, Russia.

[2]Institute of Inorganic Chemistry, Karlsruhe Institute of Technology,
D-7613, Engesserstr. 15, Karlsruhe, Germany

e-mail: ansukhanov@mail.ru

Single molecule magnets (SMMs) are well-known molecular materials with the potential for using in spintronic devices and quantum computing [1, 2]. It is well known that the SMMs have a large high-spin ground state and a large easy-axis type magnetic anisotropy. The unusual combination of high-spin ground state and magnetic anisotropy gives a magnetic bistable molecule, resulting in a significant barrier to thermally activated magnetization relaxation. The condition for SMM with a high-spin ground state and a magnetic anisotropy is not easily achieved. Now it has defined that high magnetic anisotropy is the most critical requirement for an SMM. Metal ions with unquenched orbital angular momentum including 4f ions [3] and 4d and 5d metal ions with strong spin−orbit coupling and strong anisotropic magnetic exchange [4, 5] have been targeted. Currently for SMMs based on dysprosium ion (Dy^{3+}) achieved record value (~800 K) of barrier to thermally activated magnetization relaxation [6].

The SMM behaviour observed for complexes including 4f ions is due to the large magnetic anisotropy of the individual ions, caused by strong spin–orbit coupling and the crystal field effects due to the ligand environment [7].When considering heteronuclear complexes, the situation becomes even more complicated. Understanding how 4f – 4f, 3d – 4f interactions can have important for improving the performance of new SMMs.

In this work, we present the results of investigation series complexes containing high spin iron or aluminum ions and dysprosium ions with different ligand environment. The study of a family Fe_2Dy_2 heteronuclear complexes showed that the nature and position of the substituents affect the SMMs properties [8, 9]. Here we report the results of the EPR investigation of this and similar complexes Fe_2Dy_2 and Al_2Dy_2 to understand the reason for the change of SMM properties and character of influence of the spin-spin interactions on these properties. The EPR spectra of polycrystalline samples were measured at X-, Q- and W-bands in the temperature range of 50 – 4 K.

For the family Fe_2Dy_2 heteronuclear complexes, early we were shown that between iron ions realized strong antiferromagnetic exchange interactions [10]. Also we estimated zero-field parameters of iron ions. For Al_2Dy_2 heteronuclear complex, aluminum ion is diamagnetic ion. Therefore, at low temperatures for this series complexes can be taken into account only dysprosium ions to describe EPR spectra. It is known that a ground multiplet of the Dy^{3+} ion is split by the low-symmetry crystal field of the nearest environment into eight Kramers doublets [11]. The EPR spectra of the Dy^{3+} ions are observed at low temperature and are due to the transitions between states of the lowest doublet described by the effective $S = 1/2$ with high anisotropic g-factors. The low-temperature spectrum was well described by a simulation of the Dy–Dy fragment, which took into account only the dipole–dipole interaction between Dy^{3+} ions. Simulations of EPR spectrum shown (fig.1.). Subtle changes in the nature and position of the substituents on a ligand exert a changing of effective g-factor of dysprosium ion in the family Fe_2Dy_2 heteronuclear complexes. Therefore slightly structural changing in this family and changing 3d ion lead to change the ground state of Dy^{3+} ion (table 1).

For some complexes containing iron ions and dysprosium ions observed changing shape of EPR line after first recording EPR spectrum. In principal, in high magnetic field it is often observed. This is due to the small grains were self-oriented in a high magnetic field, revealed an existence of the “easy” axis of magnetic anisotropy. In our case magnetic field is low.

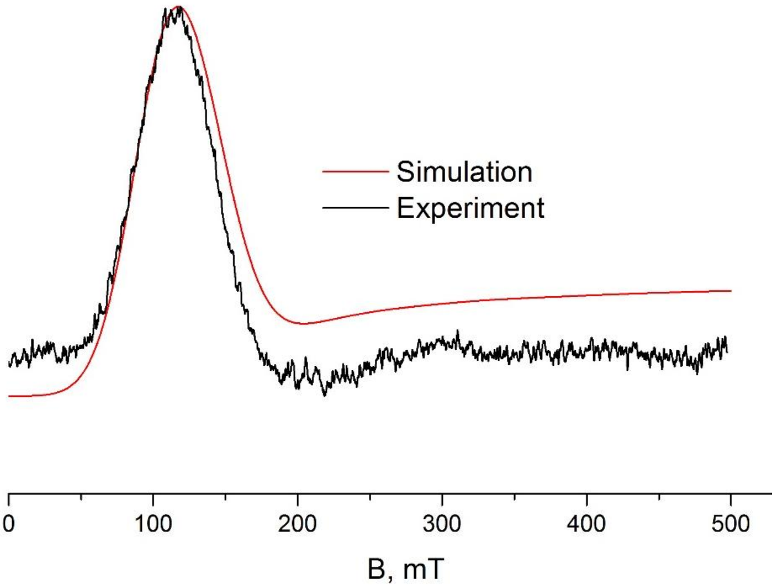

Fig.1. EPR spectra of $Fe_2Dy_2(OH)_2(teaH)_2(meta\text{-}CN\text{-}C_6H_4COO)_6$ compound in Q-band at temperature 5 K. Simulated spectrum was calculated into account the dipole–dipole interaction with parameters: $g_{x1} = g_{x2} = 0.1$, $g_{y1} = g_{y2} = 0.1$, $g_{z1} = g_{z2} = 19.8$, $r_{12} = 6.1$ (distances between Dy^{3+} ions) and $\theta = 48.1$ (angle between directions of g_z and r).

Table 1.

Compound	**Effective g-factor**	**Ground state of Dy^{3+}**
$Fe_2Dy_2(OH)_2(teaH)_2(meta\text{-}CN\text{-}C_6H_4COO)_6$	$g_x = g_y \approx 0{,}1$; $g_z = 19{,}8$	$\|J = 15/2, M_J = 15/2\rangle$ $g_z = 20$
$Fe_2Dy_2(OH)_2(teaH)_2(para\text{-}CN\text{-}C_6H_4COO)_6$	$g_x = g_y \approx 0{,}1$; $g_z = 14{,}6$	$\|J = 15/2, M_J = 11/2\rangle$ $g_z = 14{,}67$
$Fe_2Dy_2(OH)_2(teaH)_2(para\text{-}CH_3\text{-}C_6H_4COO)_6$	$g_x = g_y \approx 0{,}1$; $g_z = 19{,}8$	$\|J = 15/2, M_J = 15/2\rangle$ $g_z = 20$
$Fe_2Dy_2(OH)_2(Me\text{-}teaH)_2(NO_3\text{-}(C_6H_5COO)_2)_2$	$g_x = g_y \approx 0{,}1$; $g_z = 17{,}3$	$\|J = 15/2, M_J = 13/2\rangle$ $g_z = 17{,}33$
Al_2Dy_2–di-CF_3	$g_x = g_y \approx 0{,}1$; $g_z = 14{,}6$	$\|J = 15/2, M_J = 11/2\rangle$ $g_z = 14{,}67$

Acknowledgements

This research is supported in part by the Russian Foundation for Basic Research (project no. 13-02-01157).

References

[1] Troiani, Filippo, and Marco Affronte. "Molecular spins for quantum information technologies." *Chemical Society Reviews* 40.6 (2011): 3119-3129.

[2] Leuenberger, Michael N., and Daniel Loss. "Quantum computing in molecular magnets."*Nature* 410.6830 (2001): 789-793.

[3] Sessoli, Roberta, and Annie K. Powell. "Strategies towards single molecule magnets based on lanthanide ions." *Coordination Chemistry Reviews* 253.19 (2009): 2328-2341.

[4] Freedman, Danna E., et al. "A redox-switchable single-molecule magnet incorporating [Re (CN) 7] 3." *Journal of the American Chemical Society* 130.10 (2008): 2884-2885.

[5] Dreiser, Jan, et al. "Three-Axis Anisotropic Exchange Coupling in the Single-Molecule Magnets NEt4 [MnIII2 (5-Brsalen) 2 (MeOH) 2MIII (CN) 6](M= Ru, Os)." *Chemistry-A European Journal* 19.11 (2013): 3693-3701.

[6] Blagg, Robin J., et al. "Magnetic relaxation pathways in lanthanide single-molecule magnets." *Nature chemistry* 5.8 (2013): 673-678.

[7] Sorace, Lorenzo, Cristiano Benelli, and Dante Gatteschi. "Lanthanides in molecular magnetism: old tools in a new field." *Chemical Society Reviews* 40.6 (2011): 3092-3104.

[8] Mereacre, Valeriu, et al. "Effect of Ligand Substitution on the Interaction Between Anisotropic Dy (III) Ions and 57Fe Nuclei in Fe2Dy2 Coordination Clusters." *Journal of the American Chemical Society* 133.39 (2011): 15335-15337.

[9] Baniodeh, Amer, et al. "Para versus meta ligand substituents as a means of directing magnetic anisotropy in Fe 2 Dy 2 coordination clusters." *Chemical Communications* 49.83 (2013): 9666-9668.

[10] Baniodeh, Amer, et al. "Magnetic anisotropy and exchange coupling in a family of isostructural Fe III 2 Ln III 2 complexes." D*alton Transactions* 42.24 (2013): 8926-8938.

[11] Bleaney, B., and A. Abragam. "Electron paramagnetic resonance of transition ions." *Clarendon, Oxford* (1970).

Magnetic resonance studies of heat treated wood

E.I. Kondratyeva[1,2], K.R. Safiullin[1,2], I.G. Motygullin[1], M.S. Tagirov[1,2]

[1]Kazan Federal University, 420008, Kremlevskaya 18, Kazan, Russia
[2]Institute of Perspective Research, TAS, 420111, L.Bulachnaya 36a, Kazan, Russia

e-mail: katarina.kondratyeva@gmail.com

Heat treatment of wood is a processing technique that allows to change some wood properties such as durability, low hygroscopicity, dimensional stability, etc [1]. The use of heat during treatment leads to a production of wood with predetermined properties: color shades [2], durability, environmental resistance. During this process some chemical agents, wax, fats, phenols, elements of a hemicellulose and glucose can be evaporated from the wood tissues. As a result wood can become more stable to rot, various microorganisms and fungi, the biological resistance of the material increases.

This work is devoted to the complex study of the effect of heat treatment on the properties of wood of different species by electron paramagnetic resonance, pulse nuclear magnetic resonance, optical microscopy methods and measurement of changes of some sample properties as moisture resistance, hardness and color.

In this work such species of wood as a birch, larch, linden, pine and spruce from Kirov region, Russia, were investigated. A special vacuum oven with pump was used for the heat treatment at temperatures of 150°C and 220°C. The duration of processing varied in the range from 40 minutes to 8 hours. The wood samples moisture content values were measured by the special Hydro Condtrol device and by the laboratory scales.

Electron paramagnetic resonance (EPR) experiments were carried out on the Varian E-12 X-Band spectrometer at 9.3 GHz frequency and at the room temperature. During the experiments special reference sample were used to qualitatively and quantitatively compare the obtained EPR spectra of different samples. The signal of free radicals of wood near $g = 2.002$ has been observed.

The influence of vacuum 220°C heat treatment duration on free radicals signal amplitude has been studied. Experimentally obtained dependencies for larch, pine, spruce and linden are shown in fig.1.

The amplitude of the free radical signal in spruce samples increases linearly with the thermal treatment duration. This may indicate a break of chemical bonds in wood polymer chains that leads to the formation of free radicals. The amplitude of the signal of free radicals also increases linearly with the heat treatment duration for other wood species as larch, linden and pine trees. However, after long heat treatment duration the free radicals signal amplitude values decrease. Probably this effect is connected with the severe destructive process in the wood samples.

The home built pulsed NMR spectrometer was used in ^{1}H nuclear magnetic resonance experiments [3]. Measurements of longitudinal magnetization recovery time T_1 and transverse magnetization relaxation time T_2 of ^{1}H nuclei were performed at 11 MHz frequency and at the room temperature. Untreated and thermally treated samples of birch were used in these experiments. The standard saturation-recovery and spin-echo techniques were used to obtain T_1 and T_2 relaxation times of ^{1}H nuclei. It is found that longitudinal magnetization recovery time T_1 values are close to each other for all used samples and is close to 100 ms. The transverse magnetization relaxation time T_2 of ca. 300 μs were also found for studied samples. Thus, by results of the experiments made by a nuclear magnetic resonance on ^{1}H nuclei of wood tissues revealed us that longitudinal magnetization recovery time T_1 and transverse magnetization relaxation time T_2 of ^1H nuclei do not change after the heat treatment in spite of the fact that the concentration of free radicals in samples is different.

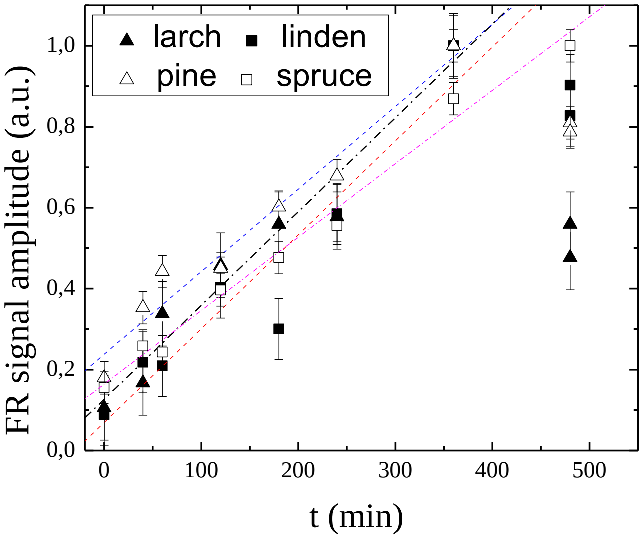

Fig.1. The normalized EPR signal amplitude of samples and its correlation with the vacuum thermal treatment duration at 220°C. Dashed line represents the linear behaviour of the obtained data.

Heat treated samples were also studied by an optical microscope at Neel's Institute (Grenoble, France). And samples with 40 min, 240 min, 480 min heat treatment duration as well as untreated samples were investigated.

The microcuts of wood of a larch obtained by an optical microscope at 100 μm scale for various duration of heat treatment are presented in fig.2.

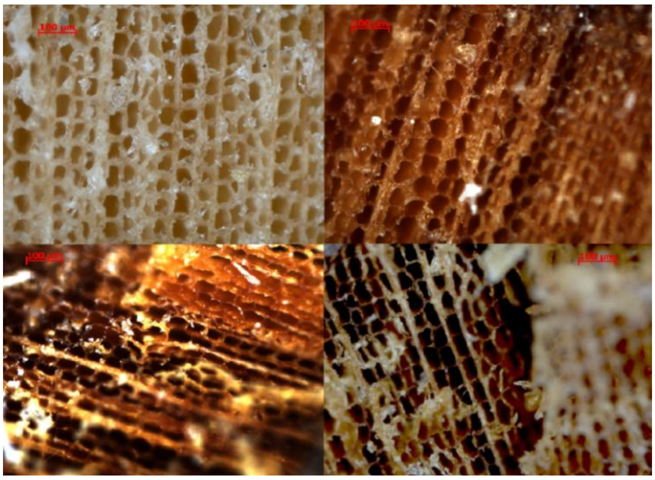

Fig.2. Optical microscope images of samples of the thermally untreated and treated at 220°C

Obtained images were analyzed and following pore area distributions were obtained. Fig.3 displays the pore area distribution changes with the thermal treatment for larch samples.

The distribution center moves to the bigger pore areas (from 750 to 1000 μm^2). This can testify that some small pores are destructed by heat. The microscopy results show that destructive changes appear in structural composition of wood after the heat treatment. Indirectly it also can be concerned as an evidence of wood polymer chains breaks that is observed in our EPR experiments.

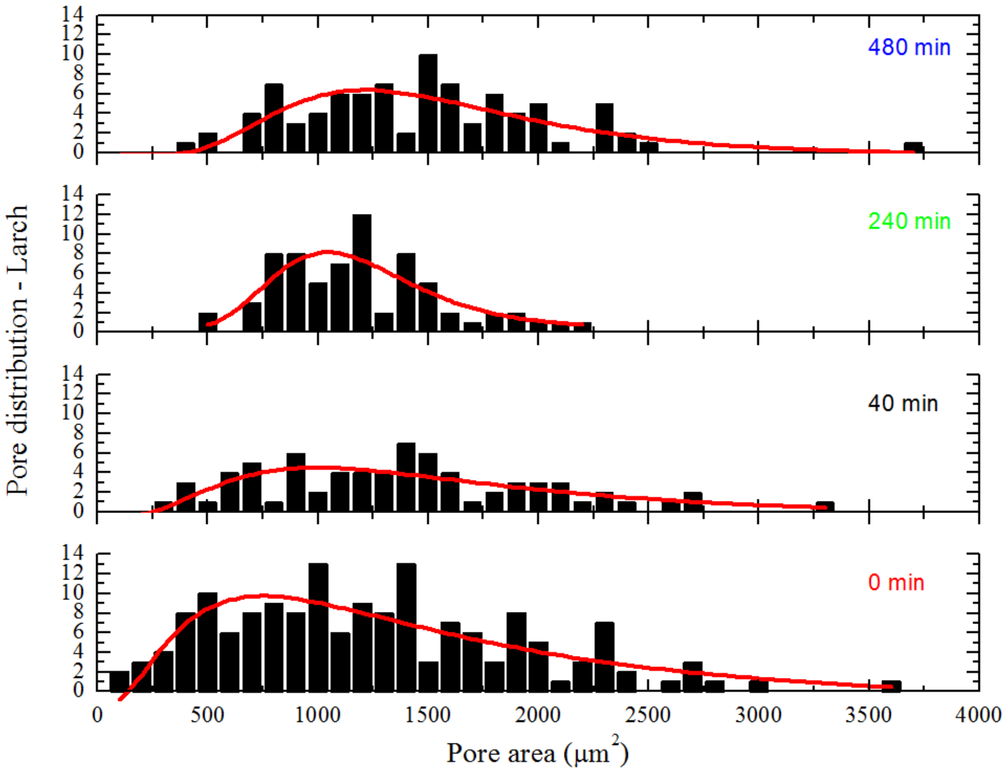

Fig.3. Pore size distribution of the thermally untreated and treated at 220°C larch samples (at 20 mbar pressure): 0 min, 40 min, 4 h and 8 h treatment.

Investigation of various thermally treated wood species by magnetic resonance methods revealed important changes in wood structure that were not available for observation by other methods. Amplitude of the signal of free radicals in wood increases linearly with the heat treatment duration that may indicate a break of polymer chains in the wood tissues and as a consequence the formation of free radicals. Despite on the amount of free radicals in the wood, the ^{1}H NMR relaxation times T_1 and T_2 do not change with the applied heat treatment. This fact leads to a conclusion that new ruptures are located far enough from the bulk ^{1}H atoms, probably they appear in long polymer chains of wood tissues.

Observed changes in samples surface quality and pore size distribution by microscopy fulfill this conclusion. Occurred deformations of wood capillary structures are in accord to the results obtained by carried magnetic resonance experiments.

This work is partially supported according to the Russian Government Program of Competitive Growth of Kazan Federal University.

References

[1] Esteves B., Pereira H. Wood modification by heat treatment: A review //BioResources. – 2008. – T. 4. – №. 1. – C. 370-404.

[2] Gunduz G., Aydemir D., Korkut S. The effect of heat treatment on some mechanical properties and color changes of uludag fir wood //Drying Technology. – 2010. – T. 28. – №. 2. – C. 249-255.

[3] Alakshin, E.M. The home-built pulse nuclear magnetic resonance spectrometer with digital quadrature detection for 3He research at low temperatures [text] / E.M. Alakshin, R.R. Gazizulin, A.V. Klochkov, V.V. Kuzmin, A.M. Sabitova, T.R. Safin, M.S. Tagirov // Magnetic Resonance in Solids. – 2013.– V.15.,N.1.– P.13104. (6 pp.).

High resolution NMR spectroscopy of water-soluble p-tert-butylthiacalix[4]arenes

E.A. Arkhipova[1], A.B. Konov[3], P.L. Padnya[1], B.I. Khayrutdinov[1,2], I.I. Stoikov[1]

[1]Institute of Physics, Kazan Federal University, Kremlevskaya str. 18, 420008 Kazan, Russia.

[2]Kazan Institute of Biochemistry and Biophysics, 420111, Lobachevsky str. 2/31, Kazan, Russia.

[3]Kazan Physical -Technical Institute, 420029, Sibirsky tract 10/7, Kazan, Russia.

e-mail: elya4445@yandex.ru

Abstract

Self-assembly of p-tert-butylthiacalix[4]arene in the cone and 1,3-alternate conformation have been investigated by using high-resolution NMR spectroscopy. 2D ^{1}H–^{1}H–NOESY spectra showed that thiacalix[4]arene in the cone conformation is characterized by a pronounced shift the monomer-micelle, but for thiacalix[4]arene in the 1,3-alternate conformation micellar transition is not observed.

Introduction

One of the strongest growing areas of chemistry is to synthesize synthetic receptors, which have the property of self-assembly in solution. Studies conducted in the field of compounds which can detect metal cations, organic matter and protein surface, i.e. are able to act as sensors. One of the structures used to create these receptors is calix[4]arene. The molecules of the substance can be in one of two states: monomer (free) and micellar (aggregated) forms. That is why it was interesting to trace the dependence of the conformation of thiacalixarenes and their concentration in the solution on the micelle forming properties.

Objects and methods

The structures of the studied p-tert-butylthiacalix[4]arenes are shown in fig.1. Both molecules have the same chemical composition ($C_{92}H_{144}$ $Br_4N_{12}O_{20}S_4$), but have different spatial structure. NMR measurements were performed at 30°C on 5 mM thiacalix[4]arene samples in pure H_2O with 10% D_2O with the help of the spectrometer Bruker Avance III 600. Internal standard trimethylsilyl propionate (TSP) has been used. All NMR spectra were processed and analyzed with TopSpin2.2. Standard pulse programs, provided by the manufacturer, were used for COSY, TOCSY, HSQC, HMBC and NOESY multipulse sequences. NOESY spectra were recorded using a mixing time of 200 ms. Full assignment of NMR signals were made by analysis of 2D homo- and hetero-correlation spectra such as: COSY, TOCSY, HSQC and HMBC.

Results

NOESY-spectrum enables us to make conclusions about the spatial configuration of the molecule. Despite of the fact that both NOESY spectra of p-tert-butylthiacalix[4]arenes are performed in the same conditions at concentration of 5 mM, one can notice significant differences. There are a few NOE cross-peaks in the spectrum of calix[4]arene in the 1,3-alternate conformation in the selected area in fig.2. That cross-peaks has opposite phase in the NOESY spectrum and correspond interaction between NH15 and H12, H16, H19 protons. On the other hand the number of NOE cross-peaks in the spectrum of calix[4]arenes in the

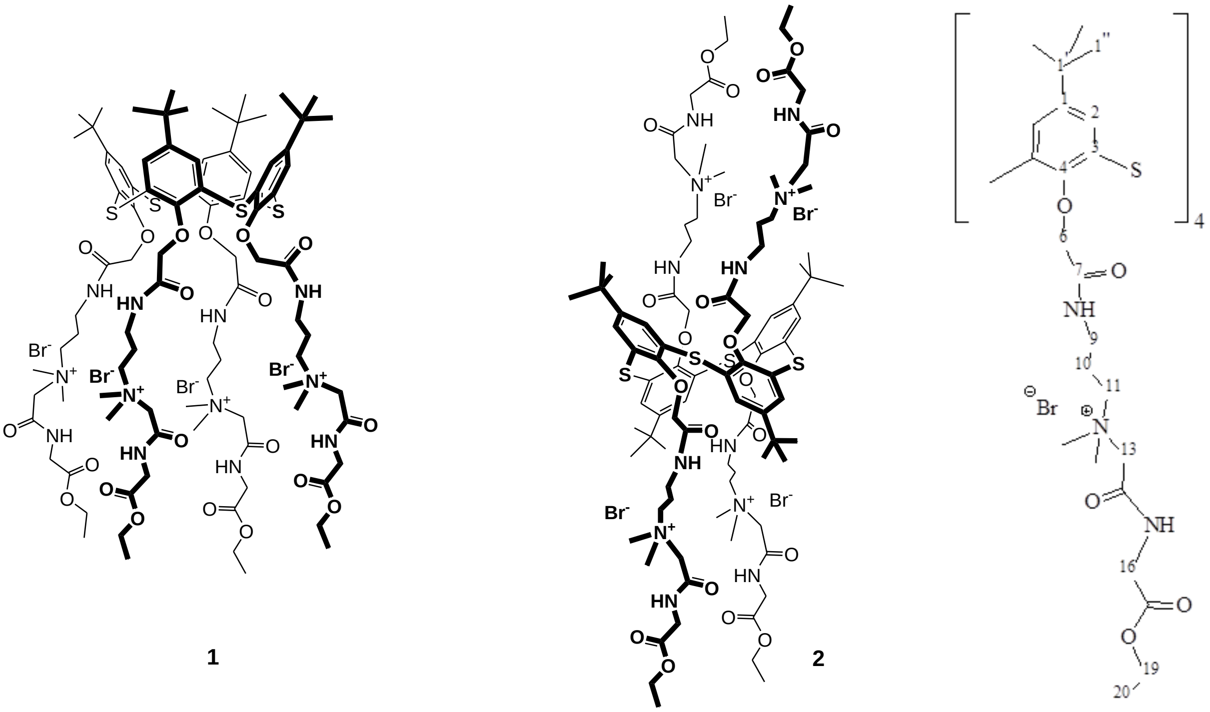

Fig.1. The structures of calix [4] arenes in the cone conformation (1) and 1,3-alternate conformation (2)

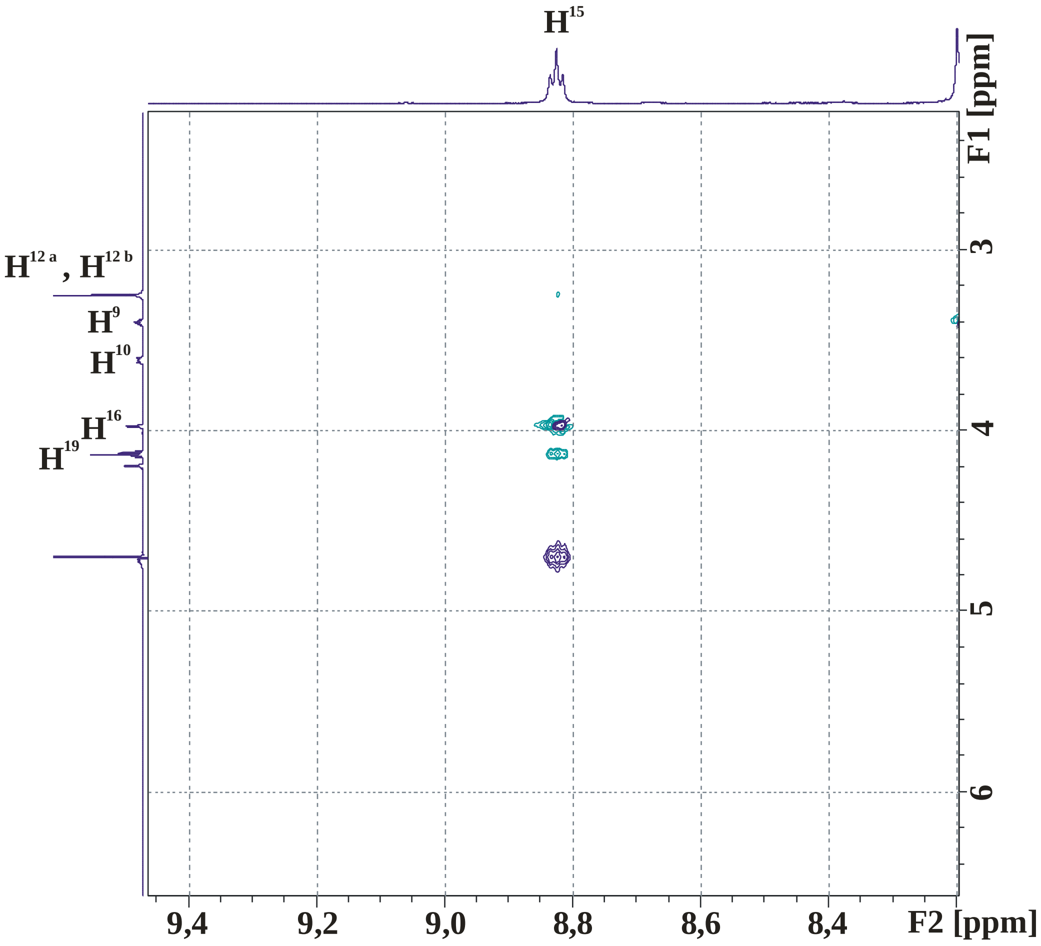

Fig.2. NOESY spectrum of p-tert-butylthiacalix[4]arene in the 1,3-alternate conformation at a concentration of 5mM at 30 °C in a solution of 10% D_2 O + 90% H_2 O.

cone conformation is larger and has higher intensity with positive phase, as shown in fig.3.

The fact of different phase of NOE cross-peaks in NOESY spectra demonstrates the difference in the correlation time for the calix[4]arenas in cone and 1,3-alternate conformation. It means that the mobility of the whole molecule of p-tert-butylthiacalix[4]arene in the cone conformation is slower than in the 1,3-alternate. Also in the NOESY spectrum of cone conformation there are visible cross-peaks between pair of protons NH8-H19 that are located far from one another in the chain and for this reason should not produce a cross-peak. Such experimental difference of NOESY spectra in cone and 1,3-alternate conformations can be explained by the micelle formation of p-tert-butylthiacalix[4]arene for cone one. On the other hand p-tert-butylthiacalix[4]arene in 1,3-alternate conformation is in monomer state.

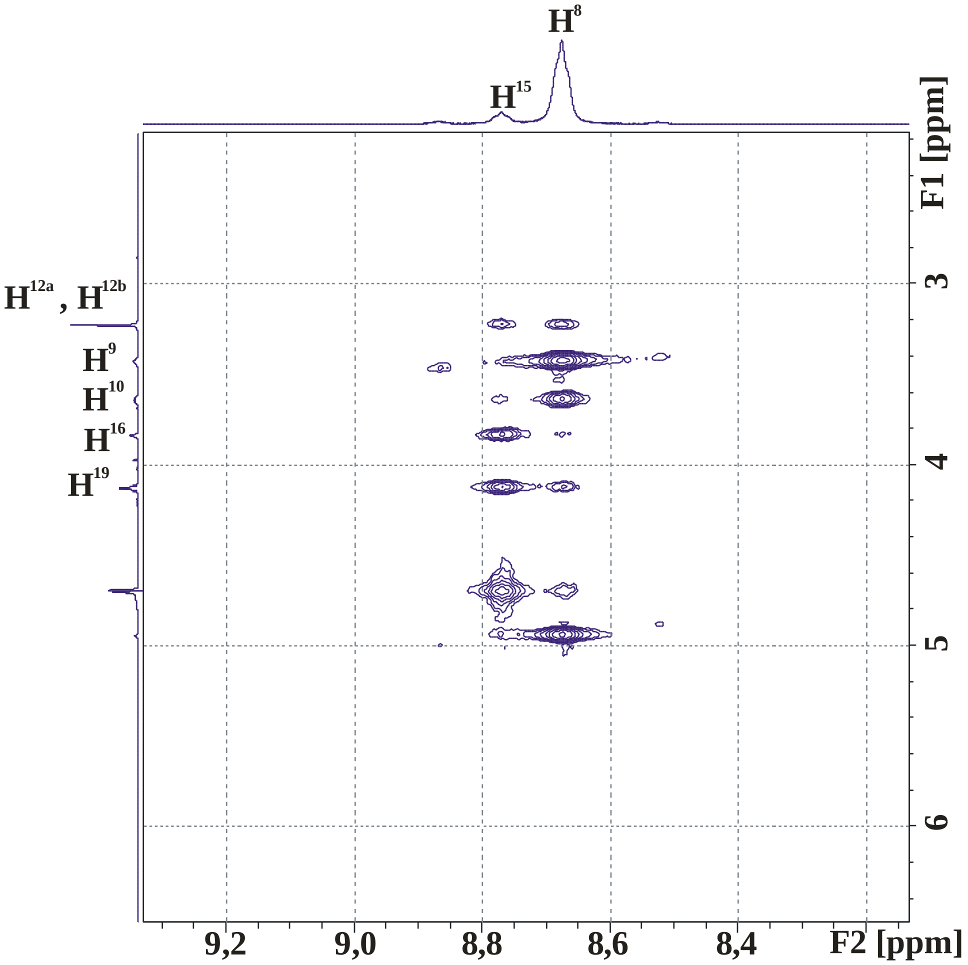

Fig.3. NOESY spectrum of p-tert-butylthiacalix[4]arene in the cone conformation at a concentration of 5mM at 30 °C in a solution of 10% D_2 O + 90% H_2 O.

Conclusion

2D NOESY spectroscopy study shows that p-tert-butylthiacalix[4]arene in the cone conformation has at a 5mM concentration the property to form micellar structures, but thiacalix[4]arene in the 1,3-alternate conformation at the same concentration has no such property and is predominantly in the monomeric state.

Studies of self-diffusion of p-tert-butylthiacalix[4]arene based water soluble compounds

L.B. Magomedova[1], A.B. Konov[3], P.L. Padnya[1], B.I. Khayrutdinov[1,2], I.I. Stoikov[1]

[1]Institute of Physics, Kazan Federal University, Kremlevskaya str. 18, 420008, Kazan, Russia.
[2]Kazan Institute of Biochemistry and Biophysics, 420111, Lobachevsky str.,2/31, Kazan, Russia.
[3]Kazan Physical -Technical Institute, 420029, Sibirsky tract 10/7, Kazan, Russia.

e-mail: dusiasparrow@yandex.ru

Abstract

In this work the aggregation properties of p-tert-butylthiacalix[4]arene are studied. Two conformations (cone and 1,3-alternate) of the object under study were examined under equal conditions and as a result we had an opportunity to compare the behavior of these two kinds of molecules in solution.

Introduction

The problem of creating receptors has become rather urgent recently and calixarene is often used as the base for synthesis of such substances. It is widely chosen for this role because the molecule can be easily functionalized and so we can get a great variety of objects with different properties. Some of them can form supramolecular structures of different configurations. Depending on the functional group and the form of aggregation they can interact with different ligands, and form host-guest complexes.

Objects and methods

The experiment has been carried out using high-resolutional NMR spectrometer Bruker Avance 400 equipped with 5 mm BBO probe with gradient coil. Self-diffusion coefficient has been measured on the proton nuclei ^{1}H (400.13 MHz). The objects under research were p-tert-butylthiacalix[4]arene in conformation cone and 1,3-alternate, both consisting of four identical monochains but having different geometrical configurations. The samples were dissolved in pure H_2O with 10% D_2O and contained trimethylsilyl propionate (TSP) as internal standard. The measurements were made at temperature 30 °C with the gradient of the magnetic field varying between 0 and 0,32 $T \cdot m^{-1}$ with the constant diffusion time and length of magnetic field gradient pulse.

Sine shape of gradient pulse was used. Diffusion relaxation was analyzed using protons of tert-butyl group because these protons give the most intensive signal, which reduces measurement error (the best signal-to-noise ratio), also the protons of this group do not participate in molecular exchange processes.

During the experiment the self-diffusion coefficients of the solutions with concentrations from 0.1 to 50 mM were measured.

Data analysis was carried using Topspin and OriginPro Software.

Results and discussion

It has been revealed, that the self-diffusion coefficient of p-tert-butylthiacalix[4]arenes decreases with increasing concentration. The figure 2 represents dependence of self-diffusion

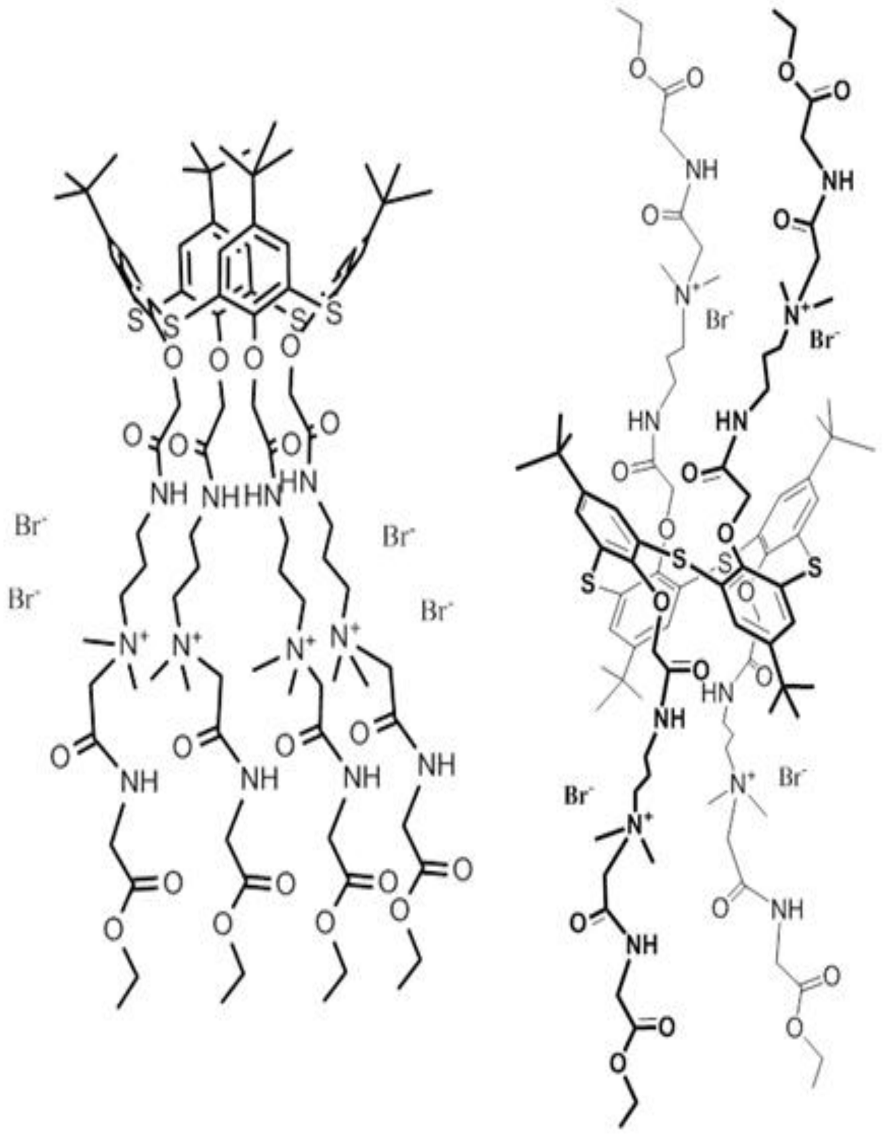

1 2

Fig.1. p-tert-butylthiacalix[4]arene in conformation cone (1) and 1,3-alternate (2).

coefficient on concentration for p-tert-butylthiacalix[4]arenas in conformation 1,3-alternate and cone. As shown in this figure decrease of self-diffusion coefficient for cone conformation took place faster than for 1,3-altenate. The value of self-diffusion coefficient depends on the proportions of molecule and in the simplest case can be described by Stokes–Einstein equation. The dependence in figure 2 corresponds to increasing radius of molecules that can be explained by formation micelle. Micelle formation of the molecule in the cone structure proceeds according to the mechanism of self-association of classical micelle-forming surfactants [1]. The self-diffusion coefficient for monomeric form is $D = 2{,}95\cdot 10^{-10}$ m^2s^{-1}, ($\varepsilon = 4\%$). Taking into account geometrical configuration of the molecule one can assume that they form spherical micelles so that the hydrophobic tert-butyl group was located in their inner part. The structure of the micelles formed by the molecules of the sample in configuration 1,3-alternate cannot be analyzed on the base of the same model.

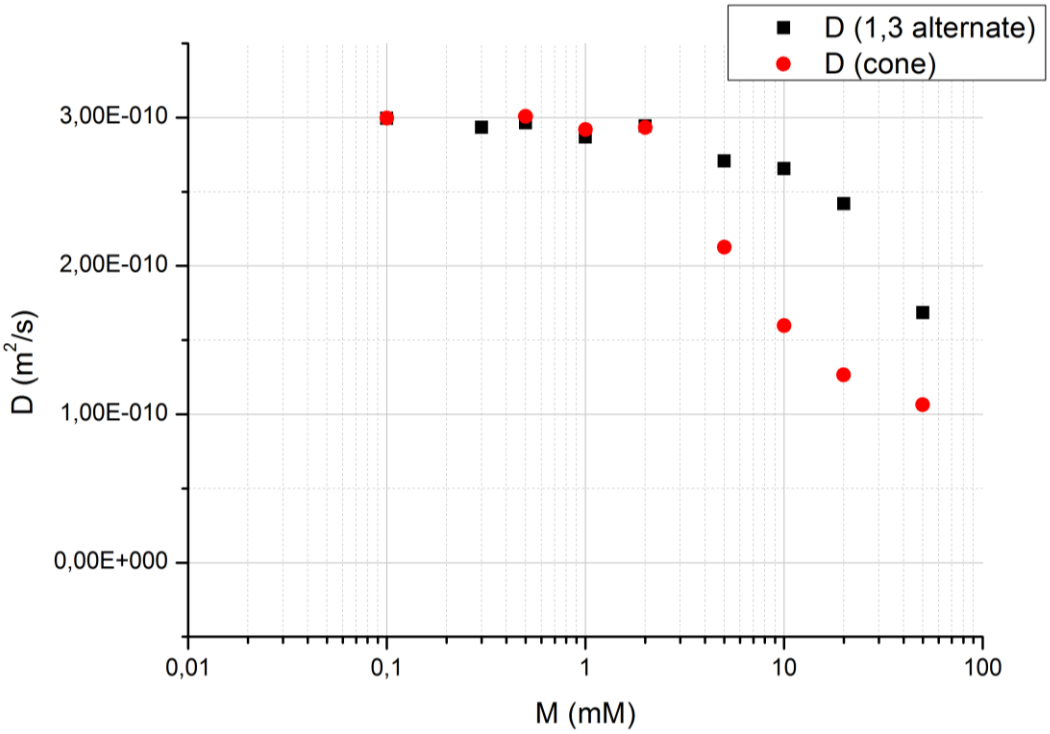

Fig.2. Dependence of the self-diffusion coefficients on the concentration for molecules in conformation 1,3-alternate and cone.

Conclusion

Thus, NMR diffusion study of p-tert-butylthiacalix[4]arene reveals that spatial configuration of the molecule affects the self-association process. Micelle formation of the molecules with cone structure starts at lower values of concentration, consequently objects of this structure form micelles more efficiently than the molecules with 1,3-alternate configuration.

References

[1] Zuev Yu.F., Gnezdilov O.I., Zueva O.S., Us'yarov O.G. Effective self-diffusion coefficients of ions in micellar solutions of sodium dodecyl sulfate. Colloid Journal.2011. T.73. C.43-49.

Spin relaxation of NV^{-} center in diamond

K.M. Yunusova, G.V. Mamin, S.B. Orlinskii, B.V. Yavkin

Kazan Federal University, 420008, Kremlevskaya Street 18, Kazan, Russia

e-mail: kam.chaos@gmail.com

Currently, the most studied defects in diamonds are nitrogen-containing ones. The nitrogen-vacancy (NV) centers in diamonds are of particular interest due to a possibility of their use in e.g. medicine [1] or in development of quantum computers [2]. Nevertheless many important questions are still open. In this report we will focus on the negatively charged NV center.

Angular dependency of the high-frequency EPR and temperature dependency of the spin-lattice relaxation of the NV^{-} center in diamond have been studied. The sample was a diamond single crystal with the size of about 250 μm, fabricated commercially by Element Six using high pressure high temperature (HPHT) synthesis. The crystal with an initial concentration of nitrogen impurities of $\sim 5\cdot10^{18}$ cm^{-3} was irradiated by electrons (energies ~ 2 MeV and flux density of $\sim 10^{18}$ cm^{-2}) and then annealed in the hydrogen atmosphere at $T = 800°C$ for 2 hours.

The measurements were performed with Bruker Elexsys 680 spectrometer operating in the W-microwave band (microwave frequency ~ 94 GHz). EPR spectra were obtained using two-pulse Hahn echo sequence $\pi/2 - \tau - \pi$ with $\pi/2$ pulse duration of 48 ns and $\tau = 280$ ns. The spin-lattice relaxation time was measured with the inversion-recovery sequence $\pi - T - \pi/2 - \tau - \pi$ with identical pulse durations and τ value. Sample temperature was controlled using continuous gas flow system and varied over a wide range (25 ÷ 300 K).

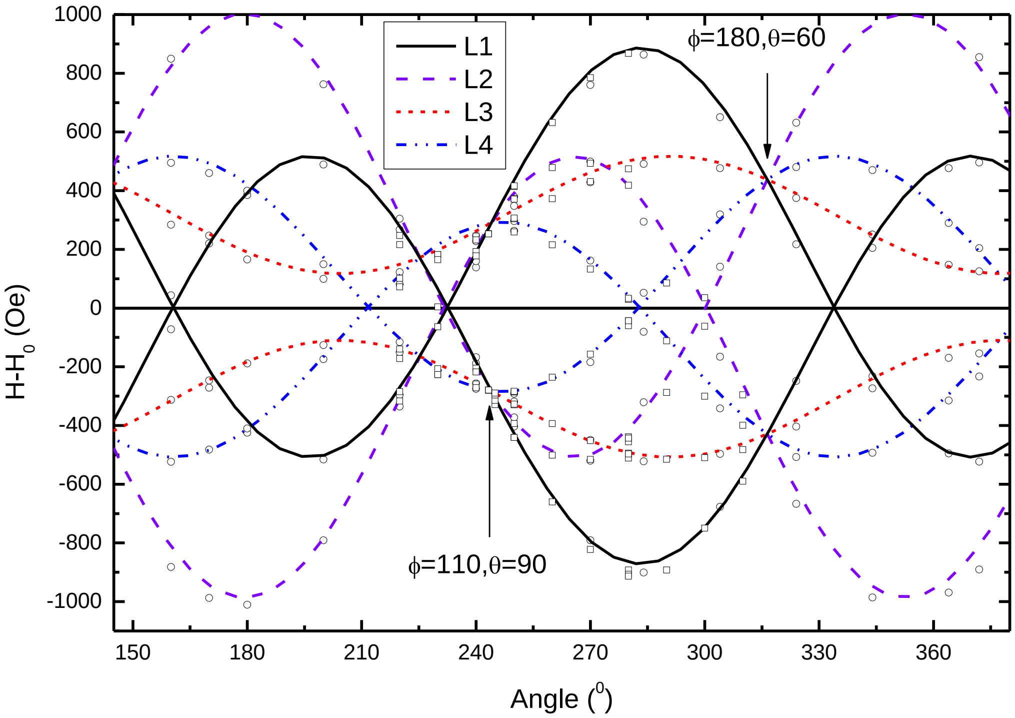

Fig.1. Angular dependency of the EPR spectra. L1 to L4 represent four magnetically inequivalent NV^{-} centers.

Analysis of the EPR spectra angular dependency has shown that the sample crystal axes didn't match perfectly the laboratory coordinate system. Eight lines are observed in spectra presented in the fig.1. A pair of lines originates from each of the four magnetically inequivalent NV^- centers. Sample tilt angle was found to be ~ 8°.

Temperature dependency of the spin-lattice relaxation time T_1 was fit taking into account the direct, Raman and Orbach-Aminov processes (fig. 2). In case of Orbach-Aminov relaxation process in the exponent we use the energy of the local mode in Kelvins calculated in [3]. It is found that this vibrational mode in diamond defines the speed of the spin-lattice relaxation of the NV^- center.

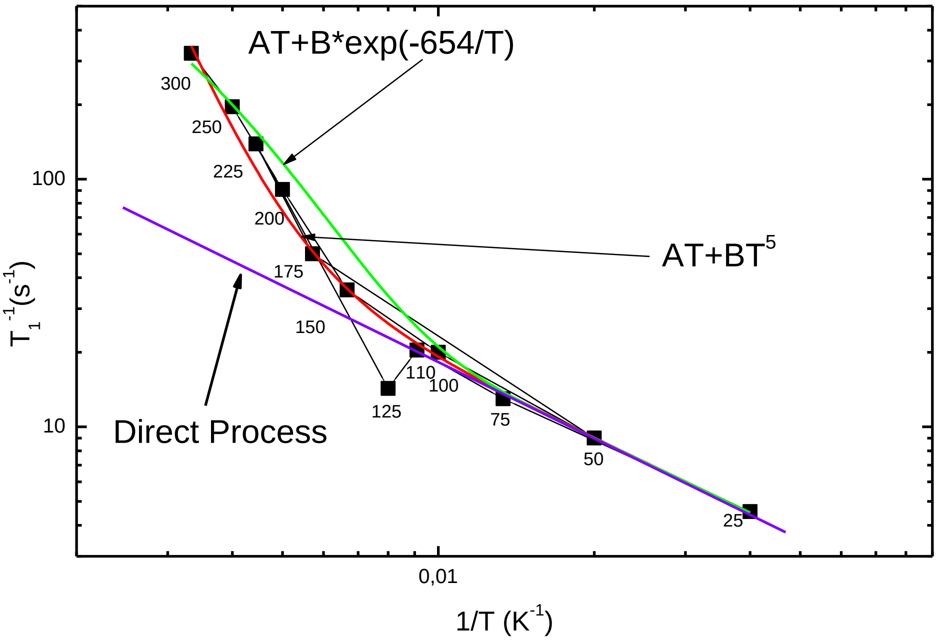

Fig.2. Temperature dependency of the spin-lattice relaxation rate. The observed dependency was fitted using the direct, Raman and Orbach-Aminov processes.

An unusual behavior is observed in two parts of the temperature dependency of the spin-lattice relaxation. First, although the direct process normally vanishes at about 50 K, in our experiment it persists up to 110 K. Second, in the temperature range from 100 to 150 K spin-lattice relaxation cannot be described adequately by any of considered models.

References

[1] Baughman R.H., Zakhidov A.A., Heer W.A. Carbon Nanotubes-the Route Toward Applications // Science. - 2002. - V. 297. - P. 787–792.

[2] Geiselmann M., Juan M. L., Regner J., Say J.M. et al. Three-dimensional optical manipulation of a single electron spin // Nature Nanotechnology. – 2013. – I. 3. – V. 8. – P. 175-179.

[3] Redman D.A., Brown S., Sands R.H., Rand S.C. Spin Dynamics and Electronic States of N-V Centers in Diamond by EPR and Four-Wave-Mixing Spectroscopy // Physical Review Letters, - 1991. – V.67. – N.24. – P. 3420-3423.

Magnetic properties in nanocomposite materials $(SrFe_{12}O_{19})_x(CaCu_3Ti_4O_{12})_{1-x}$

R.M. Eremina[1,2], Sharipov[1], I.V. Yatsyk[1,2], N.M. Lyadov[1], T.P. Gavrilova[1,2],
I.F. Gilmutdinov[2], A.G. Kiyamov[2], Yu.V. Kabirov[3], V.G. Gavrilyachenko[3], T.I. Chupakhina[4]

[1]E. K. Zavoisky Physical-Technical Institute RAS, Kazan, 420029, Russia
[2]Kazan (Volga Region) Federal University, Kazan, 420018, Russia
[3]Southern Federal University, Rostov-on-Don, 344006, Russia
[4]Institute of Solid State Chemistry RAS, Yakaterinburg, 620990, Russia

e-mail: i.yatzyk@gmail.com

Composite materials attract much attention due to the manifestation of unexpected new physical properties in them [1]. Studies of composite compounds with high values of magnetic susceptibility and dielectric permittivity are of interest. Hexaferrites, in particular strontium hexaferrite (M-ferrite) $SrFe_{12}O_{19}$ (SFO), are often used among possible magnetic single-phase materials [2], the phase transition temperature into the ferrimagnetic state T_C = 737 K [3, 4]. The compound $CaCu_3Ti_4O_{12}$ (CCTO) with phase transition into the antiferromagnetically ordered phase below 25 K and has the high value of the dielectric permittivity $\varepsilon \sim 10^4 \div 10^5$ in the wide temperature ($100 \div 600$ K) and frequency (to tens of MHz) range [5, 6].

This work is aimed at studying magnetic properties of SFO- and CCTO-based composites prepared according to the specific «core-shell» technology by the magnetic resonance and magnetometry methods.

The temperature dependence of the magnetization of $(SrFe_{12}O_{19})_{0.05}(CaCu_3Ti_4O_{12})_{0.95}$, $(SrFe_{12}O_{19})_{0.9}(CaCu_3Ti_4O_{12})_{0.1}$ and $SrFe_{12}O_{19}$ was studied in the temperature range from 4 to 300 K. Fig.1a shows the temperature dependence of the inverse quantity H/M of $(SrFe_{12}O_{19})_{0.05}(CaCu_3Ti_4O_{12})_{0.95}$ composite measured in the field of 1000 Oe. One can see kinks at temperatures of approximately 25 and 220 K in the course of the temperature dependence. It is obvious that the antiferromagnetic ordering takes place in the $CaCu_3Ti_4O_{12}$ subsystem in $(SrFe_{12}O_{19})_{0.05}(CaCu_3Ti_4O_{12})_{0.95}$ composite at the temperature of 25 K that is in agreement with literature data.

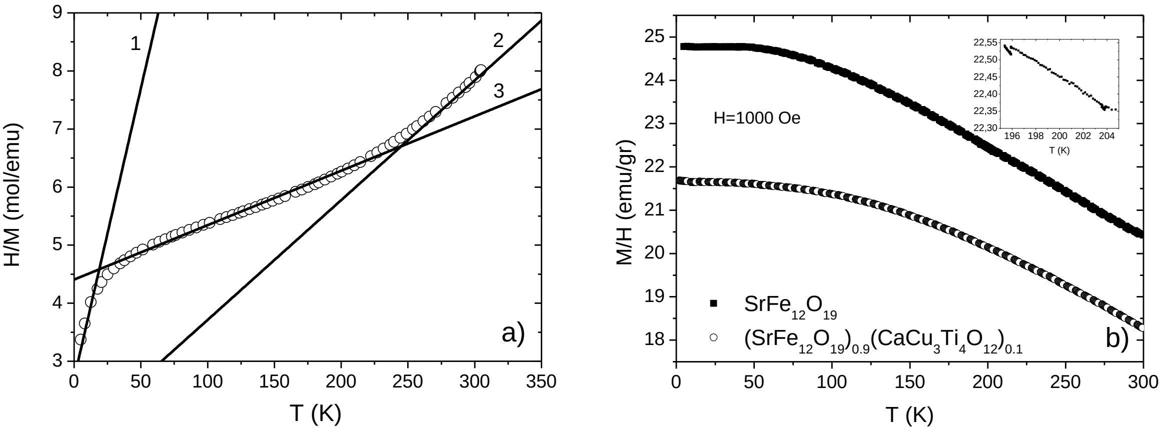

Fig.1. a) The temperature dependence H/M of $(SrFe_{12}O_{19})_{0.05}(CaCu_3Ti_4O_{12})_{0.95}$ composite; b) the temperature dependence *M/H* of $SrFe_{12}O_{19}$ and $(SrFe_{12}O_{19})_{0.9}(CaCu_3Ti_4O_{12})_{0.1}$ in the field of 1000 Oe. Inset, temperature dependencies of magnetization for $SrFe_{12}O_{19}$ in range 200 K, where two kinks were observed.

Fig.1b shows the temperature dependence M/H measured in the field of 1000 Oe for $SrFe_{12}O_{19}$ and $(SrFe_{12}O_{19})_{0.9}(CaCu_3Ti_4O_{12})_{0.1}$ compounds. The shape of the temperature dependence and the relevant values are in agreement with the literature data [7, 8]. Below 46 K the magnetic moment in is temperature-independent and all sublattices of spins of Fe^{3+} ions are completely ordered. In the inset in fig.1b the region near 200 K is singled out, in which two kinks probably associated with the ordering of one of sublattices of iron ions in $SrFe_{12}O_{19}$ are observed. The addition of 10% $CaCu_3Ti_4O_{12}$ to strontium hexaferrite reduces the magnetization value by approximately 13%.

ESR spectra of $(SrFe_{12}O_{19})_{0.05}(CaCu_3Ti_4O_{12})_{0.95}$ and $(SrFe_{12}O_{19})_{0.90}(CaCu_3Ti_4O_{12})_{0.10}$ composites on the basis of strontium hexaferrite and $CaCu_3Ti_4O_{12}$were measured in the X-band in the temperature interval from 100 to 300 K (fig.2). It was established that in $(SrFe_{12}O_{19})_{0.90}(CaCu_3Ti_4O_{12})_{0.10}$ composite, where CCTO serves as a core, the magnetic moments of spins of iron ions compensate each other at the core-shell interface leading to the decrease in the integral intensity of the magnetic resonance signal. It is shown that the ferrimagnetic core $SrFe_{12}O_{19}$ in $(SrFe_{12}O_{19})_{0.05}(CaCu_3Ti_4O_{12})_{0.95}$ composite polarizes spins of copper ions at the core-shell interface forming a single-domain particle, which manifests superparamagnetic properties in the magnetic resonance spectrum in the temperature range from 200 to 300 K. It is possible that the magnetic phase transition occurs in strontium hexaferrite at the temperature of 200 K, one of the sublattices of spins of the iron ion is ordered antiferromagnetically to others. As a result, ferromagnetic correlations at the core-shell interface of $(SrFe_{12}O_{19})_{0.05}(CaCu_3Ti_4O_{12})_{0.95}$ are destroyed at temperatures below 200 K. The phase separation into the ferrimagnetic «core» $SrFe_{12}O_{19}$ and the paramagnetic «shell» $CaCu_3Ti_4O_{12}$ takes place gradually in the wide temperature interval from 200 to 25 K due to the different sizes of $SrFe_{12}O_{19}$. The antiferromagnetic ordering is observed in the $CaCu_3Ti_4O_{12}$ shell below 25 K.

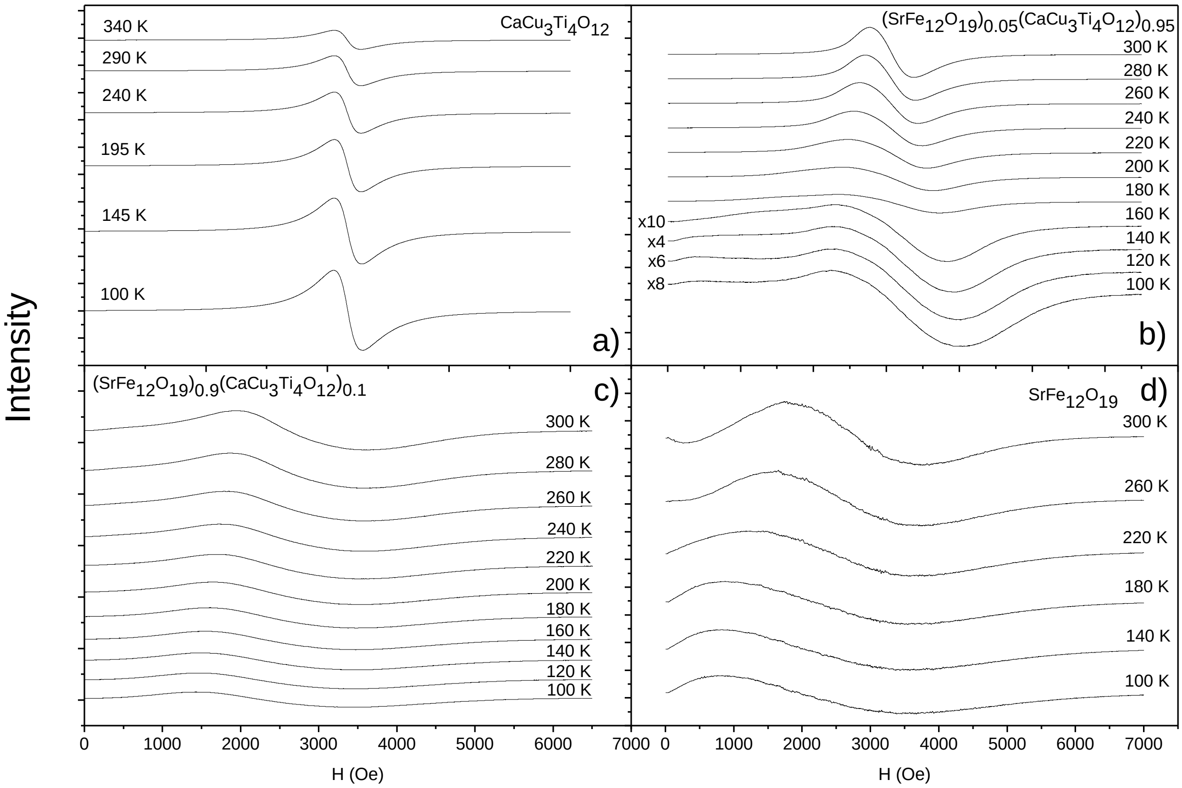

Fig.2. The evolution of EPR spectra as a function of temperature and composition in a) $CaCu_3Ti_4O_{12}$; b) $(SrFe_{12}O_{19})_{0.05}(CaCu_3Ti_4O_{12})_{0.95}$; c) $(SrFe_{12}O_{19})_{0.90}(CaCu_3Ti_4O_{12})_{0.10}$; d) $SrFe_{12}O_{19}$

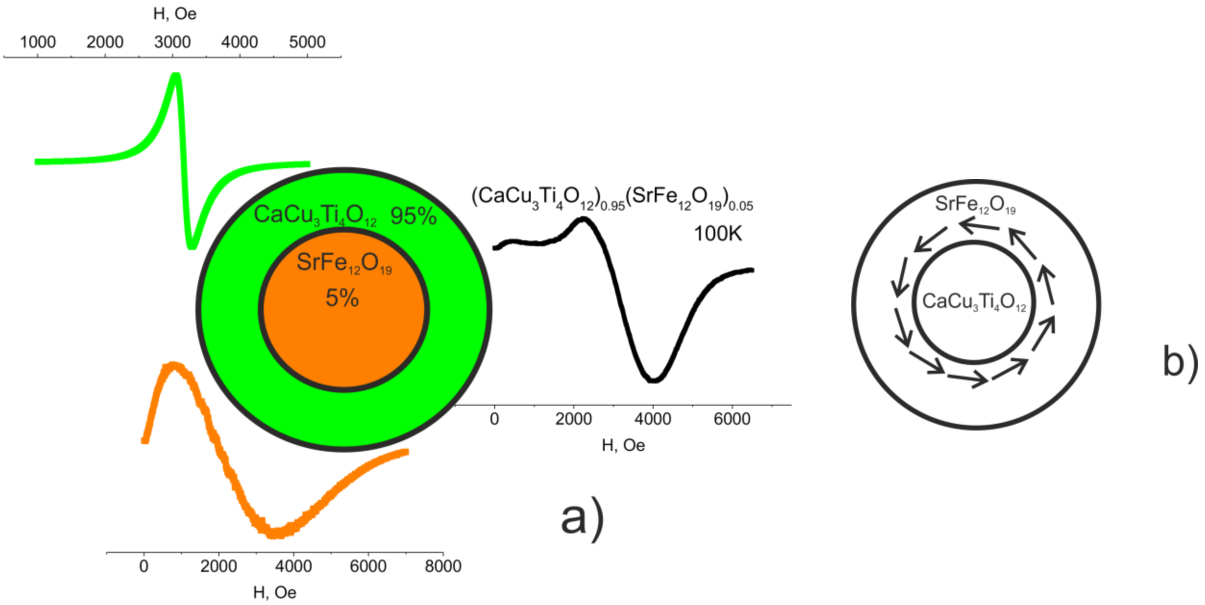

Fig.3. The model a) “core-shell” $(SrFe_{12}O_{19})_{0.05}(CaCu_3Ti_4O_{12})_{0.95}$
b) magnetic moment positions in composition $(SrFe_{12}O_{19})_{0.90}(CaCu_3Ti_4O_{12})_{0.10}$.

References

[1] S.A Gridnev, Yu.E.Kalinin, A.V. Sitnikov, O. Stogney. Nonlinear phenomena in nano- and micro-heterogeneous systems -M.: Binom. Knowledge Laboratory, 2012.-p. 352. (In Russian)

[2] Kushnir Sergey E., Gavrilov Anton I., Kazin Pavel E., Grigorieva Anastasia V., Tretyakov Yuri D., Martin Jansen, Journal of Materials Chemistry, 22, 18893- 18901 (2012)

[3] Morishita H., Amano A., Ueda H., Michioka C., Yoshimura K.: J. Jap. Soc. of Powder and Powder Metallurgy **61**, No S1, S64-S66 (2014)

[4] Jihoon Park, Yang-Ki Hong, Seong-Gon Kim, Sungho Kim, Laalitha S.I. Liyanage, Jaejin Lee, Woncheol Lee, Gavin S. Abo, Kang-Heon Hur, Sung-Yong An, JMMM **355**, 1-6 (2014)

[5] Subramanian M.A., Dong Li, Duan N., Reisner B.A., Sleight A.W.: J. Solid State Chem. **151**, 323-325 (2000)

[6] Linkenheimer P., Krohns S., Riegg S., Ebbinghaus S.G., Reller A., Loidl A. : Eur. Phys. J. Special Topics **180**, 61-89 (2010)

[7] A. Gruskova, V. Jancarik, J. Slama and M. Usakova, *ACTA PHYSICA POLONICA A*, Vol. 113 No. 1 p. 557 (2008)

[8] C.M.Fang, F.Kools, R.Metselaar, G. De.With and R. A. de Groot, J. Phys.: Condens. Matter **15,** 6229–6237 (2003)

Electron spin resonance study of the demagnetization fields of the ferromagnetic and paramagnetic films

I.I. Gimazov[1,2], Yu.I. Talanov[2]

[1]Kazan (Volga Region) Federal University, 420008, Kremlevskaya, 18, Kazan, Russia
[2]Zavoisky Physical-Technical Institute, 420029, Sibirsky tract, Kazan, Russia

e-mail: ubvfp94@mail.ru

It is well know that ESR is convenient tool for studying the local magnetic fields. There are local fields of different origins. One of them is a demagnetizing field. In this work, results of the demagnetizing field study of ferromagnetic and paramagnetic thin films are presented.

The ESR spectra at the demagnetizing field presence are well described by the Kittel's equations [2]. We used these equations in order to get the information about demagnetizing fields, magnetization and susceptibility.

In the first part of this work results of the ferromagnetic film study are presented. We use the thin film of manganite as a ferromagnetic sample. The single-crystalline manganite film of 10 nm thickness was deposited on the MgO substrate. Phase diagram of the $La_{1-x}Ca_xMnO_3$ is shown in fig.1. We chose the sample with the Ca concentration $x = 0.4$, which becomes ferromagnetic below 250 K.

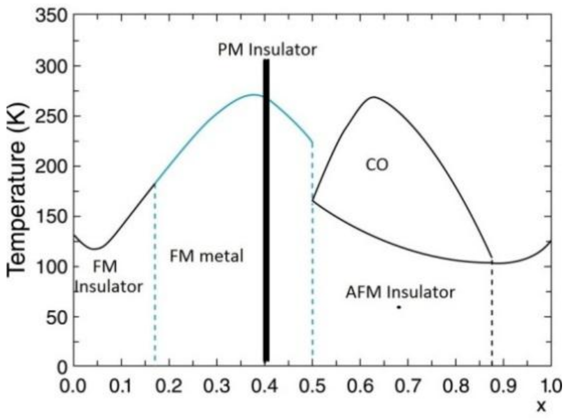

Fig.1. Phase diagram of the $La_{1-x}Ca_xMnO_3$ compounds from [1]. Bold line indicates the concentration and temperature range studied in our work.

Fig.2 demonstrates the ESR spectrum variation with temperature in the two orientations of the film plane with respect to the field direction. The temperature was changed by the flow cryostat with the step 10-20 K.

The temperature dependence of the resonance filed obtained from the spectra is shown in Fig.3 for the two orientations.

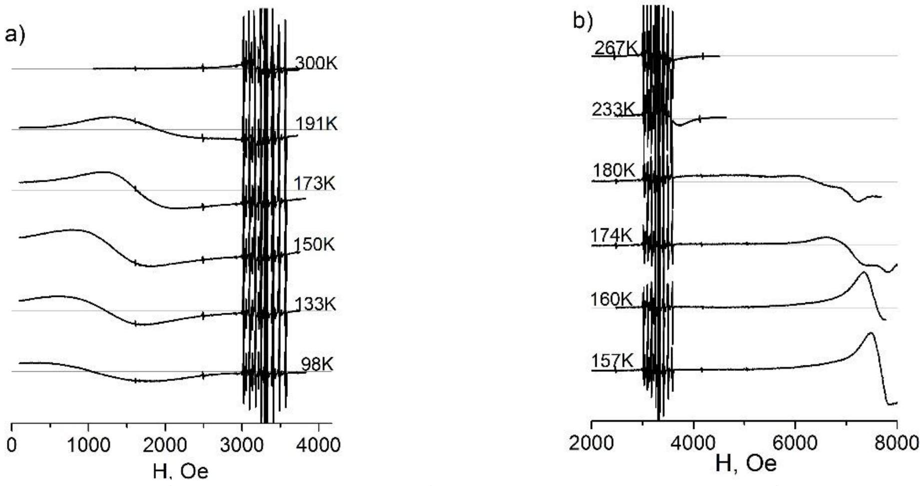

Fig.2. ESR spectra of the $La_{1-x}Ca_xMnO_3$ film on the MgO substrate for parallel (a) and perpendicular (b) orientations of the sample in the magnetic field at different temperatures.

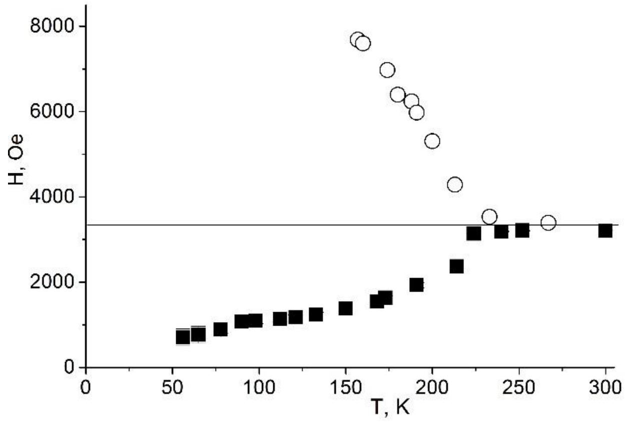

Fig.3. Temperature dependences of the resonance fields for parallel (squares) and perpendicular (circles) orientations of the film.

From these data we can estimate the demagnetizing field magnitude. It is proportional to film magnetization. The Kittel's equations relate a magnetization with a resonance field [2]: $H_{R0} = H_a - 4\pi M$ (for perpendicular orientation), $H_{R0} = \sqrt{H_a\left(H_a + 4\pi M\right)}$ (for parallel orientation), where H_{R0} is the resonance field, H_a is the external (applied) field, where the resonance signal is observed, M is the magnetization. One can estimate H_{R0} as the resonance field in the paramagnetic phase, where the magnetization is small, Estimations of the magnetization ($4\pi M$) and the demagnetizing field (H_{dem}) give 4793.5 Oe for parallel orientation and 3105.7 Oe for perpendicular orientation at 180 K.

It is seen, than in this case the demagnetizing field is great and comparable with resonance field . In paramagnetic phase the demagnetizing field contribution is small. It can be found if the ESR signal is narrow. The diphenylpicrylhydrazyl (DPPH) signal has this property. Therefore we use it to estimate the demagnetization effect of paramagnetic film.

In order to detect a weak effect of demagnetizing fields on DPPH signal position we use the signal of lithium as a reference signal. The lithium signal has a narrow width (δH = 0,1 Oe) and well-defined g-factor (g(Li) = 2.00226 [3]).

With the flow cryostat we have obtained the spectra temperature dependence in the two orientations of the field with respect to the film plane (parallel and perpendicular). The EPR spectra of DPPH and lithium dendrites were recorded with the step 5 ÷ 20 K. We have obtained information on the signal shift with respect to the lithium signal.

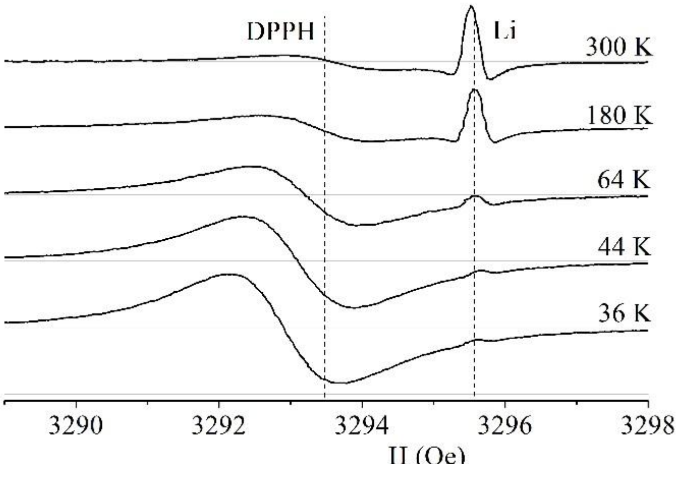

Fig.4. EPR spectra of DPPH film for parallel orientation at different temperatures.

The demagnetizing field value of the film is defined by its magnetization. The magnetization is directly proportional to the magnetic susceptibility, and the susceptibility depends on the temperature according to the Curie-Weiss law. Hence, we can obtain the dependence of the demagnetization field on a temperature. The analytical formulas of temperature dependence will be obtained below in equations (7) and (8).

In order to obtain the demagnetizing field from the EPR spectrum it is necessary to define the resonance fields of DPPH and lithium. The resonance field of lithium is defined by its g-factor: $H_{\mathrm{Li}} = h\nu / g_{\mathrm{Li}}\mu_B$. The DPPH signal position is determent not only by *g*-factor. The demagnetizing field contributes as well: $H_{\mathrm{DPPH}} = h\nu / g_{\mathrm{DPPH}}\mu_B + \Delta H_{df}$ .Hence, the distance between the signals is expressed as follows:

$$\Delta H = \frac{h\nu}{g_{\mathrm{Li}}\mu_B} - \frac{h\nu}{g_{\mathrm{DPPH}}\mu_B} - \Delta H_{df}$$

We can obtain the demagnetizing field value if we remove contribution defined by g-factors: $\Delta H_{df} = \Delta H - \left(h\nu / g_{\mathrm{Li}}\mu_B - h\nu / g_{\mathrm{DPPH}}\mu_B \right)$. This procedure can be performed for all spectra obtained at different temperatures. As a result, we get the temperature dependence of the demagnetizing field of DPPH film. This dependence is shown in fig.5 for parallel orientation (a) and for perpendicular (b) orientation.

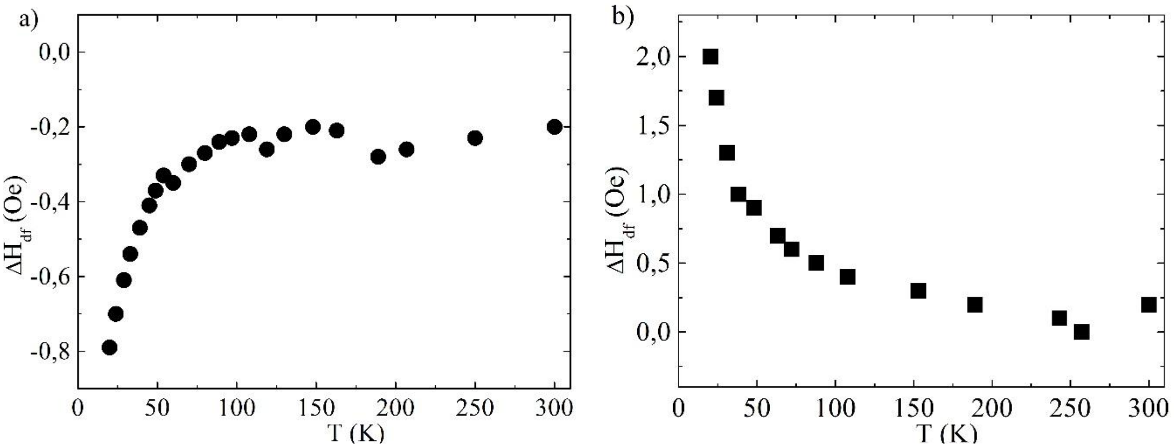

Fig.5. Temperature dependence of the demagnetizing field contribution for the magnetic field parallel (a) and perpendicular (b) to plane of the DPPH film.

From these data we can extract the DPPH susceptibility value and its temperature dependence. To do this one use Kittel's equations for resonance fields of magnetized objects [2]. For perpendicular orientation the equation is following:

$$H_{R0} = H_a \left(1 - 4\pi\chi \right), \tag{1}$$

where H_{R0} is the DPPH resonance field, H_a is the external (applied) field, where the resonance signal is observed, χ is the DPPH susceptibility.

In the case of parallel orientation the equation has the form:

$$H_{R0} = H_a \sqrt{1 + 4\pi\chi} \tag{2}$$

In paramagnetic phase the susceptibility temperature dependence obeys Curie-Weiss law:

$$\chi = \frac{C_\chi}{T - \theta} \tag{3}$$

By substituting equation (3) in Kittel's formulas (1) and (2) we can obtain following expressions:

$$H_a = \frac{H_{R0}}{1 - 4\pi C_\chi / (T - \theta)}, \tag{4}$$

$$H_a = \frac{H_{R0}}{1 + 4\pi C_\chi / (T - \theta)}. \tag{5}$$

We can use these equations to describe temperature dependence of resonance field and obtain the parameters of the Curie-Weiss law: C = 6·10–4 K·cm^3/g.

The dependence (3) with these parameters is plotted in fig.6 along with results of the susceptibility measurement [4]. It is seen well agreement.

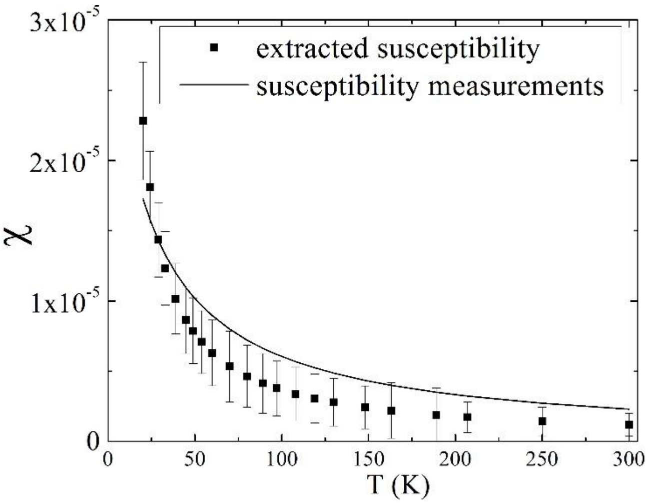

Fig.6. Temperature dependence of the DPPH susceptibility. Squares show the data obtained by EPR. The solid line is data of the direct susceptibility measurements [4].

In conclusion, we show the possibility to study the demagnetizing field of the thin ferromagnetic and paramagnetic films by ESR.

References

[1] P. Schiffer, A.P. Ramirez, W.Bao, and S.-W. Cheong. Phys. Rev. Lett. 75, 787 (1995).

[2] C. Kittel. Introduction to Solid State Physics – John Wiley (1971).

[3] Vander, N.S. Ven. Phys.Rev. 168, 787 (1968).

[4] Van Ittrbeek, A. Labro, M. Stastic. Physica 30, 157 (1965).

Temperature dependence of ESR linewidth and spin-spin correlation functions in one dimensional magnets

M.A. Fayzullin, M.V. Eremin

Institute for Physics, Kazan Federal University, Kremlyovskaya 18, Kazan, Russia

e-mail: marsel.fayzullin@yandex.ru

Low dimensional magnets are fascinating testing grounds for the fundamental understanding of quantum physics and ESR is powerful tool in the investigating of their magnetic and electronic structure. ESR signal is detected from the whole system of the exchange-coupled spins [1] and mainly determined by anisotropic exchange interactions [2]. Analysis of the ESR linewidth based on calculation of the spectral moments is a well-developed method which allows to identify the nature of spin-spin interactions and estimate their magnitudes in magnetically concentrated systems. Its benefit is that in high temperature limit ($T \to \infty$) an exact expression for linewidth can be found out for an arbitrary spin system, whatever space dimension and exchange couplings [3].

The problem of theoretical description of EPR linewidth in magnetically concentrated systems within wide temperature range remains still open. This is related to difficulties of the quantum mechanical description of many-body interacting systems. It's necessary take into account quantum fluctuations inherent in low-dimensional magnetic structures, while methods based on the mean field approximation are no longer applicable in this case.

In the present paper we apply the method of spectral moments to the 1D AF Heisenberg chain $S = 1/2$ with Dzyaloshinskii-Moriya interaction and calculate ESR linewidth in the framework of the exchange narrowing theory [1] in high temperature regime ($T >> J/k_B$, J — isotropic superexchange coupling parameter). The obtained linewidth is expressed via temperature dependent spin-spin correlation function, which we have calculated in terms of quasi-classical (Fisher) approach [4, 5] and using method of Green's function (Kondo and Yamaji) [6] for a two- and four-spin correlation functions. It remarkable that both approaches for the temperature dependence of the spin-spin correlation functions are consistent to each other and only at low temperatures the quantum approach yields more realistic results than the classical one. In contrast to the previous approach by Yamada [7, 8], Nagata and Tazuke [9], who treated the spins as classical variables, we treat the spins in terms of Pauli matrices. Our results for the linewidth are not in contradiction with the field-theory approach developed by Oshikawa and Affleck in 2002 [10] valid in temperature range $T << J/k_B$, and in a good agreement with experimental data of the angular and temperature dependencies in quasi 1D antiferromagnets Cs_2CuCl_4 [11] and $(C_7H_{10}N)_2CuBr_4$ [12].

References

[1] [1] P.V. Anderson, P.R. Weiss, Rev. Mod. Phys., **25**, 269 (1963).

[2] [2] D. Zakharov, H.-A. Krug von Nidda, M. Eremin, J. Deisenhofer, R. Eremina, A. Loidl, in Quantum Magnetism, edited by B. Barbara et.al. (Springer, Dordrecht, 2008).

[3] [3] S. Al'tshuller, B. Kozyrev, Electron Paramagnetic Resonance, Academic Press (1964).

[4] [4] M.E. Fisher, Amer. J. Phys., **32**, 343 (1964).

[5] [5] K. Nagata, Y. Tazuke, J. Phys. Soc. Japan, **32**, 337 (1972).

[6] [6] J. Kondo, K. Yamaji, Prog. Theor. Phys., **47**, 807 (1972).

[7] [7] I. Yamada, H. Fujii, M. Hidaka, J. Phys.: Condens. Matter, **1**, 3397 (1989).

[8] [8] I. Yamada, M. Nishi, J. Akimitsu, J. Phys.: Condens. Matter, **8**, 2625 (1996).

[9] [9] Y. Tazuke, K. Nagata, J. Phys. Soc. Japan, **38**, 1003 (1975).

[10] [10] M. Oshikawa, I.A. Affleck, PRB **65**, 134410 (2002).

[11] [11] M.A. Fayzullin, R.M. Eremina, M.V. Eremin, A. Dittl, N. van Well, F. Ritter, W. Assmus, J. Deisenhofer, H.-A. Krug von Nidda, A. Loidl, PRB **88**, 174421 (2013).

[12] [12] V.N. Glazkov, M. Fayzullin, Yu. Krasnikova, G. Skoblin, D. Schmidiger, S. Mühlbauer, A. Zheludev, arXiv:1507.02503 [cond-mat.str-el], accepted to publish in PRB (2015).

FMR investigation of magnetic anisotropy in ion-beam synthesized thin iron silicide films

A.V. Alekseev, G.G. Gumarov, M.M. Bakirov, V.Yu. Petukhov, V.I. Nuzhdin

E. K. Zavoisky Physical -Technical Institute, 420029, Sibirsky tract, 10/7 Kazan, Russia

e-mail: alekceevanton@gmail.com

40 keV iron ions have been implanted into single-crystal silicon wafers at room temperature. As a result, thin iron silicide films were synthesized in the near-surface region of substrates. Scanning MOKE studies showed that some films have the uniaxial magnetic anisotropy. However, ferromagnetic samples become isotropic, when the dose on the order of 2.6×10^{17} cm^{-2} is reached. Ferromagnetic resonance (FMR) studies showed that the FMR linewidth in isotropic samples increases with the temperature decrease. It was found that the FMR linewidth for samples with the uniaxial anisotropy is much less than that for isotropic ones. The observed behavior of FMR spectra can be explained on the basis of the model taking into account the effect of thermal fluctuations on the line FMR shape in disperse ferromagnets.

Introduction

It is known that the ion-beam synthesis (IBS) can be used for the preparation of thin magnetic films [1]. This may result in the local variation of magnetic properties such as the saturation magnetization, magnetic anisotropy etc [2]. Earlier we used magnetic-field-assisted ion-beam synthesis to prepare thin ferromagnetic silicide films Fe_3Si in single-crystal silicon substrates [3]. It was determined using fast electron diffraction and conversion electron Mossbauer spectroscopy that polycrystalline weakly textured α-Fe_3Si and ε-FeSi films are formed as a result of the ion synthesis [4, 5]. It was shown that the application of the magnetic field during the high-dose ion Fe implantation leads to the formation of the in-plane uniaxial magnetic anisotropy of the synthesized film [3]. The induced uniaxial magnetic anisotropy is revealed only in samples synthesized in a certain dose range. Thin iron silicide ferromagnetic films become isotropic above a certain ion implantation dose [6]. However the origin of the magnetic anisotropy remained unclear.

The study of the changes in ferromagnetic resonance (FMR) spectra under the temperature variation is one of informative methods for establishing the nature of the magnetic anisotropy in ion-synthesized thin iron silicide films. Therefore, the aim of this work was to study magnetic properties of ion-synthesized thin iron silicide films using the FMR method. The effect of IBS modes on the formation of anisotropic ferromagnetic films was also studied.

Experimental

40 keV Fe ions were implanted into single-crystal silicon wafers (111) at room temperature. The implantation fluence was varied in the range from 1.6×10^{17} to 3×10^{17} cm^{-2}, the ion current density was 4 μA/cm^2. The external magnetic field H =500 Oe was applied parallel to the sample surface in order to create the induced magnetic anisotropy during implantation. It was noted earlier that the mechanical pressure also affects the formation of the uniaxial magnetic anisotropy due to the magnetostriction effect. Therefore substrates were fixed on a special holder that does not produce mechanical stresses.

Local magnetic properties of samples were studied on a scanning magnetic polarimeter in the mode of the longitudinal magneto-optical Kerr effect (MOKE).

Ferromagnetic resonance spectra were recorded on a Bruker EMX spectrometer in the in-plane geometry in the temperature range from 100 to 300 K.

Results and discussion

MOKE studies showed that all samples synthesized in the specified implantation modes are ferromagnetic at room temperature. Ferromagnetic properties of films synthesized at the implantation fluence of less than 1.6×10^{17} cm^{-2} are absent. Samples prepared by implantation without the external magnetic field and fixed on the holder without mechanical stresses are magnetically isotropic. Samples implanted with high Fe^{+} ion fluence (in the range from 1.6×10^{17} to 2.4×10^{17} cm^{-2}) in the external magnetic field have the uniaxial anisotropy. The coercive force determined in the direction of the easy magnetization axis (EMA), and the anisotropy field determined as the saturation field along the hard magnetization axis (HMA) increase with the increase in the implantation fluence for films with the magnetic anisotropy [7]. The rectangular hysteresis loop and the hysteresisless magnetization curve are observed for EMA and HMA, respectively. However, ferromagnetic samples become isotropic, when dose on the order of 2.6×10^{17} cm^{-2} is reached.

X-ray diffraction at grazing angles also indicates the presence of the α-Fe_3Si phase and reveals structural differences between thin films with different ion implantation fluences [6]. It was found that the formation of uniaxial anisotropy is explained by the formation of nanoparticles smaller than those in isotropic samples. We determined that with the increase in ion implantation fluence the magnetic crystalline anisotropy of randomly oriented crystallites competes with the induced uniaxial anisotropy up to its suppression.

Typical FMR spectra observed for magnetically isotropic and magnetically anisotropic samples are shown in fig.1.

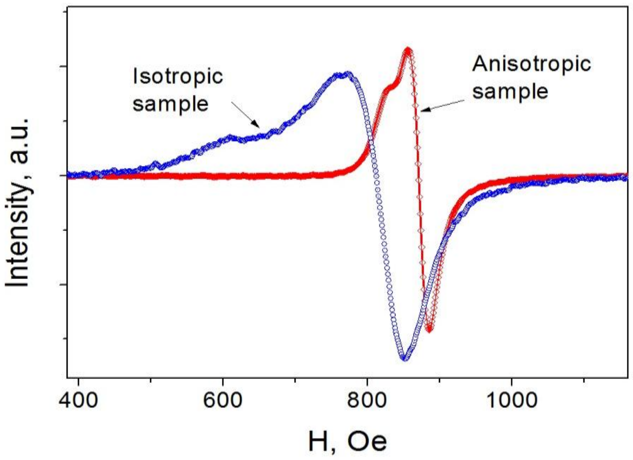

Fig.1. Ferromagnetic resonance spectra for magnetically isotropic and magnetically anisotropic iron silicide Fe_3Si films. Spectra were measured at the temperature T = 250 K in the *in-plane* geometry.

It can be seen that the FMR linewidth for anisotropic samples is much narrower than that for anisotropic ones. The FMR signal of magnetically anisotropic films demonstrates the typical orientation dependence on the angle between the EMA direction and the constant magnetic field of the spectrometer. Temperature dependences of the FMR linewidth are completely different for anisotropic and isotropic samples. (fig.2).

The FMR linewidth for anisotropic samples is almost temperature-independent in the studied temperature range. On the contrary, the FMR linewidth for isotropic samples increases with the temperature decrease (see fig.3).

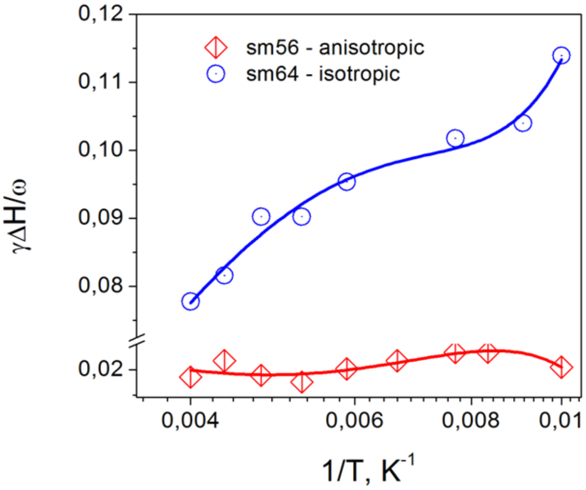

Fig.2. Inverse temperature dependence of the FMR linewidth for magnetically anisotropic and magnetically isotropic samples.

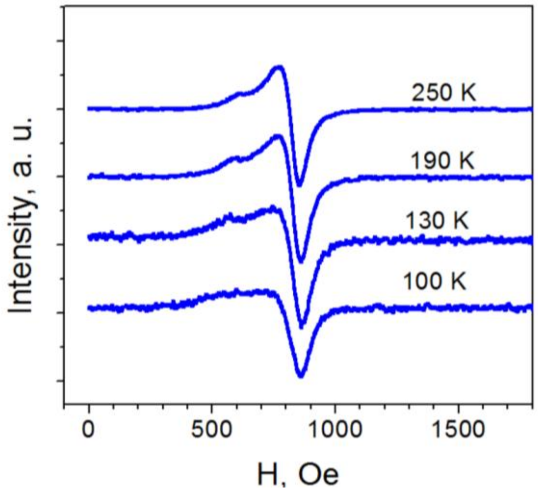

Fig.3. Ferromagnetic resonance spectra for the magnetically isotropic sample at various temperatures.

Such temperature dependences can be explained on the basis of the model of magnetic resonance in an ensemble of single-domain anisotropic particles with the random scatter of EMA directions proposed by Raikher and Stepanov [8]. In this model the FMR linewidth depends on the dimensionless parameter:

$$\xi_0 = \frac{M_s V \omega}{\gamma k_B T} \tag{1}$$

Here M_S is the saturation magnetization, V is the volume of particles, ω is the angular frequency, γ is the gyromagnetic ratio, k_B is the Boltzmann constant.

The inhomogeneous broadening in the relatively low-temperature region in this model is decribed by the asymptote:

$$\Delta H = \frac{3\omega\varepsilon\xi_0}{5\gamma}, \tag{2}$$

where $\varepsilon = K\gamma / M_s\omega$, K is the magnetic anisotropy constant. According to this model, this broadening is associated with the dispersion in the direction of the anisotropy axes of particles. With the increase in the temperature, the orientation fluctuations of the magnetic moment weaken the inhomogeneous broadening of the FMR line that leads to line narrowing.

The temperature-independent FMR linewidth for samples with the induced uniaxial anisotropy also can be explained on the basis of the Raikher model for the magnetic resonance in an ensemble of single-domain anisotropic particles. When the dispersion in the directions of anisotropy axes of the particles is absent, the same as in the case with magnetically anisotropic samples, the contribution to the inhomogeneous broadening is negligible at low temperatures. The superparamagnetic broadening in this region is also insignificant. As a consequence, the linewidth is almost temperature-independent, at least in the scale of studied variations.

It should be noted that according to the above formulas, the linewidth is proportional to the anisotropy constant and the volume of particles. However, such dependence holds only for isotropic samples. In fact, the experimental FMR linewidth for anisotropic samples decreases with the fluence increase. It was determined earlier that the anisotropy constant increases with fluence, since the anisotropy field and saturation magnetization increase. Thus, the obtained results indicate that isotropic samples consist of particles with randomly oriented magnetization axes, while for anisotropic samples EMA is determined by anisotropy of the shape of nanodispersed particles.

Conclusions

Thin nanodispersed ferromagnetic iron silicide films, which can be magnetically anisotropic and magnetically isotropic, are formed under IBS as a function of modes. FMR results indicate that isotropic samples consist of particles with randomly oriented easy magnetization axes, while EMA for anisotropic samples is determined by the anisotropy of the shape of nanodispersed particles. The considerable difference in the FMR linewidth for anisotropic and isotropic iron silicide films was observed. The FMR linewidth for isotropic films is temperature-dependent. The experimental results are in good agreement with the Raikher model describing magnetic resonance in an ensemble of single-domain anisotropic particles.

References

[1] *Петухов В.Ю., Хайбуллин И.Б., Зарипов М.М. и др.* // ФТТ. 1984. Т. 26. вып. 5. С. 1392.

[2] *Fassbender J., Ravelosona D., Samson Y.* // J. Phys. D: Appl. Phys. 2004. V. 37. P 179–196.

[3] *Gumarov G.G., Petukhov V.Yu., Zhikharev V.A.* // Nucl. Instr. Meth. Phys. Res. B. 2009. B 267. P. 1600.

[4] *Gumarov G.G., Petukhov V.Yu., Gumarov A.I. et al.* // Nucl. Instr. Meth. Phys. Res. B. 2012. B 272. P.108.

[5] *Ивойлов Н.Г., Чистяков В.А., Хрипунов Д.М. и др.//* Известия РАН. Серия физическая. 1999. Т.63, №7. С.1435.

[6] *Алексеев А. В., Гумаров Г.Г., Шустов В.А. и др.* // Поверхность. Рентген., синхротр. и нейтрон. исслед. 2014. № 11. С.37.

[7] *Gumarov G.G., Konovalov D.A., Alekseev A.V., et al.* // Nucl. Instr. Meth. Phys. Res. B. 2012. B. 282. P. 92.

[8] *Raikher Yu. L. and Stepanov V. I.* // Sov. Phys. JETP. 1992. V. 75. P. 764.

Separation of ^{3}He from ^{3}He – ^{4}He mixture using adsorption for NMR investigation

E.M. Alakshin[1,2], A.V. Klochkov[1], K.R. Safiullin[1], A.A. Stanislavovas[1], M.S. Tagirov[1,2]

[1]Kazan Federal University, 420008, Kremlevskaya 18, Kazan, Russia.
[2]Institute of Perspective Research, TAS, 420111, L.Bulachnaya 36a Kazan, Russia

e-mail: hectkctk@yandex.ru

High-purity ^{3}He is used in many physical experiments [1 – 4]. A standard trap cooled with liquid nitrogen easily cleanses ^{3}He from all impurities except for the ^{4}He. In this work we use method, which is based on used differences of energy absorption of ^{3}He and ^{4}He on active charcoal (36 K for ^{4}He, 23 K for ^{3}He) [5].

Impurity concentration of ^{4}He in ^{3}He monitored helium leak detector Pfeiffer Vacuum HLT 560. Leak detector it is a highly sensitive magnetic mass-spectrometer, tuned for registration ^{3}He and ^{4}He.

The aim of present work it is a created of chromatographyc column, assembly of installation, described by V.V. Dmitriev in article [6], and separation of ^{3}He from ^{4}He impurity through assembled installation.

Installation scheme, for a purification of ^{3}He (fig.1), used in present work, include: needle valve for a fine tuning of gas flow; mass spectrometer helium leak detector Pfeiffer Vacuum HLT 560, control with two cryopumps and two volumes, used for storing purified ^{3}He.

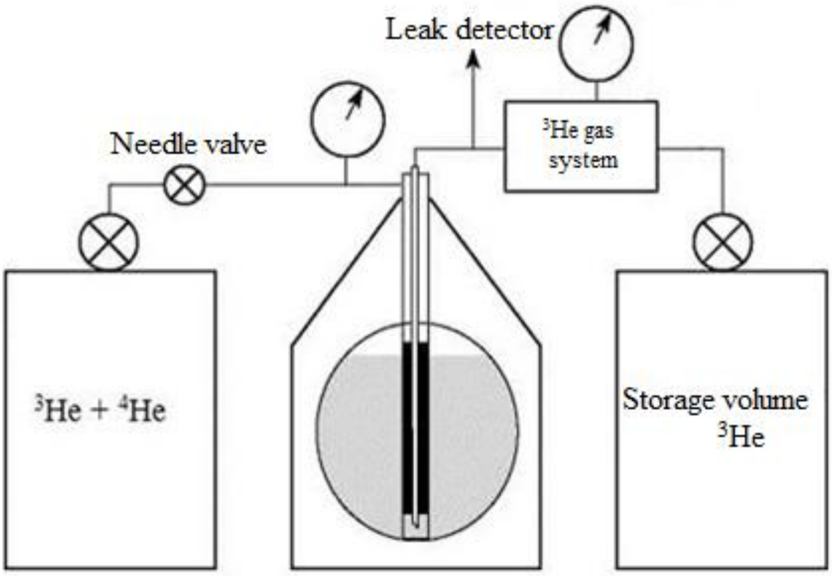

Fig.1. Installation scheme for purification of ^{3}He.

Column was connected to 3He gas system which presented in fig.2.The amount of charcoal in the column was 2g(~6 sm^3). Starting mixture was included ≈ 1% of ^{4}He. The gas - flow rate was regulated with the needle valve, which located at the entrance of column. The column was inserted into a transport Dewar (STG-25) with liquid helium. The ^{3}He-^{4}He mixture flowing though column was adsorbed on the charcoal. Valve 1, located at the entrance of gas system was opened.

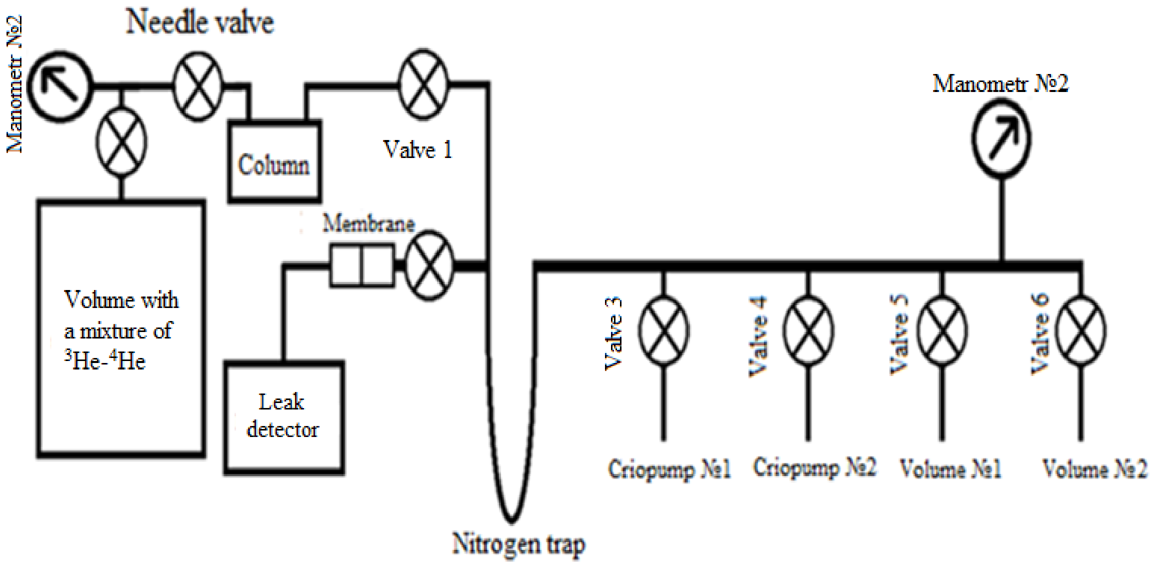

Fig.2. ^{3}He gas system.

When the pressure at the output of the column, which measured by manometer №1, located between volumes 1 and 2, markedly increased, the valves 4, 5, 6 at the entrance of cryopump 2 and volumes 1 and 2 was opened. The speed of the gas flow measured by pressure in the vacuum control, cryopump 2 and volumes and the starting of experiment was equal to 0.8 (mbar·l)/min.

Fig.3. Photo of ^{3}He gas system

Flow measurement of ^{4}He and ^{3}He was carried out for a long time using a leak detector, which was connected to the ^{3}He gas system through a calibrated membrane.

Variation of the impurity concentration of ^{4}He with the time shows in fig.4. Fig.4 shows that impurity concentration of ^{4}He decreases with time. It means that efficiency of the column increase with time. At the end the needle valve on the input of the column and the valves 3 and 5 on the input of the cryopump 1 and volume 1 were closed. The column was taken out from helium Dewar and pressure in the control panel and volume 2 was equal 380 mbar, which corresponds to number of ^{3}He ≈ 342 cm^3.

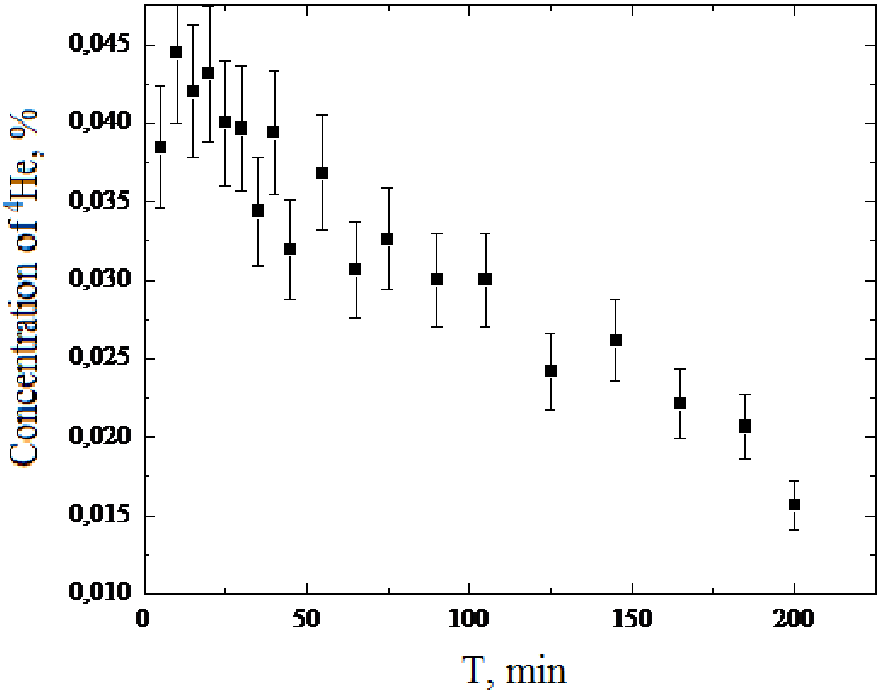

Fig.4. The time dependence of ^{4}He concentration

The column for a purification of ^{3}He from impurity of ^{4}He for NMR experiments was created. After the first cycle the mixture with initial impurity of ^{4}He 1%, was separated 340 cm^3 of ^{3}He with impurity concentration of ^{4}He 0,016%.

The work is performed according to the Russian Government Program of Competitive Growth of Kazan Federal University, partly supported by the Russian Foundation for Basic Research (project no. 14-02-31361 mol_a).

References

[1] Kuzmin V. V. // Research of ^{3}He in aerogels by NMR [text] / Kuzmin V. V. // KFU.- 2011. P. 1-105.

[2] Klochkov, A.V. // Nuclear magnetic relaxation of ^{3}He in contact with an aerogel above the Fermi temperature [text] / A.V. Klochkov, V.V. Kuzmin, K.R. Safiullin, M.S. Tagirov, D.A. Tayurskii, N. Mulders // JETP Letters.- 2008.- V.88.- N.12.- P.823-827.

[3] Li J.I.A. // Anisotropic phases of superfluid ^{3}He in compressed aerogel [text] // Li J.I.A., Zimmerman A.M., Pollanen J., Collett C.A., Halperin W.P. // Phys. Rev. Letters.- 2015.- V.114.- 105302.

[4] Bunkov Yu.M. // Magnon condensation into a Q ball in ^{3}He-B [text] // Bunkov Yu.M., Volovik G.E. // Phys. Rev. Letters.- 2007.- V.98.- 265302.

[5] L. P. Silvestrova // Helium adsorbtion on various adsorbents at low temperatures [text] / L. P. Silvestrova, V. S.Kogan, K. G. Breclavec // KIPT.- 1983.- P. 5.

[6] В.В. Дмитриев// Purification of ^{3}He from a ^{4}He Impurity Using Adsorption [text] / V.V. Dmitriev, V.V. Zavjalov, D.Ye. Zmeev, L.V. Levitin // PTE.- 2004.-№ 3.- P. 1-3.

ESR study of electron-beam-irradiated calcium gluconate

I.A. Goenko[1], V.Yu. Petukhov[1], I.V. Yatzyk[1], G.G. Gumarov[1], M.M. Akhmetov[1],
G.N. Konygin[2]

[1]E.K. Zavoisky Physical-Technical Institute, 420029, Sibirsky tract 10/7, Kazan, Russia
[2]Physical-Technical Institute Ural Branch,42600, Kirov 132, Izhevsk, Russia

e-mail: ilya.goenko@mail.ru

Calcium gluconate is one of commonly used pharmacological preparations for the therapy of diseases associated with hypocalcaemia. However, the therapeutic efficiency of currently known pharmaceutical compositions containing calcium gluconate as the active ingredient, is not sufficient for the effective treatment of osteoporosis caused by disorders of calcium metabolism in the body the same as that of all other currently known calcium preparations.

It is known that the mechanical activation of calcium gluconate results in the increased bioavailability and efficacy of therapy [1]. It is assumed that the increase in the therapeutic efficacy is associated with the change in the stereochemical structure of the molecule of the calcium salt of gluconic acid and the formation of the nanostructured X-ray amorphous state. However, the actual mechanism has not yet been studied and is of high scientific interest.

At the same time, it was found that the mechanochemical treatment of calcium gluconate is accompanied by the appearance of paramagnetic centers, which may affect the enhancement the biological activity of the drug [2]. In this work we attempted to produce paramagnetic centers using the electron beam exposure and to study the physical properties of the modified product.

Materials and methods

Powder calcium gluconate monohydrate was used in experiments. The electron beam with the energy of 9 Mev obtained on an Elekta Synergy® S linear accelerator was used as the ionizing radiation. Samples were irradiated with the dose of 100 Gy.

EPR spectra were measured on an EMX Plus spectrometer at the frequency of 9.3 GHz and room temperature.

Solid-state ^{13}C NMR spectra were measured on an AVANCE 400 spectrometer (Bruker) in the cross-polarization mode with the magic-angle rotation. Samples were placed on a 4 mm rotor rotating at the speed of 15,000 rps. The measurements were performed at room temperature. Adamantane was used as an internal standard to set the 90° pulse.

Results

ESR spectra showed the appearance of paramagnetic centers in the samples after the electron beam irradiation (fig.1A). Apparently, the resulting absorption line is a superposition of signals from two or more different paramagnetic centers. The comparison of the spectrum of electron-irradiated samples with that of mechanically activated calcium gluconate (MACG) showed that of one of the peaks of the former belongs to the signal of MACG (fig.1B). It was established that the produced paramagnetic centers are long-lived. ESR spectra were taken during 11 months and no decrease in the signal intensity was observed.

The nature of the new additional paramagnetic centers is not yet clear. However, according to the Franck-Rabinovich concept in the radiolysis of organic compounds, the breakage of the C-H bonds and the removal of the hydrogen atom from lattice are the most probable origins [3].

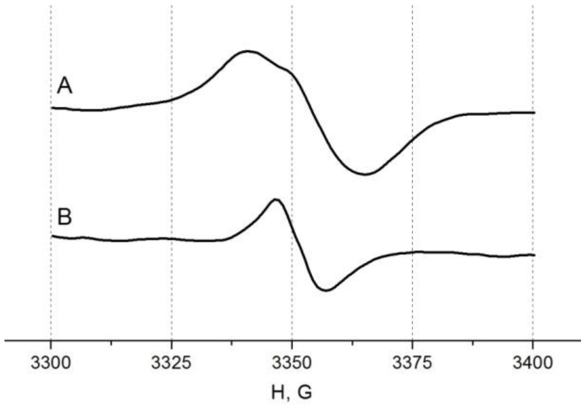

Fig.1. EPR spectra: A — electron beam irradiated calcium gluconate; B — MACG

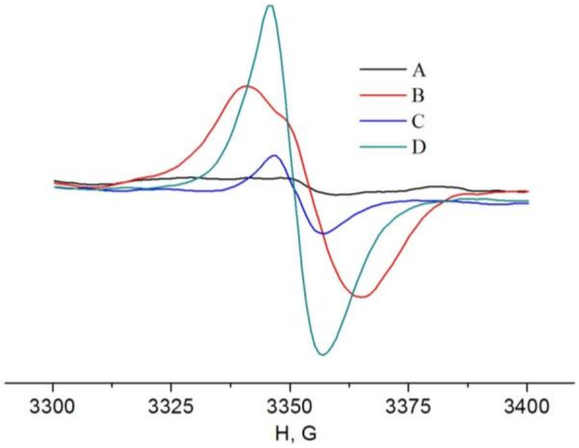

Fig.2. EPR spectra: A — calcium gluconate; B — MACG; C — electron beam irradiated calcium gluconate; D — electron beam irradiated MACG

The solid-state ^{13}C NMR experiment was performed (fig.3) to study possible changes in the structure of the calcium gluconate molecule. However, no changes in the structure of calcium gluconate before and after irradiation were observed. The clarification of this issue requires additional experiments.

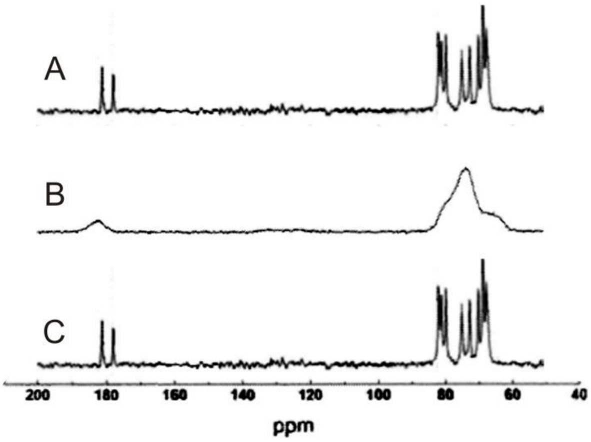

Fig.3. ^{13}C NMR spectra: A — calcium gluconate; B — MACG; C – electron beam irradiated calcium gluconate

Summary

Thus, our experiments showed that as a result of the electron irradiation of calcium gluconate, a compound with a complex EPR spectrum is formed, which contains a signal similar to that of MACG. If we base on the hypothesis of the participation of free radicals (paramagnetic centers) in the enhancement of the biological activity of calcium gluconate, this modification technique can be used as an active principle for the development of a new efficient calcium preparation.

References

[1] G.N. Konygin et al., *Conference materials ”Actual questions of pediatric surgery”, ISMA, Izhevsk*, **56** (2003)

[2] G.G.Gumarov et al., *Journal of Physical Chemistry*, **87**, 1578 (2013)

[3] L.A. Blumenfeld et al., *EPR applications in chemistry* (1962)

Studying nutation effects with pulsed EPR techniques

A.M. Kusova[1], P.V. Skvortcova[1], R.B. Zaripov[2]

[1]Kazan Federal University, Kremlevskaya, 18, Kazan 420008, Russia.
[2]E.K. Zavoisky Physical-Technical Institute, Sibirsky tract, 10/7, Kazan 420029, Russia.

e-mail: alexakusova@mail.ru

Abstract

This article describes the method of determining the spin of the system by observing the transient nutation. In a few showed samples this method allows to accurately determining the total spin of the paramagnetic system. In particular, we observed nitroxyl radical, biradical and excited fullerene C60. They quantum numbers S were equal to ½ for radicals and 1 for fullerene C60.

Transient nutation

Nutation is a periodic variation in the inclination of the axis of a rotating object. When we place the paramagnetic sample in constant field H_0, the total magnetic moment appears in the sample and precesses around the direction of the field H_0. During the acting of the pulsed field H_1 which are perpendicular to the field H_0, the total field H_{eff} is appeared. Then magnetic moments start to precess around $H_{eff.}$ (fig.1). This motion is called nutation [1].

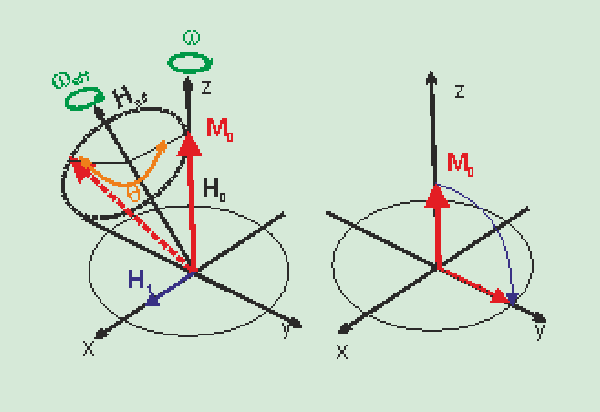

Fig.1. Vector presentation of nutation

The nutation frequency dependence on system parameters can be recorded by the formula [2]:

$$\omega_{nut}(m_s, m_s+1) = \frac{g\beta H_1}{\hbar}\sqrt{S(S+1) - m_s(m_s+1)}\,.$$

In this formula, there are three variable values: g is the effective g-factor, H_1 is pulsed field and S is the spin quantum value. In most cases the g-factor and the field H_1 is known we therefore we can determine the spin Sit is well known that $\omega_1 = g\beta H_1/\hbar$. We can calculate theoretically related ω_1 to ω_{nut}, which depends on the systems spin. There are the calculations for $S = 1$ and $S = 1/2$

$S = 1/2$	$m_s = 1/2$ $m_s = -1/2$	$\omega_{nut}(-\frac{1}{2};\frac{1}{2}) = \omega_1\sqrt{\frac{1}{2}(\frac{3}{2}) + \frac{1}{4}} = \omega_1$
$S = 1$	$m_s = 1$ $m_s = 0$ $m_s = -1$	$\omega_{nut}(-1;0) = \omega_1\sqrt{2+0} = \sqrt{2}\omega_1$ $\omega_{nut}(0;1) = \omega_1\sqrt{2+0} = \sqrt{2}\omega_1$

Comparing the experimental nutation's frequency with ω_1, it is easy to determine the value of the spin.

Specimens. This article presents the results of a studying two model systems fullerene and nitroxyl radical and biradical. The structures of the samples are shown in fig.2.

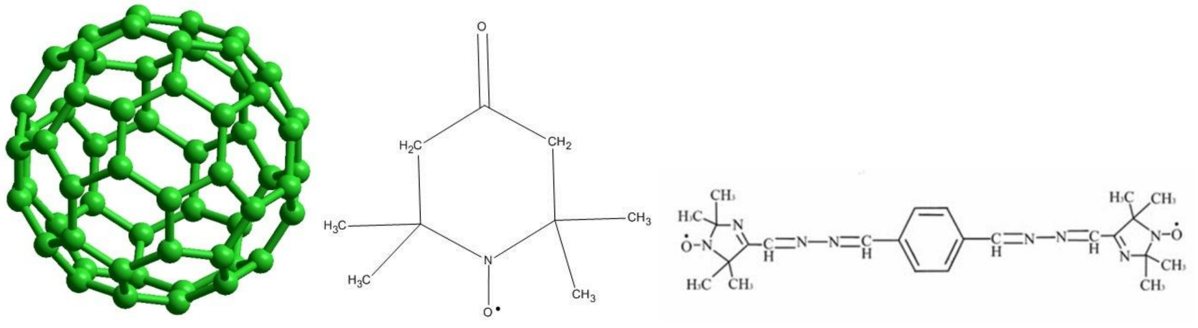

a b c

Fig.2. The structure of the test compound a) C60; b) radical; c) biradical.

1. Fullerene C60 is molecular compound, it composes of 60 carbon atoms belonging to the class of carbon allotropes and resembling a soccer ball.
2. Nitroxides are class of paramagnetic particles with one unpaired electron, its electron density is mainly focused on N-O fragment (e.g. TEMPON).
3. Biradical is the two covalently linked radicals.

The interest in the study photo excited particles is mainly determined that under the light one can create a new system with a large spin value (for example, fullerene with paramagnetic spin labels). Interest in the study biradical is mainly determined by the fact that in the short distance between the radical centers and a sufficiently strong interaction between the unpaired electrons of the system we can get a total effective spin, which will not be equal to 1/2. It is known that for large interspin distances and weak interaction between radicals the spin is equal to ½. However it is not any information for the intermediate case. Consequently, the method of transient nutation has a good potential to determine the spin-spin interaction.

Pulse sequences. In the experiment we used two pulse sequence withy FID and echo detection. To observe the FID usually used a sequence, which consists of a single pulse. And the intensity of the induction signal is recorded as a function of the duration of the pulse. In the echo experiment we used three pulse sequence. The first pulse is created nutation signal and the next two pulses used as detection pulses (90 and 180 degrees respectively). The echo was recorded as function of duration of the first pulse.

Experimental

Equipment. The experiments were performed on a pulsed EPR spectrometer ELEXSYS E 580 (Bruker) in X-band (9.8GHz) and Q-band (34.2GHz).

All experiments were performed at 80 K with a cooling system based on liquid nitrogen. The temperature was controlled by ITC 503 temperature controller.

To perform experiments with the photo excitation the YAG:Nd pulse laser Brio (Quantel) was used. The laser operates with the 532 nm and 355 nm wavelengths.

All samples was dissolved in toluene with a 1mmol/l concentration.

The experimental data.

Fullerene C60. Studying the fullerene conducted in X-band. We translate fullerene into an excited state with a laser to possession paramagnetic properties. Nutation’s frequency measured with a spin-echo method. We obtained dependence of the intensity of the spin echo signal on the first pulse duration (fig.3a). With using Fourier transform we convert signal from the time scale to the frequency presentation (fig.3b). After that we determined the frequency of nutation

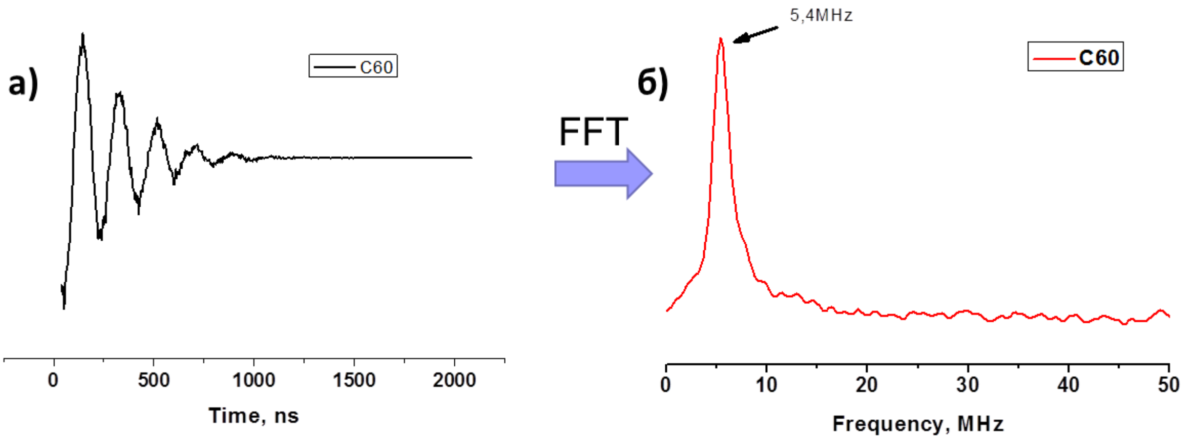

Fig.3. Dependence echo intensity on the duration of the first pulse of fullerene a) time representation, b) frequency representation.

We determined nutation frequency, and can get the ratio this frequency to ω_1. For fullerene this ratio is $\sqrt{2}$, it means that for this spin quantum number S equals to 1.

Radical and biradical. The studies of the radical systems was performed at Q-band. Nutation frequency measured with a FID method. We got dependence of the intensity of the FID signal from the first pulse duration (fig.4a). The same algorithm of determination of nutation frequencies was performed (fig.4b).

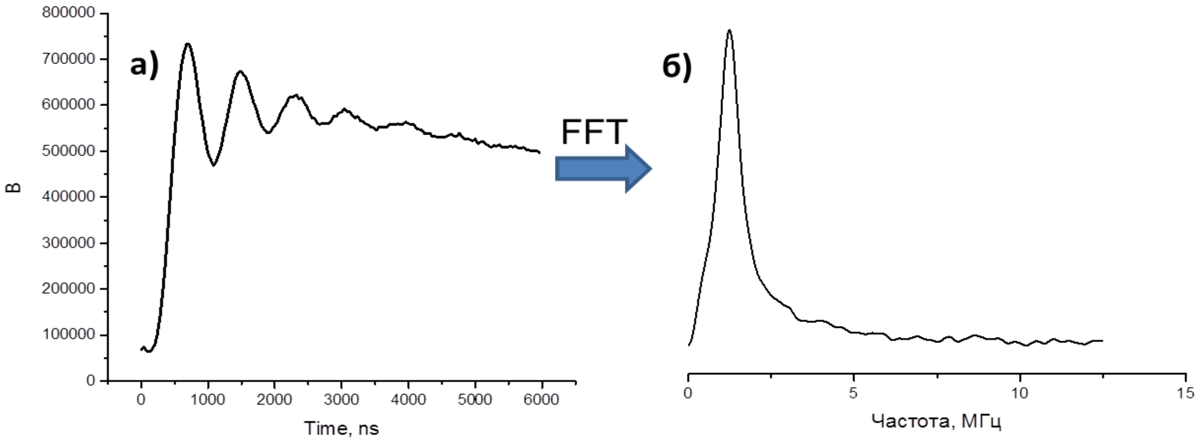

Fig.4. FID signal`s intensity from first pulse`s duration dependence a) time presentation; b) frequency presentation.

Ratio nutation frequency to ω_1 is equal to 1. It means that for this system spin equals to 1/2. For the biradical we obtained the same results. From this we can conclude that radical centers are on a large distance from each other (~2 nm), that’s why they have a weak interaction with each other.

2D experiment. In the difficult cases when it is needed to determine overlapped signals the 2D experiment can be used. In this experiments the signal (FID/echo) is recorded as function of the pulse duration in the each point of magnetic field (fig.5). The abscissa axis is the nutation frequency, the ordinate axis there is the magnetic field. The fig.5 shows that the value of every constants in magnetic field correspond to one frequency of nutation. It means that in the investigated system there is single quantum transition.

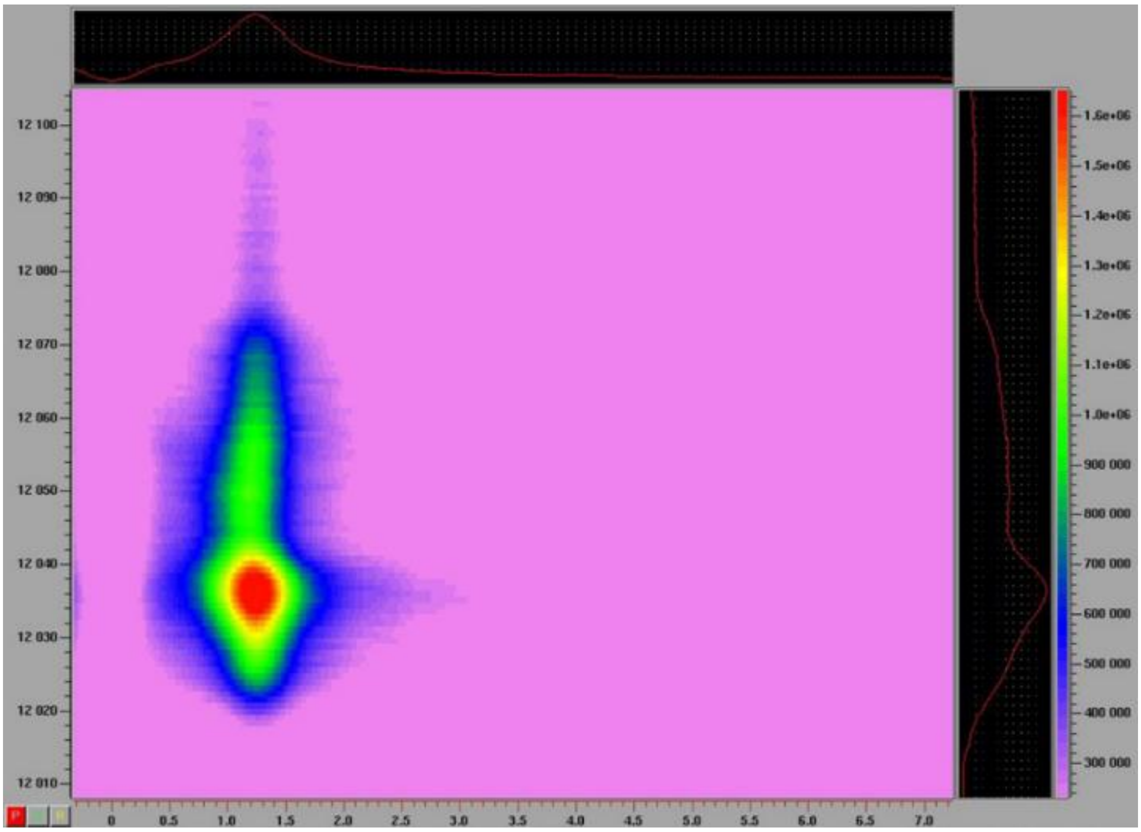

Fig.5. 2D experiment for the radical.

Conclusion

In this work we studied fullerene and radicals samples by methods of measuring the frequency of nutation with using the methods of spin-echo and FID. It was determined spin quantum number S equal to 1/2 for both nitroxide radical and biradical and to 1 for excited triplet state of fullerene C60.

Acknowledgements

This work was supported by the Program of Fundamental Research of the Presidium RAS №32.

References

[1] Salikhov K.M., Semenov A.G., Cvetkov U.D. Electron spin echo and its application. Novosibirsk: Science. 1976. C.343.

[2] Astashkin A.V., Schweiger A. Electron-spin transient nutation: a new approach to simplify the interpretation of ESR spectra // Chemical physics letters, 1990, v. 174, n. 6, p. 597

CW magnetic resonance investigations of $MnCO_3$

E.M. Alakshin[1], Yu.M. Bunkov[1,2], A.V. Klochkov[1], T.R. Safin[1], K.R. Safiullin[1,3],
M.S. Tagirov[1,3]

[1]Kazan Federal University, 420008, Kremlevskaya 18, Kazan, Russia.
[2]Institut Neel, CNRS et Universite Joseph Fourier, F-38042 Grenoble, France.
[3]Institute of Perspective Research, TAS, 420111, L.Bulachnaya 36a Kazan, Russia

e-mail: imfador@gmail.com

The spin superfluidity and Bose-Einstein condensation (BEC) of magnons, similar to an atomic BEC, have been discovered in superfluid ^{3}He at ultra low temperatures in 1984 [1]. Magnon BEC is manifested by the phase-coherent precession of magnetization (even in an inhomogeneous magnetic field). The theoretical explanation was given in [2]. Several states of magnon BEC have been found in superfluid ^{3}He phases under different experimental conditions for the last 30 years. The review of experiments can be found in [3 – 5]. Similar magnon BEC states have been discovered in solid antiferromagnets $CsMnF_3$ and $MnCO_3$ with coupled nuclear-electron precession [6 – 11]. In all cases BEC forms on excited non-equilibrium magnons. To excite them the continuous or pulse pumping at nuclear magnetic resonance (NMR) frequency was used. The question of magnetic system behavior during BEC state under continuous pumping has been raised here.

The experiment has been done at the temperature of 1.5 K, at a frequency of 547.45 MHz and magnetic field 135.3 mT. Single crystal $MnCO_3$ was used in our experiments. The experimental setup description can be found in [12]. During the excitation the additional adsorption has been observed, and the level depends on frequency modulation and modulation index, fig.1, fig.2.

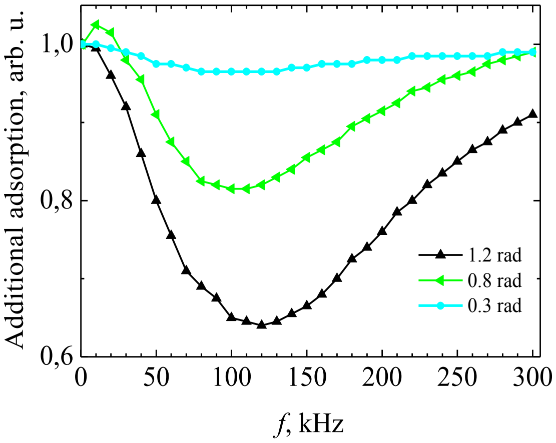

Fig.1. The additional adsorption dependence on the phase modulation frequency at different modulation index

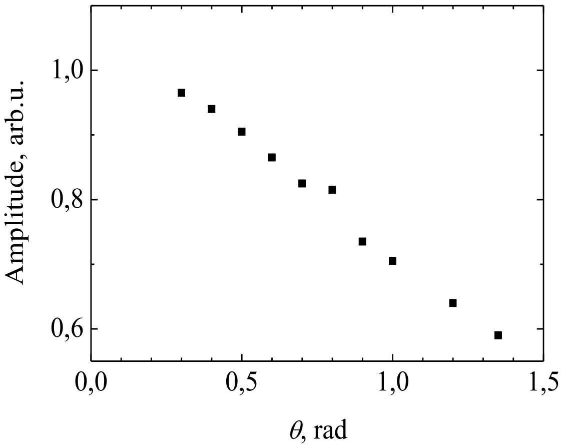

Fig.2. The amplitude dependence on the modulation index

Acknowledgments

The work is performed according to the Russian Government Program of Competitive Growth of Kazan Federal University and supported by the Russian Foundation for Basic Research (project no. 14- 02-31290 mol_a).

References

[1] A.S. Borovik-Romanov et al., JETP Lett. **40**, 1033, (1984)

[2] I.A. Fomin, JETP Lett. **40**, 1037 (1984)

[3] Y.M. Bunkov, G.E. Volovik, J. Low Temp. Phys. **150**, 135 (2008)

[4] Y.M. Bunkov, J. Phys.: Condens. Matter 21, 164201 (2009)

[5] Y. M. Bunkov, G. E. Volovik, J. Phys.: Condens. Matter 22, 164210 (2010)

[6] Yu. M. Bunkov et al., JETP Lett. 94, 68 (2011)

[7] E.M. Alakshin et al., J. Phys.: Conf. Ser. 324, 012006 (2011)

[8] Yu.M. Bunkov et al., Phys. Rev. Lett. 108, 177002 (2012)

[9] M.S. Tagirov et al., J. Low Temp. Phys. 175, 167 (2014)

[10] E.M. Alakshin et al., Appl. Magn. Reson. 44, 595 (2013)

[11] E.M. Alakshin et al., J. Phys.: Conf. Ser. 568, 042001 (2014)

[12] E.M. Alakshin et al., Appl. Magn. Reson. 44, 595 (2013)

Anomalous spin dynamics near the spin-reorientation transition in ε-$In_{0.24}Fe_{1.76}O_3$ nanowires

A.I. Dmitriev

Institute of Problems of Chemical Physics of the RAS, 142432, Acad. Semenov av. 1,
Chernogolovka, Russia

e-mail: aid@icp.ac.ru

In this paper we distinguish the contributions of the high- and low-temperature phases (HT and LT, respectively) to the dynamic magnetic susceptibility of ε-$In_{0.24}Fe_{1.76}O_3$ nanowires (fig.1).

It is found that increasing the frequency of an alternating magnetic field leads to an anomalous shift in the temperature maximum of the dynamic magnetic susceptibility in ε-$In_{0.24}Fe_{1.76}O_3$ nanowires in a direction opposite to theoretical predictions for thermally activated processes (fig.2).

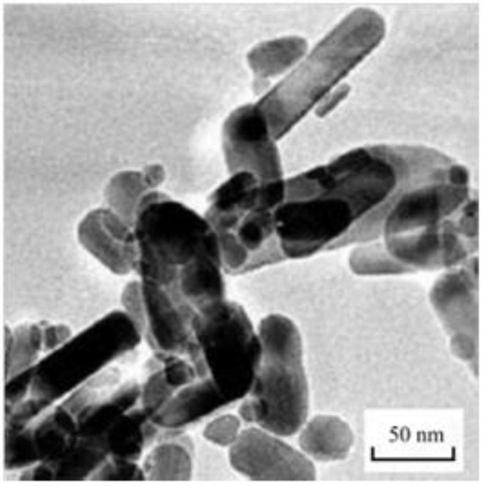

Fig.1. Transmission electron microscope image of ε-$In_{0.24}Fe_{1.76}O_3$ nanowires

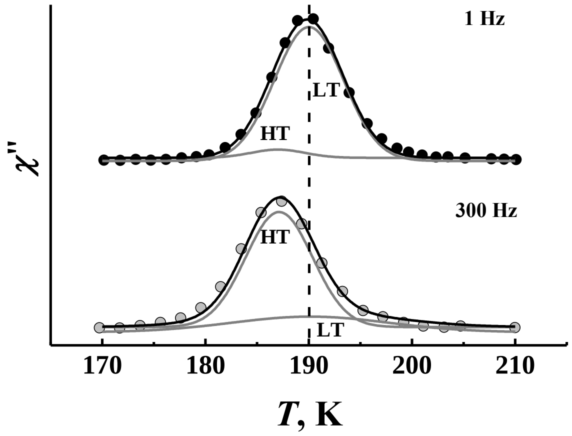

Fig.2. Temperature dependences of the imaginary part of the dynamic magnetic susceptibility χ'' at 1 Hz and 300 Hz

This unusual effect can be explained in terms of a redistribution of the contributions to the dynamic magnetic susceptibility from the high- and low-temperature phases. The contributions of these phases to the electron spin resonance spectra are identified.

A spin-reorientation transition that shows up as a turning of the axis of easy magnetization leads to a substantial restructuring of the electron spin resonance in ε-$In_{0.24}Fe_{1.76}O_3$ nanowires (fig.3).

Reducing the temperature causes a drop in the integrated intensity of the resonance line responsible for the high-temperature phase and an increase in integrated intensity of that for the low-temperature phase (fig.4).

At the lowest temperatures an additional line is observed in the spectrum near zero magnetic field; it may originate in a natural ferromagnetic resonance at zero magnetic field.

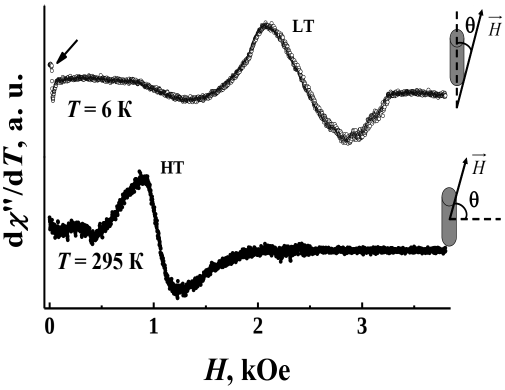

Fig.3. Electron spin resonance spectra for temperatures of 6 K and 295K.

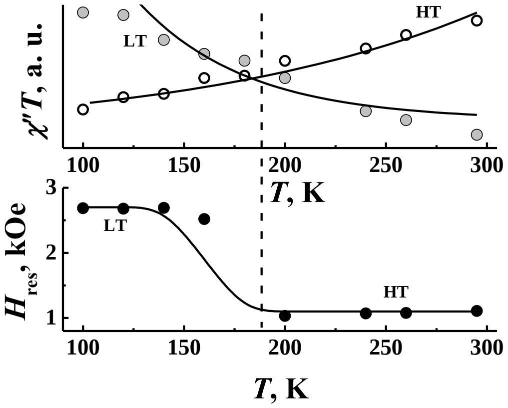

Fig.4. Temperature dependencies of $\chi''T$ and the resonance field H_{res} for the high- and low-temperature phases.

Acknowledgments

This work has been supported by the Grant of the President of Russia MK-1598.2014.3.

Author is grateful to scientific adviser Professor R.B. Morgunov and Professor S. Ohkoshi for samples providing.

Study of the formation of hydrogenation catalysts based on bis-(acetylacetonate)cobalt by ESR spectroscopy

Yu.Yu. Titova, L.B. Belykh, F.K. Schmidt

Irkutsk state university, Institute of Oil and Coal-Chemical Synthesis, 664003, Irkutsk,
Karl Marks St.,1, Russia

e-mail: ytitova60@gmail.com.

Introduction

The relevance of the study of the formation of Ziegler systems based on cobalt complexes is determined by the fact that such systems are used for industrial hydrogenation of styrene-butadiene copolymers. However, despite a more than half a century of research, the scientifically based criteria allowing to form effective catalysts have not yet been formulated.

In the systems based on Co(acac)$_{2(3)}$ with an organoaluminum compounds the generation of paramagnetic Co(0) complexes on the step of formation a hydrogenation catalyst has been found [1]. All attempts to isolate the intermediate Co(0) complex in resulted Ziegler systems have failed. But on the other hand, the high sensitivity and selectivity of the ESR method for the formatted paramagnetic particles makes it possible to study these compounds directly in the formed in situ catalytic systems, without their separation.

The aim of this study was the establishing the influence of various parameters and conditions on the Co(0) complexes formation, which are precursors in the preparation of hydrogenation catalysts in systems based on Co(acac)$_2$ – Red (Red = AlEt$_3$, AlEt$_2$(OEt), Li(*n*-Bu), (C$_6$H$_5$CH$_2$)MgCl), by ESR spectroscopy.

Experimental results and discussion

The interaction of anhydrous Co(acac)$_2$ with AlEt$_3$ in toluene/benzene at $T = 77$ K was observed biaxially anisotropic signal ($g_\perp = 2.050$, $g_\parallel = 2.355$) of Co(0) complex, the intensity of which corresponds ≈ 75 – 80 % from the original Co(acac)$_2$ (fig. 1a). It was found that an ESR spectrum intensity is essentially depends on the ratio of arene/Co and the arene nature (table 1). The molar ratio, for which the maximum concentration of the complexes of Co(0) are observed, is depending on the reducing agent nature (AlEt$_3$, AlEt$_2$(OEt), Li(*n*-Bu), (C$_6$H$_5$CH$_2$)MgCl).

Furthermore, the ESR spectrum ($T = 77$ K) of the generated in the system Co(acac)$_2$ – AlEt$_3$ Co(0) complex changed during in the time (fig. 1b). At initially step (fig. 1b, *1*) the spectrum view and *g*-factor parameters fully corresponds to a biaxially anisotropic signal ($g_\perp = 2.050$, $g_\parallel = 2.355$). After 5 minutes the appearance triaxial anisotropic signal is observed ($g_\perp = 2.0185$, $g_\perp = 2.051$ $g_\parallel = 2.332$) (fig. 1b, *2*), which after 5 – 10 minutes turn into signal without additional lines splitting from cobalt nucleus ($J = 7/2$) (fig. 1b, *3*). These lines can be easily seen on the first spectra, especially for parallel orientation.

The high sensitivity of ESR spectra parameters of the arene Co(0) complexes to the presence of water in the cobalt precursor was shown. Thus, the use as a precursor Co(acac)$_2$·0.5H$_2$O leads to the appearance of triaxial anisotropic signal of arene Co(0) complexe ($g_\perp = 2.0185$, $g_\perp = 2.051$ $g_\parallel = 2.332$) in the ESR spectrum, the concentration of which is ≈ 70 %. Use of Co(acac)$_2$·2.0H$_2$O, as a precursor, causes a sharp decrease in signal intensity of Co(0) triaxial anisotropic signal and its distortion.

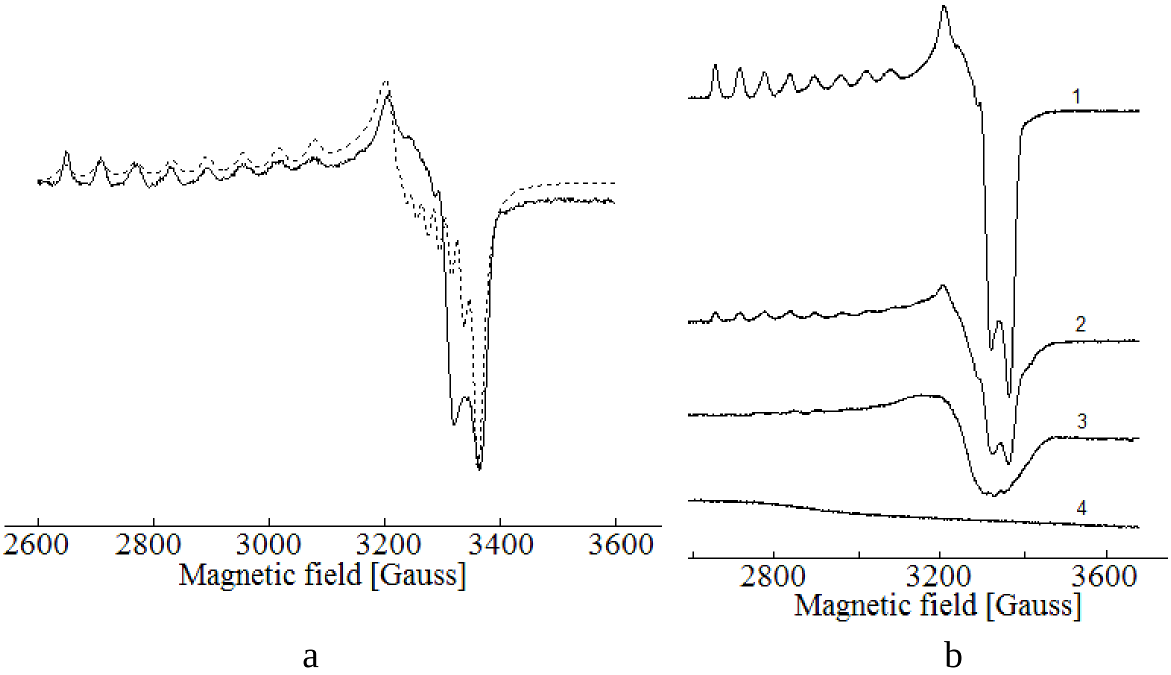

Fig.1. Experimental (—) and simulated (---) ESR spectra of $Co(acac)_2$ – $AlEt_3$ catalytic system at T = 77 K (a) and changes of ESR spectra depending on the time of formation of the system $Co(acac)_2$ – $4AlEt_3$ after 10 sec (*1*), 5 min (*2*), 20 min (*3*), 4 – 80 min (*4*) by the components mixing (b): $C_{Co} = 1\cdot10^{-2}$ mol/l, Al/Co = 4, solvent – toluene, atmosphere – argon, $T_{formation}$ = 298 K.

Table 1. The results of quantitative ESR spectroscopy of Co(0) complexes that generated in the $Co(acac)_2$ – $AlEt_3$ system in the presence of different arenes: $T_{formation}$ = 298 K, T = 77 K, atmosphere – argon.

№	$C_{Co(acac)_2}$, mol/l	Al/Co	Solvent	Arene	Arene /Co	$C_{Co(0)}$, mol/l (date of ESR)
1	5×10^{-3}	4	toluene	toluene	940	3.9×10^{-3}
2	1×10^{-2}	4	toluene	toluene	940	7.7×10^{-3}
3	2×10^{-2}	4	toluene	toluene	940	1.5×10^{-2}
4	3×10^{-2}	4	toluene	toluene	940	2.0×10^{-2}
5	2×10^{-2}	2	toluene	toluene	940	1.2×10^{-2}
6[1]	2×10^{-2}	2	toluene	toluene	940	4.9×10^{-3}
7	2×10^{-2}	6	toluene	toluene	940	7.0×10^{-3}
8	2×10^{-2}	8	toluene	toluene	940	7.0×10^{-3}
9	5×10^{-3}	4	mesitylene	mesitylene	720	4.9×10^{-3}
10	1×10^{-2}	4	mesitylene	mesitylene	720	1.0×10^{-2}
11	2×10^{-2}	4	mesitylene	mesitylene	720	8.9×10^{-3}
12	1×10^{-2}	4	*p*-xylene	*p*-xylene	820	8.2×10^{-3}
15	1×10^{-2}	4	heptane	1,2,4,5-tetra-methylbenzene	10	2.2×10^{-3}
17	1×10^{-2}	4	heptane	hexamethylbenzene	10	2.9×10^{-3}
19[2]	1×10^{-2}	4	toluene	toluene	940	7.1×10^{-3}
20[3]	1×10^{-2}	4	toluene	toluene	940	5.5×10^{-3}

[1] – system is formed in hydrogen; [2] – $Co(acac)_2\cdot0.5H_2O$ was used. [3] – $Co(acac)_2\cdot2.0H_2O$ was used.

For the first time it is managed to get the ESR spectrum of the Co(0) complex, formed in the $Co(acac)_2$ – $AlEt_3$ system, at the room temperature (fig. 2). Detailed analysis and simulation of the spectrum [2] showed that it was probably due to a superposition of signals from the cobalt atom, aluminum atom and hydrogen atoms. Such ESR spectrum can be interpreted as the coordination of $AlEt_2(acac)$ at Co(0):

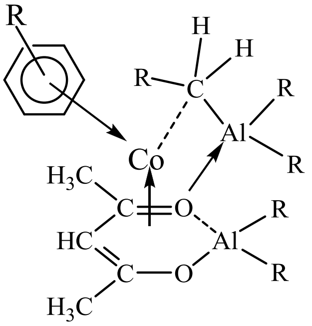

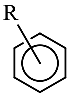

– benzene, toluene, *p*-xylene, mesitylene, 1,2,4,5-tetramethylbenzene, hexamethylbenzene.

It should be noted that the Co(0) complex spectrum (T = 293 K) can be observed for not more than 1 – 2 minutes, and it's stability depends on the type of the arene and increases in the series of benzene < toluene < *p*-xylene < mesitylene < 1,2,4,5-tetramethylbenzene < hexamethylbenzene. If $AlEt_2(OEt)$ or Li(н-Bu) instead $AlEt_3$ is used as reducing agent the signal from the arene Co(0) complex is not recorded at T = 293 K.

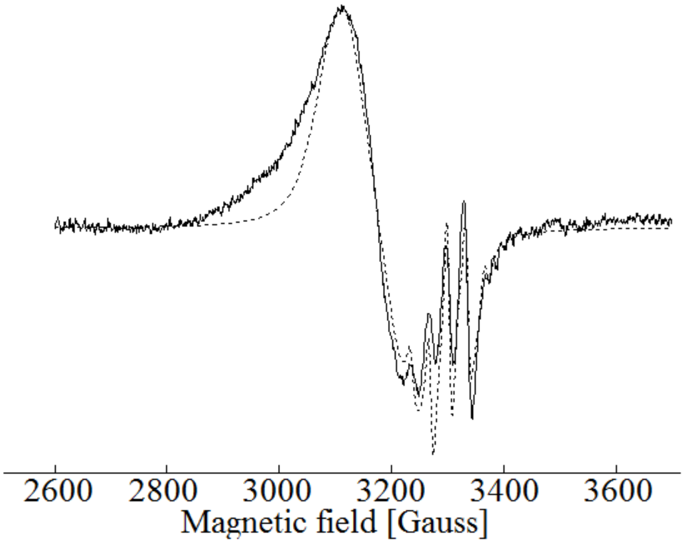

Fig.2. Experimental (—) and simulated (---) ESR spectra of $Co(acac)_2 – AlEt_3$ catalytic system at T = 293 K, solvent – toluene: $C_{Co} = 1 \cdot 10^{-2}$ mol/l, Al/Co = 4, solvent – toluene, atmosphere – argon, $T_{formation}$ = 298 K; sample was taken after 10 seconds of mixing.

During the interaction of $Co(acac)_2 – AlEt_3$ system components in the hydrogen atmosphere more than twofold decrease in the initial intensity of the ESR signal from the Co(0) complex (T = 77 K) and its complete disappearance after 4 minutes are observed. This fact is not surprising since the intermediate Co(0) complexes are highly reactive compounds. The hydrogenolysis reaction of LCoEt (L = arene, $AlEt_3$, $AlEt_2(acac)$) or oxidative addition of hydrogen molecules to Co(0) cause rapid disappearance of the signals from the Co(0) complexes in a hydrogenation catalysis.

At the same time during hydrogenation the emergence and growth of a wide signal that relating to the ferromagnetic cobalt nanoclusters (g = 2.1 – 2.2, linewidth 1500.0 G) (fig.3), which are the carriers of the catalytic activity, are observed. The formation of cobalt nanoclusters with average particle size of 2.5 ± 0.5 nm was confirmed by HRTEM (High Resolution Transmission Electron Microscopy).

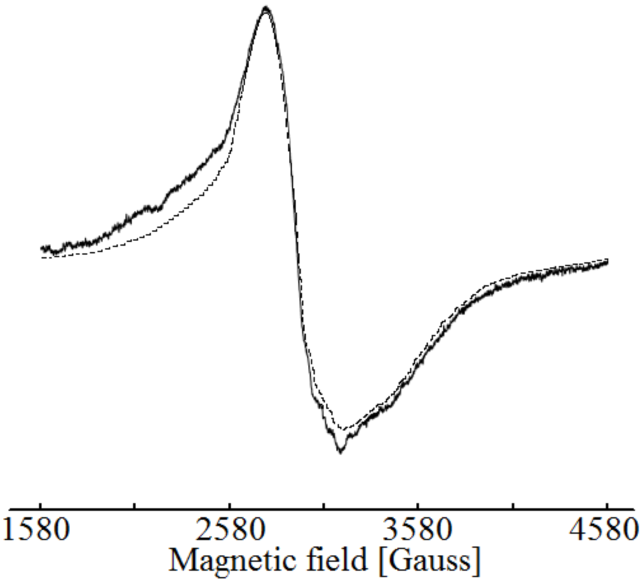

Fig.3. Experimental (—) and simulated (---) ESR spectra of $Co(acac)_2 – AlEt_3$ catalytic system after hydrogenation of 3 ml styrene: $C_{Co} = 1 \cdot 10^{-2}$ mol/l, Al/Co = 4, solvent – toluene, atmosphere – hydrogen, $T_{formation}$ = 298 K.

Conclusion

The reported patterns are the result of complex processes of Co(0) complexes formation and further cobalt clusters initiation with different nuclearity and coordination unsaturation. A detailed study of the mechanism of clusters and nanoparticles formation in these systems will be the subject of further work.

Acknowledgements

This work was supported by a base part of Government Assignment for Scientific Research from the Ministry of Education and Science, Russia (№ 2014/51, project code).

Authors gratefully acknowledge Irkutsk Supercomputer Center of the Russian Academy of Sciences http://hpc.icc.ru.

References

[1] F.K. Shmidt, Kataliz kompleksami metallov pervogo perekhodnogo ryada reaktsii gidrirovaniya i dimerizatsii (Hydrogenation and Dimerization Catalyzed by Complexes of First Row Transition Metals), Irkutsk: Irkutsk. Gos. Univ., 1986, p. 230.
[2] S. Stoll, A. Schweiger, Journal of Magnetic Resonance, 178 (2006) 42-55.

Electron spin resonance in a model S = 1/2 chain antiferromagnet with a uniform Dzyaloshinskii–Moriya interaction $K_2CuSO_4Br_2$

T.A. Soldatov[1,2], K.Yu. Povarov[1,3], M. Hälg[3], W.E.A. Lorenz[3], A. Zheludev[3], A.I. Smirnov[1,2]

[1]P.L. Kapitza Institute for Physical Problems, RAS, 119334, Kosygina street, Moscow, Russia
[2]Moscow Institute for Physics and Technology, 141700,Institutskii per., Dolgoprudny, Russia
[3]Neutron Scattering and Magnetism, Laboratory for Solid State Physics, ETH Zürich,
CH-8093, Zürich, Switzerland

e-mail: tim-sold@yandex.ru

Magnetic crystals with a low-dimensional spin structure remain in a correlated paramagnetic (spin-liquid) phase at cooling far below the Curie-Weiss temperature T_{CW}. Low temperature magnetic properties of these magnets are similar to that of a spin-liquid phase in the zero temperature limit. The suppression or even absence of the ordering is due to strong quantum fluctuations. A quasi-one-dimensional (1D) S = 1/2 dielectric antiferromagnet $K_2CuSO_4Br_2$ exhibits spin correlations emergent in a wide temperature range below T_{CW} = 20 K, while Néel point is at much lower temperature T_N = 70 mK. The Cu^{2+} S = 1/2 ions form spin chains with the intrachain exchange J = 20.5 K which is much stronger than the interchain exchange J' = 0.034 K. A feature of this compound is a ***uniform*** Dzyaloshinskii-Moriya (DM) interaction between spins within a chain [1]. This feature is of importance for spin dynamics because the two-spinon continuum of an S = 1/2 Heisenberg antiferromagnetic chain was predicted to be modified by the uniform DM interaction via a shift in **q**-space by a vector $q_{DM} = \pi D/Ja$ [2], here **D** is a vector of DM interaction and a is a period of the chain. Due to this shift, in a magnetic field $\mathbf{H} \parallel \mathbf{D}$, the electron spin resonance (ESR) should split into a so called spinon doublet with frequencies at the boundaries of the unshifted continuum at $q = q_{DM}$. At $\mathbf{H} \perp \mathbf{D}$ there should be no split, while a gap of ESR absorption is expected in zero field.

The spinon ESR doublet and a zero-field gap were indeed observed in the spin-liquid phase of a quasi-two-dimen-sional (2D) antiferromagnet Cs_2CuCl_4 [3]. In crystals of Cs_2CuCl_4, the Cu^{2+} S = 1/2 magnetic ions are placed on stacked 2D layers with a distorted trian-gular lattice with a strong exchange J = 4.35 K along the base of the triangu-lar unit and weaker exchange integral J' = 0.34 J along lateral sides of the triangle. Frustration of J'-bonds results in effective decoupling of spin chains leading to one-dimensionality. The object of the present study corresponds much better to the theoretical model of spinon doublet because of a perfect one-dimensionality of the spin system ($J/J' \approx 600$). The structure of this orthorhombic P_{nma} mineral is shown in fig.1.

The model Hamiltonian of a spin chain including Heisenberg exchange and uniform DM interaction may be written as:

$$\widehat{H} = \sum_i J\mathbf{S}_i\mathbf{S}_{i+1} + \mathbf{D}\cdot\mathbf{S}_i \times \mathbf{S}_{i+1}$$

Here J is the intrachain exchange integral and vector **D** is the parameter of DM interaction.

Crystallographic symmetry analysis shows that for $K_2CuSO_4Br_2$ the DM vectors in adjacent chains are of the same absolute value but are directed along opposite directions [1]. The simple collinear structure of DM vectors in this compound enables one to adjust the magnetic field parallel to all DM vectors, which was impossible for Cs_2CuCl_4, where a few

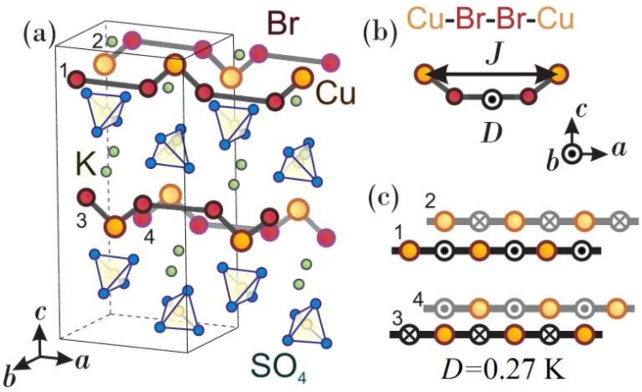

Fig.1. (a) Schematic representation of $K_2CuSO_4Br_2$ crystal structure.
(b) Magnetic interactions between the Cu^{2+} ions as given in Hamiltonian (1). Vector **D** presents the symmetry allowed parameter of Dzyaloshin-skii–Moriya interaction.

(c) Two sets of nonequivalent spin chains with the opposite direction of DM vector.

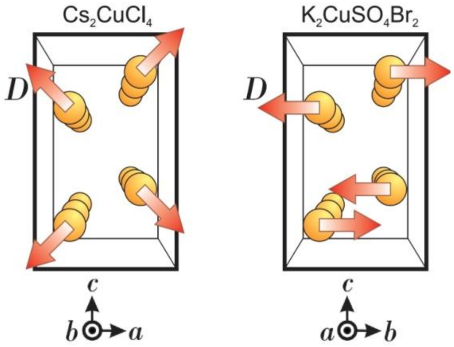

Fig.2. Schematic representation of structure of DM vectors in Cs_2CuCl_4 and $K_2CuSO_4Br_2$

non-parallel DM vector directions exist in adjacent chains, see fig.2. The observation of the splitting of the EPR line in $K_2CuSO_4Br_2$ at the frequency $\nu = 26.86$ GHz at cooling below 20 K was briefly reported in [1].

Now we describe the investigation of the ESR spectrum of this compound in a wide frequency and temperature range. Our measurements cover the sub-gap and over-gap frequency domains, reconstructing the entire frequency-field dependence of ESR absorption.

The anisotropy of the effect is also checked to be consistent with the spinon-based theory [2]. Besides, we follow the temperature dependence of the gap and of the splitting of the doublet at cooling down to the temperature of 0.45 K corresponding to the energy of DM interaction.

Experiments were performed using a set of ESR spectrometers, combined with a superconducting 12 T solenoid and a ^{3}He cryostat, providing temperature down to 0.45 K. Backward wave oscillators, Gann diods and klystrons were microwave sources, covering the

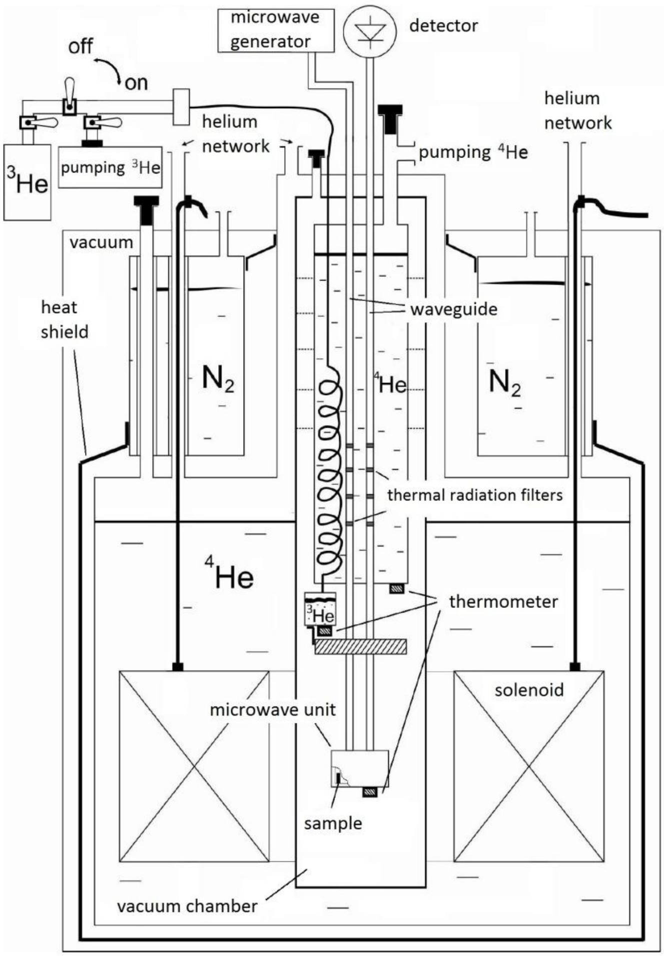

Fig.3. ^{3}He-pump spectrometer.

frequency range 0.5 – 250 GHz. The microwave units with cylindrical, rectangular, cut-ring and spiral resonators were used for recording the resonance absorption of microwaves. The samples used in our measurements were the single crystals of $K_2CuSO_4Br_2$ from the same batch as in [1]. The sample was fixed by Apeizon N grease inside the microwave unit, which was placed in vacuum and connected via a heat transfer link to the chamber of the ^{3}He pump refrigerator. A RuO_2 thermometer placed on the bottom of the microwave unit monitored the temperature of the microwave unit in the process of measurement.

Frequency-field diagram of the ESR for the magnetic field applied along the *b*-axis and parallel to the DM vector **D** is shown in fig.4. The temperature evolution of the 27.83 GHz ESR line corresponding to this orientation of the magnetic field is presented in fig.5.

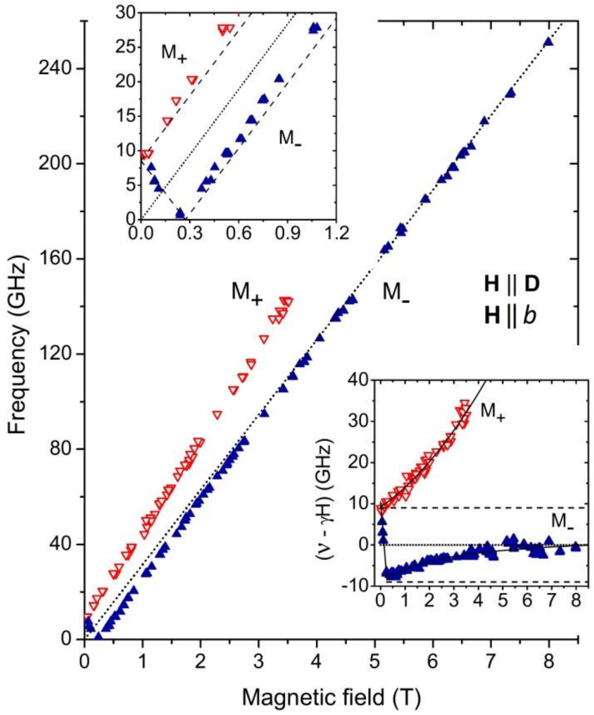

Fig.4. Frequency-field diagram for **H** || **D** at *T* = 0.5 K. Dashed lines present theoretical prediction for *D* = 0.27 K.

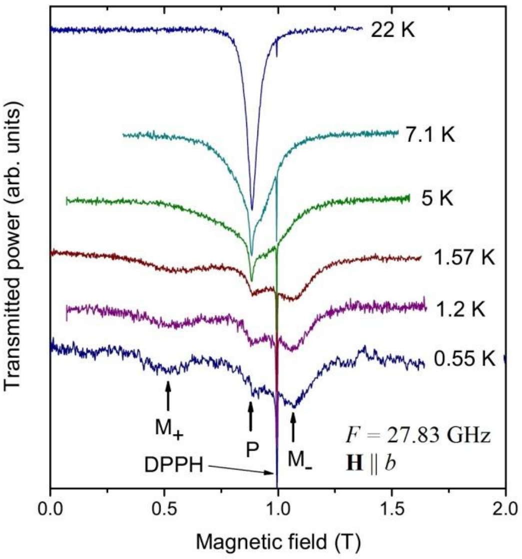

Fig.5. Temperature evolution of the 27.83 GHz ESR line at **H** || *b*. M_+ and $M_–$ label the components of the doublet.

Frequency-field diagram for the magnetic field oriented perpendicular to the DM vector **D** is shown in fig.6. The temperature evolution of 27.75 GHz ESR spectrum at **H** || *a* is presented in fig.7.

Fig.5 and fig.7 demonstrate the transformation of the Larmor-type ESR spectrum into M_+, $M_–$ components of the spinon doublet and the single mode with the gap in zero magnetic field with decreasing the temperature respectively.

As the result, the observed formation of the ESR doublet M_+, $M_–$ in the temperature range below the temperature $T_J = J = 20.5$ K is fully consistent with the scenario of the spin chain entering a quantum critical regime upon cooling. The anisotropic behavior of the doublet is also in a perfect agreement with the symmetry considerations for DM vector **D**. The symmetry of the orthorhombic $Z = 4$ P_{nma} structure of $K_2CuSO_4Br_2$ implies **D** || *b*, as shown in fig.1. The theoretical prediction [2, 3] is that the ESR doublet should be observable only when the magnetic field has a component along the vector **D**. In a full correspondence with the above symmetry restrictions we observe a spinon doublet at **H** || *b* and a single line at **H** ⊥ *b*.

These experimental results confirm directly the predicted transformation of the spinon continuum of a Heisenberg $S = 1/2$ chain due to the action of uniform DM interaction.

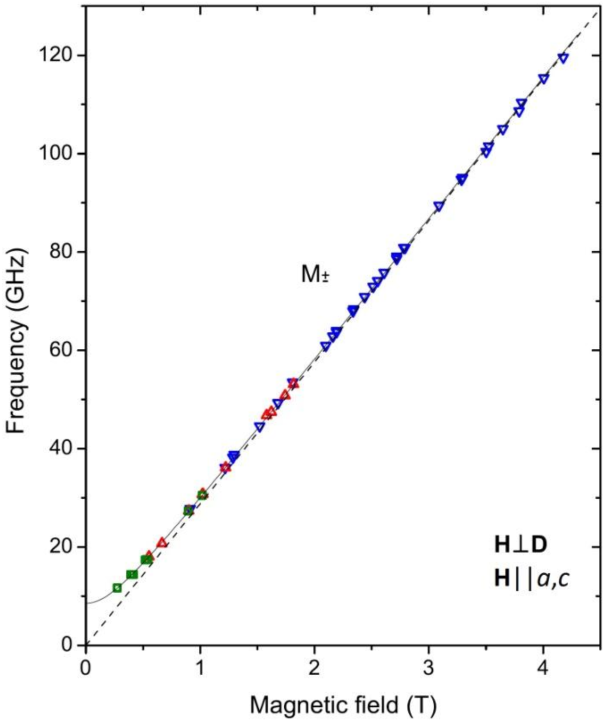

Fig.6. Frequency-field diagram for **H** ⊥ **D** in the low-temperature limit. Solid line pre-sents the theory with parameter $D = 0.27$ K.

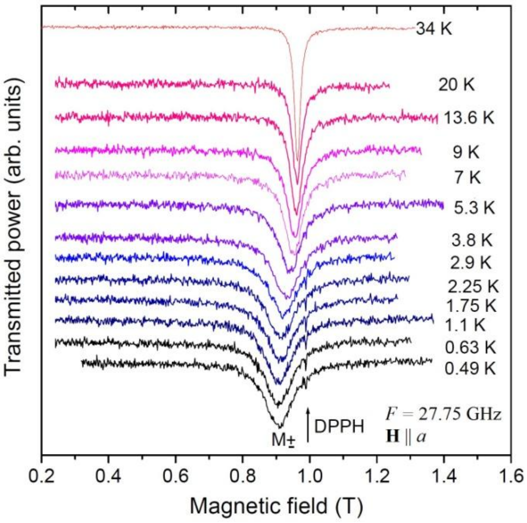

Fig.7. Temperature evolution of ESR line at frequency 27.75 GHz, **H** || *a*.

References

[1] M. Hälg, W.E.A. Lorenz, K.Yu. Povarov, M. Månsson, Y. Skourski, and A. Zheludev. Phys. Rev. B 90, 174413 (2014).

[2] S. Gangadharaiah, J. Sun, O.A. Starykh. Phys. Rev. B 78, 054436 (2008).

[3] K. Yu. Povarov, A. I. Smirnov, O. A. Starykh, S. V. Petrov, A. Ya. Shapiro. Phys. Rev. Lett. 107, 037204 (2011).

Nuclear magnetic resonance study of atomic motion in the complex hydride $Li_3(NH_2)_2I$

R.V. Skoryunov[1], A.V. Skripov[1], A.V. Soloninin[1], O.A. Babanova[1], M. Matsuo[2], S. Orimo[2,3]

[1]Institute of Metal Physics, Ural Branch of the Russian Academy of Sciences,
620990, S. Kovalevskoi 18, Ekaterinburg, Russia
[2]Institute for Material Research, Tohoku University, 980-8577, Sendai, Japan
[3]WPI-Advanced Institute for Material Research, Tohoku University, 980-8577, Sendai, Japan
e-mail: skoryunov@imp.uran.ru

Introduction

Complex hydrides are ionic crystals, consisting of metal cations and complex anions, such as $[BH_4]^-$, $[NH_2]^-$, $[NH]^{2-}$, $[AlH_6]^{3-}$, $[B_{12}H_{12}]^{2-}$, or $[B_{10}H_{10}]^{2-}$. Some of these systems can be potentially used as solid electrolytes in batteries [1]. Apart from the prospective practical applications, these compounds are of interest as model systems for studies of the mechanisms of cation diffusion. Indeed, complex anions are known to exhibit a rotational (reorientational) motion, and this localized motion may affect the translational diffusion of cations [2]. In this work, we present the results of the nuclear magnetic resonance study of atomic motion in the novel complex hydride $Li_3(NH_2)_2I$, showing fast-ion conduction [3]. Measurements of the ^{7}Li and ^{1}H NMR spectra and spin-lattice relaxation rates were performed over wide ranges of temperatures (98 – 488 K) and resonance frequencies (14 – 90 MHz).

Experimental methods

NMR measurements were performed on a pulse spectrometer with quadrature phase detection at the frequencies $\omega/2\pi = 14$ and 28 MHz for ^{7}Li and 14, 28, and 90 MHz for ^{1}H. The magnetic field was provided by a 2.1 T iron-core Bruker magnet. A home-built multinuclear continuous-wave NMR magnetometer working in the range 0.32 − 2.15 T was used for field stabilization. For rf pulse generation, we used a home-built computer-controlled pulse programmer, the PTS frequency synthesizer (Programmed Test Sources, Inc.), and a 1 kW Kalmus wide-band pulse amplifier. Typical values of the $\pi/2$ pulse length were 2 – 3 μs for all nuclei studied. For the measurements at $T < 460$ K, a probehead with the sample was placed into an Oxford Instruments CF1200 continuous-flow cryostat using helium or nitrogen as a cooling agent. The sample temperature, monitored by a chromel-(Au − Fe) thermocouple, was stable to ±0.1 K. Measurements at $T \geq 460$ K were performed using a furnace probehead; for this setup, the sample temperature, monitored by a copper−constantan thermocouple, was stable to ±0.5 K. The nuclear spin-lattice relaxation rates were measured using the saturation-recovery method. NMR spectra were recorded by Fourier transforming the solid echo signals (pulse sequence $\pi/2_x - t - \pi/2_y$). For NMR experiments, the sample was flame-sealed in a glass tube under vacuum.

Results and discussion

The temperature dependence of the ^{7}Li NMR line width Δ_{Li} (full width at half-maximum) is shown in fig.1. Such a behavior of $\Delta_{Li}(T)$ is typical of the line narrowing due to atomic motion. The ^{7}Li NMR line narrowing is observed near 200 K. Such drop of Δ_{Li} indicates the onset of Li^+ jump motion. In the region of the high-T plateau, the value of Δ_{Li} is very small (~ 0.35 kHz), much smaller than the expected line width (~ 8.0 kHz) for the ^{7}Li−^{7}Li dipolar contribution to the “rigid-lattice” second moment for $Li_3(NH_2)_2I$. Therefore, the ^{7}Li−^{7}Li dipole−dipole interaction must be averaged out in the region of the high-T plateau; this can occur only in the case of long-range diffusion of lithium ions.

Fig.2 shows the behavior of the ^{7}Li spin−lattice relaxation rates R_1^{Li} at two resonance frequencies as functions of the inverse temperature. Such frequency-dependent peak is typical of the case of spin−lattice relaxation due to atomic motion [4]; it is expected to occur at the temperature at which the atomic jump rate $\tau_d^{-1}(T)$ (governed by the Arrhenius law) becomes nearly equal to the resonance frequency ω. This means that the Li$^+$ jump rate in $Li_3(NH_2)_2I$ reaches the value of about 10^8 s^{-1} near room temperature. It is reasonable to assume that the $R_1^{\mathrm{Li}}(T)$ peak originates from the same Li$^+$ diffusion process that is responsible for the line narrowing at lower temperatures. The amplitude of the peak is determined by the strength of interactions (quadrupole and/or dipole-dipole) that are caused to fluctuate due to atomic jump motion. The observed amplitude of the $R_1^{\mathrm{Li}}(T)$ peak in $Li_3(NH_2)_2I$ is much higher than that expected for dipole−dipole interactions of ^{7}Li spins. Hence, we can conclude that the $R_1^{\mathrm{Li}}(T)$ peak in $Li_3(NH_2)_2I$ is dominated by fluctuations of the quadrupole interaction. The experimental results for $Li_3(NH_2)_2I$ have been described in terms of the model with Gaussian distribution of activation energies in the range 228 – 401 K. The results of the fit are shown by the solid lines in fig.2. The Li$^+$ diffusion process responsible for the peak is characterized by the activation energy of 0.38 eV.

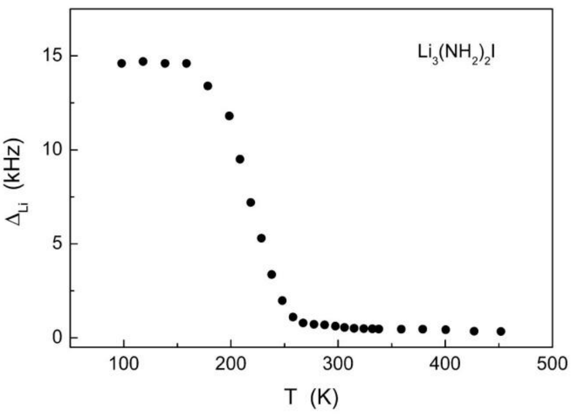

Fig.1. Temperature dependence of the width (full width at half-maximum) of the ^{7}Li NMR line measured at 28 MHz for $Li_3(NH_2)_2I$.

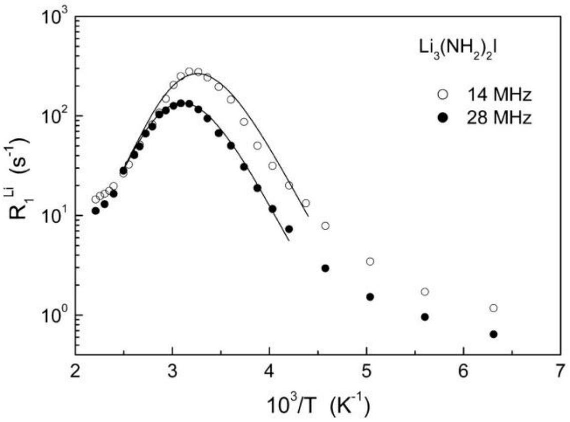

Fig.2. ^{7}Li spin−lattice relaxation rates measured at 14 and 28 MHz for $Li_3(NH_2)_2I$ as functions of the inverse temperature. The solid lines show the simultaneous fit of the model with a Gaussian distribution of the activation energies to the data in the range 228 − 401 K.

The temperature dependence of the ^{1}H NMR line width Δ_H (full width at half-maximum) is shown in fig.3. It can be seen that the temperature dependence of Δ_H exhibits two “steps”; this suggests the presence of two motional processes with strongly differing characteristic jump rates. The low-temperature “step” of $\Delta_H(T)$ is observed in the same temperature range as the “step” of $\Delta_{Li}(T)$ (see fig.1). Therefore, the faster motional process leading to the narrowing of the ^{1}H NMR line can be attributed to Li$^+$ jumps. The high-temperature “step” of $\Delta_H(T)$ should be attributed to another (slower) motional process. Possible candidates for this slower process are reorientations of NH_2 groups and translational diffusion of NH_2 groups. If NH_2 groups exhibit only fast reorientations, the expected ^{1}H NMR line width can be estimated using the assumption that fast reorientations average out the ^{1}H − ^{1}H dipole−dipole interactions within NH_2 groups (“intramolecular” interactions) but do not average the ^{1}H − ^{1}H interactions between different NH_2 groups (“intermolecular” interactions). Since the observed line width at the high-T end of our experimental range (Δ_H = 4.6 kHz at 488 K) is considerably smaller than this estimated value (Δ_H = 14.6 kHz), we can conclude that the high-T line narrowing occurs due to the translational diffusion of NH_2 groups.

Fig.4 shows the behavior of the ^{1}H spin−lattice relaxation rates R_1^{H} at three resonance frequencies as functions of the inverse temperature. The frequency-dependent $R_1^{\mathrm{H}}(T)$ peak is observed in the same temperature range as the $R_1^{\mathrm{Li}}(T)$ peak. Therefore, the ^{1}H relaxation rate peak is likely to originate from the same motional process (Li^+ jumps) as the ^{7}Li relaxation rate peak. To demonstrate it more clearly, we have tried to describe the $R_1^{\mathrm{H}}(T)$ data in the region of the peak using the set of Li motional parameters found from the analysis of the ^{7}Li relaxation rates (see above). Consequently, the only fit parameter of this model is the amplitude factor represented by the fluctuating part of the ^{1}H − ^{7}Li dipolar second moment, ΔM_{HLi}. The results of this model description in the temperature range 240 – 430 K are shown by the dashed lines in fig.4. As can be seen from this figure, a satisfactory description of the ^{1}H relaxation rate data near the peak at three resonance frequencies can be achieved using the motional parameters for Li^+ diffusion; the corresponding value of ΔM_{HLi} is $3.6 \times 10^9\ \mathrm{s}^{-2}$, which is close to the calculated "rigid-lattice" M_{HLi} value ($6.1 \times 10^9\ \mathrm{s}^{-2}$). Thus, it is not necessary to invoke any NH_2 reorientational process to describe the ^{1}H relaxation rate peak induced by Li^+ diffusion.

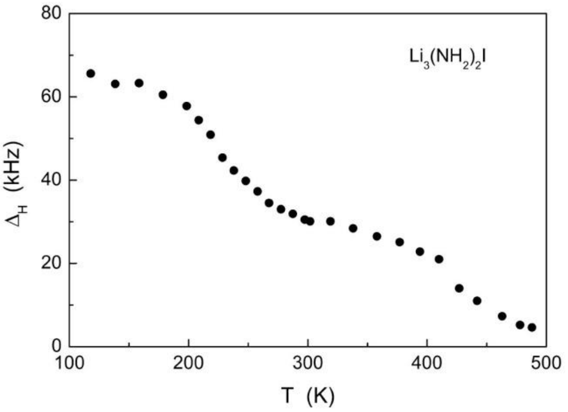

Fig.3. Temperature dependence of the width (full width at half-maximum) of the ^{1}H NMR line measured at 28 MHz for $Li_3(NH_2)_2I$.

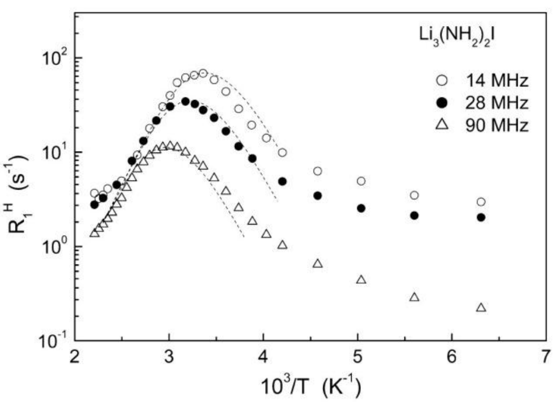

Fig.4. Proton spin−lattice relaxation rates measured at 14, 28, and 90 MHz for $Li_3(NH_2)_2I$ as functions of the inverse temperature. The dashed lines show the calculated ^{1}H − ^{7}Li dipole-dipole contribution using the motional parameters of Li ions found from the ^{7}Li relaxation data.

References

[1] A. Unemoto, S. Yasaku, G. Nogami, M. Tazawa, M. Taniguchi, M. Matsuo, T. Ikeshoji, S. Orimo, *Appl. Phys. Lett*. 2014, 105, 083901.

[2] A.V. Skripov, A.V. Soloninin, M.B. Ley, T.R. Jensen, Y. Filinchuk, *J. Phys. Chem. C* 2013, 117, 14965−14972.

[3] M. Matsuo, T. Sato, Y. Miura, H. Oguchi, Y. Zhou, H. Maekawa, H. Takamura, S. Orimo, *Chem. Mater.* 2010, 22, 2702−2704.

[4] A. Abragam, *The Principles of Nuclear Magnetism*, Clarendon Press: Oxford, 1961.

Mobility and reactivity of 4-substituted TEMPO derivatives in metal-organic framework MIL-53(Al)

A.S. Poryvaev[1,2], A.M. Sheveleva[1,2], D.I. Kolokolov[3], I.K. Shundrina[5], S.A. Gromilov[4],
A.G. Stepanov[3], E.G. Bagryanskaya[2,5], M.V. Fedin[1,2]

[1]International Tomography Center SB RAS, 630090, Institutskaya st. 3a, Novosibirsk, Russia
[2]Novosibirsk State University, 630090, Pirogova st. 2, Novosibirsk, Russia
[3]Boreskov Institute of Catalysis SB RAS, 630090, Lavrentiev av. 5, Novosibirsk, Russia
[4]Nikolaev Insititute of Inorganic Chemistry SB RAS,
630090, Lavrentiev av. 3, Novosibirsk, Russia
[5]N. N. Vorozhtsov Novosibirsk Institute of Organic Chemistry SB RAS,
630090, Lavrentiev av. 9, Novosibirsk, Russia

e-mail: poryvaev@mail.tomo.nsc.ru

Abstract

Post-synthetic adsorption of stable nitroxide probes in diamagnetic metal-organic frameworks (MOFs) allows application of Electron Paramagnetic Resonance (EPR) for studying structure, functions and corresponding guest-host interactions in such MOFs. This approach was recently demonstrated using (2,2,6,6-tetramethylpiperidin-1-yl)oxyl (TEMPO) embedded in structurally-flexible MIL-53(Al) [1], with the mobility and reactivity of TEMPO reflecting structural dynamics of MOF. In the present work we embed three derivatives of TEMPO (4-oxo-TEMPO, 4-hydroxo-TEMPO, 4-acetamido-TEMPO) in MIL-53(Al) and investigate structural "breathing" of this MOF with temperature in order to gain deeper understanding of underlying guest-host interactions. Different substituents in piperidin ring lead to different mobility and reactivity of corresponding nitroxides. The obtained EPR data and Molecular Dynamics (MD) calculations show that the efficiency of nitroxide reaction with μ_2-hydroxo group of MIL-53(Al) strongly correlates with the character of its molecular motion, and the reversibility of this reaction upon structural "breathing" is a general phenomenon.

Introduction

Metal-organic frameworks (MOFs) have drawn enormous attention during last decade [2]. Particular interest are flexible MOFs which might exhibit various structural transitions between different forms being induced by temperature or sorption/desorption of guest molecules.[3] MIL-53(Al) is one of the brightest representatives of flexible MOFs with 3D structure undergoing temperature-induced structural transition with a significant hysteresis.[3, 4]. Recently we have proposed post-synthetic adsorption of stable nitroxide radicals and following electron paramagnetic resonance (EPR) detection as a perspective approach for studying breathing behavior and guest-host interactions in structurally-flexible MOFs [1].

In this work we attempt to gain deeper understanding of guest-host interactions between adsorbed nitroxides and MIL-53(Al), with a particular focus on reversible reaction of nitroxide with MOF. To verify this, in the present work we study three derivatives of TEMPO (4-oxo-TEMPO, 4-hydroxy-TEMPO, 4-acetamido-TEMPO) embedded in MIL-53(Al). Below we describe the developed experimental approaches, theoretical (MD) modeling and experimental EPR data on these three systems and compare the results with those obtained for TEMPO previously. The observed correlation between structure, mobility and reactivity of nitroxides in MIL-53(Al) supports previously proposed mechanism and allows general suggestions on selection of nitroxides for in-MOF EPR studies.

Experimental

Materials. The TEMPO derivatives used were 4-oxo-TEMPO (TEMPONE), 4-hydroxy-TEMPO (TEMPOL), and 4-acetamido-TEMPO, all obtained from Aldrich and used as received. The hydrothermal synthesis of MIL-53(Al) was performed according to procedure described previously [5].

Sample preparation. *Gas-phase sorption.* The weighted quantity of MOF (20 mg, polycrystalline powder) was placed in a tube equipped with vacuum valve. Prior to adsorption of radical, the MOF was evacuated at 10^{-5} Torr during 2 hours at room temperature, then it was maintained for 12 hours at 150°C (activation procedure). The adsorption of nitroxide into MOF was performed at room temperature from the gas phase and then the sample was sealed in the quartz tube. *Impregnation method*. First, MOF was activated under vacuum at 150°C (see above). Then the polycrystalline powder was saturated with an excess of dilute solution of nitroxide dissolved in a diethyl ether (concentration $2 \cdot 10^{-4}$ M) and let to dry under ambient conditions. Afterwards the sample was again thermally activated under vacuum (10^{-5} Torr, first 2 hours at room temperature, next 12 hours at 150°C) and sealed in the quartz tube.

Molecular Dynamics. MD simulations were performed in the canonical (NVT) ensemble at 300 K using Gromacs-MD package. The equations of motion were integrated for 100 ns with a time step of 10 fs with accurate leap-frog stochastic dynamics integrator. The Ewald summation was used for calculating electrostatic interactions, whereas the short range interactions were calculated with a cut-off distance of 11 Å.

EPR measurements. CW EPR spectra were measured at X-band (9 GHz) using the commercial spectrometer Bruker Elexsys E580 equipped with Oxford Instruments temperature control system (ER 4112HV with helium cryostat ER 4118CF-O). Modulation amplitude was 0.1 mT, mw frequency ~9.7 GHz, mw power ~0.2 ÷ 0.002 mW was chosen to avoid saturation of spectral lines. For calibration experiments we used X-band Bruker MD-5 resonator with sapphire ring inside as a reference. Theoretical modeling of EPR spectra was performed using EasySpin toolbox (Version 5.0.2) for Matlab [6].

Results and Discussion

Molecular Dynamics Calculations. We begin our investigation of TEMPONE, TEMPOL and 4-acetamido-TEMPO in MIL-53(Al) from theoretical MD computation of their mobility depending on structure.

First, the mobility of three nitroxides was studied in the LP state of MIL-53(Al). Fig.1 clearly demonstrates that the mobility of three studied radicals in MIL-53(Al) is principally different. TEMPONE tends to conform to the orientations having NO bond parallel to the Z axis of MIL-53(Al), whereas TEMPOL tends to occupy orientations perpendicular. Molecular motion 4-acetamido-TEMPO can be characterized by small-angle librations.

In case of NP state of MIL-53(Al) we can conclude that TEMPONE and TEMPOL are trapped in orientations with piperidine ring of radical being closely parallel to the long diagonal of the lozenge (see fig.1). NO group of the trapped radical can have different orientations. That is orientations across and along the nanochannel of MIL-53(Al). When NO group is directed across the channel, it is remote from the μ_2-hydroxo group of the MOF; at the same time, when NO group is directed along the nanochannel, the complex formation between radical and MIL-53(Al) via μ_2-hydroxo group is quite possible (distance NO…OH is

~2 Å for TEMPONE and TEMPOL). 4-acetamido-TEMPO remains immobile in NP state, the only possible orientation refers to NO group oriented across the nanochannel.

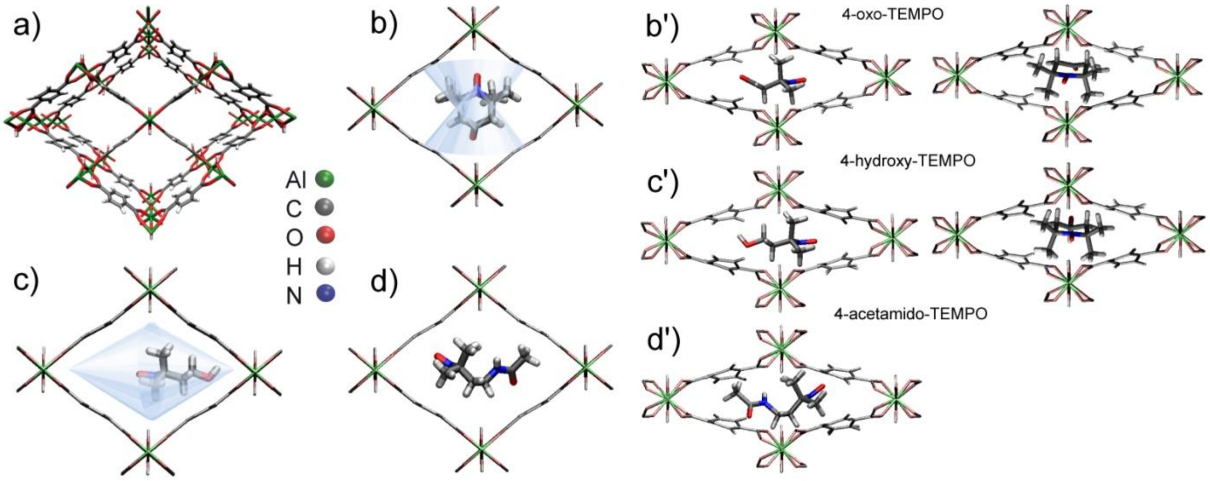

Fig.1. (a) Structure of MIL-53(Al). Illustration of radical's motion in LP(b) and NP(b′) of MIL-53(Al) according to MD simulations; (b, b′) TEMPONE; (c, c′) TEMPOL; (d, d′) 4-acetamido-TEMPO.

Thus, MD calculations predict that TEMPONE and TEMPOL undergo fast restricted reorientational motion in LP state and become immobilized in NP state, possibly forming complexes with μ_2-hydroxo group of the MOF. Instead, 4-acetamido-TEMPO is essentially immobile in both states, and the formation of complexes with MOF is hindered.

EPR Study. We prepared samples using two different approaches. First, we have employed the method sorption of radicals into the pores of MOF from the gas phase.[1] CW EPR spectra of such samples at room temperature being superpositions of spectra of immobilized nitroxide and unexpected strong singlet with $g \approx 2.0026$. Also, we have prepared the sample with unsubstituted TEMPO using the same approach, and previously reported results were reproduced. It seems that the TEMPO derivatives get adsorbed largely on the surface of MIL-53(Al) yielding strong singlet exchange-narrowed line due to high local concentrations. In case of the volatile TEMPO, radicals easily diffuse deep into the volume of MOF.

Having not succeeded with the gas-phase sorption, we implemented the impregnation method using volatile diethyl ether as a solvent. This approach led to much better results. The strong unwanted singlet was not observed. But still the conversion from LP to NP state with temperature was not complete for TEMPO derivatives. EPR spectra demonstrate that thermal LP→NP switching efficiency is ~44% for TEMPONE and ~40% for TEMPOL. EPR spectrum 4-acetamido-TEMPO does not exhibit any noticeable changes.

We explain the low percentage of switching for 4-substituted-TEMPO@MOF by poor homogeneity of radicals inside the framework. And we suppose that the main reason is that derivatives can form better hydrogen bonds with μ_2-hydroxo groups of MIL-53 (Al) compare TEMPO.

Fig.2 shows the CW EPR spectra of three 4-substituted-TEMPO@MIL-53(Al) samples and corresponding simulations.

EPR spectra of 4-acetamido-TEMPO@MIL-53(Al) show that this nitroxide remains essentially immobile even at room temperature. The best agreement was obtained using again the librational model with g = [2.095, 2.0068, 2.0026], A = [0.57, 0.46, 3.40] mT and ξ=0.96. This reasonably agrees with theoretical expectations from MD modeling.

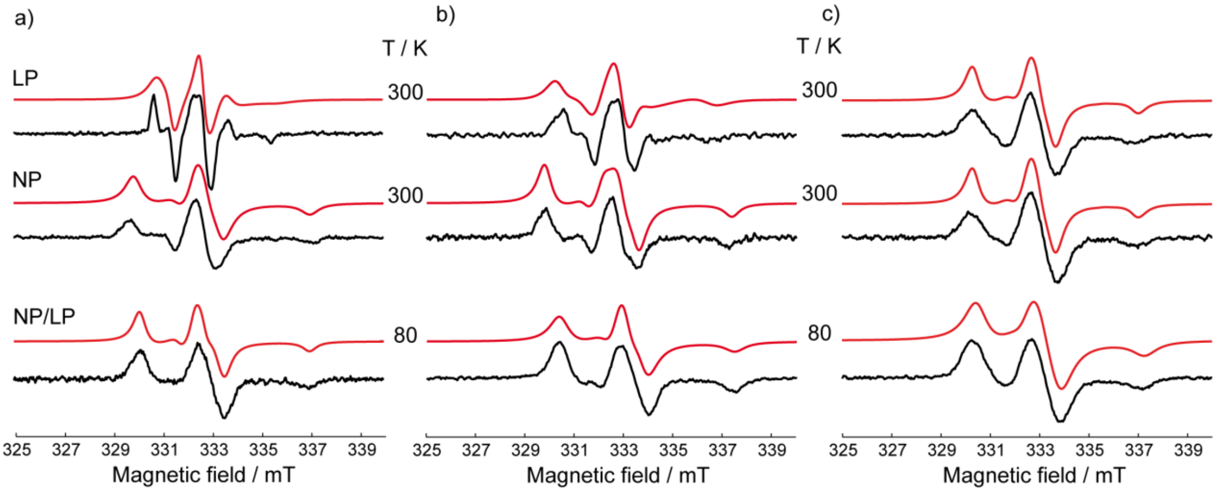

Fig.2. X-band EPR (ν_{mw}≈9.7 GHz) spectra of TEMPO derivatives in MIL-53(Al) prepared with impregnation method (a) TEMPONE (b) TEMPOL (c) 4-acetamido-TEMPO. All spectra are normalized. Simulations are shown in red.

Room-temperature spectra of TEMPONE and TEMPOL in MIL-53(Al) strongly differ from those at 80 K. Reasonable agreement between simulated and experimental spectra of in LP state was achieved assuming restricted molecular motion of radical (MOMD model). The best agreement for TEMPONE at LP state was obtained using g = [2.009, 2.0067, 2.002] and A = [0.65, 0.53, 3.44] mT, λ =1.0, τ_c = 2.7 ns. In case of TEMPOL simulations yielded g = [2.01, 2.0074, 2.0028] and A = [0.68, 0.59, 3.55] mT, λ = –0.3, τ_c = 7 ns. Shorter value of τ_c found for TEMPONE shows that it is more mobile inside cavity compared to TEMPOL, in good agreement with MD results. Moreover, we calculated the available range of orientations for radicals inside the pores of MIL-53(Al), which gave us the angular distribution function. We got reasonable agreement in shapes of angular distribution and orienting potential for TEMPONE and TEMPOL.

In addition to mobility changes induced by transition from LP to NP state, we examined the changes in magnetic susceptibility of each sample. Second integrals CW EPR spectra of radicals were measured relative to signal of sapphire ring. TEMPONE demonstrates the largest change of magnetic susceptibility ~41%. The same value for TEMPOL is only ~14%, and no changes of magnetic susceptibility for 4-acetamido-TEMPO. Comparing changes of the second integral with the amount of switched compound we conclude that under transition ~93% TEMPONE radicals and ~35% of TEMPOL radicals convert to EPR-silent form. In previous work we supposed that changes in magnetic susceptibility upon LP↔NP conversion refer to formation of hydroxylamine in narrow pores of MIL-53(Al). As was shown by EPR and MD above, TEMPONE shows the most appropriate orientation in LP state, and thus during structural transition it is more likely to be trapped with orientation favoring the interaction of NO group with μ_2-hydroxo group of MIL-53(Al). The preferred orientation for TEMPOL less promotes interaction of NO group with μ_2-hydroxo group, resulting in the smaller fraction of EPR-silent hydroxylamine formed in NP state. If we take into account our previous results on unsubstituted TEMPO, its angular distribution in LP state of MIL-53(Al) is in intermediate state between TEMPONE and TEMPOL. This again perfectly correlates with the amount of radicals converted to hydroxylamines in NP state (~66%).

Conclusions

In this work we have studied the guest-host interactions between “breathing” MOF MIL-53(Al) and series of nitroxides adsorbed into its pores. We implemented MD simulations and experimental/theoretical X-band EPR studies to address mobility and reactivity of three derivatives of TEMPO, namely TEMPONE, TEMPOL and 4-acetamido-TEMPO. We have found a clear correlation between the angular distribution of this series of nitroxides and their ability to form complexes with μ_2-hydroxo groups of MIL-53(Al), and previous study on unsubstituted TEMPO perfectly agrees with this correlation [1].

Acknowledgement

This work was supported by the Russian Foundation for Basic Research (No. 14-03-00224) and the RF President’s Grant (MD-276.2014.3).

References

[1] Sheveleva, A. M.; Kolokolov, D. I; et al. // J. Phys. Chem. Lett. **2014**, 5, 20−24

[2] Zhou, H. C.; Long, J. R.; Yaghi, O. M. // Chem. Rev. **2012**, 112, 673-674.

[3] Yue, Y. F.; et al. // J. Phys. Chem. C **2015**, 119, 9442-9449.

[4] Liu, Y.; Her, J. H.; Dailly, A.; et al. // J. Am. Chem. Soc. **2008**, 130, 11813-11818

[5] Loiseau, T.; Serre, C.; Huguenard, C.; et al. // Chem. Eur. J. **2004**, 10, 1373-1382.

[6] Stoll, S.; Schweiger, A., // Epr. J. Magn. Reson. **2006**, 178, 42-55.

New experimental method of measurement of ESR oscillating magnetization value in strongly-correlated metals

M.I. Gilmanov[1,2], A.V. Semeno[1], A.N. Samarin[1,2], S.V. Demishev[1,2]

[1]Prokhorov General Physics Institute of RAS, 38 Vavilov str., 119991 Moscow, Russia
Moscow Institute of Physics and Technology, 9 Institutskiy per., 141700 Dolgoprudny, Moscow region, Russia

e-mail: wlesavo@gmail.com

Oscillating magnetization is a number of magnetic moments that participate in magnetic resonance and its determination is one of the important and nontrivial problems in electron spin resonance (ESR) experiments. Here we report a direct experimental method of measurement of the oscillating magnetization in metallic samples. In the base of our method lie measurements of ESR in two different geometries: Faraday's and Voigt's (Fig.1). The position of the resonance in these two cases depends differently on the oscillating magnetization: $\omega_0 = \gamma(H_1 + 4\pi M_0)$ and $\omega_0^2 = \gamma^2 H_2 (H_2 + 4\pi M_0)(1 + a^2)$ in Faraday and Voigt geometries respectively. Here ω_0 and H_1, H_2 — resonance frequency and fields, M_0 — magnetization and a for a dissipation coefficient. This difference in resonance position is strong enough to precisely calculate the value of oscillating magnetization.

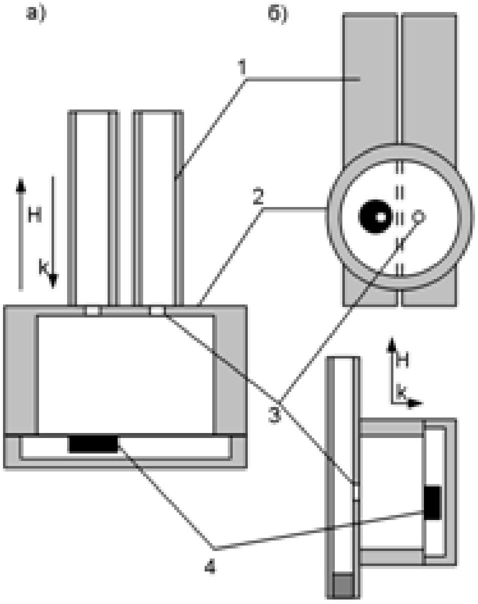

Fig.1. Faraday's (a) and Voigt's (b) geometries of ESR experiment.
1 – waveguides,
2 – cylindrical resonator,
3 – communication holes,
4 – sample on thin cupper.

Presented technique was applied on two strongly-correlated metallic systems: EuB_6 and CeB_6. Received values of oscillating magnetization was equal 920 Oe for EuB_6 at $T = 4.2$ K and 96 Oe for CeB_6 at $T = 1.8$ K which are in a good agreement with quantities obtained by different methods [1, 2].

This work was supported by Programmes of Russian Academy of Sciences "Electron spin resonance, spin-dependent electronic effects and spin technologies", "Electron correlations in strongly interacting systems".

References

[1] A.V. Semeno, V.V. Glushkov, A.V. Bogach, N.E. Sluchanko, A.V. Dukhnenko, V.B. Fillippov, N.Yu. Shitsevalova and S.V. Demishev, Physical Review B, 79, 014423, 2009

[2] S.V. Demishev, A.V. Semeno, A.V. Bogach, N.A. Samarin, T.V. Ishchenko, V.B. Filipov, N.Yu. Shitsevalova and N.E. Sluchanko, Physical Review B, 80, 245106, 2009

^{55}Mn NMR study of magnetic inhomogeneities in cubic perovskite-type manganite $Sr_{0.98}La_{0.02}MnO_3$

A. Germov[1], K. Mikhalev[1], A. Korolev[1], E. Konstantinova[2], I. Leonidov[2]

[1]Institute of Metal Physics, Ural Branch of the Russian Academy of Sciences, 620990,
S. Kovalevskaya st. 18, Yekaterinburg, Russian Federation.

[2]Institute of Solid State Chemistry, Ural Branch of the Russian Academy of Sciences, 620990,
Pervomaiskaya st. 91, Yekaterinburg, Russian Federation.

e-mail: germov@imp.uran.ru

Introduction

The manganese perovskites derived from $SrMnO_3$ exhibit very interesting magnetic and transport properties including a colossal magnetoresistance which makes them attractive for applications. Recently, the transition from insulator to metal state has been discovered in lightly electron-doped cubic single crystal manganites [1]. The metal state has been considering in the model of double exchange homogeneous G-type antiferromagnetic metal with a tiny spin canting. However, the most up to date experimental data evidence for doped manganites to be a phase separated magnetic compounds [2, 3, 4]. One of the most convenient and reliable method to investigate the magnetic state of these compounds is nuclear magnetic resonance (NMR).

Experimental results and discussion

We have obtained the NMR spectra of ^{55}Mn in electron-doped cubic polycrystalline manganite $Sr_{0.98}La_{0.02}MnO_3$ in zero magnetic field at the temperature range from 4 K to 255 K. The dependencies of magnetic susceptibility versus temperature and magnetic field have been measured as well.

The NMR spectra (fig.1) demonstrate two different lines. High intensity (AFM) line ($\nu_{L,AFM}$ = 264 MHz) is referred to signal from Mn^{4+} ions which form G-type

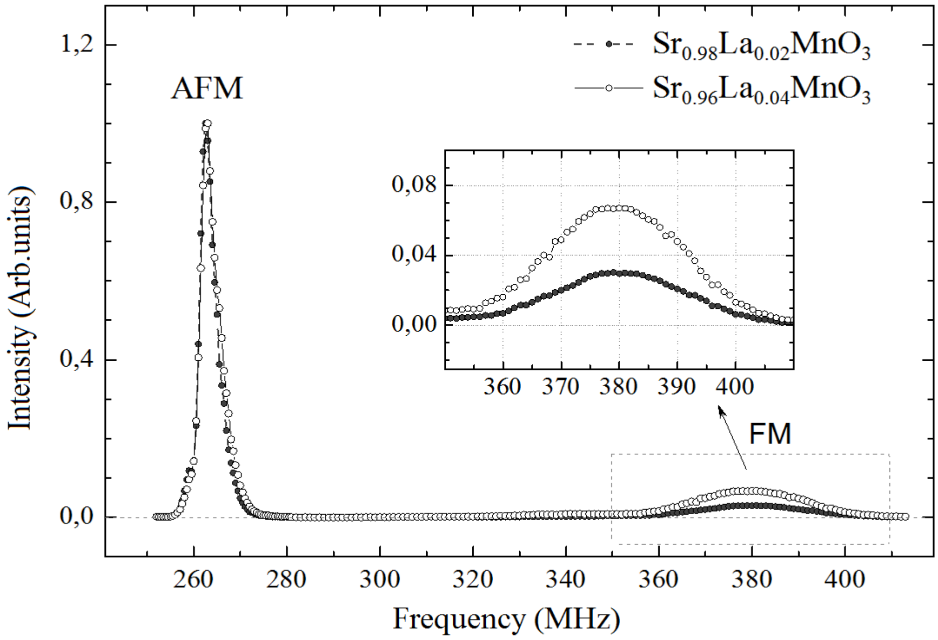

Fig.1. ^{55}Mn NMR spectra of $Sr_{1-x}La_xMnO_3$: x = 0.02; 0.04 in zero magnetic field at 4 K.

antiferromagnetic ordering at these manganites [2, 5]. Shifted to high frequency range ($\nu_{L,FM}$ = 380 MHz) low intensity (FM) line is related to ferromagnetic clusters [2, 5]. Additionally, the spectra of a higher doping concentration compounds are given. It could be expected that spin canting depends on the concentration of La. It should lead to shift of AFM line because of change in distribution of local fields. But both lines have maximum at the same frequency (264 MHz). It proves that spin canting does not occur. These facts are evidence for inhomogeneous magnetic state which consists of antiferromagnetic phase and ferromagnetic clusters.

It is worth noting that intensity of FM line grows in 2 times with 2-fold increasing of doping level (insertion in fig.1). It corresponds to the increasing of the volume part of ferromagnetic regions.

Both lines at the spectra are shifted to low frequency range with decreasing temperature (fig.2), whereas the FM line is still visible up to 255 K. Estimates of the temperature dependencies of relative shifts give values of the Neel temperature T_N = 237(10) K and the Curie temperature T_C = 321(30) K. The obtained results are consistent with our measurements of magnetic susceptibility. The results prove the existence of ferromagnetic clusters above the Neel temperature.

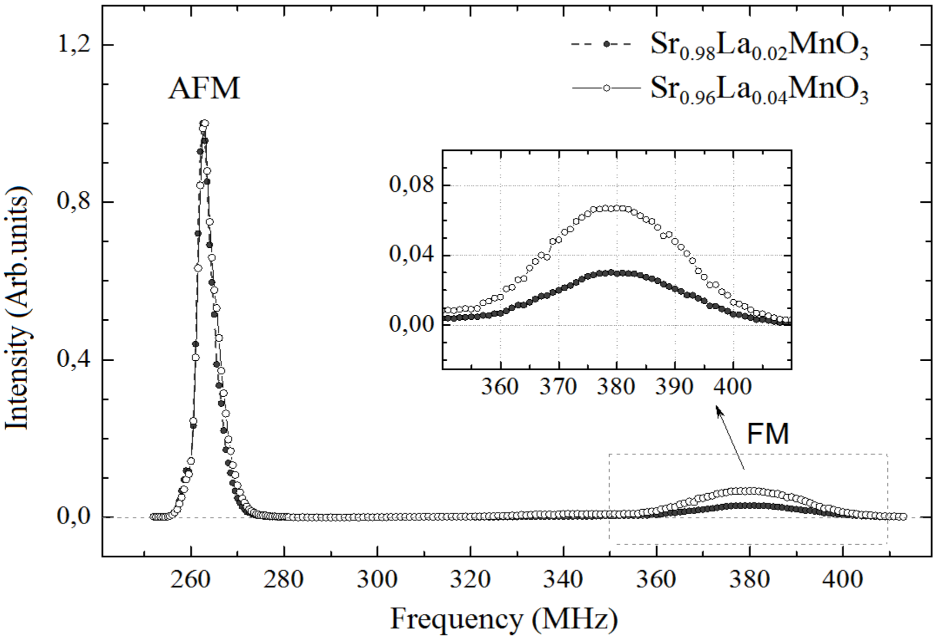

Fig.2. Temperature dependencies of the relative shifts of Larmor frequencies $\nu_L(T)/\nu_{L,max}$ of the AFM (●) and FM (○) lines from fig.1.

The temperature dependence of a full width at half maximum (width) is given on fig.3. It can be seen that the width of the FM line greatly exceed that of the AFM line. It could be connected with different distribution of induced local fields on Mn ions. The width of both lines remains unchanged at low temperatures. It increases from 4 MHz to 8 MHz for the AFM line with increasing temperature. Apparently, a small growth of the AFM line width connected with the distribution of the Neel temperature in polycrystalline sample.

For the FM line, the width decreases to the same value as the temperature increases. Interesting behavior of the FM line above T = 77 K should be associated with the motion of the FM clusters within the volume of the sample, with considering Mn ions are motionless. The motion leads to averaging of local induced fields resulting in decreasing of the line width.

The dynamic nature of FM regions allows using magnetic polaron model to describe the magnetic state of the manganite.

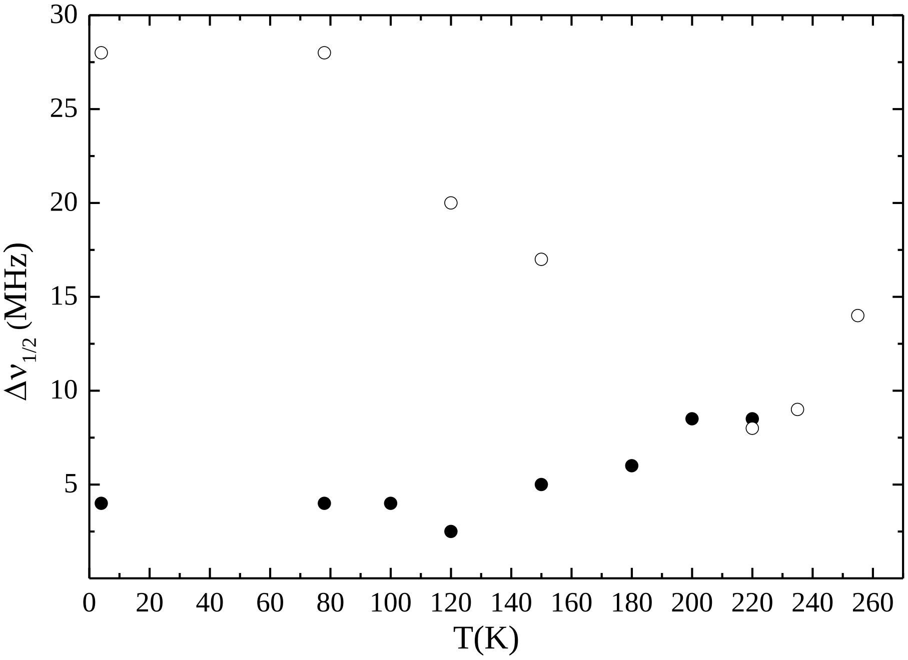

Fig.3. Temperature dependence of full width at half maximum for AFM (●) and FM (○) lines of the ^{55}Mn NMR spectra of $Sr_{0.98}La_{0.02}MnO_3$.

It has been shown that there is a microscopic phase separation to an antiferromagnetic matrix and ferromagnetic clusters. Quantitative estimates of the Neel temperature of antiferromagnetic phase and the Curie temperature of the ferromagnetic clusters have been obtained.

Acknowledgements

This study is supported by the project of fundamental researches of the Ural Branch of the Russian Academy of Sciences № 15-9-2-49 in the assignment of the state program «Spin» № 01201463330.

References

[1] H. Sakai, S. Ishiwata, D. Okuyama, A. Nakao, H. Nakao, Y. Murakami, Y. Taguchi, and Y. Tokura, Phys.Rev.B. **82,** 180409 (2010).

[2] E. Dagotto, T. Hotta, A. Moreo, Phys. Rep. **344**, 1 (2001).

[3] E. Nagaev, Phys. Rep. **346**, 387 (2001).

[4] K. Mikhalev, Z. Volkova, A. Gerashenko, The Physics of Metals and Metallography. **115**, 1139 (2014).

[5] G. Matsumoto. J, of Phys. Soc. Jpn. **29**, 606 (1970).

Low temperature ESR in spin ladder with uniform Dzyaloshinskii-Moriya interaction

Yu.V. Krasnikova[1,2], V.N. Glazkov[1,2], M.A. Fayzullin[3], D. Schmidiger[4], A. Zheludev[4]

[1]P.L. Kapitza Institute for Physical Problems RAS, 119334, Kosygin str. 2, Moscow, Russia
[2]Moscow Institute of Physics and Technology, 141700, Dolgoprudny, Russia
[3]Kazan Federal University, 420008, Kremlyovskaya str. 18, Kazan, Russia
[4]Neutron Scattering and Magnetism, Laboratory for Solid State Physics, ETH Zurich, 8006, Zurich, Switzerland

e-mail:krasnikova.mipt@gmail.com

Studying of low dimensional spin systems is hot topic nowadays. Spin ladder is one of the model low dimensional systems. It consists of two antiferromagnetic spin chains bounded by antiferromagnetic exchange interaction, chains form ‘legs’ of the ladder and interchain bonds form ‘rungs’ (fig.1). Heisenberg spin ladder is fully described by two constants: intrachain coupling J_{leg} and interchain coupling J_{rung}. For any nonzero J_{rung} there is a gap between the singlet ($S = 0$) ground state and the exited triplet ($S = 1$) states. Compound $(C_7H_{10}N_2)_2CuBr_4$ (DIMPY for short) can be described by spin ladder model. Exchange couplings constants and value of gap were determined by neutron scattering methods [1, 2]: $J_{leg} = 1.42$ meV, $J_{rung} = 0.82$ meV and the gap is $\Delta = 0.33$ meV. Intrachain exchange coupling dominates and DIMPY is a rare example of the strong-leg ladder with very weak anisotropic interactions.

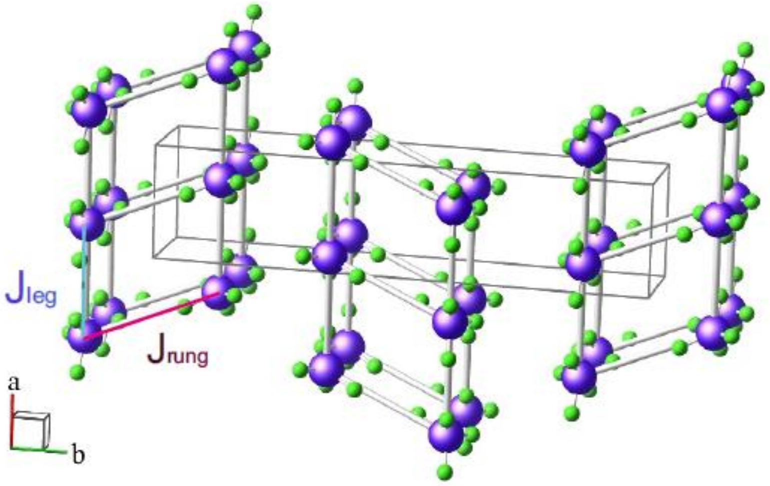

Fig.1. Crystallographic structure of $(C_7H_{10}N_2)_2CuBr_4$ (DIMPY) with two magnetically nonequivalent spin ladders. Big labels (purple) are Cu ions, small labels (green) are Br ions. 2,3-dimethylpyridinium complex is not shown. a, b — crystallographic axes.

There are two types of spin ladders in DIMPY, one differs from another by orientation with respect to crystal axes (fig.1). Dzyaloshinskii-Moriya (DM) interaction is allowed by DIMPY symmetry. Due to the existence of inversion center on the rung of the ladder DM interaction is allowed only along the chains and DM vectors have opposite directions on the legs of the ladder. Along the legs DM interaction is uniform. Uniform DM interaction sometimes leads to nontrivial changes in spectrum of low dimensional magnet [3]. Thus, it is interesting to look for the effects of uniform DM coupling on the properties of spin ladder.

We were studying ESR absorption spectra from 300 K to 450 mK in various magnetic field orientations. The field was up to 12 T and frequencies were from 18 to 105 GHz.

As it was mentioned before, DIMPY has two types of ladders. This results in the appearance of two absorption components in ESR experiment. For low temperature measurements we have chosen field orientation when two types of ladders have the biggest difference between absorption peaks (field applied at 45° from a to b). The temperature dependence of absorption in DIMPY from 26 K to 0.45 K is shown on fig.2. Absorption intensity freezes out below 5 K because of energy gap. At temperature about 1 K we observed additional splitting of components. This splitting was observed for both spectral components at various frequencies (fig.3). Splitting vanishes above the critical field $H_c = \Delta/(g\mu_B)$ (for DIMPY ESR resonance field exceeds H_c at frequencies above 80 GHz). Splitting magnitude is field dependent, it decreases by a factor of two at $H = H_c/2$. Intensities of the split subcomponents are different, both subcomponents freeze out on cooling but characteristic activation energies are different (fig.4).

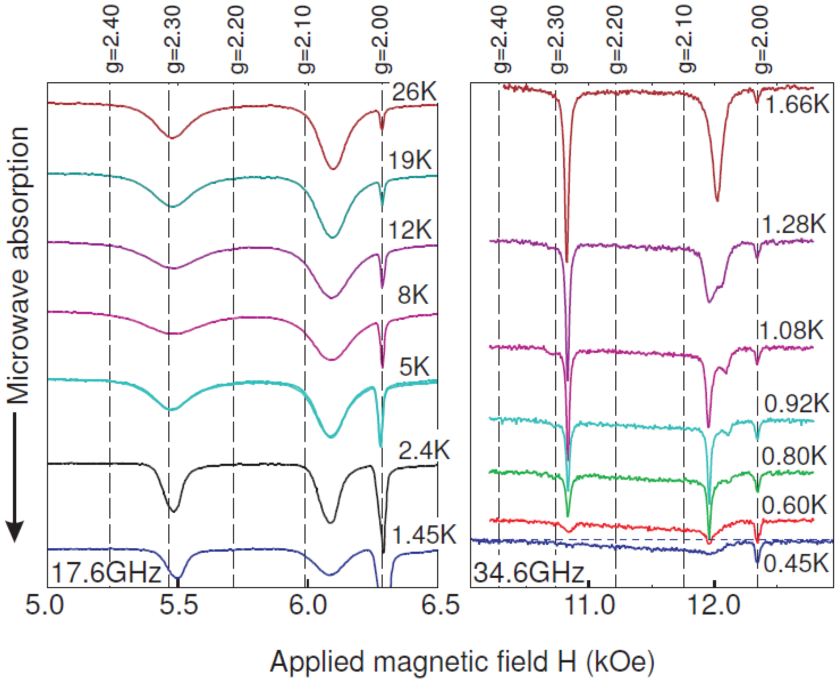

Fig.2. ESR absorption spectra at low temperatures. Vertical dashed lines mark resonance fields corresponding to the shown *g*-factor values. Horizontal dashed line at 0.45 K curve is a guide to the eye at zero absorption level. Narrow absorption line at $g = 2.00$ is a DPPH marker.

Observed splitting of ESR absorption is the effect of zero field splitting of triplet level. Anisotropic spin-spin interactions (DM included) could lift triplet level degeneracy adding anisotropic term like $C_{eff}S_z^2$ to the effective Hamiltonian, here *z* is magnetic field direction. In this case resonance dipolar absorption is observed in the fields $g\mu_B H = \hbar\omega \pm C_{eff}$. It is known that effective anisotropy constant depends on magnetic field orientation and changes sign for the field orthogonal to the anisotropic axis [5]. This explains why weaker subcomponent is located differently for left and right absorption components (fig.3). Difference between activation energy for weak and strong subcomponents is due to the different energies of $S_z = 1$ and $S_z = 0$ triplet sublevels in magnetic field (see inset of fig.4). This conclusion is supported by activation energies' field dependence (fig.4), which can be described model-free using known zero field gap as the only parameter.

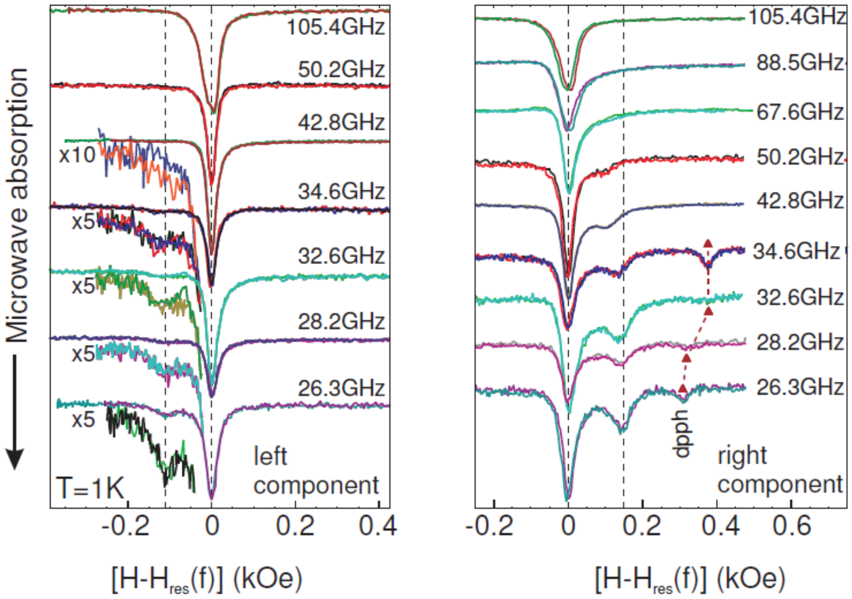

Fig.3. ESR absorption spectra at the temperature $T = 1$ K at different frequencies. All spectra are shifted along the field axis to fit positions of the main absorption subcomponents. Left panel: left absorption component ($g = 2.28$), weak absorption subcomponent is magnified by the factor of 5 or 10 for better presentation. Right panel: right absorption component ($g = 2.05$). Vertical dashed lines mark positions of the absorption subcomponent at lowest frequency. Triangles on the right panel mark position of the DPPH marker absorption ($g = 2.00$).

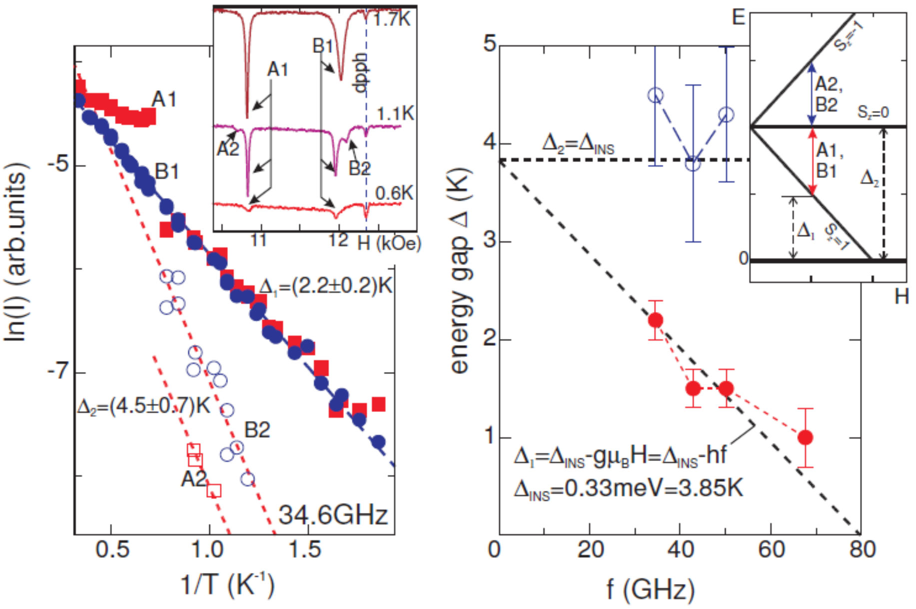

Fig.4. Left panel: temperature dependence of the ESR intensity below 1 K at $f = 34.6$ GHz. Inset: examples of ESR absorption and ESR components and subcomponents notations. Symbols - experimental data, dashed lines - fits with thermoactivation law $I \sim \exp(-\Delta/T)$. Right panel: dependence of the determined activation gaps for different spectral subcomponents. Filled symbols: intense A1 and B1 subcomponents, open symbols — weak A2 and B2 subcomponents. Lines: parameters-free model dependence calculated with the zero-field gap value Δ_{INS} known from the inelastic neutron scattering experiments [2, 4]. Inset: scheme of the energy levels of a spin-gap magnet in a magnetic field. Solid vertical arrows show transitions corresponding to the observed ESR absorption, dashed vertical arrows mark activation gaps for these transitions.

We estimated zero field splitting of the triplet level for model of weakly bounded dimers with uniform DM interaction along the chains. To solve this problem we used perturbation theory. Perturbation operator was DM part of Hamiltonian. We have found that for antiparallel orientation of DM vectors on the legs of the ladder there are no first order corrections. DM term mixes single-particle and two-particle excited states with $S_z = \pm 1$. This result in second order correction to the $S_z = \pm 1$ sublevel $\delta E = -D^2/(2J)$.

Maximal observed subcomponent splitting of 150 Oe corresponds to triplet level zero field splitting of approximately 10 mK. Substituting energy gap $\Delta = 3.4$ K as a measure of characteristic exchange coupling we obtained estimation for DM coupling constant $D \approx 0.2$ K. Similar estimate of DM interaction strength was obtained from the high temperature ESR line width analysis [6].

Thus, our ESR study confirms that DIMPY is indeed an almost perfect Heisenberg spin ladder. However, high energy resolution of ESR technique gives access to fine structure of energy spectrum which is due to anisotropic interactions. We have demonstrated that uniform DM interaction is the main anisotropic interaction in DIMPY.

Acknowledgments

We thank Dr. K. Povarov, Prof. M.V. Eremin and Prof. A.I. Smirnov for valuable and stimulating discussions. The work was supported by Russian Foundation for Basic Research Grant No.15-02-05918, Russian Presidential Grant for the Support of the Leading Scientific Schools No.5517.2014.2. M .F. work was supported by the Russian Government Program of Competitive Growth of Kazan Federal University. This work was partially supported by the Swiss National Science Foundation, Division 2.

References

[1] D. Schmidiger, P. Bouillot, S. Muhlbauer, S. Gvasaliya, C. Kollath, T. Giamarchi, and A. Zheludev Phys. Rev. Lett. 108, 167201 (2012)

[2] D. Schmidiger, S. Muhlbauer, S. N. Gvasaliya, T. Yankova, and A. Zheludev Phys. Rev. B 84, 144421 (2011)

[3] A. I. Smirnov, T. A. Soldatov, K. Yu. Povarov, A. Ya. Shapiro, Phys. Rev. B 91, 174412 (2015)

[4] T. Hong, Y. H. Kim, C. Hotta, Y. Takano, G. Tremelling, M. M. Turnbull, C. P. Landee, H.-J. Kang, N. B. Christensen, K. Lefmann, K. P. Schmidt, G. S. Uhrig, and C. Broholm, Phys. Rev. Lett. 105, 137207 (2010)

[5] S.Al’tshuler, B.Kozyrev, Electron Paramagnetic Resonance, Academic Press (1964)

[6] V.N. Glazkov, M. Fayzullin, Yu. Krasnikova, G. Skoblin, D.Schmidiger, S.Muhlbauer, and A.Zheludev4, arXiv:1507.02503, accepted to PRB

The interaction between transverse and longitudinal resonant modes in polar phase of superfluid ^{3}He

V.V. Dmitriev[1], A.A. Soldatov[1,2], A.N. Yudin[1]

[1]P.L. Kapitza Institute for physical problems of RAS,
119334, Kosygina st. 2, Moscow, Russia
[2]Moscow Institute of Physics and Technology,
141700, Institutskiy per. 9, Dolgoprudny, Russia

e-mail: ark-soldatov@yandex.ru

Depending on external conditions in bulk ^{3}He three superfluid phases exist — A, A_1, B [1]. To investigate the effect of impurities on superfluid ^{3}He high-porosity aerogels are used. First experiments with ^{3}He confined in aerogel were done with isotropic silica aerogel, which has strands with diameter of ~3 nm and distance between strands of ~100 nm. It is established that superfluid phases of ^{3}He in silica aerogel (A-like, A_1-like and B-like) have the same order parameters as A, A_1 and B phases of bulk superfluid ^{3}He. Another type of aerogel which can be used in experiments with ^{3}He is "nematically ordered" aerogel (N-aerogel). It consists of strands which are almost parallel to one another. It was theoretically predicted [2] that in such an aerogel a new superfluid phase can be stable just below the superfluid transition temperature — the polar phase. In the first experiments with ^{3}He in N-aerogel samples of "Obninsk aerogel" consisting of AlOOH strands were used. It was found that in this case the observed A-like and B-like phases have order parameters which correspond to A and B phases with a strong polar distortion [3]. But the existence of the pure polar phase even near the superfluid transition temperature of ^{3}He in aerogel (T_{ca}) was not proved [4]. However, in ^{3}He in nafen [5, 6, 7] — much denser N-aerogel with Al_2O_3 strands — polar phase was clearly observed [8] in wide range of pressures and temperatures below T_{ca} (fig.1).

Here we report the results of experiments with the polar phase at low NMR frequencies, when interaction between transverse and longitudinal resonant modes occurs. Spin dynamics of superfluid ^{3}He is described by Leggett equations [1]. From these equations we have derived the following continuous wave (CW) NMR spectrum of the polar phase:

$$\omega_{\pm}^2 = \frac{1}{2}\ \ \omega_L^2 + \Omega_L^2 \pm \sqrt{(\omega_L^2 + \Omega_L^2)^2 - 4\omega_L^2\Omega_L^2 \sin^2\varphi}\ \ , \tag{1}$$

where φ is an angle between the external steady magnetic field H and the aerogel anisotropy axis ς, Ω_L is the Leggett frequency of the polar phase $\Omega_L = \Omega_L(P, T)$, $\Omega_L(P, T_{ca}) = 0$, $\Omega_L(P, T)$ is maximal at zero temperature) and $\omega_L = \gamma H$ is the Larmor frequency. From fig.2 the so-called repulsion effect is clearly seen. Two resonant modes — transverse ($\omega = \gamma H$) and longitudinal ($\omega = \Omega_L$) transform due to mutual interaction into two nonintersecting branches — high-frequency branch ω_+ and low-frequency branch ω_- — according to eq. (1).

We carried out CW NMR experiments with ^{3}He in nafen-243 at angles φ in range of 70° ÷ 90°. We applied a steady magnetic field $H_{\parallel}$ (along ς) and swept $H_{\perp}$ (transverse to ς) so that $H_{\parallel}/H_{\perp} = \mathrm{tg}\ \varphi \neq \mathrm{const}$ during the experiment. For this case eq. (1) can be rewritten in terms of $H_{\parallel}$ and $H_{\perp}$:

$$\gamma H_{\perp}\ \ ^2 = \omega^2\left[1 - \ \gamma H_{\parallel}\ \ ^2 /\ \ \omega^2 - \Omega_L^2\ \ \right], \tag{2}$$

where ω is the NMR frequency.

We found that results of CW NMR experiments at $\varphi \approx 70°$ are in good agreement with theory (fig.3).

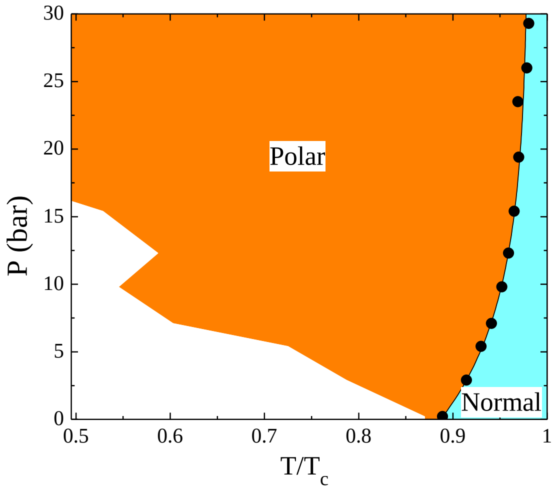

Fig.1. Phase diagram of ^{3}He in nafen sample with density 243 mg/cm^3 (nafen-243) [8]. The *x*-axis represents the temperature normalized to the superfluid transition temperature in bulk ^{3}He.

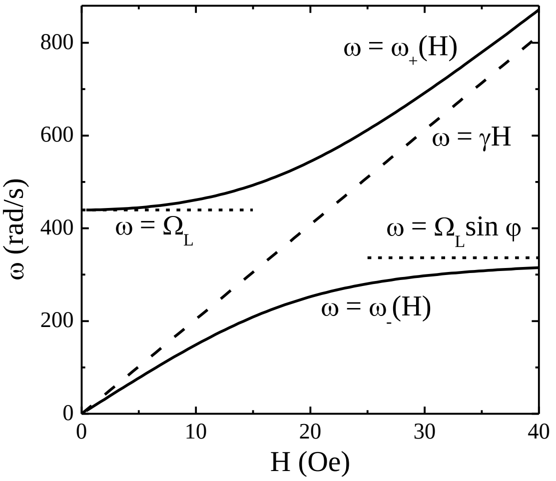

Fig.2. Frequency-field dependence of NMR resonance in polar phase according to eq. (1). $\Omega_L/2\pi = 70$ kHz, $\varphi = 50°$, $\gamma = 20376$ rad/(s·Oe). Dashed line is NMR of free ^{3}He atom. Short-dashed lines are asymptotes.

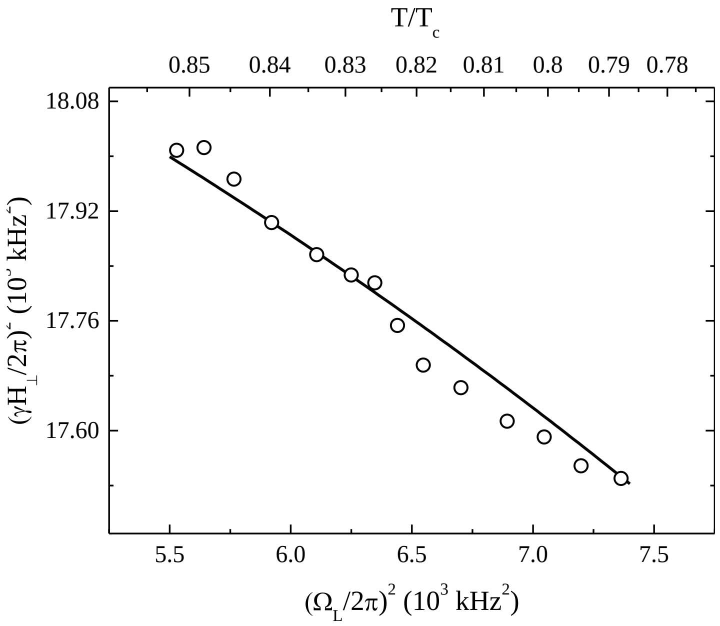

Fig.3. CW NMR transverse magnetic field as a function of Leggett frequency in polar phase (lower scale) and temperature (upper scale). Open circles are experimental data at P =29.3 bar, $\omega/2\pi = 146.8$ kHz, $H_{\parallel} \approx 16$ Oe, $H_{\perp} \approx 41$ Oe so that $\varphi \approx 70°$. Solid curve is a fit by Eq. (2) with a single fit parameter of $H_{\parallel}$. Temperature dependence of Ω_L was determined in experiments at $\varphi = 0°$.

We also have done experiments at $\varphi \approx 90°$ (fig.4). At the lowest temperatures NMR line is clearly observed that corresponds to low frequency resonance mode where $\Omega_L > \omega$. On warming small negative shift appears. This is due to that φ is not precisely equal to 90° in our experiment. At $\Omega_L \approx \omega$ the NMR signal almost disappears. Then it appears again, but with the positive shift from the Larmor frequency. On further warming the shift tends to 0. The temperature dependence of the CW NMR peak position is shown in fig.5.

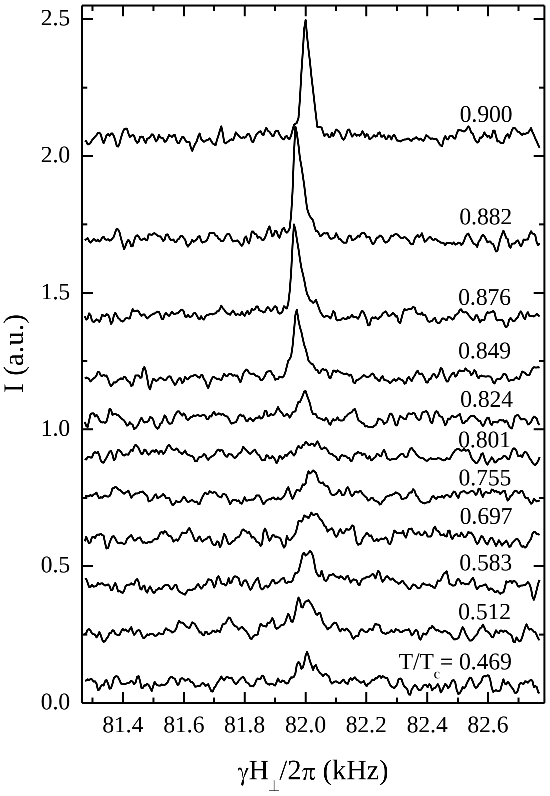

Fig.4. Absorption lines of transverse CW NMR on warming in polar phase.
P =29.3 bar, $\omega/2\pi$ = 82 kHz, $H \approx 25$ Oe, φ=(90±0.5)°.

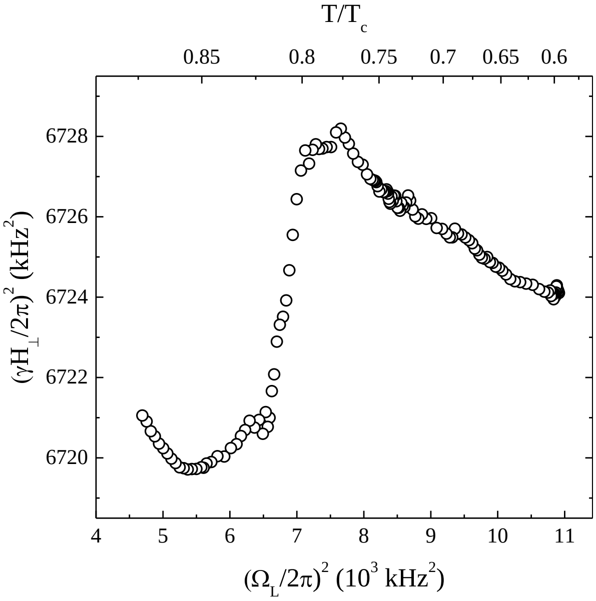

Fig.5. CW NMR transverse magnetic field as a function of the Leggett frequency in the polar phase (lower scale) and the normalized temperature (upper scale). Raw data was averaged by 10 subsequent NMR lines. P = 29.3 bar, ω/2π = 82 kHz, $H \approx 25$ Oe, $\varphi = 90 \pm 0.5$ °.

References

[1] D. Vollhardt and P. Wölfle, The Superfluid Phases of Helium 3 (Taylor & Francis, 1990).

[2] K. Aoyama and R. Ikeda, Phys. Rev. B **73**, 060504 (2006).

[3] R.Sh. Askhadullin, V.V. Dmitriev, D.A. Krasnikhin, *et al.*, JETP Lett. **95**, 326 (2012).

[4] R.Sh. Askhadullin, V.V. Dmitriev, P.N. Martynov, *et al.*, JETP Lett. **100**, 662 (2014).

[5] V.E. Asadchikov, R.Sh. Askhadullin, V.V. Volkov, *et al.*, JETP Lett. **101**, 613 (2015).

[6] http://www.nafen.eu

[7] V.V. Dmitriev, L.A. Melnikovsky, A.A. Senin, *et al.*, JETP Lett. **101**, 808 (2015).

[8] V.V. Dmitriev, A.A. Senin, A.A. Soldatov, and A.N. Yudin, arXiv:1507.04275 (to be published in Phys. Rev. Lett., 2015).

Charge recombination kinetics in P3HT/PC$_{60}$BM/5CB blend studied by light-induced EPR

D.A. Nevostruev[1,2], E.A. Lukina[1,2], A.G. Matveeva[1,2], L.V. Kulik[1,2]

[1]Voevodsky Institute of Chemical Kinetics and Combustion of Siberian Branch of Russian Academy of Sciences, Institutskaya 3, Novosibirsk 630090, Russia.

[2]Novosibirsk State University, Pirogova 2, Novosibirsk 630090, Russia.

e-mail: goddan1993@inbox.ru

Introduction

Organic photovoltaic cells (OPC) are promising alternatives to inorganic ones. OPC have a number of positive characteristics: ease of manufacture, low cost, ability to use on any surfaces, flexibility and etc. Active layer of OPC is a composite of conductive polymers and fullerene derivatives [1]. In our case it's poly(3-hexyltiophene) (P3HT) and [6,6]-phenyl-C61-butyric acid methyl ester (PC$_{60}$BM) respectively. In composite materials the presence of two phases with uncontrolled size makes it difficult to understand the mechanism of recombination of persistent charges, because of this we decided to choose 4-cyano-4'-pentylbiphenyl (5CB) as solvent. 5CB is interesting because its structure can be controlled by external influence also P3HT and 5CB are mutually orient relative to each other [2][3]. To compare received data the new sample was prepare and o-terphenyl was used as solvent to get an isotropic media.

In the present work kinetics of light-induced signal decay in the temperature range of 170-300K were obtained, and the models to approximate curves were proposed.

Sample preparation and Experimental session

P3HT and PC$_{60}$BM (weight ratio 1:1) were dissolved in 5CB or o-terphenyl (120mkl). Several freeze-pump-thaw cycles were performed and the tube was sealed. After this, sample was heated to dissolve P3HT and PC$_{60}$BM completely. Before every experiment the sample was heated. To measure light EPR signal the sample was irradiated by halogen lamp. In order to obtain light-induced EPR (LEPR) signal light minus dark EPR spectrum was calculated. To obtain EPR signal decay magnetic field was fixed in the maximum of light-induced CW EPR signal and the light was turned off during the measurement. The decay of this signal is associated with charge recombination [4]. All the measurements were perform on X-band EPR spectrometer Bruker ESP 380.

Table.1. Temperature dependence of 5CB phase state [5].

T, K	Phase state
< 210	Brittle glass
210 – 250	Flexible glass
250 – 298	Crystal
298 – 309	Nematic
> 309	Liquid

Charge recombination mechanisms

3 recombination mechanisms were examined:

1. n-molecular recombination [1], $\frac{N}{N_0} = \left[1 + K_0\left(p-1\right)N_0^{p-1}t\right]^{-\frac{1}{p-1}}$; (1)

2. electron tunneling recombination mechanism. There are 2 cases:

2.1. in liquid state [6], $\frac{n(t)}{n_0}=\left[1+\frac{4}{3}n_0\pi\frac{a^3}{8}\ln^3\left(\frac{t}{\tau_0}\right)\right]^{-1}$; (2)

2.2. in composites [7], $\frac{n(t)}{n_0}=\frac{n_1}{n_0}\left[1+\left(\frac{n_1}{n_0}\right)\frac{\pi}{6}n_0a^3\left\{\ln^3\left(\frac{t}{\tau_0}\right)-\ln^3\left(\frac{t_1}{\tau_0}\right)\right\}\right]^{-1}$; (3)

3. diffusion recombination mechanism accelerated by electron tunneling [8], **(t<τ$_d$)**$\rightarrow \frac{n(t)}{n_0}=\left[1+\frac{4}{3}n_0\pi\frac{a^3}{8}\ln^3\left(\frac{t}{\tau_0}\right)\right]^{-1}$; **(t>τ$_d$)**$\rightarrow \frac{n(t)}{n_0}=\left[1+n_0\left(4\pi RDt+\frac{4}{3}\pi R^3\right)\right]^{-1}$. (4)

Received kinetics were approximated by using eq. 1 ÷ 4.

Results and discussion

P3HT/PC$_{60}$BM/5CB blend. Dark and light EPR signal were measured in wide temperature range from 170 K to 300 K. Probably the dark signal can be observed because of residual oxygen that acts as an electron acceptor.

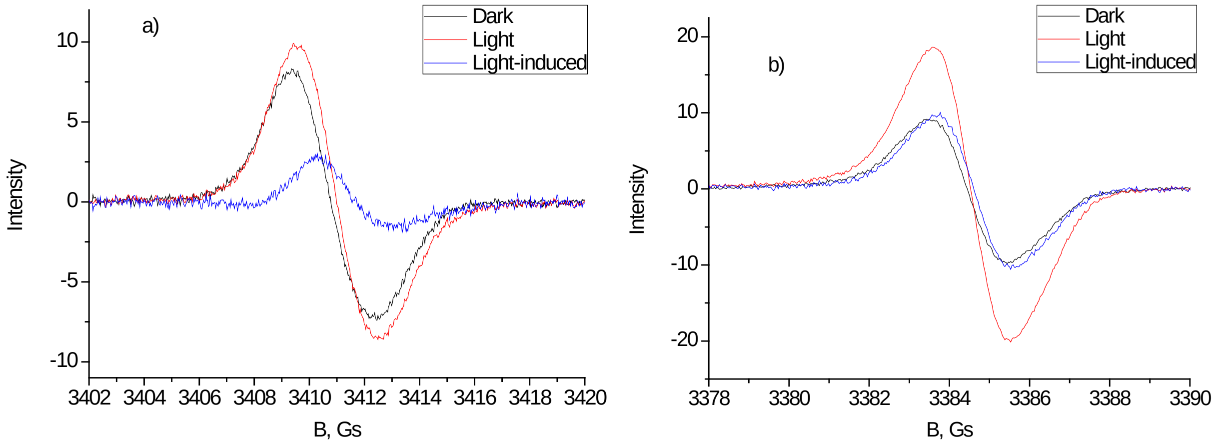

Fig.1. CW spectrum of dark, light and light-induced EPR signal at 170 K (a) and 300 K (b) in P3HT/PC$_{60}$BM/5CB blend.

To simplify the approximation of kinetics the eq. (2) can be present in form $y=\left[1+c\ln^3(x/t)\right]^{-1}$ (2') and eq. (4) → at **(t<τ$_d$)** in form $y=\left[1+c\ln^3(x/t)\right]^{-1}$, at **(t>τ$_d$)** in form $y=\left[1+Sx+V\right]^{-1}$ (4'). At low temperatures (fig.2a), there is a rapidly decreasing component ($t < 30$ s) and long one. With increasing temperature, the contribution of this rapidly decreasing component is reducing and the kinetics can be described very well by eq. (2'). It is interesting to note that during the transition from $T = 250$ K to $T = 260$ K the shape of kinetics radically change , it is caused by phase transition of 5CB (from flexible glass state to crystalline one) and, likely, the diffusion of charge carriers become significant. Long smooth curves were obtained at higher temperature (fig.2b), also recombination rate decreases while temperature increases. These kinetics can be approximated by eq. (4') rather to eq. (2'). Unfortunately, kinetics at $T = 260 \div 270$ K cannot be fitted by eq. (2') or eq. (4'). It must be noted that all curves were approximated by eq. (1) and eq. (3), but these treatments did not produce good fitting and will not be discussed further.

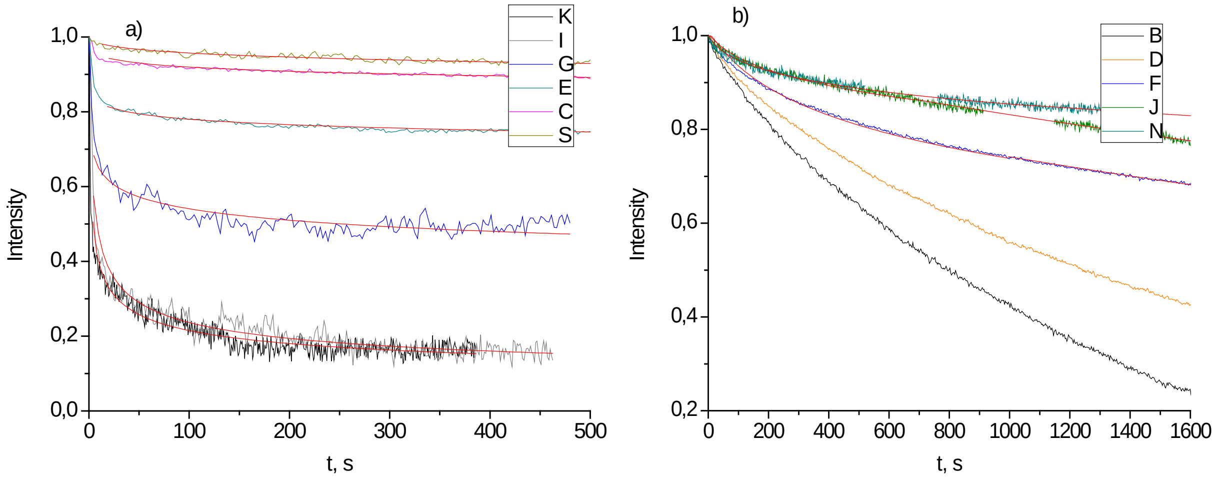

Fig.2. Kinetics of light-induced signal decay in P3HT/PC$_{60}$BM/5CB blend at 200 ÷ 250 K (a) and 260 ÷ 300 K (b) and their approximation by eq. (2') and eq. (4') respectively.

From eq. (2) for kinetics at $T = 185 \div 250$ K the parameters a and can be obtained (a — effective localization radius, τ_0^{-1} — attempt to recombine frequency, although the exact meaning is unknown).

Table.2. Temperature dependence of and a.

T, K	,s	a, nm	T, K	,s	a, nm
185	$3{,}35\cdot10^{-2}$	5,9	**230**	$1{,}75\cdot10^{-9}$	1,1
200	$1{,}09\cdot10^{-2}$	4,8	**240**	$7{,}64\cdot10^{-5}$	0,5
210	$3{,}73\cdot10^{-2}$	5,7	**250**	$2{,}47\cdot10^{-2}$	0,9
220	$6{,}26\cdot10^{-6}$	1,7			

The dramatic changes in parameter values can be seen at $T = 210 \div 220$ K, it is associated with another phase transition of 5CB (from brittle glass state to flexible one).

P3HT/PC$_{60}$BM/o-terphenyl blend. It can be seen on fig.3a that there are two peaks of P3HT$^+$ and PC60BM$^-$, but at higher temperature (fig.3b) there is the only one peak. Probably, disappearance of the PC$_{60}$BM$^-$-peak is caused by reducing of T2-relaxation time with increasing temperature. Further, kinetics of the PC$_{60}$BM$^-$ signal decay will not be discussed.

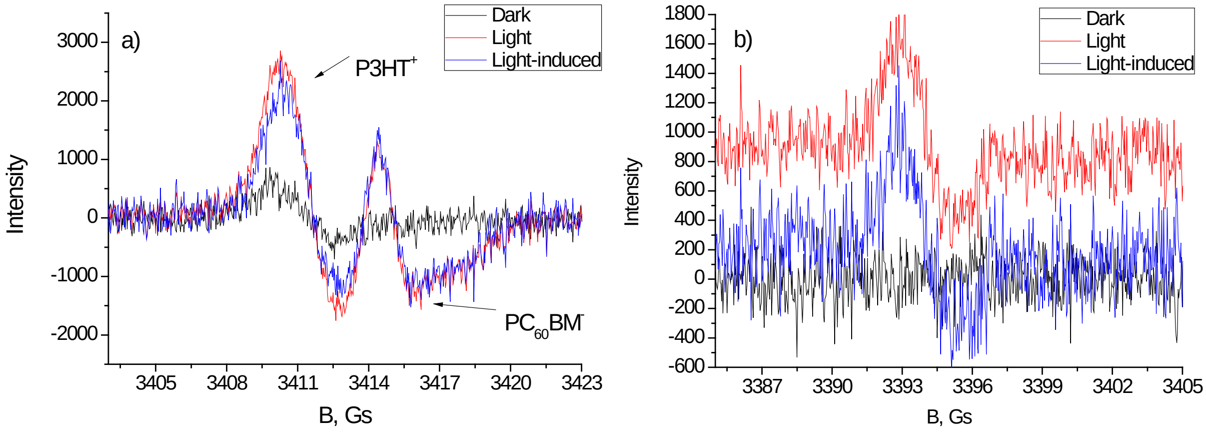

Fig.3. CW spectrum of dark, light and light-induced EPR signal at 177 K (a) and 252 K (b) in P3HT/PC$_{60}$BM/o-terphenyl blend.

At T = 177 K curve can be fitted by eq. (2') and at higher temperature only by using eq. (4'), probably, because diffusion of charge carriers become significant (fig.4).

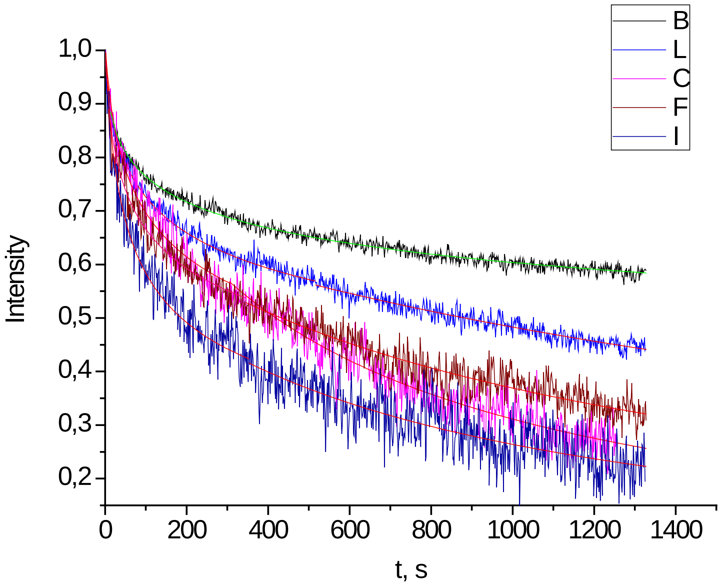

Fig.4. Kinetics of light-induced signal decay (P3HT$^+$) and their approximation by eq. (2) (green line) and eq. (4) (red line) in P3HT/PC$_{60}$BM/o-terphenyl blend.

Conclusion

LEPR signal in P3HT/PC$_{60}$BM/(5CB or o-terphenyl) was observed in wide temperature range. Charge recombination in P3HT/PC$_{60}$BM/5CB blend was described by eq. (2) and eq. (4) depending on phase state of 5CB and temperature; in P3HT/PC$_{60}$BM/o-terphenyl blend was described by the same equations depending only on temperature. The presence of phase transitions was confirmed.

References

[1] Lukina E.A., Uvarov M.N., Kulik L.V., J. Phys. Chem. C 2014, 118, 18307−18314.

[2] J. Seo, S. Park, S. Nam, H. Kim, Y. Kim, Scientific reports, 2013.

[3] S. Watanabe, Appl. Phys. Lett. 96, 173302 (2010).

[4] Marumoto, K.; Muramatsu, Y.; Kuroda, S. Appl. Phys. Lett. 2004, 84, 1317−1319.

[5] George W. Smith, International Journal of Modern Physics B, 7, 25 (1993) 4187 –4213.

[6] В.Н. Пармон, Р.Ф. Хайрутдинов, К.И. Замараев, Физ. тверд. Тела, 16, 2572 (1974).

[7] N.A. Schultz, M.C. Scharber, C.J. Brabec, N.S. Sariciftci, Physical Review B, 2001.

[8] Р.Ф. Хайрутдинов, Химия высоких энергий, 1976.

High frequency electron spin resonance in $Eu_{1-x}Gd_xB_6$ and $Eu_{1-x}Ca_xB_6$

A.N. Samarin[1,2], A.V. Semeno[1], V.V. Glushkov[1,2], M.A. Anisimov[1], M.I. Gilmanov[1,2], S.V. Demishev[1]

[1]Prokhorov General Physics Institute of RAS, Vavilova st. 38, 119991 Moscow, Russia
[2]Moscow Institute of Physics and Technology, 9 Institutskiy per., 141700 Dolgoprudny, Russia

e-mail: sasha@lt.gpi.ru

In the present work we report the results of the systematic study of high frequency (60 GHz) low temperature (1.8 – 50 K) electron spin resonance (ESR) in $Eu_{1-x}Gd_xB_6$ and $Eu_{1-x}Ca_xB_6$ solid solutions in the concentration ranges $x < 0.04$ (for Gd) and $x < 0.24$ (for Ca). The applied original experimental technique [1] allowed us to exclude demagnetization effects leading to ESR line splitting.

For studying of the ESR in $Eu_{1-x}Gd_xB_6$ and $Eu_{1-x}Ca_xB_6$, we have used original line shape analysis method which allows finding full set of spectroscopic parameters including oscillating magnetization M_0, g-factor and line width W. It is found that small increase of the concentration of Gd (up to $x = 0.01$) or Ca (up to $x = 0.1$) suppresses the anomalous low temperature broadening of the line width (fig.1). Subsequent increase of x leads to the growth of the ESR line width in the whole temperature range.

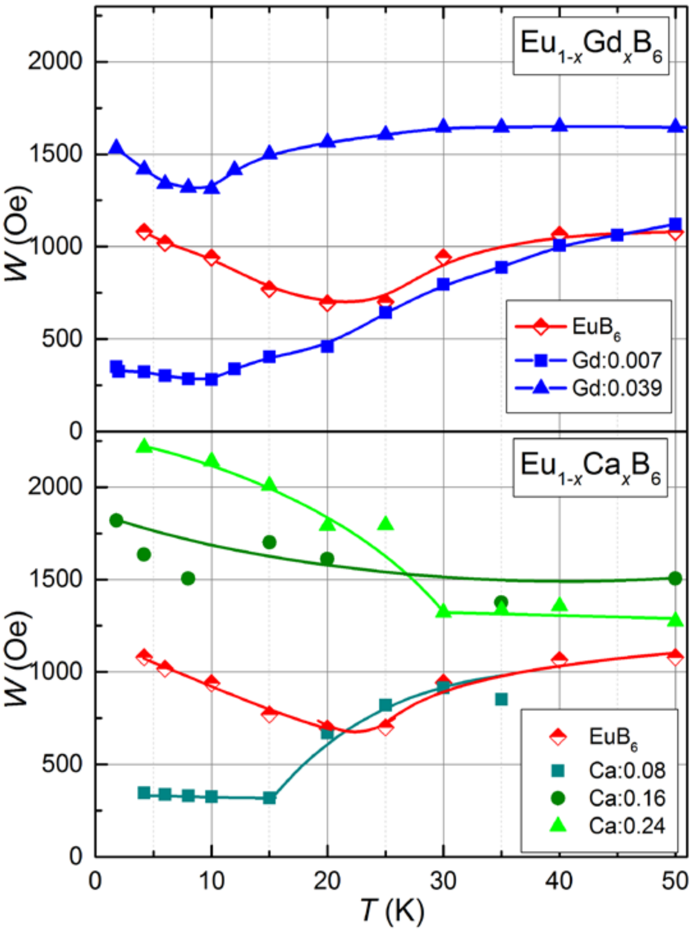

Fig.1. Temperature dependencies of ESR line width in $Eu_{1-x}Gd_xB_6$ (top) and $Eu_{1-x}Ca_xB_6$ (bottom)

In the case of $Eu_{1-x}Ca_xB_6$ the imaginary part of the complex sample conductivity becomes significant, which requires modification of the data analysis method used for $Eu_{1-x}Gd_xB_6$. The simultaneous accounting of the complex magnetic susceptibility and complex conductivity allowed extracting not only spin relaxation time but also transport relaxation time from the ESR line approximation (fig.2).

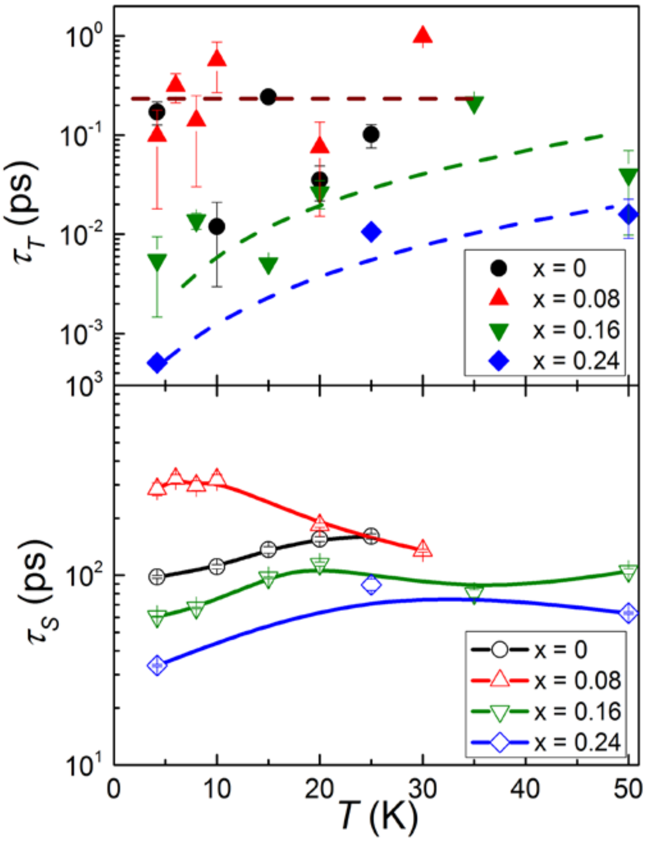

Fig.2. Transport (top) and spin (bottom) relaxation times in $Eu_{1-x}Ca_xB_6$.

This work was supported by the Programes of RAS “Electron spin resonance, spin-dependent electronic effects and spin technologies” and “Electron correlations in strongly interacting systems”.

References

[1] A.V. Semeno, V.V. Glushkov, A.V. Bogach, N.E. Sluchanko, A.V. Dudenko, V.B Fillippov, N.Yu. Shitsevalova, and S.V. Demishev, Phys.Rev.B 79, 014423 (2009)

Ab initio study of exchange interaction in $Lu_2V_2O_7$, $Y_2V_2O_7$

D. Nazipov, A. Nikiforov, V. Chernyshev

Ural Federal University, 620002, Ekaterinburg, Russia

e-mail: qwear0@gmail.com

Magnetic oxides with pyrochlore structure $R_2M_2O_7$ (R — rare-earth ion or Y, M — transition metal ion) are objects of particular attention among researchers owing to their remarkable magnetic properties [1]. Pyrochlore compounds are well known as strongly frustrated materials due to their specific geometric structure. $Lu(Y)_2V_2O_7$ is unusual because of it is a 3d ferromagnetic Mott insulator, contrary to the common belief that ferromagnetism leads usually to metallic behavior [2]. Recently vanadium based compounds $Lu(Y)_2V_2O_7$ have drawn extensive research interest due to discovering of magnon Hall effect [3]. Therefore analysis of microscopic mechanisms of ferromagnetic ordering of V^{4+} ions in pyrochlore lattice is a relevant task at the present time.

In this work first principles study of electron structure and exchange coupling constants in $Lu_2V_2O_7$ and $Y_2V_2O_7$ crystals has been performed in terms of unrestricted Hartree-Fock method [4] using the solid state calculations package CRYSTAL [5]. For O^{2-} and magnetic ion V^{4+} full-electron gauss-type basis set has been used. Rare-earth ion Lu and Y are non-magnetic, thus for their description we have used pseudopotential.

Calculated value of exchange coupling constant is $J = 10.5$ meV and $J = 9.7$ meV for $Lu_2V_2O_7$ and $Y_2V_2O_7$ correspondingly. From ab initio we approved that in investigated compounds collinear ferromagnet structure energetically more favorable than antiferromagnetic states. Using model approach splitting of 3d level of V^{4+} ion in crystal field have been obtained for both investigated compounds in approximation of point charges including spin-orbital interaction. In fig.1 result for $Lu_2V_2O_7$ is presented.

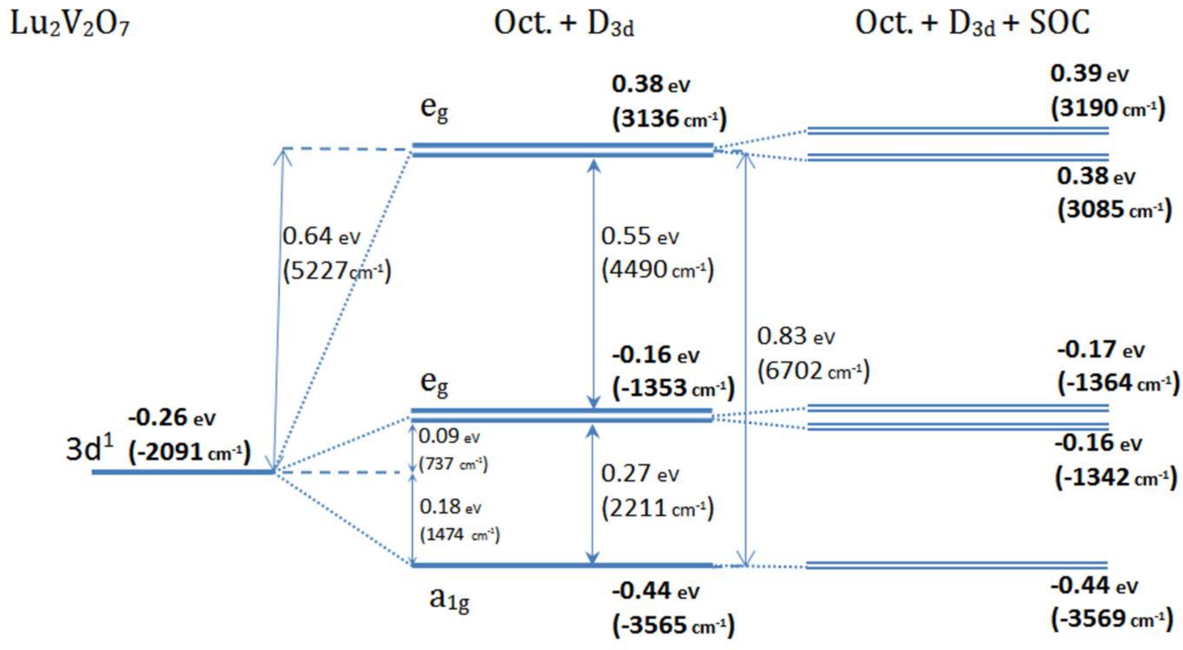

Fig.1. Splitting of $3d^1$ level of V^{4+} ion in crystal field in $Lu_2V_2O_7$

Calculated spin density is also analyzed to investigate the orbital ordering of $Lu(Y)_2V_2O_7$.

Therefore we have obtained the orbital structure of Jahn-Teller ion V^{4+} (t'_{2g}) and isotropic exchange interaction constants for pyrochlore compounds $Lu_2V_2O_7$, $Y_2V_2O_7$.

References

[1] J. S. Garden *et al*, Rev. Mod. Phys. **82**, 53-107 (2010).
[2] S. Shamoto *et al*., J. Phys. Chem. Solids **63**, 1047 (2002).
[3] Y. Onose *et al*, Science **329**, 5989, 297-299 (2010).
[4] M. Towler, R. Dovesi, Phys. Rev. B, **52**, 10150 (1995).
[5] URL: http://www.crystal.unito.it

Analyzing ^{103}Rh NMR shielding in $[Cp^*{}_2Rh_2X_2]_2$ X = Cl, Br, I using spin-free localized molecular orbitals

I.V. Mirzaeva[1], D.A. Mainichev[1,2]

[1]Nikolaev Institute of Inorganic Chemistry SB RAS,
630090, Lavrentiev ave., 3, Novosibirsk, Russia

[2]National Research University Higher School of Economics,
190008, Soyuza Pechatnikov, 16, St.Petersburg, Russia

e-mail: dmitrymainichev@narod.ru

A search for correlations between structure, electronic structure, and NMR parameters of transition metal complexes encounters various problems, for example, great variety of chemical bonding patterns or relativistic effects. Recently, the procedure[1] was developed to decompose the magnetic shielding calculated with two-component relativistic methods into the sum of the individual impacts of natural localized molecular orbitals (NLMOs) based on natural bond orbitals (NBOs) as introduced by Weinhold and coworkers[2]. In this work, we try to analyze ^{103}Rh NMR shieldings in three well known and widely used complexes, $[Cp^*{}_2Rh_2X_2]_2$ X = Cl, Br, I.

Geometry optimization (BLYP/ TZ2P/Scalar ZORA) and calculation of the NMR parameters (BLYP/TZ2P/different level of accounting for relativistic effects) were performed in ADF program suit [3]. NBOs and NLMOs were generated by the NBO5 code[4].

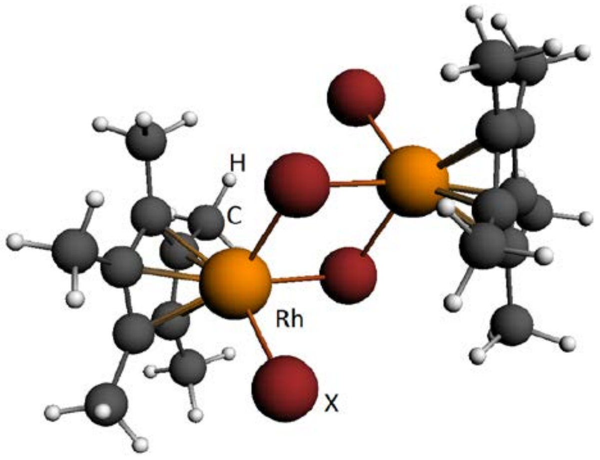

Fig.1. Geometry of $[Cp^*{}_2Rh_2X_2]_2$ X = Cl, Br, I

To compare the results with experimental chemical shifts (δ_{exp}) we need to know the shielding constant of the reference compound (σ_{ref}). From these terms, the calculated chemical shift, δ_{calc}, is obtained as $\sigma_{ref} - \sigma_{calc}$. For rhodium, there is no such a reference compound, therefore we have obtained σ_{ref} from the intercept of the linear correlation between δ_{calc} and δ_{exp}.

To study the impact of relativity effects on the ^{103}Rh shielding, we performed the calculations with three levels: without accounting for relativity effects, with only scalar effects, and with addition of spin-orbit effects (table 1). The spin-orbit coupling contribution to the shielding constant is rather large. However, due to the chemical similarity of the complexes, it is roughly constant for all three systems, therefore, it cancels out in the calculation of the chemical shift.

According to NBO/NLMO analysis, the electronic structure of all three complexes is very similar (table 2). For each Rh atom, there are five three-center Rh-C-C bonds that are quite delocalized; the Rh-X bond to the terminal X atom is classified either as bond orbital with large portion of X contribution, or as delocalized X lone pair. Other valence electrons around Rh are classified as rather localized Rh or X lone pairs (latter represent bonding of Rh to bridging X atoms).

Our calculation method allows to partition the total shielding constant into the diamagnetic and a sum of paramagnetic and spin-orbit terms. The diamagnetic term is generally constant for a given nucleus in different compounds, because it depends mainly on the core-shell electrons, which are not involved in chemical bonding. The sum of paramagnetic and spin-orbit terms also contains a small core impact, but mainly is defined by the Rh lone pairs contribution (table 3).

Table 1. The role of relativistic effects in magnetic shielding (ppm) of ^{103}Rh nucleus in $[\mathrm{Cp^*{}_2Rh_2X_2}]_2$ X = Cl, Br, I

X	δ_{exp} [5]	no relatvity		Scalar ZORA		Spin-Orbit ZORA	
		σ_{calc}	δ_{calc}	σ_{calc}	δ_{calc}	σ_{calc}	δ_{calc}
Cl	2 303	–3 283	2 253	–3 477	2 186	–2 910	2 228
Br	2 068	–3 112	2 082	–3 345	2 054	–2 750	2 068
I	1 426	–2 495	1 465	–2 850	1 559	–2 184	1 502
σ_{ref}		–1 030		–1 291		–682	

Table 2. The list of NLMOs in $[\mathrm{Cp^*{}_2Rh_2X_2}]_2$ X = Cl, Br, I, which are localized around each Rh atom (values in Structure column are averaged over three complexes).

	Structure	Amount
Rh lone pairs	95%Rh d-orbitals	3
Rh-X bond/X lone pair	~20%Rh, ~75%X	1
X lone pairs	99%X p-orbitals	2
Rh-C1-C2 bonds	~40%Rh, ~30%C1, ~20%C2	5

Table 3. NLMOs contributions (ppm) to the paramagnetic+spin-orbit terms of ^{103}Rh shielding.

	Cl	Br	I
Rh core	–306	–252	–216
Rh lone pairs	–6 895	–6 539	–6 272
Rh-X bond	–172	–234	–179
X lone pairs	–313	–307	–331
Rh-C-C bonds	584	424	541

The work was supported by the RFBR grant № 14-03-31333 mol_a.

References

[1] J. Autschbach, J. Chem. Phys. 128 (2008) 164112.

[2] E.D. Glendening, C.R. Landis, F. Weinhold, Wiley Interdiscip. Rev. Comput. Mol. Sci. 2 (2012) 1–42.

[3] ADF: SCM, Vrije Universiteit, Theoretical Chemistry: Amsterdam, The Netherlands, http://www.scm.com, (n.d.).

[4] NBO 5.0,Theoretical chemistry institute, University of Wisconsin, Madison, http://www.chem.wisc.edu/nbo5, (2001).

[5] L. Carlton, Annu. Rep. NMR Spectrosc., 63 (2008) 49–178.

Static and dynamic magnetic properties of quasi-2D Honeycomb lattice tellurates $A_2Ni_2TeO_6$ (A = Li, Na, K)

D.R. Rudovskaya[1], E.A. Zvereva[1], M.I. Stratan[1], V.B. Nalbandyan[2], I.L. Shukaev[2],
A.N. Vasiliev[1]

[1]Faculty of Physics, Moscow State University, 119991, Leninskie Gory, Moscow, Russia
[2]Chemistry Faculty, South Federal University, 344090, Zorge, Rostov-na-Donu, Russia

e-mail: daniya_92@mail.ru

Introduction

Layeredoxidesofalkali and transition metals are presently being intensively investigated due to their potential applications as solid electrolytes and electrode materials in modern ionics as thermoelectric materials and even as superconductors [1].

Here, we report on the static and dynamic magnetic properties of new layered honeycomb lattice oxides $A_2Ni_2TeO_6$ (A = Li, Na, K). Compounds have layered crystal structure: magnetically active mixed cation layers of nickel and tellurium alternate with non-magnetic alkali-metal layers (fig.1).

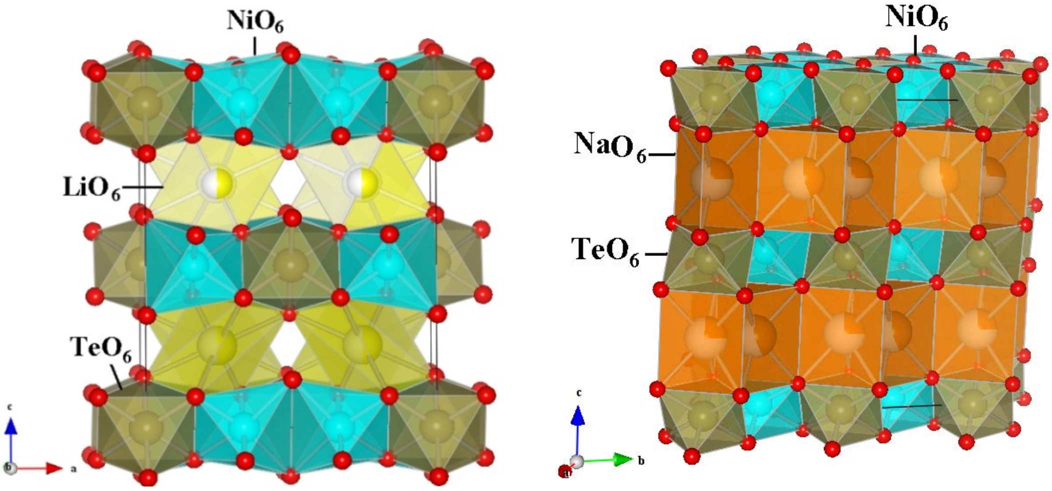

Fig.1. Crystal structure of $Li_2Ni_2TeO_6$– orthorhombic Cmca and $A_2Ni_2TeO_6$ (A = Na, K) – hexagonal P63/mcm.

Experiment

Magnetic andspecific heat measurements were performed by means of a Quantum Design PPMS-9 system. The temperature dependence of the magnetic susceptibility was measured at the magnetic field $B = 0.1$ T in the temperature range 1.8 – 300 K and in applied fields up to 9 T. The isothermal magnetization curves were obtained in static magnetic fields $B \leq 9$ T at $T = 2$ K after cooling the sample in zero magnetic field. Specific heat data were collected at $B = 0$ T and 5 T in the temperature range 2 – 300 K.

Electron spin resonance (ESR) studies were carried out using an X-band ESR spectrometer CMS 8400 (ADANI) ($f = 9.4$ GHz, $B \leq 0.7$ T) equipped with a low-temperature mount, operating in the range $T = 6 – 300$ K. The effective g-factors of our samples have been calculated with respect to an external reference for the resonance field. We used BDPA (*a*,*g* - bisdiphenyline-*b*-phenylallyl) $g_{et} = 2.00359$, as a reference material.

Results

The static and dynamic magnetic properties of $A_2Ni_2TeO_6$ (A = Li, Na, K) are similar for all three samples. The temperature dependence of magnetic susceptibility $\chi(T)$ passes through a maximum indicating an onset of antiferromagnetic (AFM) order at low temperature. The Néel temperature T_N was estimated from the maximum of $d\chi/dT(T)$ and was found to be ~ 25, 27 and 25 K for Li, Na and K sample, respectively.

At high temperatures the magnetic susceptibility nicely follows the Curie-Weiss law with addition of a temperature-independent term. The Curie-Weiss temperature was found to be negative, i.e. $\Theta \sim -24$ K (Li), $\Theta \sim -20$ K (Na) and $\Theta \sim -12$ K (K) indicating predominance of AFM correlations. Upon decrease of the temperature the $\chi(T)$ deviates from the Curie-Weiss law showing increased relevance of AFM interactions upon approaching T_N from above. The effective magnetic moment is ~4.5 μ_B/f.u. and agrees well with theoretical estimations using determined effective g-value ~2.19 and assuming high-spin configuration of Ni^{2+} ($S = 1$).

The magnetization curves demonstrate an upward curvature suggesting the possible presence of a magnetic field induced spin-flop transition at $B_C \sim 5 \div 6$ T.

The evolution of ESR spectra with temperature for $A_2Ni_2TeO_6$ (A = Na, Li, K) is shown at the fig.2. We observe a single broad line, but a proper analysis of the ESR lineshape requires fitting by sum of two Lorentzians:

$$\frac{dP}{dB} \propto \frac{d}{dB}\left[\frac{\Delta B}{\Delta B^2+\left(B-B_r\right)^2}+\frac{\Delta B}{\Delta B^2+\left(B+B_r\right)^2}\right] \tag{1}$$

where P is the power absorbed in the ESR experiment, B — magnetic field, B_r — resonance field, ΔB — the linewidth.

We assume that one line L_1 is the main signal from the matrix, while another one L_2, which is much less intensive, can be related to the presence of small amount of the impurity in the samples.

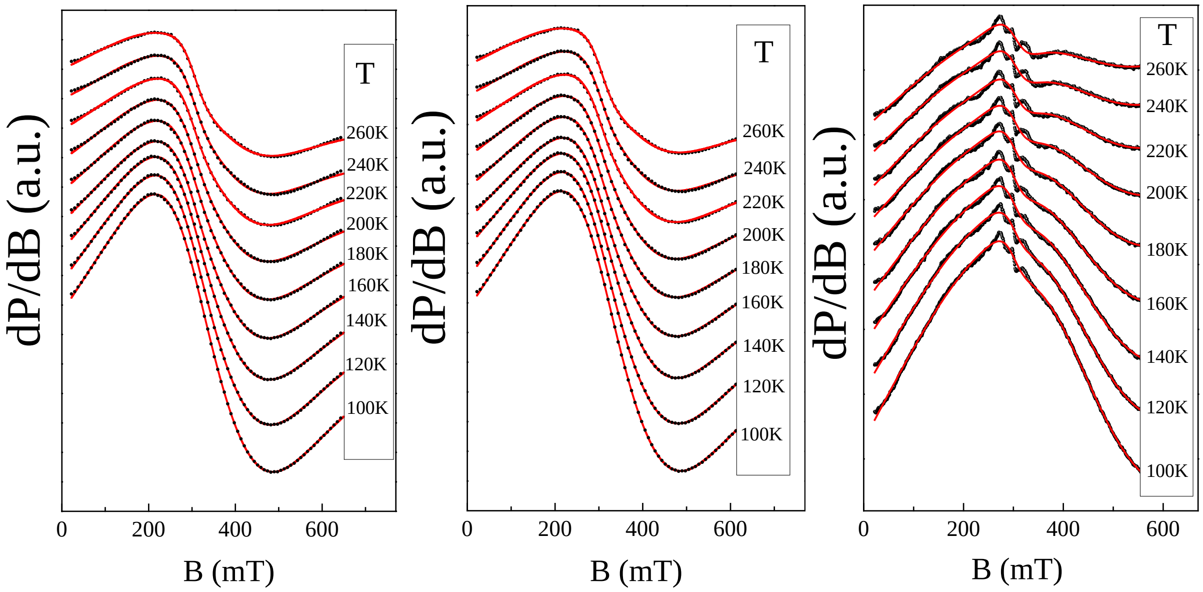

Fig.2. Evolution of EPR spectra for $A_2Ni_2TeO_6$ (A = Li, Na, K) with temperature.

Parameters determined from the lineshape fitting are collected in fig.3. The absorption is characterized by an isotropic temperature independent effective g-factor $g = 2.2 \pm 0.005$

(upper panel in fig.3). The ESR line broadens with decreasing the temperature, then the linewidth passes through a maximum in the vicinity of order-disorder transition and eventually changes the trend (middle panel in fig.3). The temperature dependence of the *g*-value also demonstrates a sharp anomaly in the vicinity of T_N, however the visible shift of the resonant field to higher magnetic fields begins only in the immediate proximity to the Néel temperature. The integral ESR intensity (lower panel in fig.3), which is proportional to the number of magnetic spinswas estimated by double integration of the first derivative ESR spectrum for each temperature. The contribution of the minor line is insignificant. The behavior of the main resonance mode follows Curie-Weiss type growth and agrees with static magnetic susceptibility data.

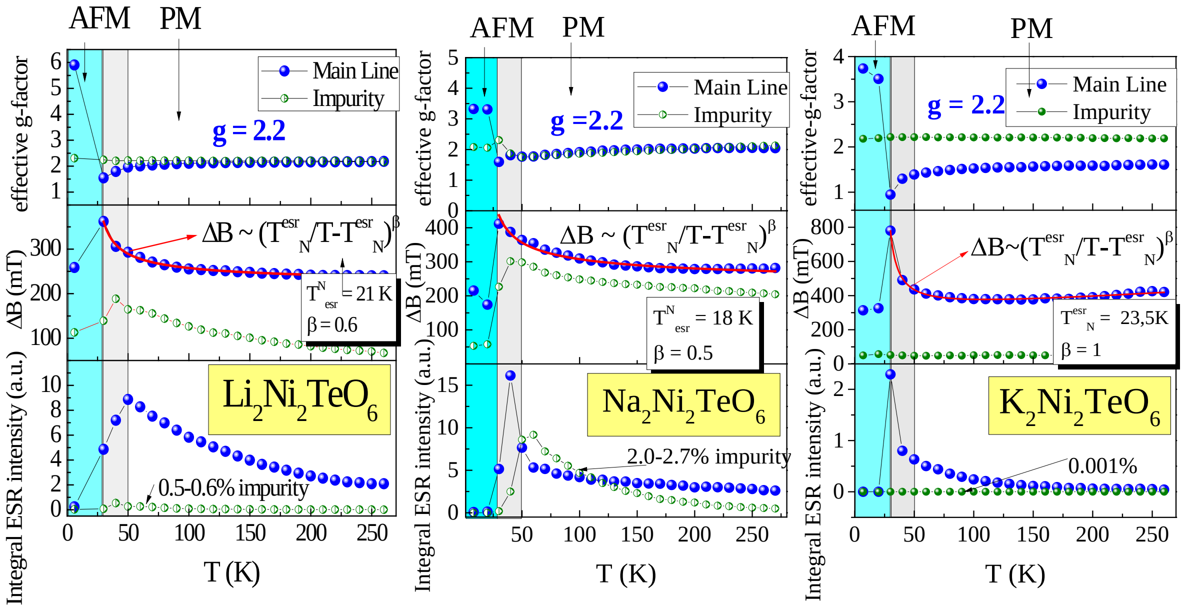

Fig.3. Temperature dependencies of the main EPR parameters for samples$A_2Ni_2TeO_6$.

We have analyzed the temperature behavior of the linewidth in the frame of Kawasaki-Mori-Huber theory [2–5]. According the model the EPR linewidth for an uniaxial antiferromagnet near the Néel point reads:

$$\Delta B(T) = \Delta B^* + A\left[\frac{T_N^{ESR}}{T - T_N^{ESR}}\right]^{\beta} \qquad (2)$$

Here ΔB denotes the ESR linewidth, A is an empirical parameter, ΔB^* — is the limiting minimum value of the linewidth, T_N^{ESR} is the temperature of the order-disorder transition, β is a «critical exponent». Solid red lines shown in fig.3 at middle level represent a least squares fitting of the experimental data according to eq. (2). Apparently, this formula remains valid in our system for a wide temperature range 25 ÷ 270 K.

References

[1] B. Xu, D. Qian, Z. Wang, Y.S. Meng, *Mater. Sci. Eng. R*73, 51 (2012).

[2] K. Kawasaki, *Prog. Theor. Phys.*39, 285 (1968).

[3] K. Kawasaki, *Phys. Lett.*26A, 543 (1968).

[4] H. Mori, K. Kawasaki, *Progr. Theor. Phys.*28, 971 (1962).

[5] D.L. Huber, *Phys. Rev. B*6, 3180 (1972).

EPR study of frustrated antiferromagnets A_2MnXO_4 (A = Li, Na, Ag; X = Si, Ge)

R.S. Denisov[1], E.A. Zvereva[1], V.B. Nalbandyan[2], I.L. Shukaev[2], A.A. Petrenko[2],
V.V. Politaev[2], M. Tzschoppe[3], R. Klingeler[3], A.N. Vasiliev[1]

[1]Faculty of Physics, Moscow State University, Moscow, 119991 Russia
[2]Chemistry Faculty, Southern Federal University, Rostov-on-Don, 344090 Russia
[3]Kirchhoff Institute for Physics, Heidelberg University, D-69120 Heidelberg, Germany

e-mail: rsdenisov@gmail.com

Introduction

A family of A_2MXO_4 compounds, where A = Li, Na, Ag; M = Be, Mg, Mn, Fe, Co, Zn, Cd; X = Si, Ge, represents a variety of tetrahedral structure types and unusual physical properties due to non-trivial topology of magnetic exchange interactions. The A_2MXO_4 compounds attract lots of attention recently due to various potential practical applications [1 – 3]. Li_2MSiO_4 (M = Mn, Fe, Co and their combinations) are most intensely studied as materials for positive electrodes of lithium-ion batteries. Their sodium counterparts are of interest for emerging sodium-ion batteries or capacitors. Several compounds of this family are solid-state Na^+ or Ag^+ cation conductors, hosts for luminescent ions, etc.

This paper reports static and dynamic magnetic properties several new members of this family, in particular study of A_2MnSiO_4 (A = Li, Na, Ag) and A_2MnGeO_4 (A = Li, Na).

Experimental

The magnetic properties measurements were performed using a Quantum Design SQUID magnetometer in the temperature range 1.8 – 300 K and at the magnetic field $B \leq 5$ T. Electron spin resonance (ESR) studies were carried out using an X-band ESR spectrometer CMS 8400 (ADANI) ($f \approx 9.4$ GHz, $B \leq 0.7$ T) equipped with a low-temperature mount, operating in the range $T = 7 – 300$ K. The effective g-factors of our samples have been calculated with respect to an external reference for the resonance field. We used BDPA (a,g - bisdiphenyline-b-phenylallyl)as the reference material, for which $g_{ref} = 2.00359$.

Results and discussion

It was found that the temperature dependence of the magnetic susceptibility $\chi = M/B$ at low magnetic fields demonstrates sharp maxima at about ~12 K, ~4.5 K, ~9 K and ~4.5 K for the Li_2MnSiO_4, Na_2MnSiO_4, Li_2MnGeO_4 and Na_2MnGeO_4 samples, respectively; that indicates an onset of long-range antiferromagnetic order in these compounds. At the same time, the magnetic susceptibility χ for the Ag_2MnSiO_4 sample shows Curie-Weiss-type growth over the whole temperature range studied implying the absence of a long-range magnetic order down to 1.8 K. The high temperature magnetic susceptibility for all samples nicely follows the Curie-Weiss law. Our analysis yields the negative and relatively large value of the Weiss temperature Θ for all compounds, which indicates the predominance of the antiferromagnetic interactions. At the same time the frustration factor $f = \Theta/T_N$ is essentially higher than typical for classical antiferromagnets value, indicating the complicated spin-configuration with competing FM and AFM couplings. The ESR data for all A_2MnXO_4 (A = Li, Na, Ag; X = Si, Ge) samples in the paramagnetic phase ($T > T_N$) show similar behaviour and reveal a single exchange-narrowed absorption line ascribable to Mn^{2+} ions in tetrahedral coordination (fig.1). Thorough analysis, however, shows that for the better description of the line shape in the case of the A_2MnSiO_4 silicates, we have to use a sum of two Lorentzians with essentially different relative intensities (see representative examples on insets of fig.1 (a – c)). Obviously, the mode L_1 shown in blue in insets on fig.1 (a – c) brings the main contribution to the absorption. We suppose that the second small absorption mode corresponds to the presence of small amount impurity in the sample. The main ESR parameters (effective *g*-factor, the ESR linewidth and the integral ESR intensity) were deduced by fitting the experimental spectra with either one (for the A_2MnGeO_4) or two (for the A_2MnSiO_4) Lorentzian profiles taking into account two circular components of the exciting linearly polarized microwave field on both sides of $B = 0$ since the ESR line is relatively broad,

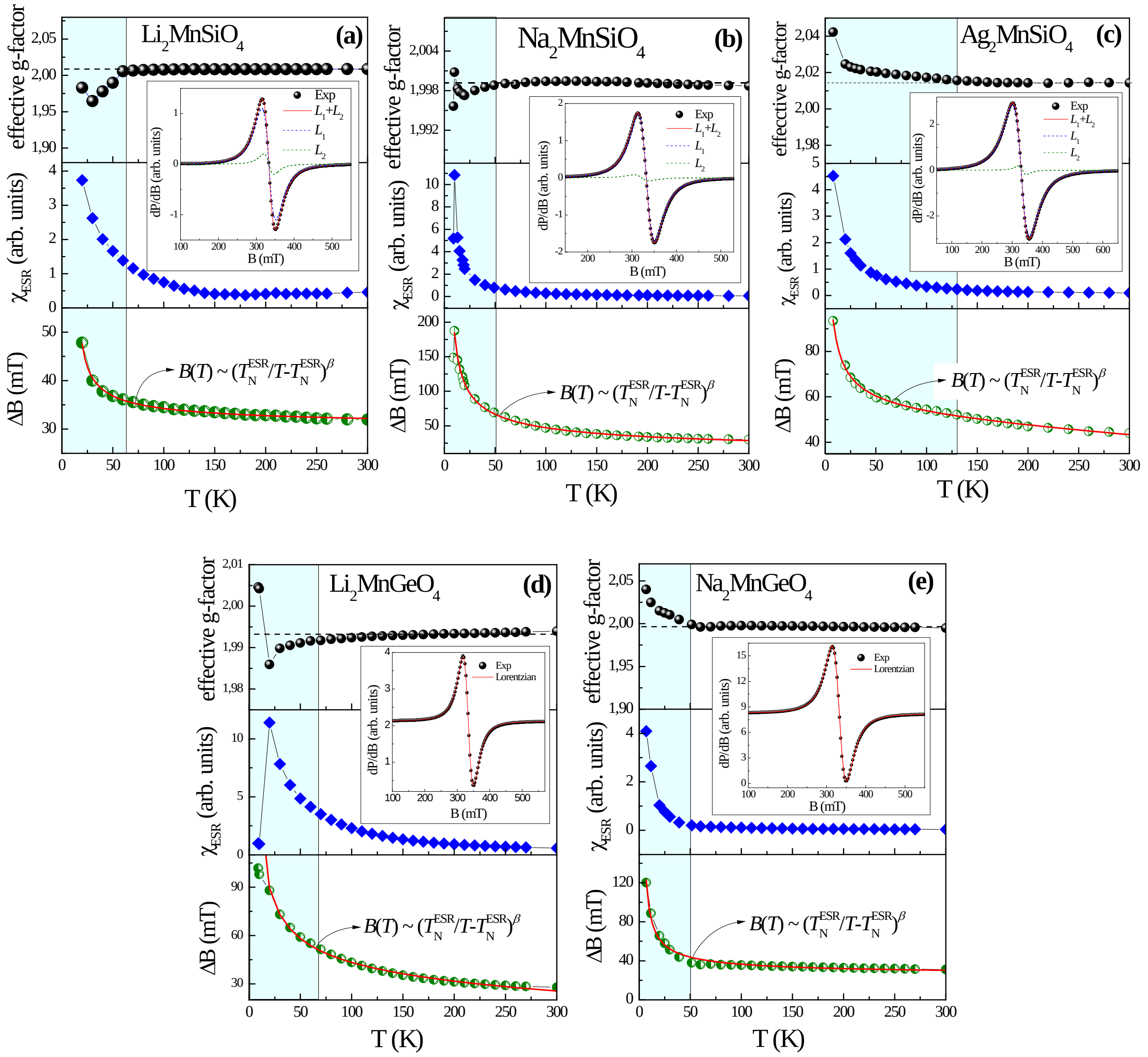

Fig.1. Temperature dependence of the effective g-factor (upper panels), theintegral ESR intensity (middle panels) and the ESR linewidth (lower panels) and forA_2MnXO_4 (A = Li, Na, Ag; X = Si, Ge). Red solid curves are approximation in the frame of Mori-Kawaski-Huber theory. On insets: representative examples of ESR spectra fitting with either two (at T = 250 K (a), 230 K (b), 200 K (c)) or one (at T = 250 K (d, e)) Lorentzians: black circles are experimental data, the blue and green curves are resolved components and red solid one is their sum.

$$\frac{dP}{dB} \propto \frac{d}{dB}\left[\frac{\Delta B+}{\Delta B^2+\left(B-B_r\right)^2}+\frac{\Delta B}{\Delta B^2+\left(B+B_r\right)^2}\right], \qquad (1)$$

where P is the power absorbed in the ESR experiment, B the magnetic field, B_r the resonance field, and ΔB the linewidth.

The parameters of the main resonance mode L_1 deduced from the fitting are collected in fig.1 for all samples. The integral ESR intensity χ_{esr}, which is proportional to the number of magnetic spins, was estimated by double integration of the first derivative ESR spectrum dP/dB. The parameters for the antiferromagnetic A_2MnXO_4 samples (with Li and Na) demonstrate anomalies in the vicinity of the Néel temperature. One can see that with decreasing temperature below ~100 K the absorption line broadens markedly and passes through a maximum at about T_N. The effective g-factor remains almost temperature-independent down to 50 – 70 K for different samples being on average $g \approx 2$ for all samples.

The broadening of the ESR line were treated in terms of the Mori-Kawaski-Huber theory for the critical behaviour of ESR linewidth due to slowing down of spin fluctuations in the vicinity of an order-disorder transition [4 – 6]:

$$\Delta B\left(T\right) = \Delta B^{*} + A \cdot \left[\frac{T_N^{ESR}}{T - T_N^{ESR}}\right]^{\beta}, \tag{2}$$

where the first term ΔB^{*} describes the exchange narrowed linewidth, which is temperature independent, while the second term reflects the critical behaviour with T_N^{ESR} being the temperature of the order-disorder transition and β being the critical exponent. Solid red curves on lower panels of fig.1 represent a least- squares-fitting of the $\Delta B(T)$ experimental data in accordance with eq. (2). The best fitting was attained with the parameters listed in table 1. Obviously the value of T_N^{ESR} is in a reasonable agreement with the Néel temperature obtained from the static magnetic susceptibility. The value of the critical exponent related to the divergence of correlation length is higher than theoretically expected in the framework of the Heisenberg model value of 1/3 for 3D antiferromagnets, that indicates either low-dimensional or frustrated charter of magnetic correlations in the A_2MnXO_4 system.

Table 1. The parameters yielded from fitting of temperature dependencies of the ESR linewidth ΔB in accordance with eq. (2) for A_2MnXO_4 (A = Li, Na, Ag; X = Si, Ge).

	T_N (K)	T_N^{ESR} (K)	ΔB^{*} (mT)	β
Li_2MnSiO_4	10.1	13.3±0.5	30±1	0.55±0.05
Na_2MnSiO_4	4.2	4.6±0.5	4±1	0.50±0.05
Ag_2MnSiO_4	-	0.01±0.01	48±1	0.66±0.05
Li_2MnGeO_4	7.7	6.5±0.5	2±1	0.37±0.05
Na_2MnGeO_4	4.0	3.1±0.5	24±1	0.65±0.05

References

[1] Z. Gong and Y. Yang. *Energy Environ. Sci.* **4**, 3223 (2011).

[2] V.V. Politaev, A.A. Petrenko, V.B. Nalbandyan, B.S. Medvedev and E.S. Shvetsova. *J. Solid State Chem.* **180**, 1045 (2007).

[3] H. Duncan, A. Kondamreddy, P.H.J. Mercier, Y.Le Page, Y. Abu-Lebdeh, M. Couillard, P.S. Whitfield and I. J. Davidson. *Chem. Mater.* **23**, 5446 (2011).

[4] K. Kawasaki, *Prog. Theor. Phys.* **39,** 285 (1968); *Phys. Lett.*, **26A**, 543 (1968).

[5] H. Mori, K. Kawasaki, *Progr. Theor. Phys.* **28**, 971 (1962).

[6] D.L. Huber, *Phys. Rev. B,* **6**, 3180 (1972).

Spin dynamics in layered triangular lattice antiferromagnet $MnSb_2O_6$

A.S. Polovkova[1], E.A. Zvereva[1], V.B. Nalbandyan[2], A.Yu. Nikulin[2], I.L. Shukaev[2], C. Koo[3], J. Werner[3], R. Klingeler[3], A.N. Vasiliev[1]

[1] Faculty of Physics, Moscow State University, Moscow, Russia
[2] Chemistry Faculty, Southern Federal University, Rostov-na-Donu, Russia
[3] Kirchhoff Institute for Physics, Heidelberg University, Heidelberg, Germany

e-mail: polovkova.nst@mail.ru

We report on the static and dynamic magnetic properties of two polymorphs of the triangular lattice antiferromagnet $MnSb_2O_6$, which are characterized by two different layered trigonal crystal structures: space groups (P321) and (P31m) respectively (fig.1). Based on neutron powder diffraction data and DFT calculations, the first one (P321 form) has been recently predicted to be multiferroic with a unique ferroelectric switching mechanism [1]. However, no systematic experimental studies of its magnetic properties have been performed up to now. The second polymorph under study (P31m form) was synthesized and investigated for the first time.

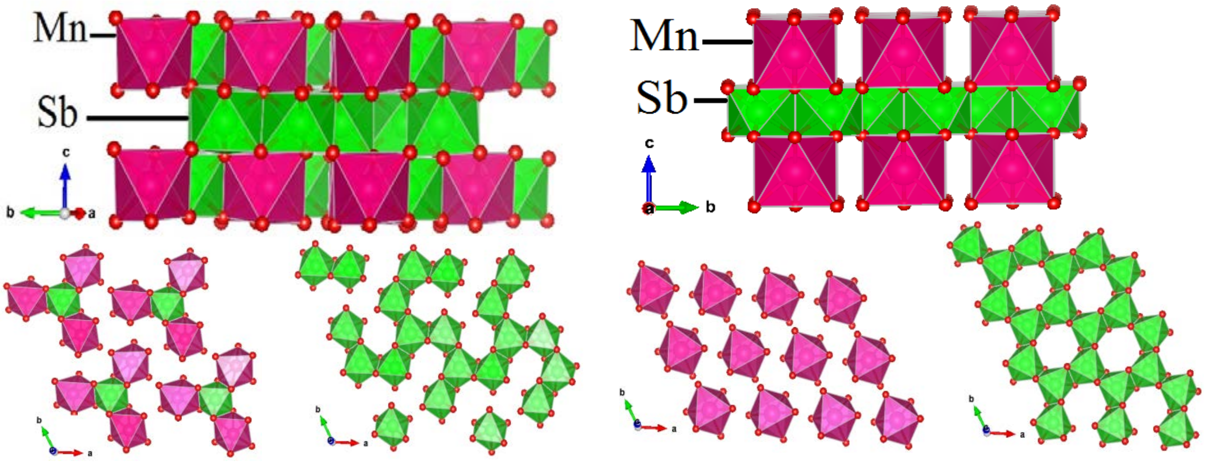

Fig.1. Layered trigonal crystal structures: for known, space group (P321), (left) and new, space group (P31m), (right) antiferromagnet $MnSb_2O_6$, respectively.

It was found that both compounds exhibit long-range antiferromagnetic order with $T_N \sim 12$ K for (P321) form and $T_N \sim 8.5$ K for (P31m) form, respectively (fig.2). The Weiss temperatures are negative indicating predominance of antiferromagnetic interactions. The effective magnetic moment for both compounds is about 5.9(2) μ_B/f.u., which agrees well with theoretical estimations using the measured effective g-factors and assuming high-spin configuration of Mn^{2+}. The magnetization curves exhibit the presence of magnetic field induced spin-flop transitions at $B_C \sim 1$ T for (P321) form and $B_C \sim 0.7$ T for (P31m) form, respectively. In addition, there is a weak ferromagnetic component detected in the magnetic susceptibility below $T_1 = 41.5(5)$ K for the (P31m) sample. The ESR studies corroborate the static magnetization data and reveal non trivial spin dynamics in the (P31m) form. The ESR spectra have been fitted by Lorentzian profile. The main parameters are collected in fig.3. The broadening of the ESR linewidth were treated in terms of the critical behavior of the ESR linewidth due to slowing down of spin fluctuations in the vicinity of an order-disorder transition [2 – 4]. In consistence with our experimental findings, the magnetic phase diagrams have been constructed for both compounds.

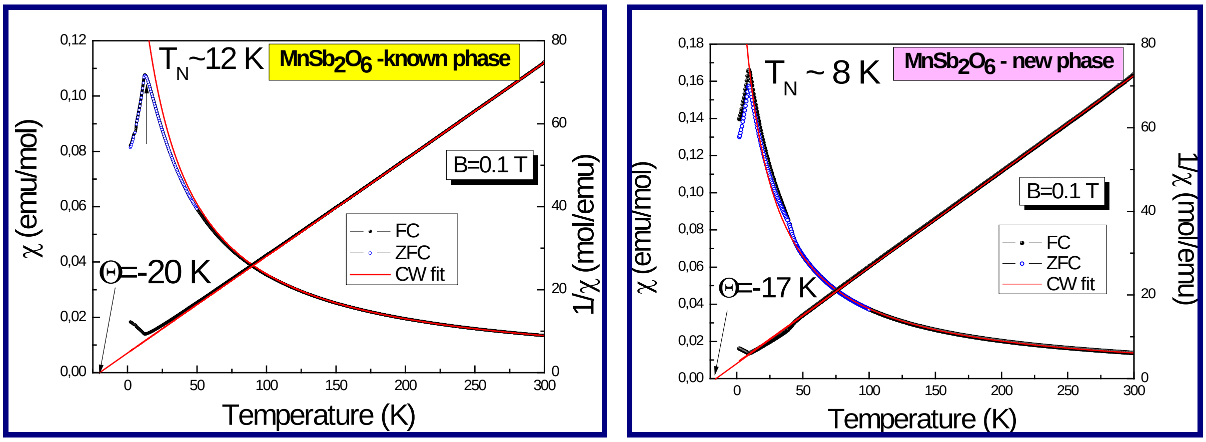

Fig.2. The temperature dependence of the magnetic susceptibility and its inverse value for known (P321 — left) and new (P31m — right) form of $MnSb_2O_6$, respectively.

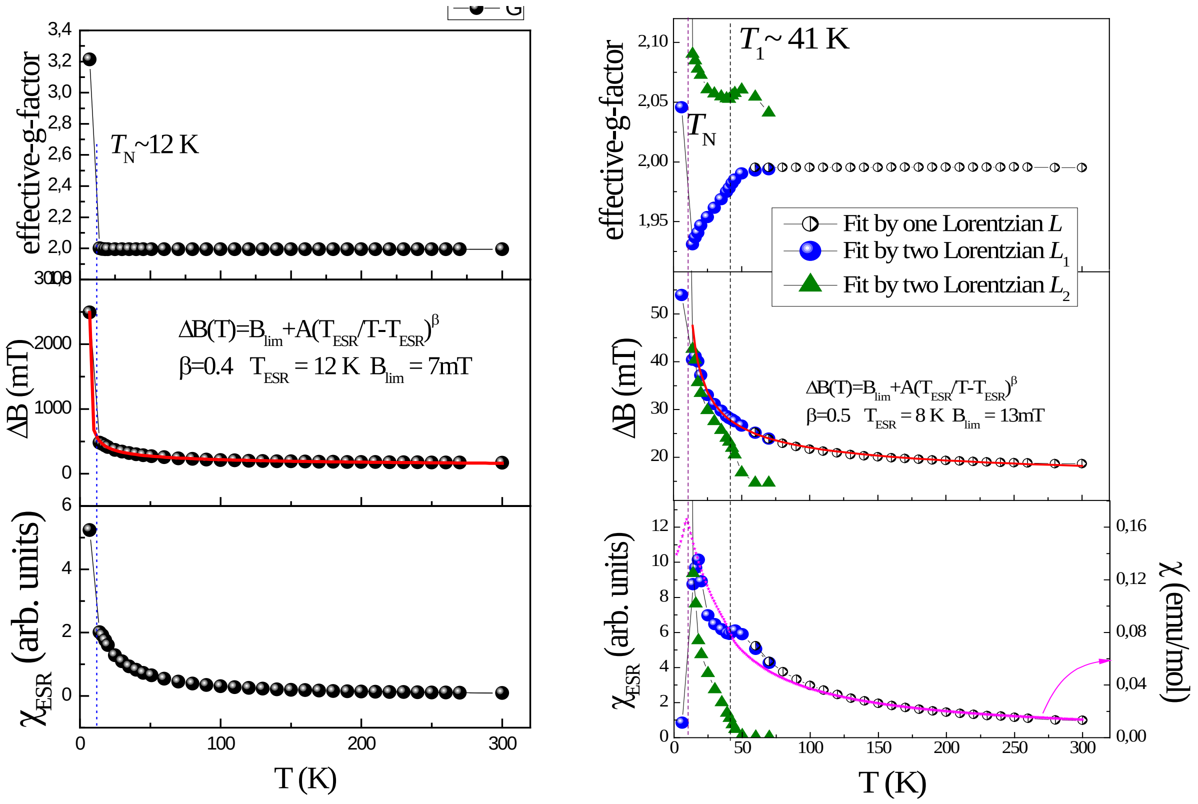

Fig.3. The main ESR parameters (effective g-factor, the linewidth and the integral ESR intensity) versus temperature for known (P321 — left) and new (P31m — right) form of $MnSb_2O_6$, respectively.

References

[1] Johnson R.D., Cao K., Chapon L.C., Fabrizi F., Perks N., Manuel P., Yang J.J., Oh Y.S., Cheong S.-W., Radaelli P.G. Phys. Rev. Lett., 111, 017202, 2013.

[2] K. Kawasaki, *Prog. Theor. Phys.* **39,** 285 (1968); *Phys. Lett.*, **26A**, 543 (1968).

[3] H. Mori, K. Kawasaki, *Progr. Theor. Phys.* **28**, 971 (1962).

[4] D. L. Huber, *Phys. Rev. B,* **6**, 3180 (1972).

Spin dynamics in quasi 2D-honeycomb-lattice tellurate $Na_2Co_2TeO_6$

M.I. Stratan[1], E.A. Zvereva[1], V.B. Nalbandyan[2], M.-H. Whangbo[3], H.-J. Koo[4], A.N. Vasiliev[1]

[1]Physics Faculty, Moscow State University, Moscow, Russia
[2]Chemistry Faculty, Southern Federal University, Rostov-on-Don, Russia
[3]Department of Chemistry, North Carolina State University, Raleigh, USA
[4]Department of Chemistry and Research Institute for Basic Sciences, Kyung Hee University, Seoul, Republic of Korea

e-mail: stratan@physics.msu.ru

Introduction

Synthesis of new layered oxides of alkali and transition metals, which are expected to be promising materials as solid electrolytes or electrode materials, stimulates the intensive studies of their physical properties and, first of all, their magnetism, since the processes of ionic transfer are connected with the change of the valence and spin states of transition metals. A great interest of scientists attracts recently a new generation of layered complex metal oxides: antimonates $A_2M_3SbO_6$ (where A and M are the alkali and transition metal respectively) and tellurates $A_2M_2TeO_6$, which represent an ordered superlattice derived from the α-$NaFeO_2$ structure type with $M^{2+}/Sb^{5+}(Te^{6+})$ ordering on Fe^{3+} sites in a “honeycomb” fashion.

In present work in order to construct magnetic phase diagram and elucidate complex quantum ground state of quasi 2D honeycomb-lattice oxide $Na_2Co_2TeO_6$ we have studied comprehensively its magnetic properties employing magnetic susceptibility, specific heat, magnetization, electron spin resonance (ESR) as well as density functional theory calculations. The crystal structure of $Na_2Co_2TeO_6$ was determined as two-layer hexagonal (space group $P6_322$) employing powder neutron diffraction method (fig. 1) [1].

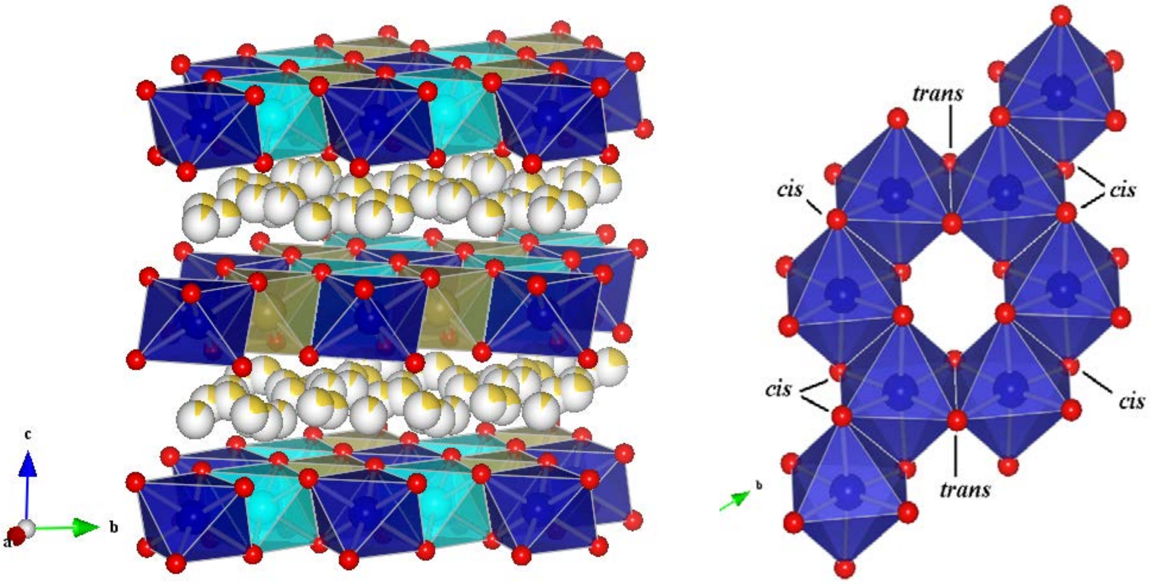

Fig.1. The crystal structure of $Na_2Co_2TeO_6$.Two non-equivalent types of CoO_6 octahedra are shown in blue and cyan, TeO_6 octahedra are gray, oxygens are small red spheres and partially occupied (split) sodium sites are white spheres in trigonal prismatic oxygen environment. A general view (left) and magneto-active honeycomb layer (right), tellurium atoms omitted for the sake of simplicity.

Experimental

The polycrystalline $Na_2Co_2TeO_6$ sample was prepared by conventional solid-state reactions at 900 – 1090 K followed by quenching and analyzed by redox titration and powder X-ray diffraction. The magnetic measurements were performed using a Quantum Design MPMS-7 SQUID magnetometer in the temperature range 1.8 – 300 K under variation of the magnetic field $B \leq 7$ T. Electron spin resonance (ESR) studies were carried out using an X-band ESR spectrometer CMS 8400 (ADANI) ($f \approx 9.4$ GHz, $B \leq 0.7$ T) equipped with a low-temperature mount, operating in the range $T = 6 – 300$ K. The effective g-factors of our samples have been calculated with respect to an external reference for the resonance field. We used BDPA (a,g - bisdiphenyline-b-phenylallyl), $g_{ref} = 2.00359$., as the reference material. Specific heat measurements were carried out by a relaxation method using a Quantum Design PPMS system ($B \leq 9$ T, $T = 2 – 300$ K).

Results

In agreement with previously reported data [1] it was found that the compound orders antiferromagnetically with Neel temperature ~26 K, however, the detailed investigations in various magnetic fields show that the behavior is rather complicated. As one can see from fig.2 the magnetic susceptibility confirmed by specific heat data demonstrates at least three different anomalies ($T_{N1} \sim 26$ K, $T_{N2} \sim 17$ K and $T_3 \sim 12$ K) at low magnetic field and jump-like increasing the susceptibility at $T_{N1} \sim 26$ K and $T_{N2} \sim 17$ K indicates the presence of ferro- (or ferri-) magnetic contributions. It is also obvious that the system is very sensitive to the magnetic field and increasing the applied field leads to shift of anomalies at T_3 and T_{N2} to higher temperatures and following suppression of those phase transitions at about 1 T and 4 T respectively. In the paramagnetic phase the temperature dependence of the magnetic susceptibility nicely follows the Curie-Weiss law with a positive value of Weiss temperature Θ of about 5 K, indicating a predominance of ferromagnetic correlations and effective

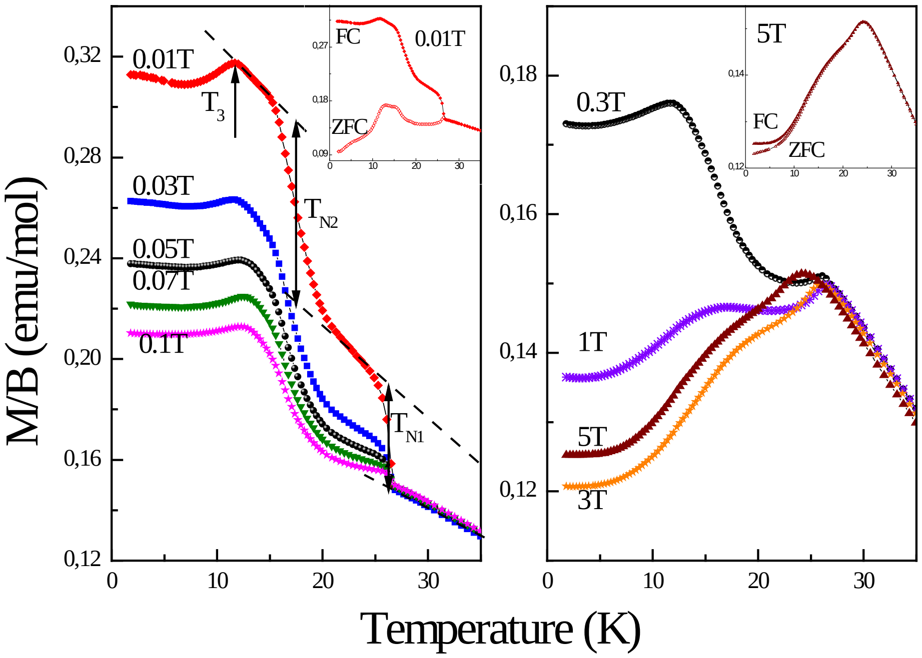

Fig. 2. The temperature dependence of the magnetic susceptibility χ (FC regime) in the low-temperature range at various magnetic fields.On insets: $\chi(T)$ dependencies recorded in ZFC regime (open symbols) and FC regime (filled symbols) at lowest ($B = 0.01$ T) and highest ($B = 5$ T) magnetic field. The arrows highlight the positions of phase transitions revealed.

magnetic moment $\mu_{eff} \approx 6.9\ \mu_B$/f.u., which is in reasonable agreement with theoretically estimates assuming high-spin state for Co^{2+} ions ($S = 3/2$) and using determined from our ESR studies g-factor.

Electron spin resonance (ESR) spectra show a single strongly anisotropic absorption line attributed to Co^{2+} ion in octahedral coordination with almost temperature independent effective g-factor $g = 1/3(g_\perp + g_\parallel) = 2.40 \pm 0.05$. A rough estimation for an exchange anisotropy according to expression $J_\perp/J_\parallel = g_\perp/g_\parallel$ yields a value $J_\perp/J_\parallel \sim 0.85$ indicating relatively weak anisotropy in $Na_2Co_2TeO_6$, which is in consistency with strong sensitivity to applied magnetic field strength. With decreasing temperature the line narrows slightly probably owing to decreasing role of the spin-lattice relaxation mechanism. At the temperature lower than T_{N2} a noticeable degradation of the absorption line occurs. This signal fading could be indicative of the opening of an energy gap for resonance excitations due to the establishment of the long-range AFM order at low temperatures.

The main spin exchange interactions in $Na_2Co_2TeO_6$, which are shown in fig.4, have been obtained from GGA+U calculations. It was found that all the interlayer interactions are ferromagnetic ($J_a = 18\pm4$ K, $J_b = 8\pm1$ K and $J_c = 5\pm1$ K), while the intralayer exchange interactions are competing ferro- ($J_1 \sim 8$ K) and antiferromagnetic ($J_2 \sim -10$ K and $J_3 = \sim -17$ K) ones, which lead to the *zigzag* ferromagnetic chains ordered antiferromagnetically in each honeycomb layer with preferred spin orientation to be parallel to c-axis as the magnetic ground state of $Na_2Co_2TeO_6$. Based on the results of magnetic and thermodynamic studies in applied fields up to 9 T we propose the magnetic phase diagram in agreement with our experimental findings (fig.5).

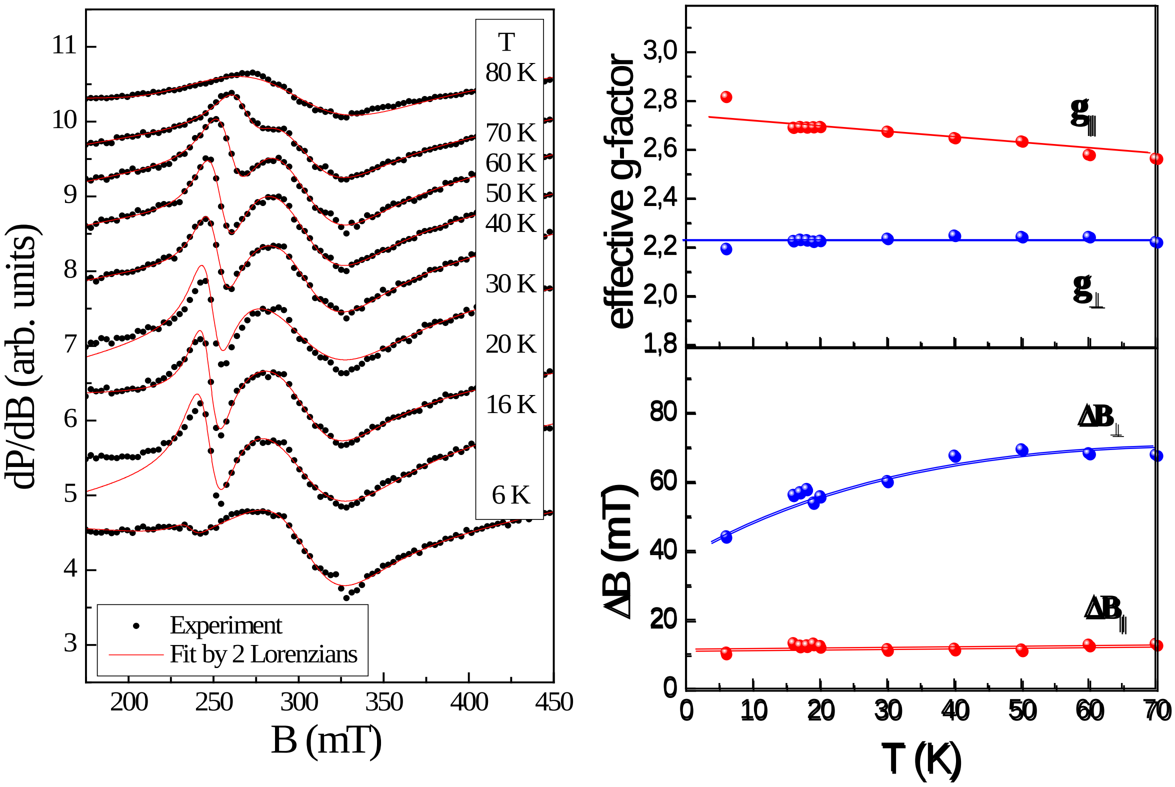

Fig.3. Evolution of ESR spectra with temperature (left) and temperature dependencies of the effective g-factor and the linewidth for $Na_2Co_2TeO_6$.

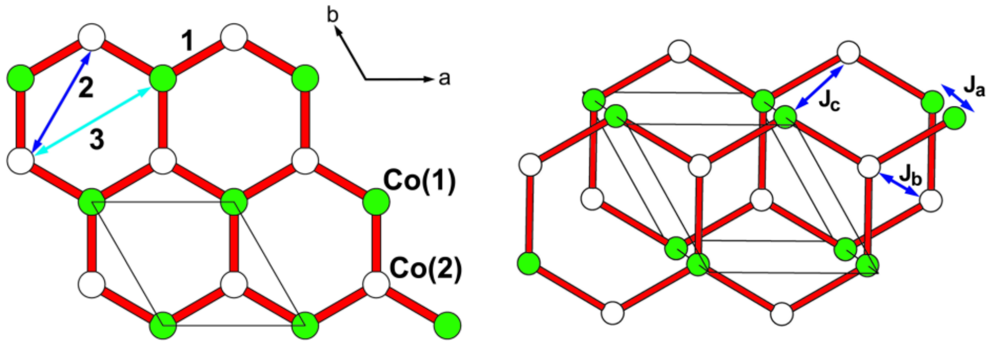

(a) (b)

Fig. 4. The (a) intralayer and (b) interlayer spin exchange paths in honeycomb-lattice compound $Na_2Co_2TeO_6$.

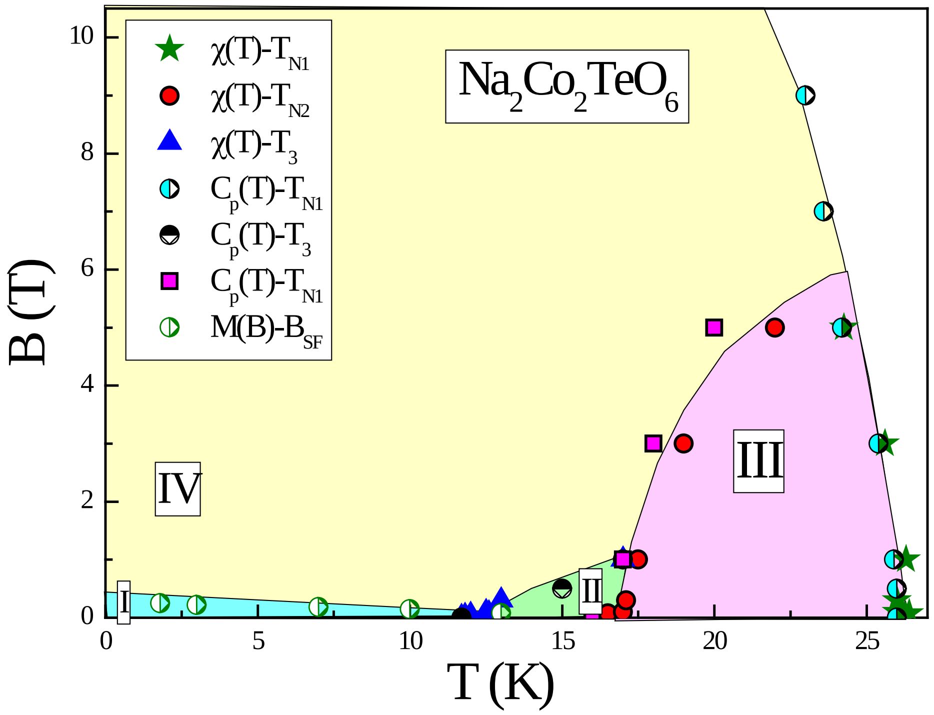

Fig.5. The magnetic phase diagram of $Na_2Co_2TeO_6$.

This work has been supported by Russian Foundation for Basic Research (grants 11-03-01101, 13-02-00374 and 14-02-00245). The authors gratefully thank Dr. M.A. Evstigneeva who prepared samples of $Na_2Co_2TeO_6$ used in the present study.

References

[1] [1] L. Viciu, Q. Huang, E. Morosan, H.W. Zandbergen, N.I. Greenbaum, T. McQueen, R.J. Cava, J. Solid State Chem. **180**, 1060 (2007).

ESR and magnetization measurements in honeycomb layered mineral urusovite $CuAl(AsO_4)O$

A.V. Koshelev[1,2], A.N. Vasiliev[1,2], O.S. Volkova[1,2], E.A. Zvereva[1], D.A. Chareev[1]

[1]Lomonosov Moscow State University, 119991, Leninskie Gory, Moscow, Russia
[2]Institute of Experimental Mineralogy, 142432, Academica Osypyana, Chernogolovka, Russia

e-mail: anatolkosh@mail.ru

The urusovite with chemical formula $CuAl(AsO_4)O$ was prepared through the wet chemistry route and it's purity was controlled by X-ray diffraction.

The urusovite, $CuAl(AsO_4)O$, has monoclinic primitive cell [1] with four formula units per unit cell. The basic structural unit consists of Cu atom in the center of a distorted oxygen pyramid. The Cu-O bondlengths have an average value of 2.05 Å. Two neighboring CuO_5 pyramids share a common edge to form a dimer unit while two such neighboring units share a common corner in the *bc*-plane and form a honeycomb like structure, as shown of fig.1. Two such layers of honeycomb are connected via AsO_4 and AlO_4 tetrahedrons, as shown in the left panel of fig.1. The *bc* planes containing honeycomb structures are stacked on top of each other along the *a*-direction.

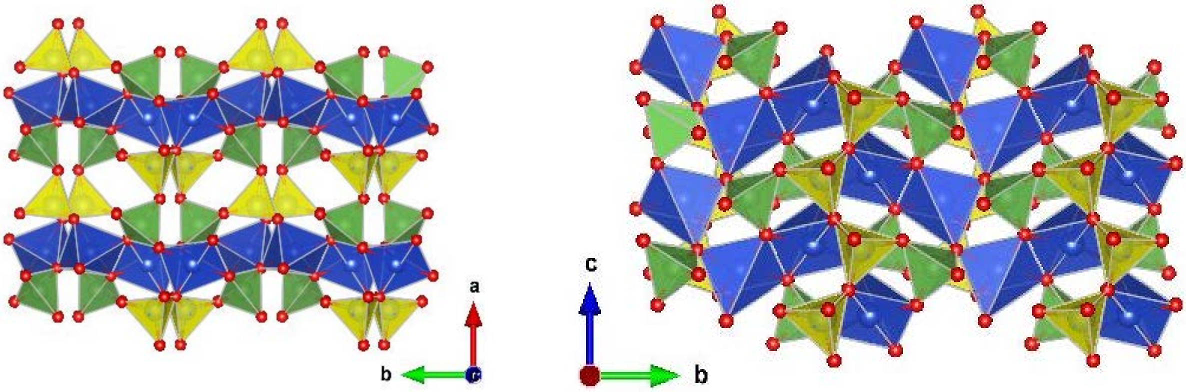

Fig.1. The crystal structure of urusovite, $CuAl(AsO_4)O$, in polyhedral representation in *ab* plane (left panel) and *bc* plane (right panel). The corrugated layers of edge-sharing and corner-sharing CuO_5 pyramids (blue) are separated by AlO_4 (green) and AsO_4 (yellow) tetrahedra.

The evolution of ESR spectra with temperature in the powder sample of $CuAl(AsO_4)O$ is shown in fig.2. Obviously, one can distinguish two principally different regions over the temperature range studied. At high temperatures ($T \geq 90$ K), almost isotropic single broad absorption line ascribable to Cu^{2+} ions is observed. Its amplitude passes through maximum and then decreases with decreasing temperature. Further decrease of the temperature lead to significant changes in the character of ESR spectra and strongly anisotropic absorption line with visible hyperfine structure ($T \leq 60$ K) is observed.

Since the resonant signal is relatively broad at high temperature (the same order as the resonance field) two circular components of the exciting linearly polarized microwave field have to be taken into account. Therefore, for analysis, the ESR signals on both sides of $B = 0$ have to be included into the fitting formula, which has been taken in a conventional form:

$$\frac{dP}{dB} \propto \frac{d}{dB}\left[\frac{\Delta B}{\Delta B^2+\left(B-B_r\right)^2}+\frac{\Delta B}{\Delta B^2+\left(B+B_r\right)^2}\right]. \tag{1}$$

This formula describes a symmetric line, where P is the power absorbed in the ESR experiment, B_r is the resonance field and ΔB is the linewidth. The results of ESR lineshape fitting are shown by the solid lines in fig.2 (left panel). Apparently, the fitted curves are in a good agreement with the experimental data. The temperature dependencies of the effective *g*-factor, the linewidth ΔB and the integral ESR intensity χ_{ESR} (which is proportional to the number of magnetic spins) as derived from this fitting procedure are summarized in fig.3.

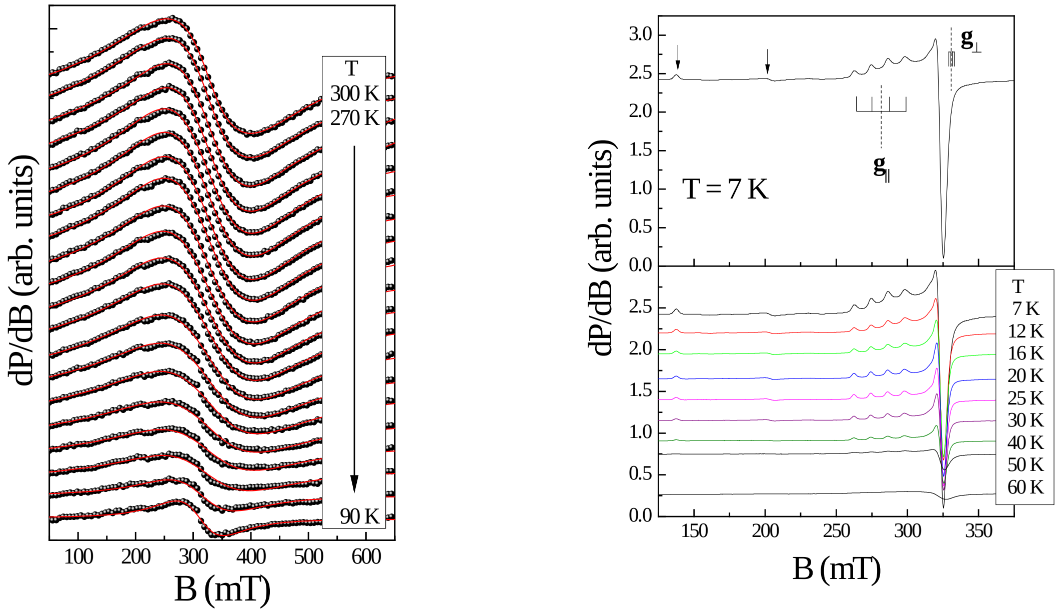

Fig.2. Temperature dependences of X-band ESR signal from the matrix (left panel) and from the impurities/defects (right panel) in CuAl(AsO_4)O.

The average effective *g*-factor at room temperature is found to be $g = 2.05$ (upper panel in fig.3), which is a reasonable value for Cu^{2+} ions in the pyramidal coordination.[2] This value is influenced by internal magnetic field in the matrix, however. With lowering temperature, the measured *g*-factor remains essentially independent of temperature down to ~ 90 K, afterwards it shifts to higher values. This shift is the artefact related to switching of main ESR signal from the matrix to impurity. The linewidth demonstrates non-monotonic behavior indicating different spin-dynamic regimes over the temperature range under study (middle panel in fig.3). At high temperatures ($T > 200$ K) the linewidth remains almost constant, which is typical for exchange-narrowed ESR absorption line. Decreasing temperature below ~ 200 K leads to a slow increase of the linewidth which is due to development of short-range magnetic correlations, tentatively. It passes through a smooth maximum at $T \sim 130$ K which may reflect a saturation of spin correlation length, and then it decreases progressively down to ~ 70 K, when the ESR signal from the matrix vanishes eventually. Similar behavior was found earlier for the spin-gap compound η-$Na_{1.286}V_2O_5$ and interpreted basing on the concept of memory function *F*(T), which is the sum of spin-correlation functions. The linewidth in this approach is proportional to the memory function, *F*(T), divided by $\chi_0(T) \times T$. This, for instance, leads to linear dependence of ΔB vs. T (Oshikawa-Affleck law) in the case of $S = 1/2$ AFM Heisenberg chain when $F(\mathrm{T}) \sim T^2$. At the same time, in the case of spin-gapped systems one would expect more rapid decrease ΔB with temperature.[3] So, narrowing of the line below ~130 K might be interpreted as a strong depletion of the spin fluctuation density due to the opening of the spin gap.

At temperatures below 60 K there is another ESR signal which might be related to the presence of impurity/defects, two very weak additional resonance modes (marked by arrows on fig.2 (right panel)) at low fields are also visible. The ESR powder pattern is characteristic of Cu^{2+} ions with anisotropic *g*-tensor. The intensity of this signal increases with lowering temperature in accordance with Curie-Weiss law. It is worth to note, that the presence of paramagnetic impurities was also detected in the static magnetic susceptibility data. In addition, the well-resolved anisotropic hyperfine structure appears at low temperatures due to interaction between the electron magnetic moment of unfilled electron *d*-shell of Cu^{2+} ions and nuclear magnetic moment of ^{63}Cu ($I = 3/2$, natural abundance 69%) and ^{65}Cu ($I = 3/2$, natural abundance 31%) isotopes. Both principal components of *g*-tensor remain almost temperature independent in the *T*-range 7 – 60 K and were determined from the parallel and perpendicular components of hyperfine structure. On average $g_{\|} = 2.37 \pm 0.01$ and $g_{\perp} = 2.02 \pm 0.01$ resulting in effective *g*-factor $g = 2.14$. The hyperfine-interaction constants were estimated to be about $^{63,65}A_{\|} \approx 381$ MHz and $^{63,65}A_{\perp} \approx 34$ MHz, respectively.

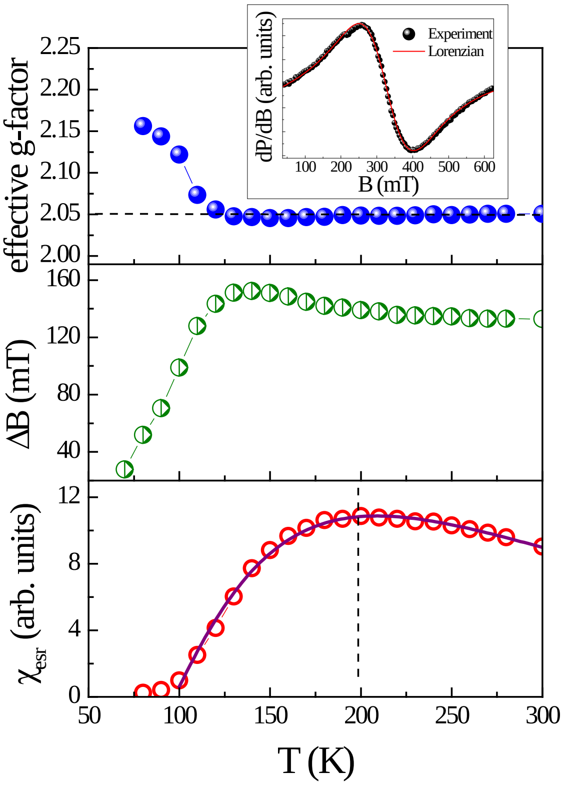

Fig.3. The temperature dependences of main ESR parameters of the matrix of $CuAl(AsO_4)O$: the effective g-factor (upper panel), the linewidth ΔB (middle panel), the intensity χ_{ESR} (lower panel). The inset: the first derivative of ESR absorption line at $T = 200$ K: circles are experimental data, red solid line is the fitting to Lorenzian profile.

The temperature dependence of magnetic susceptibility χ taken in the range 2 – 1000 K at $B = 1$ T in $CuAl(AsO_4)O$ is shown in fig.4. At low temperatures, it shows prevailing contribution of impurities/defects related term, the magnetic susceptibility passes through broad maximum below room temperature and non-monotonously decreases at elevated temperatures. To reveal the matrix contribution, the measurements of χ were repeated also at highest available field $B = 9$ T in the range 2 – 400 K, as shown in the inset to fig.4. At $T_{max} \sim 215$ K, the magnetization passes through broad maximum and decreases progressively with increasing temperature. The $\chi(T)$ dependence taken at $B = 1$ T was fitted in the range 2 – 1000 K by the formula for the non-interacting dimers with inclusion of the temperature independent term and the impurities/defects related term

$$\chi = \chi_0 + \frac{C_{imp}}{k_B T} + \frac{N_A \mu_B^2 g^2}{k_B T\left[3 + \exp(J_1 / k_B T)\right]} \qquad (2)$$

where N_A, μ_B and k_B are Avogadro, Bohr and Boltzmann constants, respectively. The fit is shown by solid line in fig.4.

Equation (2) contains four independent parameters, i.e. $\chi_0 = -7.9\times10^{-5}$ emu/mol which represents the temperature independent contribution, the defects/impurities concentration $C_{imp} = 0.0034$ emu/mol K, *g*-factor of Cu^{2+} ions $g = 2.185$ which differs from the value of *g*-factor estimated in ESR study at about room temperature, and J_1 = 350 K — the intradimer exchange interaction parameter equal to the gap Δ in the spectrum of magnetic excitations. The temperature independent term represents the summation of diamagnetic Pascal's constants of individual ions [4] in chemical formula of $CuAl(AsO_4)O$ and paramagnetic van Vleck term[5] associated with splitting of d-shell of Cu^{2+} ions. Above $T^* \sim 800$ K, the derivative $d\chi/dT$ increases somewhat indicating further deviations from the fitting curve, as shown in fig.4. The fit by eq. (2) in the range 2 – 800 K, shown by dashed line in fig.4, gives essentially the same values for every independent parameter.

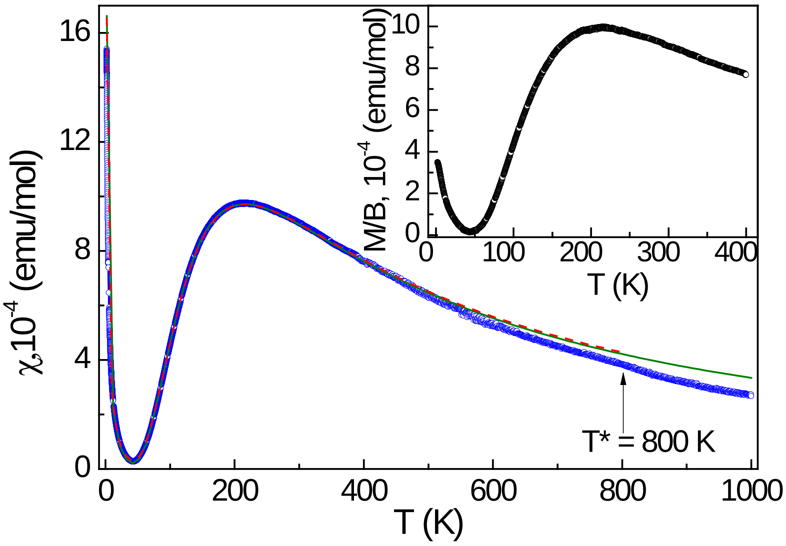

Fig.4.The temperature dependence of magnetic susceptibility in urusovite, $CuAl(AsO_4)O$, taken at B = 1 T. The solid line in the range 2 – 1000 K represents the fit in the model of non-interacting dimers. The dashed line represents the fit in the range 2 – 800 K. The inset represents the *M/B* vs. *T* dependence taken at B = 9 T

The title compound is chemically stable at ambient air pressure up to 1000°C. The measurements of magnetic susceptibility were performed however under conditions of dynamic high vacuum. In this case, the partial decomposition of the sample into $AlAsO_4$ and CuO phases can occur, as was confirmed by independent X-ray diffraction study. While the measurements of magnetic susceptibility on the fresh samples are quite reproducible, the repeatable measurements on the same sample lead to systematic lowering in the measured values of χ above T^* = 800 K.

References

[1] L.P. Vergasova, S.K. Filatov, M.G. Gorskaya, A.A. Molchanov, S.V. Krivovichev, and V.V. Ananiev, Russia. European Journal of Mineralogy **12**, 1041 (2000).

[2] R.M. Krishna and S.K. Gupta, Bull. Magn. Resonance, **16**, 239 (1994).

[3] F. Chabre, A.M. Ghorayeb, P. Millet, V.A. Pashchenko, and A. Stepanov, Phys. Rev. B **72**, 012415 (2005).

[4] G.A. Bain and J.F. Berry, J. Chem. Educ., **85**, 532 (2008).

[5] H. Lueken, Magnetochemie. Teubner, Leipzig 1999.

EPR spectra peculiarities of sportsmen's blood plasma

A.I. Chushnikov[1], M.I. Ibragimova[1], G.V. Cherepnev[2], V.Yu. Petukhov[1], I.V. Yatsyk[1]

[1]Zavoisky Physical-Technical Institute, Kazan, 420029, Russia
[2]Tatarstan Republic Clinical Hospital №2, Kazan, 420043, Russia

email: shuran2003@mail.ru

Introduction

Modern professional sport is associated with intense physical activity, so monitoring of sportsmen health status require a special approach. Usually used medical methods are not always allowed to detect the abnormal changes in organism. The EPR technique allows revealing weak dysmetabolic variations from the appearance of new lines in the spectra, which may be the diagnostic markers of metabolic disorders. Recently we reported on an appearance of new absorption lines in ESR spectra (X-band, 77 K) of serum samples collected from professional sportsmen [1]. The significant portion of new signals was assigned to Fe and Cu ions incorporated into cytochrome-*c*-oxidise. In the present study we extend the range of EPR measurements to lower temperatures (5 – 80 K) that will assess the diagnostic capability of the method to detect metabolic disorders.

Materials and method

Serum samples were collected from 22 Continental Hockey League professional players (25 ± 8 years old) and 3 control male volunteers from Clinical Republican Hospital No 2 Health Ministry of Tatarstan Republic by using standard procedure (centrifugation of venous blood was carried out at room temperature for 10 min at a speed of 1500 rev/min). EPR spectra from samples with equal volume (0,3 ml) were recorded using "Bruker EMX-300" spectrometer at frequency 9,38 GHz and microwave power 2 mW in temperature range 5 – 80 K. Each spectrum was recorded in accumulation mode (number of scans was 5).

Experimental results

Nearly all ESP spectra recorded at 5 K showed a combination of two new signals at $g = 5{,}85$ and 8,6 and regular absorption lines from Fe^{3+} in transferrin ($g_\perp = 4{,}21$) and Cu^{2+} in ceruloplasmin ($g_\perp = 2{,}058$) (fig.1).

Importantly, the amplitude of these new signals was rather small and slightly distinguishable (fig.1a) but in some cases ($n = 5$) the intensity of the line at $g = 5.85$ was significantly higher, the ratio of line intensities increasing up to 12:1 (fig.1b). The value of *g*-factor and unchangeable shape of the lines one may assign to high-spin Fe^{3+} ($S = 5/2$) in heme. The inverse temperature-dependent pattern of signal intensities in the range of 5 – 40 K (decrease up to zero at 40 K) is characteristic of cytochromes, more likely cytochrome *c* (fig.2).

At the same time such rhombic distortion of cytochrome *c* heme was not observed earlier, while lines at $g \sim 8$ and 8,52 were assigned to high-spin ferric form of cytochrome *P*-450 and rhombically distorted heme of bovine liver catalase, respectively [2, 3]. Hence, two different explanations are possible: either they correspond to 2 different centers (with nearly tetragonal iron environment) or to rhombically distorted Fe^{3+} heme.

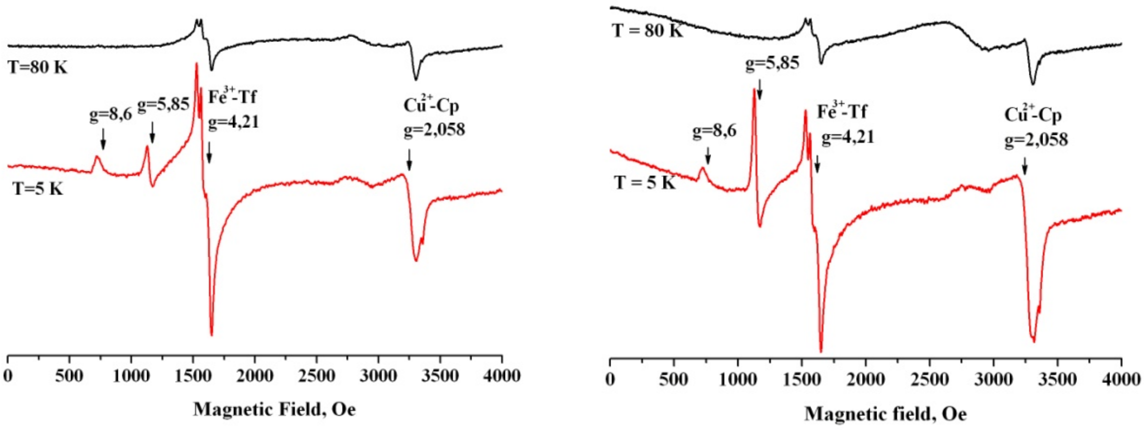

a b

Fig.1. EPR spectra received at $T = 80$ K and $T = 5$ K.
a — intensities of the signals with $g = 8{,}6$ and $g = 5{,}85$ was slightly distinguishable,
b — the ratio of line intensities up to 12:1

In two sportsmen's serum ESP spectra showing relatively low signals at $g = 5{,}85$ and 8,6 there was a new more intensive absorption line at $g = 3{,}15$ with specific for cytochrome temperature-dependent pattern (fig.3). This signal we assigned to low spin heme Fe^{3+}.

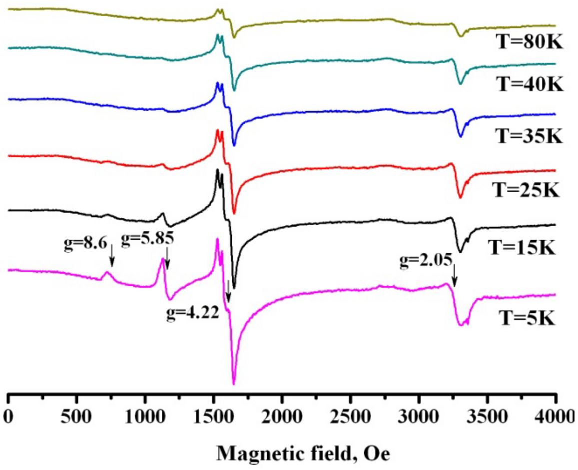

Fig.2. Temperature dependence of line intensities in the range of $T = 5 – 80$ K

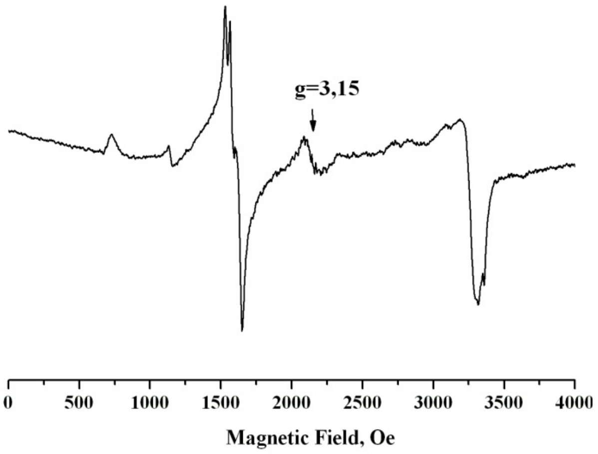

Fig.3. EPR spectra recorded at $T = 5$ K

Noteworthy are unexpected results obtained for two serum blood ESR spectra (see fig.4). The intensive broad unresolved absorption line at temperature range of 30 – 80 K was registered. Unusual features of this signal are the shift of g-factor value proportional to the temperature increase (from $g = 2{,}95$ at 30 K to 2,31 at 80 K) and line width changes. Somewhat similar was observed in solids, namely, in chain-polymer complex including triple-spin exchange-coupled systems in temperature range of 70 – 220 K [4]. This phenomenon was explained by spin exchange between the different multiplet triple-spin systems.

One study subject presented with well-resolved triplet with $g_1 = 2{,}037$; $g_2 = 2{,}008$ and $g_3 = 1{,}980$ recorded at 80 K. To identify this spectrum the serum sample was supplemented with industrial nitroxyl spin label TEMPO (fig.5).

Again, the similar triplet was found with $g_1 = 2{,}017$; $g_2 = 2{,}002$; and $g_3 = 1{,}982$ from nitroxyl radical. The reason for nitroxyl complex formation in serum blood of sportsmen is not yet clear. Routine serum plasma chemistry tests in study subjects showed no significant deviations from the normal range.

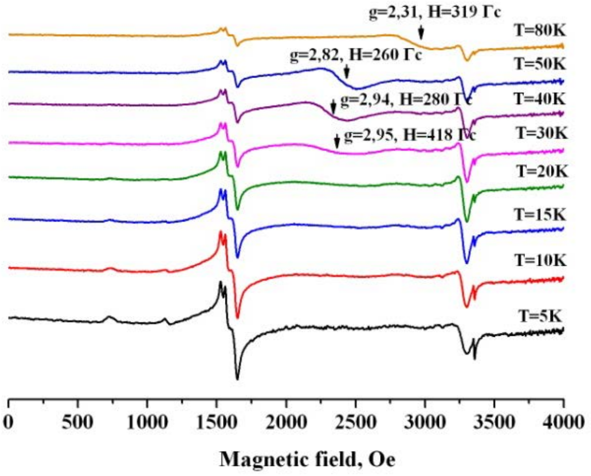

Fig.4. EPR spectra of serum blood recorded in the temperature range of 5 – 80 K

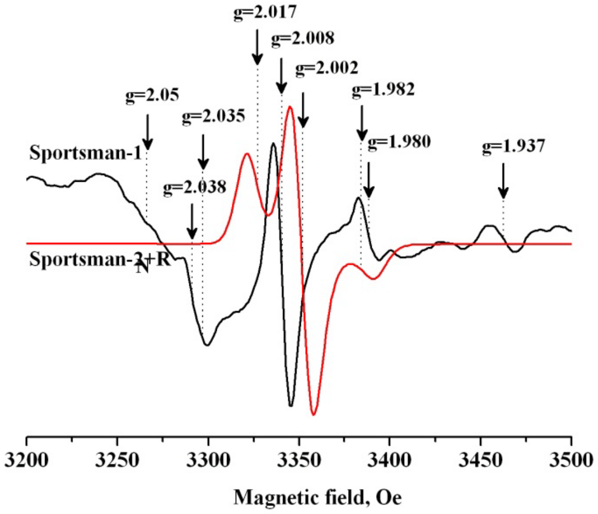

Fig.5. EPR spectra from two sportsmen. EPR spectrum from sportsman-1 (black line) and EPR spectrum from sportsmen-2 (red line) with the addition of industrial nitroxide spin labels TEMPO (containing radical NO) in to serum sample

Conclusion

Studies have shown that the EPR spectra at liquid-helium temperatures contain the additional lines. However, more research is needed to establish the nature of their occurrence, which may give the answer to the question about the possibility of their use as markers of metabolic disorders.

References

[1] Ibragimova M.I. *et al*. Biofisika (2014) 59, 520-526.

[2] Shergill J.K. *et al*. Biochem. J. (1995) 307, 719-728.

[3] Williams-Smith D.L., Patel K. Biochim.Biophys Acta (1975) 405, 243-252.

[4] Veber S. Author's abstract of dissertation, Novosibirsk, 2009.

Synthesis of lanthanide trifluorides for magnetic resonance research

E.M. Alakshin[1], A.V. Klochkov[1], S.L. Korableva[1], F.F. Shafikov[1], A.A. Stanislavovas[1],
M.S. Tagirov[1,2], M.Yu. Zakharov[1]

[1]Kazan Federal University, 420008, Kremlevskaya 18, Kazan, Russia.
[2]Institute of Perspective Research, TAS, 420111, L. Bulachnaya 36a Kazan, Russia

e-mail: mikhailzakharo@yandex.ru

Lanthanide nanoparticles can be used as biolabels, lasers, optical amplifiers, optical-display phosphors [1 – 10]. Investigation of PrF_3 is interesting because of possibility of dynamic ^{3}He nuclear polarization using dielectric Van Vleck paramagnetic were suggested in [11]. The results of "^{141}Pr – ^{3}He" system investigation are presented in [12 – 16]. Gd^{3+} EPR of LaF_3 nanoparticles doped with Gd is an actual problem, because the theory of contrast agents requires information about electron relaxation of Gd which used as “core material” of nanoparticle. DyF_3 and TbF_3 crystals have magnetic phase transition at $T_c = 2.55$ K and $T_c = 3.95$ K correspondingly and it is interesting to find out how will be T_c for nanosized crystals. LnF_3 (Ln =Pr, La, Dy, Tb) nanoparticles were obtained by methods of colloidal chemistry. Recent results and current progress will be reported. The nanosized samples were synthesized by using the methods described in [13, 17].

The crystal structure of the samples has been characterized by X-ray diffraction (XRD) (fig.1). Crystallinity was calculated using plots of XRD. The shape of peaks indicates high crystallinity of PrF_3 and LaF_3 (>80%). Crystallinity of DyF_3 and TbF_3 are less.

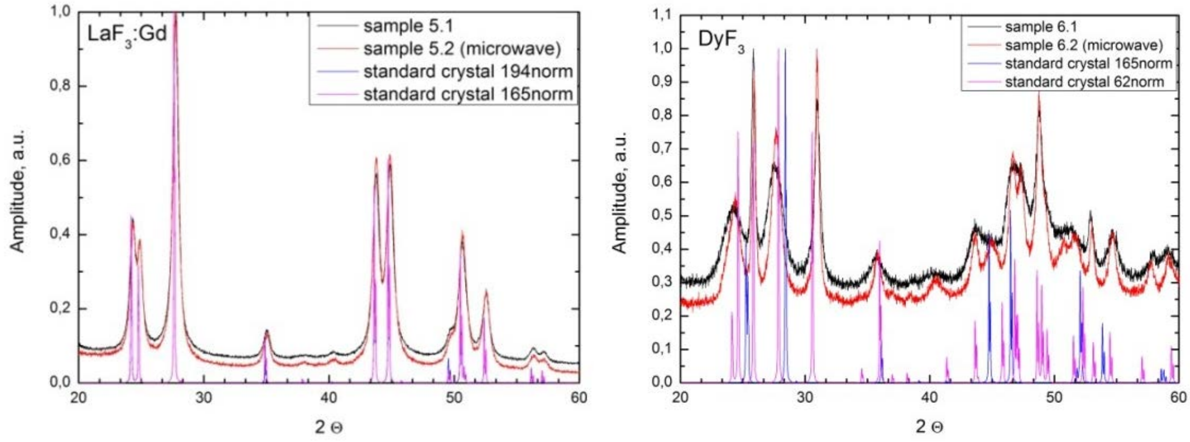

Fig.1. XRD results of LnF_3:Gd samples(left) and DyF_3 nanoparticles(right).

High-resolution transmission electron microscopy (HRTEM) images of synthesized samples are presented on fig.2, fig.3 and fig.4.

Acknowledgments

The work is performed according to the Russian Government Program of Competitive Growth of Kazan Federal University and supported by the Russian Foundation for Basic Research (project no. 14- 02-31290 mol_a).

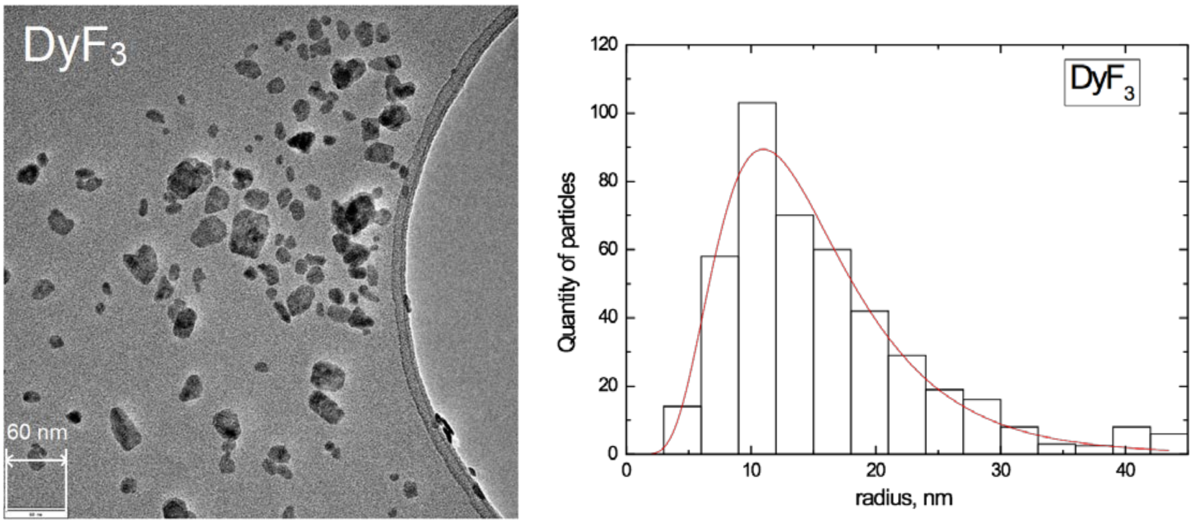

Fig.2. HRTEM image of DyF_3 nanoparticles and size distribution.

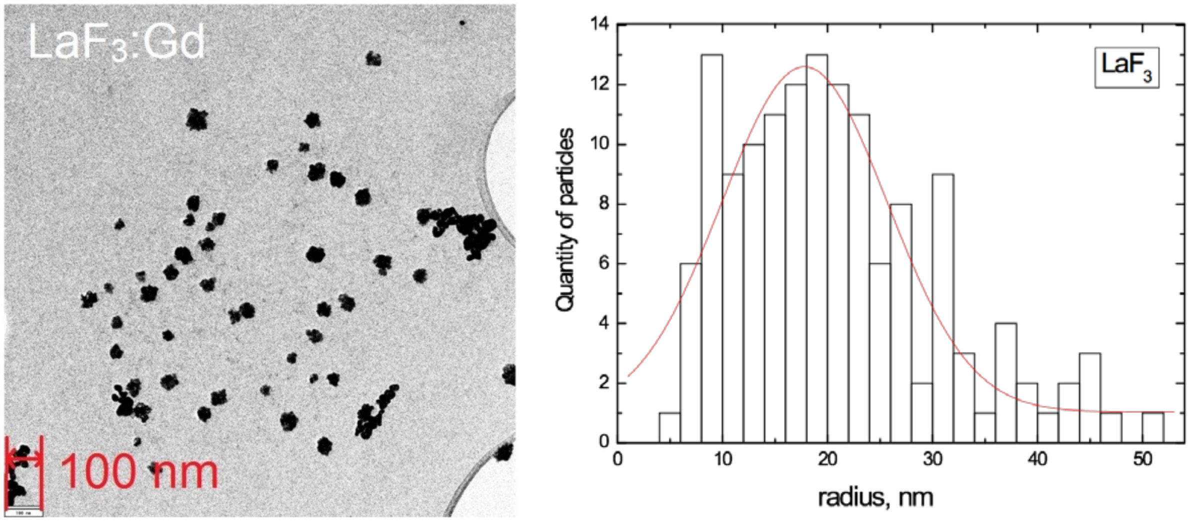

Fig.3. HRTEM image of LaF_3 nanoparticles (sample 4) and size distribution.

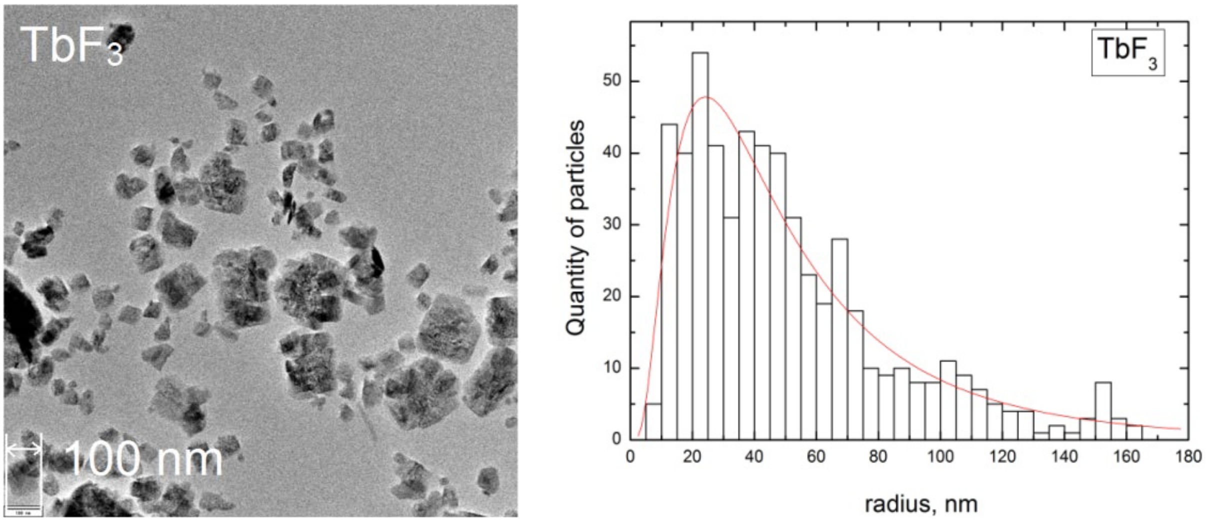

Fig.4. HRTEM image of TbF_3 nanoparticles (sample 1) and size distribution .

References

[1] F. Vetrone and J. A. Capobianco, Int. J. Nanotechnol.,V.5, P.1306, (2008).

[2] B. M. Tissue, Chem. Mater.,V.10, P.2837, (1998).

[3] Z. G. Chen, H. L. Chen, H. Hu, M. X. Yu, F. Y. Li, Q. Zhang, Z. G. Zhou, T. Yi and H. Huang, J. Am. Chem. Soc.,V.130, P.3023, (2008).

[4] D. K. Chatteriee, A. J. Rufalhah and Y. Zhang, Biomaterials,V.29, P.937, (2008).

[5] P. R. Diamente, M. Raudsepp and F. C. J. M. van Veggel, Adv. Funct. Mater.,V.17, P.363, (2007).

[6] S. Sivakumar, P. R. Diamente and F. C. J. M. van Veggel, Chem.–Eur. J., V.12, P.5878, (2006).

[7] X. Teng, Y. Zhu, W. Wei, S. Wang, J. Huang, R. Naccache, W. Hu, A. I. Y. Tok, Y. Han, Q. Zhang, Q. Fan, W. Huang, J. A. Capobianco and L. Huang, J. Am. Chem. Soc., V.134, P.8340, (2012).

[8] V. Mahalingam, F. Vetrone, R. Naccache, A. Speghini and J. A. Capobianco, Adv. Mater.,V.21, P.4025, (2009).

[9] S. Sarkar, C. Hazra and V. Mahalingam, Chem.–Eur. J., V.18, P.7050, (2012).

[10] S. Sarkar, B. Meesaragandla, C. Hazra and V. Mahalingam,Adv. Mater.,V.25, P.856, (2013).

[11] Tagirov, Tayurskii, JETP Letters, 1995, 61: 652–655

[12] E.M. Alakshin, B.M. Gabidullin, A.T. Gubaidullin, et al., arXiv:condmat., V.1104., P.0208. - http://arxiv.org/abs/1104.0208 (2011).

[13] E.M. Alakshin, R.R. Gazizulin, A.V. Egorov, et al., Journal of Low Temperature Physics V.162, N.5/6, P.645 – 652, (2011).

[14] E.M. Alakshin, D.S. Blokhin, A.M. Sabitova, et al., JETP Letters. V.96, N.3, P.194-196 (2012).

[15] E.M. Alakshin, A.S. Aleksandrov, A.V. Egorov, et al., JETP Letters V.4, N.3, P.259-261, (2011).

[16] E.M. Alakshin, R.R. Gazizulin, A.V. Klochkov, et al., JETP Letters. V.97, N.10, P.665-668 (2013).

[17] L. Ma et al., Materials Letters, 61, 2765 (2007).

Electric field effect in electron paramagnetic resonanceof the $SrTiO_3$:Mn crystals

B.F. Gabbasov, D.G. Zverev, A.A. Rodionov, E.Y. Pokryshkina, R.V. Yusupov

Kazan Federal University, Kazan, Tatarstan, 420008 Russia

e-mail: bulgabbasov@gmail.com

Introduction

Strontium titanate $SrTiO_3$ (STO) is a strongly polarized dielectric belonging to the class of ABO_3 oxides. Although it is investigated for a quite long time, new effects interesting from both applied and fundamental points of view are found. It is known that STO crystals at room temperature have cubic perovskite structure and below 105 K undergo antiferrodistortive structural phase transition to the tetragonal phase associated with rotation of the oxygen octahedra about the [001] cubic axis. Due to the equivalence of the three four-fold axes in the cubic phase the structural domains can be formed with the differently oriented tetragonal *c*-axis.

Strontium titanate represents the so-called incipient ferroelectrics. This type of compounds exhibit all signs of an impending phase transition to the polar phase, however, the transition do not occur up to the lowest temperatures. Already at room temperature STO has a high value of the dielectric constant (about 300) whereas at low temperature is increases drastically (up to $2{\cdot}10^4$ at 4.2 K).

Incipient ferroelectrics reveal a pronounced sensitivity to various external perturbations. There are papers that demonstrate significant modification of different STO characteristics under application of the uniaxial stress, electric field, UV light or doping. Recently, interesting results were obtained on STO doped with Mn ions: anomalies of magnetic and electric properties in single crystal and ceramics were found. The so-called magnetoelectric multiglass phase was presumably formed [1]. This phase reveals long-range order effects in both the dielectric and magnetic properties. Later, however the magnetic response was related to the segregation of manganese impurities and formation of Mn_3O_4 inclusions ferrimagnetic below ~ 43 K. Appearance of ferroelectric anomalies associated with Mn doping remains an open question.

STO:Mn is studied for quite long time using EPR spectroscopy. It is a powerful experimental tool for determination of the microscopic structure and properties of impurity centers. Three types of manganese centers (with different valences) were found in the EPR spectra. Manganese ions can substitute for strontium ions in the cuboctahedral and for titanium ions in the octahedral coordinations. At the moment Mn^{2+} impurity is most likely to replace the Sr ion in the crystal lattice whereas Mn^{3+} and Mn^{4+} replace Ti ions.

Mn^{2+} ions EPR spectra reveal an unusual temperature dependence: EPR lines experience significant broadening when temperature decrease from 300 K to ~ 80 K [2]. Observation of the spectra at lower temperatures is rather complicated. The temperature transformation of the EPR spectrum is opposite to the relaxation broadening observed for e.g. Mn^{4+} ions. However, such dependence is typical for paramagnetic centers of the dynamic origin. In this case narrowing of the EPR lines at elevated temperatures is associated with the motional averaging when the anisotropic components of the spectra are averaged out. In this case the broadening is related to slowing down of the center dynamics. EPR spectra of Mn^{2+} ions are almost not observable down to ~ 10 K. However, at $T < 10$ K EPR spectra of low-symmetry centers with $S = 5/2$ are detected. This behavior could be explained by the transition of the dynamic Mn^{2+} centers to static ones because of the locking in one of the adiabatic potential minima inequivalent due to interaction with random strains or electric fields.

It is found that the magnitude of dielectric anomalies increases together with concentration of the Mn^{2+} ions in sample. This indicates that Mn^{2+} ions participate in the formation of the polar phase in strontium titanate doped with manganese. Possibility of this formation is associated with presence of re-orientable dipolar momentum on Mn^{2+} centers. Furthermore the only possibility of the existence of the dynamical Mn^{2+} center is the off-center location in “big” Sr position and the electric field of this dipole induces spontaneous polarization in the crystal. We should notice that this off-center Mn^{2+} impurity ion should not have center of inversion.

Later, Müller reported in one of the early articles that at the temperatures above 105 K (cubic phase of strontium titanate crystal) in the EPR spectrum Mn^{4+} ion shows the axial symmetry. As for the case of Mn^{2+} ion authors attributes this fact to Mn^{4+} ion displacement from the central position [3].

Thus, the aim of this investigation is determination of the presence of an inversion symmetry for Mn^{2+} and Mn^{4+} ions. Traditional approach in this case is study of the electric-field effect (EFE) in the EPR spectra. In a typical EPR experiment paramagnetic centers in the inversion-nonequivalent positions yield identical spectra. Applying the electric field leads to shift of EPR lines. In this case, observation of the linear dependence of this shift on the electric field testifies about the absence of the center of inversion. On the other hand, if the effect is quadratic then the case of the central position is realizes.

Materials and Methods

High quality $SrTiO_3$:Mn single crystals (Furuuchi Chemical Corp., Tokyo) grown by the Verneuil method from high purity (99.999%) initial components were taken for investigation. The series of STO:Mn crystals that was at our disposal consisted of 12 samples grown in different atmosphere (oxidizing/reducing/neutral), with different stoichiometry compositions and doped with either MnO or MnO_2.

EPR spectra were measured with a commercial Bruker ESP300 spectrometer operating in the microwave X range (9.4 GHz) in a standard ER4102ST rectangular cavity with the TE_{102} microwave mode. The sample temperature was controlled by an ER4112HV continuous flow helium system produced by Oxford Instruments.

Low temperature measurements of strontium titanate using EPR method are quite complicated. Dielectric permeability of STO crystals is huge and strongly dependent on the temperature. Moreover, permeability fastly increases when the temperature approaches 4.2 K to the values of the order of 10^4 and is substantially disturbs the distribution of the electromagnetic field in the microwave cavity. To lower this effect, the sample size should be smallest possible.

Results and Discussion

At relatively high temperatures in the EPR spectra of $SrTiO_3$:Mn single crystal manganese ions in different oxidation states are detected. When B || [001] the EPR spectra of Mn^{2+} ($S = 5/2$) and Mn^{4+} ($S = 3/2$) ions are detected in the vicinity of $g \sim 2$ (fig.1). Both centers have cubic symmetry and represent six EPR transitions originating from the hyperfine interaction of the electronic spin with host nucleus (^{55}Mn, $I = 5/2$, nat. ab. 100%). Relatively strong hyperfine interaction leads to the observation of the fine structure with the splitting value prevailing for the low- and high-field hyperfine components.

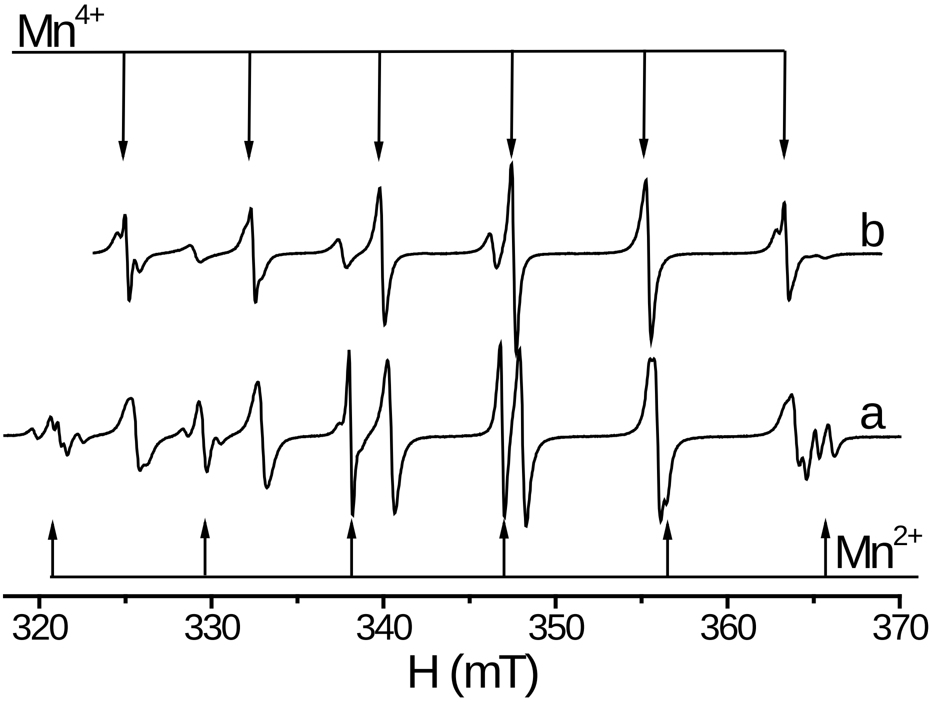

Fig.1 EPR spectra of $SrTiO_3$:Mn in orientation B || [100] at T = 300 K (a) and T = 200 K (b)

Application of the electric field to the (001)-oriented platelet sample at T = 150 K leads to clearly-resolved modification of the fine structure of the EPR spectrum for both centers. For Mn^{4+} we observed quadratic dependency of the fine structure components splitting (fig.2 right) and, thus, confirm the inversion symmetry for this ion. Therefore Mn^{4+} ion should occupy the center of the octahedron formed by the oxygen ions. This model contradicts with the hypothesis of K.A. Muller [3] on the off-center position of the Mn^{4+} ion.

We would like to note the large magnitude of the Mn^{4+} ion fine component splitting as usually the quadratic electric-field effect is small. Moreover, the observed effect had about ten times larger value than predicted due to the effect of the electrostriction. However, this splitting could be explained by relatively strong influence of the ionic and/or electronic polarizations to the crystal field [4].

The effect of the influence of external electric field was performed also for Mn^{2+} ion at two temperatures 300 K and 4.2 K. At T = 300 K after application of the electric field in the EPR spectra we observed broadening of the Mn^{2+} ion fine structure components. It is known that at room temperature Mn^{2+} is dynamic (there are jumps between three (or six) equivalent positions) and, therefore, this behavior could be explained by the deceleration of this dynamic [2]. At T = 4.2 K it is possible to observe two paramagnetic centers associated with Mn^{2+} with different symmetry. One of them is axial Mn^{2+} ion with crystal field component B_{20} oriented along [001] axis of the crystal and second one has orientation of the B_{20} along [001]. For both centers no any influence of the electric field on the fine structure was observed. It seems that Mn^{2+} ions have a strongly polarized surrounding with huge local electric field intensity and, therefore, the influence of the relatively small external electric field is insignificant for observation the visible changes in the magnetic properties of the ion.

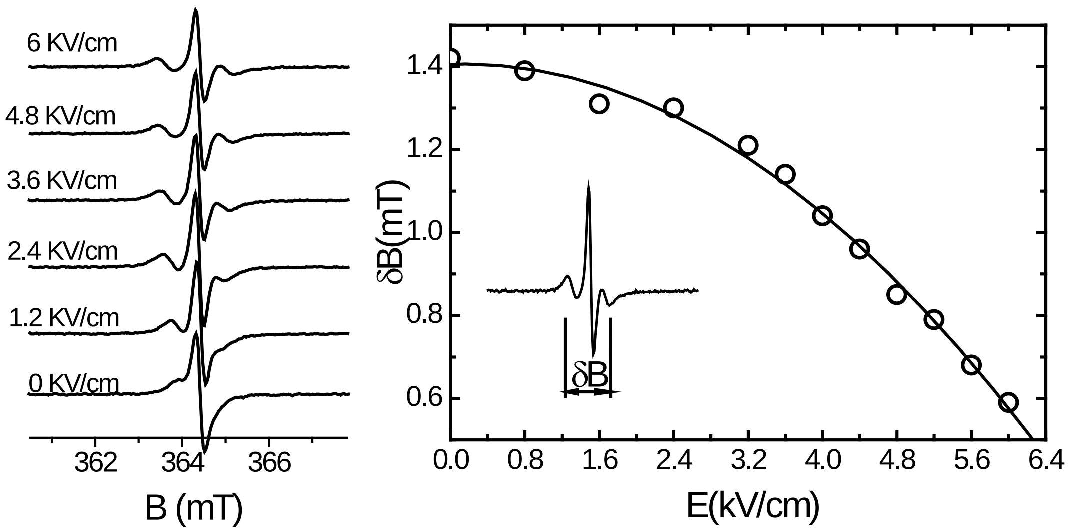

Fig.2 Left figure shows EPR spectra of the high-field hyperfine component of the Mn^{4+} center in $SrTiO_3$ single crystal for different external electric field values at T = 150 K and B || [001]. Right figure depicts the dependence of the splitting between the fine structure components on the electric field value.

Acknowledgement

The EPR spectra presented in the paper were measure with the equipment of the Federal Center of Shared Facilities of Kazan Federal University. This work was supported by Russian Foundation for Basic Research (project no. 14-02-31166 mol_a).

References

[1] Shvartsman V. V. et al, Phys. Rev. Lett., 2008. V. 101. P. 165704

[2] Zverev D.G. et al, Opt. and Spectr. 2014., V. 116. P. 818.

[3] Müller K. A., Phys. Rev. Lett. 1959., V. 2. P. 341

[4] Unoki H. and Sakudo T., Journ. Phys. Soc. J., 1973. V. 35. P. 1128

[5] Rupprecht G. and Winter W. H., Phys. Rev., 1967. V. 155. P. 1019

The coherent precession of magnetization in yttrium iron garnet

Yu.M. Bunkov[1,2], P.M. Vetoshko[3], M.S. Tagirov[1], N.A. Tukmakova[1]

[1]Kazan Federal University, 420008, Kremlevskaya 18, Kazan, Russia.
[2]Institute Neel, CNRS et University Joseph Fourier, F-38042 Grenoble, France.
[3]Institute of Radio Engineering and Electronics, RAS, 125009, Moscow, Russia

e-mail: Nadejdatukmakova@yandex.ru

Results of demagnetizing effect in yttrium iron garnet (YIG) $Y_3Fe_5O_{12}$ single crystal thin films will be reported.

Experiments were performed on X-band EPR spectrometer Varian E-12 ($f \approx 9.3$ GHz) at room temperature. The samples were grown in “Carat” company (Lvov) by standard isothermal LPE method during the joint work with the Institute of Kotelnikov Radio Engineering and Electronics of the RAS [1].

The YIG is a well-studied crystal with the ferrimagnetic ordering ($T_c = 560$ K). One-layer YIG films were studied in the experiments. The top layer was a thin film of yttrium iron garnet with a thickness from 6 to 9 μm. The substrate was made of gadolinium gallium garnet, which thickness was from 460 to 490 μm. The samples were circles of irregular forms or small pieces of about 1 mm.

The typical YIG thin film FMR spectrum with perpendicular orientation of the external magnetic field is shown in fig.1a. The power of the microwaves was 10 mW, the amplitude of modulation was 5 mOe, the temperature was about 300 K. Fig.1b is the integral of the FMR spectrum, which shown in fig.1a.

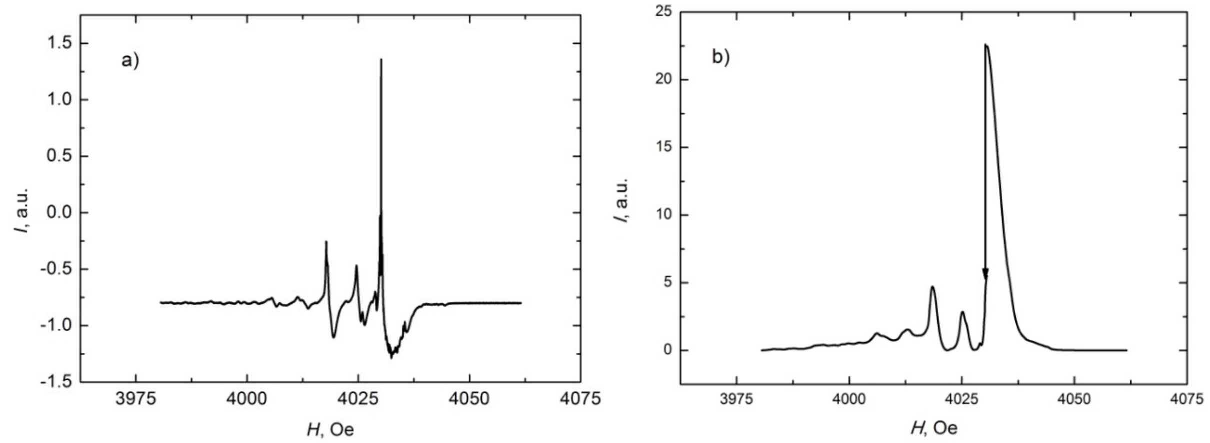

Fig.1. a) The FMR spectrum of YIG thin film (perpendicular orientation $H \perp$ film surface), b) The integral of the spectrum shown in fig.1.a.

Fig.2 shows integrated experimental spectra with different direction of the magnetic field sweeping at the few microwave power values. Fig.3 shows integrated experimental spectra with different direction of the magnetic field sweeping at the 30 mW microwave power.

Fig.4 shows the simulated dependence of the absorption intensity on the magnetic field shift (concerning the value of the resonance magnetic field in the absence of the microwave power). AW — parameter, A — dimensional coefficient, W — microwave power. The results shown in fig.4, and the related direct broach the magnetic field (in the direction of increasing values of ΔH), while the results shown in fig.4b correspond to a sweeping of the field in the opposite direction. It should be noted that at the increasing of the magnetic field sweeping the values of the resonance magnetic field higher than at the decreasing of the magnetic field sweeping. Relation to the resonance frequencies of absorption [2]:

$$\omega_{res} = \gamma\left(H_{0res} - 4\pi M_s\right)$$

$\gamma = 2.8$ MHz/Oe for YIG, M_s — saturation magnetization of sample, H_{0res} — resonance field value.

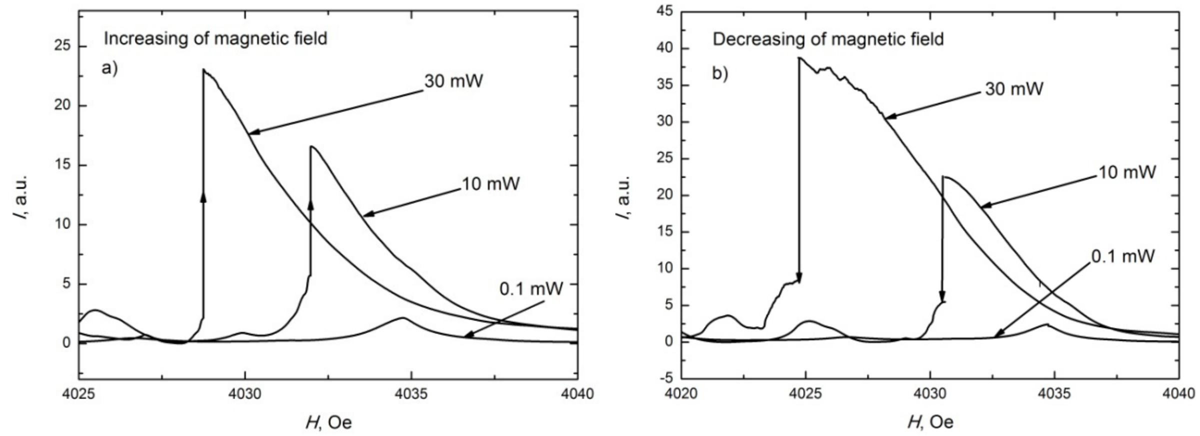

Fig.**2**. Integrated experimental spectra (perpendicular orientation).

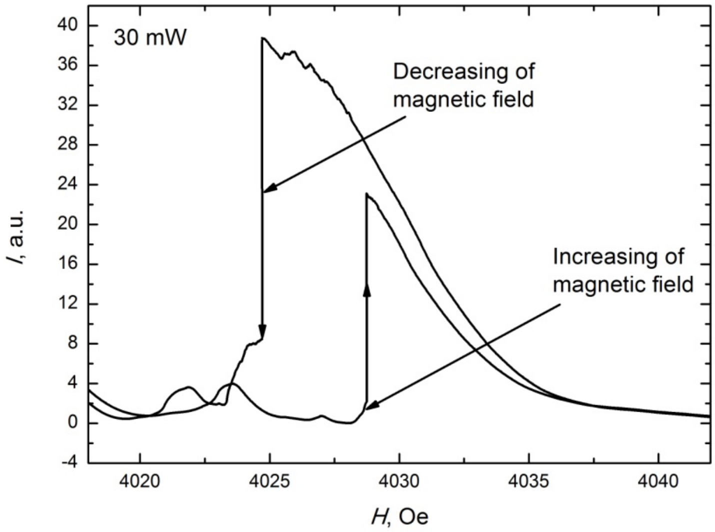

Fig.3. YIG thin film FMR spectra at 30 mW microwave power.

From relation to the resonance frequencies of absorption it follows that for a large value of the magnetization M_S at a constant frequency absorption corresponds to a larger value of the resonant field. Microwave power leads to appearance of the magnons. Fig.5 shows simulated FMR spectra at the different directions of the magnetic field sweeping ($AW = 30$ Oe, A — dimensional coefficient, W — microwave power).

The results presented here are very well matched to ideas about Boze nonequilibrium magnon condensation. In particular, in magnetic systems with a large dynamic offset frequency. Such as antiferromagnets with Suhl-Nakamura interaction [3, 4] and the A-phase of superfluid ^{3}He [5 – 7]. It should be noted that in YIG films have already observed effect meaningful as Bose condensation of magnons [8]. In this case, the magnetic field was parallel to the film surface. This raises the minimum magnon energy for some non-zero *k*. It was shown by methods of magneto-optics that magnons with non-zero k condensed in this minimum. However, they do not emit a signal induction. This type of magnons BEC is very exotic. On the contrary, under our experimental conditions with YIG, in a magnetic field perpendicular to the film surface minimum energy is at zero in (uniform magnetization precession). This BEC mechanism is shared of many magnetically ordered systems [9]. Therefore, the continuous magnetic resonance, we observe large signal emission magnons that is coherent RF field. However, as shown by studies in other systems, this signal is not induced by the RF field. This is a signal of the magnons BEC state correlated in phase with the signal of the RF field. Listed here pioneer experimental results require further study, and interpreting.

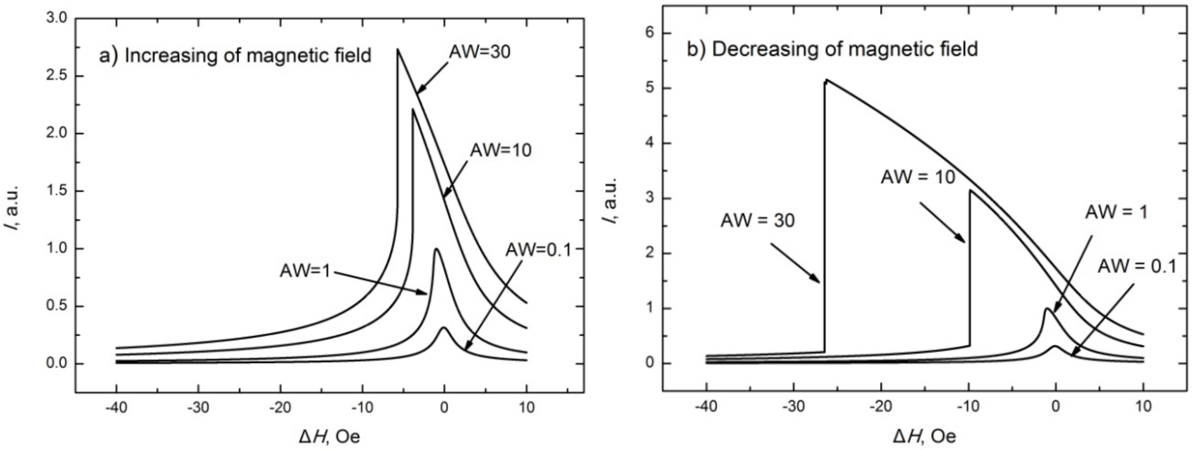

Fig.4. Simulated FMR spectra.

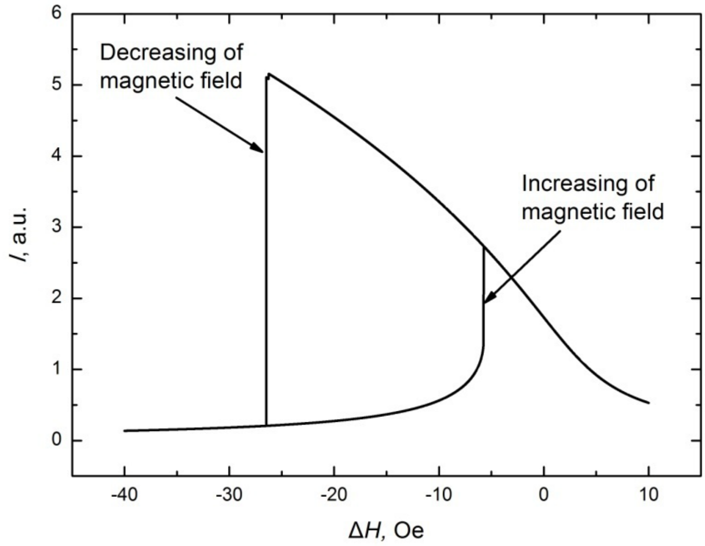

Fig.5. Simulated FMR spectra at the different directions of the magnetic field sweeping
(AW = 30 Oe, A — dimensional coefficient, W — microwave power).

Acknowledgments

We are grateful to I.G. Motygullin for measuring of FMR spectra and illuminating discussions. The work is performed according to the Russian Government Program of Competitive Growth of Kazan Federal University.

References

[1] I.I. Syvorotka, P.M. Vetoshko, V.A. Skidanov, V.G. .Shavrov, and I.M. Syvorotka, IEEE T. Magn., 51 2000703, (2015)/

[2] Ferromagnetic Resonance. (Ed. S.V. Vonsovskii,) – P. 41. – State Publishers of Physical and mathematical literature M. – (1961). – in Russia.

[3] Yu.M. Bunkov, E.M. Alakshin, R.R. Gazizulin, A.V. Klochkov, V.V. Kuzmin, V.S. L'vov, and M.S. Tagirov, Phys. Rev. Lett. 108, 177002 (2012).

[4] Yu.M. Bunkov, E.M. Alakshin, R.R. Gazizulin, A.V. Klochkov, V.V. Kuzmin, T.R. Safin, M.S. Tagirov, JETP Letters, 94, 68-72 (2011).

[5] T. Sato, T. Kunimatsu, K. Izumina, A. Matsubara, M. Kubota, T. Mizusaki, and Yu.M. Bunkov, Phys. Rev. Lett. 101, 055301 (2008).

[6] P. Hunger, Y.M. Bunkov, E. Collin and H. Godfrin, J. of Low Temp. Phys 158, 129-134 (2010).

[7] Yu.M.Bunkov, G.E.Volovik, Europhys. Lett, v. 21, p. 837 (1993).

[8] S.O. Demokritov, V.E. Demidov, O. Dzyapko et al., Nature 443, 430 (2006).

[9] Yu. M. Bunkov, Physics-Uspekhi, 53, 843 (2010).

Selective multidimensional multinuclear NMR spectroscopy: radiofrequency pulse shapes in the MUSLE experiment

M.G. Morozov, Yu.E. Chernysh

[2]Southern Federal University, Institute of Physical and Organic Chemistry,
344090, 194/2 Zorge st, Rostov-on-Don, Russia

e-mail: morozov.rf.nmr@gmail.com

Selective pulses are well established in NMR spectroscopy as an indispensable tool for selective excitation, inversion, refocusing, decoupling. Usually, a rectangular, gauss, sinc or top-hat response to the selective pulse is desired, meaning that the magnetization is fully inverted (for an inversion pulse) or excited with a constant phase (for an excitation pulse) within a specified region of the spectrum, while remaining unperturbed outside of this spectral band [1].

The new technique — MUSLE (MUltiplet Single Line Excitation) is proposed [2]. This technique is supposed to solve problems of molecular structure determination and its dynamics behavior. Also using the MUSLE technique leads to sufficient NMR spectrum simplification and hence has advantages in investigation of chemical processes, a spin exchange and molecule dynamics behavior in multicomponent spin systems.

It is a more modified and powerful analytical tool of the early developed one and successfully verified technique by scientists of Institute of Physical and Organic Chemistry of Southern Federal University — MUSEX (MUltiplet Selective EXcitation). [3, 4].

In a new experiment different combinations of radiofrequency pulses can be used. The main five combinations are presented below.

1. $(\pi/2)_x - t_1 - (\pi/2)_x (A^1) - t_2$
2. $(\pi/2)_x (A^1) - t_1 - (\pi/2)_x - t_2$
3. $(\pi/2)_x (A^1) - t_1 - (\pi/2)_x (X^3) - t_2$
4. $(\pi/2)_x (A^1) - t_1 - (\pi/2)_x (A^1) - t_2$
5. $(\pi/2)_x (A^1) - t_1 - (\pi/2)_x (A^2) - t_2$

$(\pi/2)_x (A^1)$ means excitation of single line of A spin doublet. Each of these pulse sequences is suitable for a concrete dynamic NMR problem. Here we discuss observables for the weakly-coupled spin system AX. The schematic spectrum of such spin system is shown in fig.1.

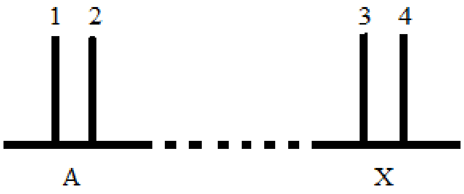

Fig.1. The schematic view of a weakly-coupled spin system one-dimensional spectrum.

The successful application of this method requires not only appropriate equipment but also effective mathematical models that provide an opportunity to make precise quantum mechanical calculation of spectral parameters and to analyze NMR spectrum of investigated spin systems. For this aim the special mathematical tool based on product operator formalism (POF) has been developed. In this model selective pulses acting on single multiplet lines are described by linear combination of product operators [5.6]. The model ensures a rigorous quantum mechanical NMR pulse experiments description. The main feature of this model is that the operators have pure physical meaning.

The evolution of product operators under chemical shift operator is shown in detail in the fig.2. The treatment $-I_y^{A_1}\cos\omega_1 t_1 + I_x^{A_1}\sin\omega_1 t_1, -I_y^{A_2}\cos\omega_2 t_1 + I_x^{A_2}\sin\omega_2 t_1$ corresponds to two lines of *A* spin doublet.

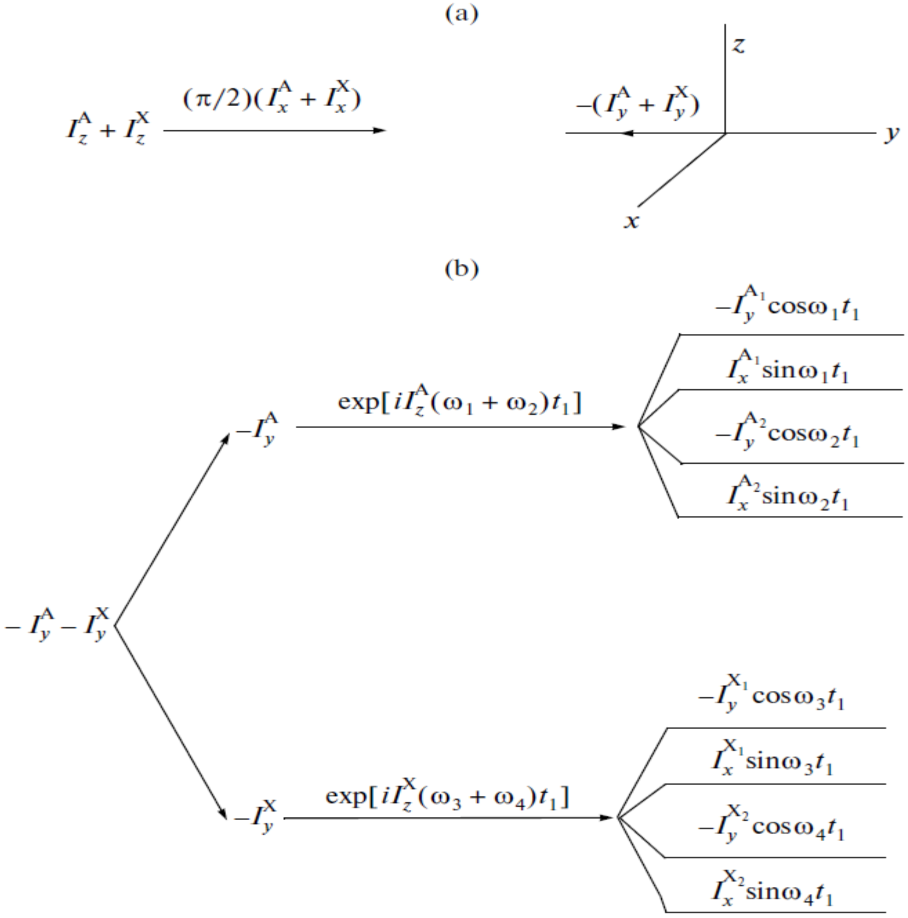

Fig.2. Evolution of spin system AX after first non-selective pulse under chemical shifts.

The real spectrum under consideration is presented on fig.3. Where one can observe 2 doublet of doublets patterns. For our purpose we can consider each pattern separately because the signals don’t overlap each other. The problem of carrying out the MUSLE experiment lies in the fact that using appropriate the pulse shape and influence of phase cycling on the resulting spectrum. Solving the problem is very important for fulfilling the experiment. The shape and duration of selective pulses acting on a multiplet single line must be chosen very accurately to excite just one line without any neighbor signal. Otherwise we obtain a signal with a high level of noise. (fig.4) Therefore our goal is to find all possible pulse shapes able to produce high quality selective excitation in an idealized experiment.

Also as was shown in [4] the DANTE sequence may be used to produce selective pulses acting as on the whole multiplet or on the single line only.

Care is to be taken to create selective radiofrequency pulse. After accurate phase modulation and choosing appropriate pulse shape one can obtain the following signal of single line on the one-dimensional spectrum. (fig.5)

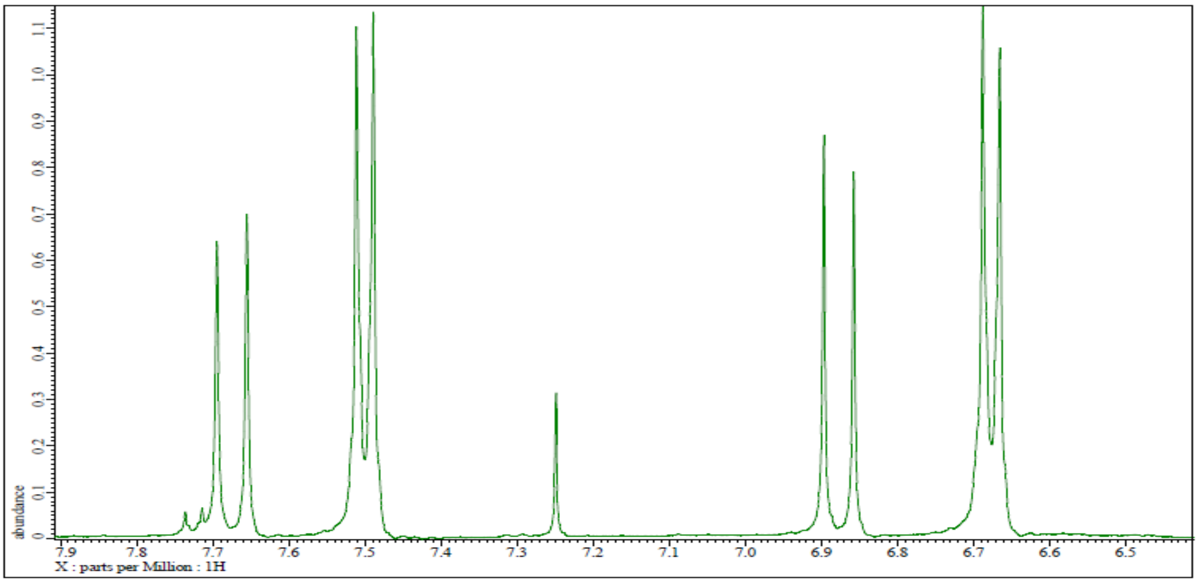

Fig.3 .The one-dimension spectrum of the investigated compound with a doublet of doublets.

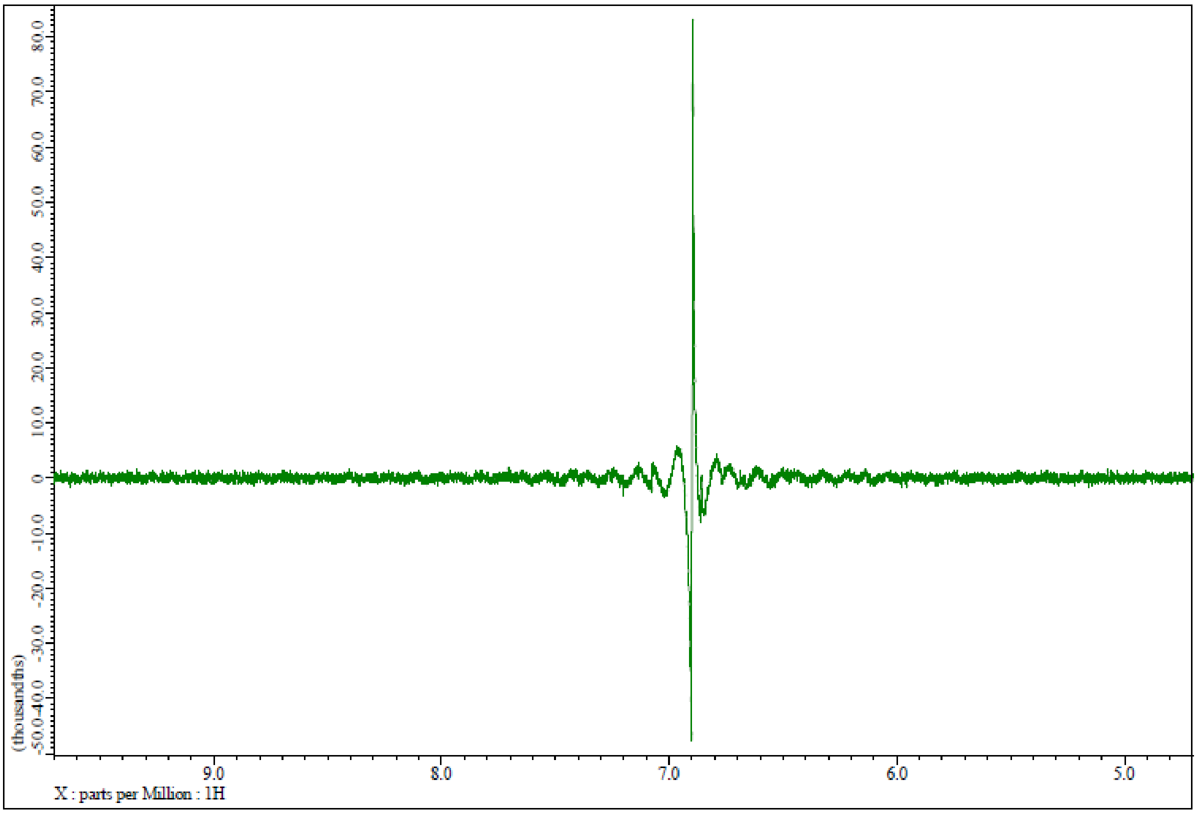

Fig.4. The multiplet single line excitation without appropriate phase modulation and the pulse shape.

On the fig.5 we have used 5 Hz sinc-pulse. There is a pure spectrum of a single line on 6.9 ppm without any noise. Any given selective excitation pulse can be scaled to produce an arbitrary excitation bandwidth. In real systems, however, the total duration of the pulse is usually limited by relaxation. Normally, the shorter the time required to achieve the excitation of a certain bandwidth, the smaller the losses are. Consequently, pulses with a narrower excitation bandwidth for a given excitation time, that is, more selective, pulses, are usually the most practical ones.

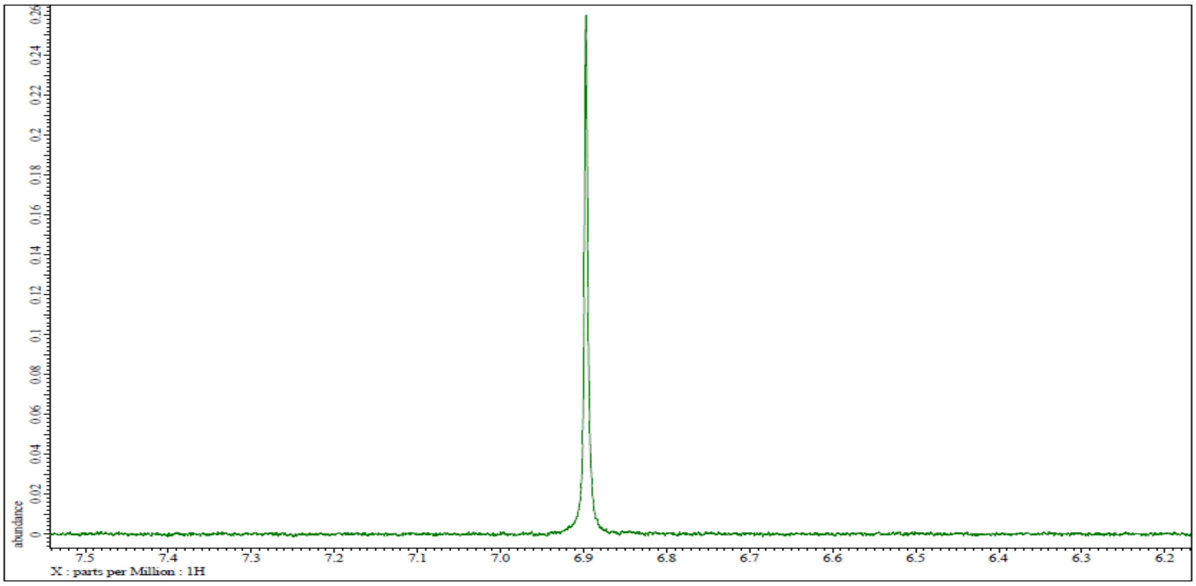

Fig. 5. The multiplet single line excitation with appropriate phase modulation and the pulse shape.

References

[1] M. Veshtort, R.G. Griffin. High-performance selective excitation pulses for solid- and liquid-state NMR spectroscopy.ChemPhysChem 2004,5,834-850.

[2] M.G. Morozov, Yu.E. Chernysh, V.A. Volynkin, R. Freeman. Multiplet Single Line Excitation (MUSLE) experiment to interpret complicated multicomponent systems spectra. Proc. of the XII International Conference: “Spectroscopy of Coordination Compounds”. 2015-c.280.

[3] Yu.E. Chernysh, G.S. Borodkin, B.S. Luk’yanov,et al., Selective NMR Fourier Spectroscopy and Its Application to Investigating Molecular Dynamics Processes (SKNTsVSh, Rostov_on_Don, 2002) [in Russian].

[4] M.G. Morozov, Yu.E. Chernysh. Selective NMR Fourier Spectroscopy: MUSEX-COSY and MUSLE-COSY experiments. Proc. of the XII International Conference: “Spectroscopy of Coordination Compounds”. -cc.276-277

[5] O.W. Sɵrensen, G.W. Eich, M.H. Levitt, G. Bodenhausen and R.R. Ernst, 1983, 16, 163-192

[6] Yu. Chernysh,V. Volynkin. Description of Pulse NMR Experiments by Means of the Product Operator Formalism. Journal of Physical Chemistry B, 2013, Vol. 7, No. 4, pp. 371–382

List of authors

LIST OF AUTHORS

Table of Contents

TABLE OF CONTENTS

TABLE OF CONTENTS

Для заметок

ACTUAL PROBLEMS OF MAGNETIC RESONANCE AND ITS APPLICATION

XVIII International Youth Scientific School

Program
Lecture Notes
Proceedings

Kazan
26 – 30 October 2015

Подписано в печать 20.10.2015.
Бумага офсетная. Печать цифровая.
Формат 60x84 1/8. Гарнитура «Times New Roman». Усл. печ. л. 8,60
Уч.-изд. л. 8,47. Тираж 70 экз. Заказ 68/10

Отпечатано с готового оригинал-макета
в типографии Издательства Казанского университета

420008, г. Казань, ул. Профессора Нужина, 1/37
тел. (843) 233-73-59, 233-73-28